FREMOUW, Edward Joseph, 1934-
RADIOWAVE SCATTERING STRUCTURE IN THE DISTURBED AURORAL IONOSPHERE: SOME MEASURED PROPERTIES.

University of Alaska, Ph. D., 1966
Physics, electronics and electricity

University Microfilms, Inc., Ann Arbor, Michigan

RADIOWAVE SCATTERING STRUCTURE IN THE DISTURBED AURORAL IONOSPHERE: SOME MEASURED PROPERTIES

A

DISSERTATION

Presented to the Faculty of the

University of Alaska in Partial Fulfillment

of the Requirements

for the Degree of

Doctor of Philosophy

by

Edward Joseph Fremouw, B.S., M.S.

College, Alaska

May, 1966

RADIOWAVE SCATTERING STRUCTURE

IN THE DISTURBED AURORAL IONOSPHERE:

SOME MEASURED PROPERTIES

APPROVED:

R. Parthasarathy

J. Tryon

L. Owren / K.W.P.
L. Owren

K. W. Philip
Chairman, K. Philip

Department Head

APPROVED: _____ DATE 4/28/66
Dean of the College of Mathematics,
Physical Science, and Engineering

Vice President for Research and
Advanced Study

ABSTRACT

A technique for quantitative description of radiowave scattering structure in the disturbed auroral ionosphere is developed in this work. Application is made by means of multi-spacing interferometric observations of a radio star. The work is based on the observed fact that sufficient scattering causes a measurable decrease in correlation of output voltages from neighboring antennas. Such correlation decreases are called visibility fades herein and have been called long-duration fades and radio-star fadeouts by other workers.

Random noise theory is employed, and it is assumed that the angular spectrum of the source, as received at the ground after scattering, is randomly phased. However, the usual assumption of a gaussian autocorrelation function to describe the scattering structure is circumvented, and provision is made for the existence of quasi-periodic structure. Further, the usual assumption of weak (single) or strong (multiple) scatter is avoided. The statistical characteristics of amplitude, phase, and complex signal are developed for the general case of arbitrary degree of scatter, using a numerical method.

The technique is applied to observations with phase-switch and phase-sweep interferometers, yielding two important parameters of the received wavefront, the coherence ratio and the wavefront autocorrelation function. The coherence ratio is defined as the ratio of nonscattered to scattered flux received from the source. The wavefront autocorrelation function is defined as the spatial

autocorrelation function of the scattered portion of the (complex) wavefront.

Two quantities which describe the ionospheric scattering region are obtained from the coherence ratio and wavefront autocorrelation function. First, the optical depth of the region (considered as a purely scattering medium) is determined from the coherence ratio. Second, the ionospheric structural autocorrelation function is established jointly from the wavefront autocorrelation function and the optical depth, yielding a statistical description of the average size and idealized shape of the ion-density irregularities which produced the scattering.

Forty-nine visibility fades observed at College, Alaska, between November of 1964 and February of 1966, inclusive, are analyzed. A majority of the fades revealed optical depths in excess of unity at 68 MHz. Optical depth is numerically equal to mean-square fluctuation in radio-frequency phase across a plane at the base of the scattering region, so the fades were characterized by rms phase deviations in excess of one radian at 68 MHz. An approximately inverse-square dependence of optical depth on frequency was obtained from simultaneous observations at 68, 137, and 223 MHz.

At 68 MHz, tri-spacing observations were carried out on east-west baselines of 110 meters (25 λ), 220 meters (50 λ), and 330 meters (75 λ). The observations seldom were consistent with the demands of a gaussian autocorrelation function, as is commonly assumed. Rather, the disturbed auroral ionosphere displays

evidence of quasi-periodic structure in the dimensional range of tens and hundreds of meters. The structure observed is comparable in size to auroral rays.

While most of the observations were consistent with the assumption of a randomly phased angular spectrum, a significant minority was not. Quantitative results could not be obtained in these instances, and they imply the existence of highly developed quasi-periodicity. Theoretical work is needed to bridge the gap between quasi-periodic structure in the sense of random-noise theory and strict periodicity.

Narrow-beam photometers were mounted on one of the interferometer antennas tracking the radio star. Auroral luminosity was recorded along the line of sight during 100% of the visibility fades which occurred at night under clear-sky conditions and during many night-time fades which occurred under cloudy conditions. Thus, VHF radio-star visibility fades in the auroral zone result from scattering by irregularities directly associated with auroral forms, at least at night.

PREFACE

This dissertation culminates several years' work on the problem of radio-wave scattering in the auroral ionosphere. For the opportunity to make whatever small progress is contained herein, I am indebted to Professor Leif Owren. Dr. Owren first introduced me to the problem and to the techniques of radio interferometry, which have been used in this work to attack it. It was he who pointed out to me that techniques familiar in radio astronomy ought to be adaptable to quantitative measurement of ionospheric structure during radio-star visibility fades. The techniques had been adapted by previous workers, but it seemed that more quantitative information ought to be available than had been obtained. This has turned out to be the case, the prime difference between the radio-astronomical situation and the ionospheric one being the highly dynamic nature of the disturbed auroral ionosphere.

A considerable portion of the dissertation is devoted to a detailed review of previous theoretical work by one man, E. N. Bramley. The concepts developed by Bramley are fundamental to the theoretical considerations underlying the experiment. I found a thorough understanding of Bramley's work to be essential before any original contribution could be made to interpretation of interferometric observations in terms of scattering structure in the ionosphere. Accordingly, much of Chapters II and III represent merely foundations for generalization of Bramley's work.

The reader who is familiar with Bramley's work on spaced-aerial reception of scattered waves and with the work by Rice on signal statistics, which underlies Bramley's considerations, probably will find that much of sections IIC, IID1, and IID2 may be omitted. Such a reader also will find the concepts discussed qualitatively in section IIA to be familiar. The reader unfamiliar with these concepts and with Bramley's work probably will find the above-mentioned sections necessary for understanding section IID3, which is a generalization of Bramley's work. It is this generalization which allows experimental determination of quantitative results concerning the disturbed auroral ionosphere.

In Chapter III, the reader who has worked actively on the problem of ionospheric scatter again will find many familiar concepts. In particular, the reader who is thoroughly familiar with Bramley's work on scattering, per se, as opposed to observational considerations, may omit sections D1 and D2. Sections D3 and D4 represent generalizations on this work. Related work is reviewed and generalized very simply in section IIIC. The other sections of Chapter III are essentially reviews of well-known concepts, applied to the experimental problem attacked in later chapters. The generalizations achieved in Chapter III allow relaxation of assumptions, which were previously necessary, concerning the nature of ionospheric irregularities.

The experimental work reported in Chapters IV and V involved the efforts of several people. Salient among these were Mr. R. C. Domke and Mr. W. O. Starner. As electronic technicians at the Geophysical Institute, they contributed a great deal of time and ability to development of the experimental apparatus and to gathering

of data. Contributions were made by Mrs. Nita Balvin and Mrs. Carolyn Grover in the scaling and reduction of data.

I should like to thank the director, Professor K. B. Mather, and staff of the Geophysical Institute for many instances of cooperation and aid and for the professional freedom alloted to graduate students at the Institute. The work obviously would have been impossible without the facilities made available by the Institute under NASA Contract NAS5-3940 and NSF Grant GP947. I am indebted to staff members Professor E. J. Gauss and Dr. R. N. DeWitt for useful discussions which contributed to the theoretical aspects of this dissertation.

The services of Institute draftsmen, Mr. D. C. Wilder and Mr. P. H. Koelsch, and stenographers, Mrs. M. McCoy and Mrs. M. Hayes, in preparing the manuscript are gratefully acknowledged.

Without the active cooperation of Mr. J. M. Lansinger, this work could not have been accomplished successfully without considerable delay. The reliable and versatile phase-sweep interferometer developed under his direction at Boeing Scientific Research Laboratories in Seattle lay at the heart of the experiment. I am further indebted to Mr. Lansinger for data reduction of the phase-sweep observations and for making available the computer facilities of the Boeing Company, which were used in both the theoretical and experimental phases of the work.

Many thanks are due, of course, to the members of my academic committee. Aside from Dr. Owren, these include Professors K. W. Philip, J. G. Tryon, and R. Parthasarathy. Dr. Philip carried the greatest

load in review of the manuscript, having been appointed chairman of the committee after the work was well under way and immediately upon arrival from Yale University to join the faculty of the University of Alaska. In contrast, my association with Dr. Tryon is now one of several years' standing, having begun by correspondence before my acceptance as a graduate student at Alaska. His encouragement at more than one stage of my graduate career is hereby duly and gratefully acknowledged. Similarly, my association with Professor Parthasarathy has been pleasant and profitable not only in the dissertation work but in the many discussions - both technical and nontechnical - which I have carried out with him as my senior colleague in the next office at the Geophysical Institute.

Dr. Owren's contribution to this work did not end with his departure to join the faculty of Dartmouth College, and his continued interest, criticism, and encouragement are greatly appreciated.

The ultimate thanks go to Mrs. Rita Fremouw for the ultimate patience.

College, Alaska
April, 1966

TABLE OF CONTENTS

TABLE OF CONTENTS (CONT'D)

TABLE OF CONTENTS (CONT'D)

TABLE OF CONTENTS (CONT'D)

LIST OF ILLUSTRATIONS

LIST OF TABLES

CHAPTER I

SURVEY OF STUDIES OF IONOSPHERIC IRREGULARITIES

1A EARLY STUDIES

The irregular structure of the terrestrial ionosphere is perhaps its most long-standing unexplained major observed feature. The discovery of the ionosphere, whose existence had been inferred by Balfour Stewart as early as 1878[1], is usually dated as 1901, the year of Marconi's first transatlantic wireless transmission. In 1902, Kennelly and Heaviside independently postulated the existence of a high-atmospheric conducting layer to explain Marconi's success. There followed nearly a quarter century of theoretical and experimental work aimed at proving or disproving the existence of such a layer. This early work yielded results, such as development of the magneto-ionic theory, which were later to be of fundamental importance to the study of the ionosphere and to its utilization for long-distance radio communications. Yet, throughout this period, there was doubt as to the ionosphere's very existence. Obviously, descriptive ionospheric research had not yet begun.

It was in 1925 that Appleton and Barnett clearly received a component of BBC transmissions propagating downward after reflection from the ionosphere. Immediately thereafter, a number of workers employed upward directed antennas. Notable among these were Breit and Tuve, who in 1926 employed pulse modulation in the first ionospheric sounder. Now the job of describing the ionosphere could and did begin

---

[1] Kelso (1964) credits Gauss with a still earlier suggestion, made in 1839.

in earnest. By the time of the second International Polar Year, 1932-33, many of the major features of the ionosphere were known and some were on their way to explanation. The normal E and F layers were recognized and their equivalent heights were established. Some knowledge existed about the seasonal and diurnal variations of the E and F ionization maxima at middle latitudes. Chapman already had developed his theory on the ionizing effect of monochromatic radiation incident on the atmosphere. This theory proved capable of explaining a remarkable number of the observed characteristics of the "regular" ionosphere.

As early as 1930, Appleton observed effects of irregular ionospheric structure. Still today, however, there is no comprehensive theory to explain the existence of localized irregularities of ionization. The abnormal E region ionosonde returns which Appleton had observed have since become known as sporadic E, and the phenomenon received considerable attention during the second Polar Year. Much has been learned about it since, but most present-day ionospheric physicists probably still would add "amen" to the statement of Appleton, Naismith and Ingram (1937) that "we feel that a completely satisfactory explanation of its occurrence on all occasions is still lacking."

While the earliest sporadic E traces reported in the literature were regarded as abnormal, there was no reason to interpret them as being produced by a spatially irregular reflecting region. One of the most direct early observations of ionospheric irregularities, as the term generally is used today, was reported by Eckersley (1937). Eckersley observed "momentary ionospheric echoes from irregular heights, occasionally as low as 60 km, but generally between 100 and 300 km," and commented that "we

can scarcely avoid the conclusion that the echo signals are not regularly refracted from a uniform layer in the ionosphere but are scattered from irregularities or clouds." Earlier instances of "lateral deviation" of radio signals reported by Ratcliffe and Pawsey (1933) probably were caused by scattering from similar but longer-lived ionospheric irregularities. It appears that Pawsey actually observed drifts of such irregularities as early as 1935, using spaced receivers (Ratcliffe, 1956).

One of the most commonly observed effects of ion-density irregularities is the spreading of ionosonde F-layer traces, the so-called spread-F phenomenon. To some extent, spread F has been considered a nuisance in the routine scaling of ionosonde records for F-layer parameters such as virtual height and critical frequency. As a consequence, many modern sounders have been adjusted in such a manner as to decrease their utility for studying the irregular structure of the F layer. Still, a considerable amount of effort has gone into study of the spread-F phenomenon itself. The first such effort appears to have been that of Booker and Wells (1938), who interpreted spread-F ionosonde returns in terms of Rayleigh scattering by spatial irregularities in the F layer.

Not surprisingly, little progress in describing ionospheric irregularities was reported in the open literature during the years of World War II. E-layer irregularities were considered by Eckersley (1939) and by Eckersley, Millington and Cox (1944), however, in explaining a number of signal propagation modes. Immediately after the war, exploration of ionospheric structure received renewed attention and the benefit of wartime advances in radio technology. Wells, Watts and George (1946) reported observations of rapidly moving irregularities in the F region

during a magnetic storm, using a new ionosonde with increased time resolution. They attributed the irregularities to an influx of extraterrestrial particles and interpreted the motions as being downward from great heights into the F layer. However, their method allowed measurement only of range change and not of the angle of motion. Postwar radio and radar techniques of considerable variety led to ever increasing observations of various types of irregular ionospheric structure. While they did not produce a comprehensive understanding of the structure, the expanded numbers and types of observations did begin to reveal the complexity of the problem.

From advances in the statistical description of electrical signals, was born a series of theoretical studies which allowed more effective use of the new wealth of observational material. One of the first papers in this vein was by Ratcliffe (1948), in which it was suggested that "if the roughness of the ionosphere is supposed to vary in a random manner, then the salient phenomena of the fading of a single wave can be explained." This paper explored the observations to be expected from a vertical-incidence sounder due to "diffractive reflexion" from randomly placed scattering centers, which were assumed to be in random motion. The paper applied to the ionospheric problem the work of Furth and MacDonald (1947) on the statistics of random noise signals.

Of more general application were - and continue to be - the fundamental papers on analysis of random noise by Rice (1944, 1945). An important feature of Rice's work is that it included the case of a sinusoidal signal in the presence of noise. McNicol (1949) recognized the importance of this case to the problem of ionospheric reflection which

includes a specular component as well as scattered components. He applied Rice's work to normal-incidence and oblique-incidence receptions at a single point, determining the ratio of specularly reflected to scattered power. By applying also the work of Booker, Ratcliffe and Shinn (1950), then in the process of publication, he was able to calculate an effective velocity of the ionospheric irregularities responsible for the signal fading which he observed. Working with a single receiver, however, McNicol was not able to ascertain whether his effective velocity measured an ordered ionospheric drift, a random motion of irregularities or a combination of the two.

As important as Rice's results to the problem of ionospheric scattering was work by Booker and Clemmow (1950), which generalized the concept of a polar diagram to that of an angular spectrum of plane waves. This generalization allowed familiar Fourier transform techniques to be brought into play. A marriage of the statistical concepts of Rice and the Fourier techniques of Booker and Clemmow brought forth the fundamentally important paper of Booker, Ratcliffe and Shinn (1950).

Booker, Ratcliffe and Shinn, in basing their work on the derivations of Booker and Clemmow, stated their considerations within the context of diffraction processes. To some extent such a context tends tacitly to introduce unnecessary restrictions on application of the results. The term diffraction brings to mind a discontinuous medium, with significant changes in transmission parameters taking place in the propagation direction within distances comparable to the observing wavelength. In point of fact, no such restriction exists in the work. The derivation of the angular spectrum starts with consideration of an irregular electromagnetic

wave-field assumed to exist without statement of its originating mechanism. Thus, any form of scattering which can produce an irregular wave-field and an associated angular spectrum can be examined with the mathematical tools provided by this paper. Several workers have used the tools to attack the problem of scattering by an inhomogenous, phase-changing medium - a process which might descriptively be called differential refraction, but which, by and large, has continued to be called diffraction. The situation is similar to use of the term reflection to describe the return of radio signals from the ionosphere. Except for the lowest frequency radio waves, the term refraction more accurately describes the physical process involved, but the two terms are used somewhat interchangeably.

Immediately after publication of the work by Booker, Ratcliffe and Shinn, a number of papers appeared which restated, simplified, and extended its results and underlying concepts and applied them to experimental problems. The experiments performed on this basis generally fell into three classes: single-receiver measurements carried out on ionospherically returned, man-made signals; spaced-receiver measurements of similar signals; and measurements carried out on signals received from radio stars. Representative of the first type of work was that reported by McNicol (1949), mentioned above. The considerable amount of information available from spaced-receiver measurements based on the results of Booker, Ratcliffe and Shinn was described in a rather complete treatment by Briggs, Phillips and Shinn (1950).

IB INTRODUCTION OF RADIO ASTRONOMICAL TECHNIQUES

The above-mentioned single-receiver and spaced-receiver methods both depend upon return from the ionosphere, by one or several possibly complicated propagation modes, of a signal transmitted from the earth. Discovery during the 1940's of discrete extraterrestrial radio sources, the so-called radio stars, led to an alternative means of investigation in which the basic propagation mode is simple transmission through the ionosphere. Some of the earliest observations of the strong source in Cygnus - Cyg A - revealed irregular fluctuations in the strength of the received signal (Hey, Parsons and Phillips, 1946; Bolton and Stanley, 1948). The fluctuations in the received intensity of Cyg A and of the stronger source discovered by Ryle and Smith (1948) in Cassiopeia - Cas A - became the subject of considerable investigation.

Simultaneous observations at Cambridge and Jodrell Bank by Smith (1950) and Little and Lovell (1950) showed no correlation for most of the variations, demonstrating that they were not inherent in the radio sources. The latter authors carried out spaced receiver measurements on baselines of 100 meters and 3.9 kilometers and concluded that the flucuations originated near the earth. They suggested as a mechanism a process analagous to the twinkling - or scintillation - of optical stars, due, in the radio case, to localized electron clouds in the F region.

The almost simultaneous appearance of the theoretical work on random scattering by Booker, Ratcliffe and Shinn and the experimental conclusions of Little and Lovell led immediately to application of the tools of radio astronomy to ionospheric physics. Perhaps the earliest paper reporting work which might be termed ionospheric radio astronomy was one by Ryle

and Hewish (1950). Carrying on from the suggestion of Little and Lovell that radio-star scintillations might be caused by phase variations suffered during passage through F-layer ionization irregularities, Ryle and Hewish established the diurnal variation of scintillation intensity and compared it with that of spread F. They found that, as for mid-latitude spread F, the scintillations which they observed in England represented a nighttime phenomenon. They found a cross-correlation coefficient between indices of the two phenomena of between 42 and 45 percent. From this result they concluded that radio-star scintillations and spread F are related (at middle latitudes) and that the two may be caused by the same F-layer irregularities.

That radio astronomical observations could effectively supplement the older methods of ionospheric measurement was demonstrated in consideration of the diurnal variations of spread F and scintillation. In the case of spread F, it was not known whether the scattering irregularities themselves displayed a diurnal variation of occurrence or rather existed round the clock, being masked during the day by reflection from a normal F layer below them. Since a radio star signal necessarily traverses the entire ionosphere, the observed diurnal variation of scintillation is a direct indication of the diurnal behavior of the scattering irregularities.

The instrumentation developed for radio astronomical observation also supplements that of the earlier ionospheric techniques. In particular, having a need for high angular resolution in observing discrete celestial radio sources, radio astronomers introduced the radio interferometer (Ryle, 1950). From one point of view, the radio interferometer is an extension of the spaced receivers used earlier by ionospheric researchers (although

the development was by analogy with an optical instrument, the Michelson steller interferometer). The extension involves retaining phase coherence between the two receivers by using a common local oscillator and adding the intermediate-frequency signals so that the resultant depends upon the phase difference between the two received signals. At the expense of losing discrimination between ordered drift and random change of the amplitude pattern on the ground, the instrument permits observation of the phase as well as the amplitude of the irregular wavefront arriving from the ionosphere.

That the phase distribution of the wavefront contains ionospheric information not available in the amplitude distribution alone was demonstrated by Hewish (1951) in his extension of the work of Booker, Ratcliffe and Shinn (1950) for the case of a structured phase-changing ionospheric layer. From measurements involving both the amplitude and phase of the wavefront, Ryle and Hewish (1950) and Hewish (1951) concluded that ionospheric structure with a horizontal scale of a few kilometers and consisting of less than one percent variation in the phase path thickness of the ionosphere could explain their observed scintillations.

Carrying out a somewhat more extensive program of amplitude observations, Little and Maxwell (1951) also found scales of a few kilometers and a close association with spread F. In addition, using the radio star Cygnus A, they found scintillation amplitude to be very nearly proportional to atmospheric path length when the line of sight traversed the mid-latitude ionosphere but to increase sharply when the source was viewed through the auroral-zone ionosphere.

Meanwhile, Hewish (1952) was extending the observational program

based on his earlier theoretical considerations, using both spaced receivers and a greatly improved interferometric instrument, the phase-switch interferometer (Ryle, 1952). He found that many of his observations could be explained by the drift of otherwise fairly stable ionospheric structure, mainly along east-west lines. The scales which he deduced averaged about five kilometers, and the ionospheric drift velocities ranged generally between 100 and 300 meters per second. He found a clear relationship between the velocity and geomagnetic activity. Devising a means of deducing the height of the irregularities from simultaneous measurements of amplitude and phase fluctuations, he estimated the height at about 400 kilometers.

Hewish's considerable success in deducing certain characteristics of the scintillation-producing irregularities was limited by two simplifying assumptions in his theoretical work. First, following Booker, Ratcliffe and Shinn (1950), he worked within the context of a thin defracting screen, which allowed very little consideration of the scattering process actually taking place in the ionosphere. Essentially, Hewish had to postulate a wavefront containing deviations in phase immediately below the scattering layer. He then analyzed what happens to the wave in subsequent propagation to the ground. Second, Hewish emphasized the special case of small phase deviations (less than one radian variation across the screen). While most of Hewish's observations met the requirements for this special case, we shall see later that generalization is required for discussion of certain scatter events, particularly in the auroral zone.

In an ambitious and significant theoretical work, Fejer (1953) seems to have made the first step toward considering a scattering medium of

greater physical plausibility, namely a thick slab containing irregular variations in refractive index. In this work, Fejer made use of various methods and concepts previously used in analysis of radio-wave scattering by tropospheric turbulence (Booker and Gordon, 1950), sound-wave scattering by small random variations in refractive index (Ellison, 1952), and scattering of x-rays by particles larger than the wavelength (Dexter and Beeman, 1949). Fejer's analysis included an extension of the work of Booker, Ratcliffe and Shinn by considering the case of a thin screen with irregular structure in two dimensions rather than in one. More fundamentally, he went on to consider also the case of a thick scattering region with three-dimensional irregularities in refractive index.

In considering the thick-slab case, Fejer first made the simplifying assumption that scattering takes place only from the incident wave - i.e., he first considered the case of single scatter. In this case, Fejer's results are essentially the same as those of Booker and Gordon (1950) except for choice of a physically more realistic autocorrelation function to describe the random nature of the irregular dielectric through which the wave passes. The most significant advance made by Fejer's paper was his analysis of multiple scattering by a thick layer having an irregular dielectric constant. For this important case, Fejer worked out the angular spectrum and the autocorrelation function of the scattered wave for a thick medium containing spherically symmetric irregularities. Thus Fejer overcame the first of the two limitations of Hewish's earlier work.

Fejer was able to discuss the physical significance of Hewish's other limitation - namely, the special case of small phase deviations. He showed that if the slab were sufficiently thin and/or its dielectric irregularities

sufficiently weak, then the conditions of Hewish's special case would be met. Quantitatively, these conditions correspond to a scattering layer which allows a fraction of the incident power, equal to or greater than about e^{-1}, to emerge unscattered. More generally, Fejer showed that the mean-square phase deviation imposed on the wavefront by the screen is equal to the thick-slab parameter which he called "the effective depth of scattering." This latter parameter was given by Fejer as

$$B_o = \int_o^{z_o} A \, dz$$

where z_o is the thickness of the slab and A is the fraction of flux scattered from an incident beam by a unit thickness of the slab.

Further consideration of the relationship between Fejer's thick-slab model and the thin diffracting screen assumed by Hewish and by Booker, Ratcliffe and Shinn was carried out by Bramley (1954). The primary goal of Bramley's short paper was to show "that the angular spectrum, as derived by considerations of multiple scattering, for transmission through a thick stratum containing normally distributed and statistically isotropic irregularities of dielectric constant with autocorrelation function of the form exp $(-r^2/l^2)$, can equally well be evaluated by considering an equivalent thin phase-changing screen." This he did, and the relationship between a thick scattering layer and an equivalent thin screen, which he elucidated, is useful. There is a danger, however, in thinking in terms of the equivalent screen rather than in terms of the more realistic thick layer. It is often convenient from an observational point of view, but it tends to draw

attention away from the ionospheric phenomena which are, after all, the final goals of this whole endeavor. It is to be noted, happily, that Bramley did not fall into his own trap. We shall have occasion in Chapter II to examine more of his work in detail (Bramley, 1951, 1953, 1955).

IC WORK DURING AND SINCE THE IGY

Much of the work described in the foregoing, as well as the results of other workers, was summarized in an excellent review paper by Ratcliffe (1956). Since Ratcliffe's review, investigations of irregular ionospheric structure have been extended greatly. The International Geophysical Year accelerated experimental investigation in this field as in all branches of geophysics. Regarding ionospheric irregularities, the IGY left primarily a two-fold experimental legacy. First, the standard instruments of the ionospheric physicist - in particular, the ionospheric sounder - were deployed around the world. Second, new techniques were introduced - most notably techniques employing artificial earth satellites.

The very existence of artificial satellites in orbit about the earth and transmitting back to it provides a powerful technique to complement the radio astronomical methods. Just as the signals received from radio stars scintillate due to scattering in the ionosphere, so do signals received from satellites orbiting above the scattering layer. Clearly the relatively fast-moving satellites can be applied in combination with the slower natural radiators for descriptive studies of certain spatial and temporal characteristics of ionospheric irregularities. When rapid advances in miniaturization of electronic circuits allowed placement of ionospheric sounders themselves in orbit, another new and at least equally powerful technique was made available - that of "topside sounding."

Ionospheric scattering layers can now be observed from above as well as from below.

The tremendous number of observational data made available during and after the IGY gave impetus to new theoretical investigations, as is to be expected. On the whole, the theoretical work took a somewhat different turn from the majority of that carried out before Ratcliffe's 1956 review paper. Most of the earlier work necessarily was directed toward interpretation of observations in terms of ionospheric scattering processes. That is, the theories developed strived to describe the scattering processes themselves. This work leaned heavily on the techniques of signal statistics, which arose largely in engineering problems of radar development.

The later theoretical work has taken a more geophysical turn, concentrating on the dynamics of irregularity development and motion. The seeds of such investigation, of course, were sown earlier, and Ratcliffe's review article describes observations and analytical techniques employed in the study of irregularity motion. (Another comprehensive review of this aspect of pre-IGY irregularity studies was given by Briggs and Spencer, 1954.) In the early studies of irregularity motion, the existence of the irregularities usually was accepted and the dynamical aspects of the problem were confined to the drift (possibly coupled with some kind of random motion or growth and decay) of what were taken to be clouds of excess ionization. There was always a question as to the relation between motion of ionization and gross motion of high-atmosphere neutral gas. The later workers have questioned also the relation between ionospheric motions and the very nature of the observed irregularities.

In much of the recent work, attention has been given to the possibility that moving irregularities do not necessarily represent directly the motion of atmospheric ionization - let alone that of the neutral gas. In this case, the irregularities are viewed as propagating waves, which simply perturb the ionization density as they travel. Some of this work has been summarized briefly by Hines (1964). Even the seeds for this line of thought had been sown much earlier. Observations carried out as early as 1937 were interpreted before the IGY in terms of compressional waves or "travelling ionospheric disturbances" (Munro, 1950). This term was originally and usually still is applied only to irregularities with a scale of many tens of kilometers, whose propagation can be traced by ionosondes over distances of many hundreds of kilometers.

The more recent work strives also to interpret smaller-scale irregularities in terms of wave phenomena. For instance, Farley (1963) has investigated the possibility of the production of field-aligned irregularities by means of a two-stream plasma instability in the equatorial electrojet. He concluded that the mechanism ought to produce ion waves having many of the characteristics displayed by one type of equatorial sporadic E.

Thus, not only are planetary-scale dynamic phenomena important to irregularity motions but possibly to irregularity existence as well. Certainly the general interdependence of ionospheric irregularities, however produced, and global circulation effects, especially those of the atmospheric dynamo, will receive much attention in the next few years. The world-wide observations already carried out, however, argue against hope for a simple comprehensive theory to explain irregular ionospheric structure in the way that Chapman's theory explained regular layer formation

so early in the development of ionospheric research. We probably are dealing with several originating mechanisms, which may not necessarily be very closely related.

The multiplicity of observed characteristics of ionospheric irregularities has often led to classification according to at least two variables. First, there is often a classification on the basis of height - usually according to particular ionospheric layers or regions. Thus, there exist collected results of E-layer irregularity studies (Smith and Matsushita, 1962) and of F-layer irregularity studies (Newman and Penndorf, 1966). Second, there is often classification according to latitude. The latter classification is sometimes made on the basis of observed characteristics, as for instance the spread-F occurrence minimum near 30 degrees magnetic latitude (Lyon, Skinner and Wright, 1962). On the other hand, the latitude classification may arise only for the obvious reason that individual experimenters find their observations confined to distinct latitude ranges. For instance, Bowles and Cohen (1962) have pointed out similarities between certain types of E-region irregularities observed in equatorial regions and certain aurorally associated irregularities observed at high latitudes. In addition, physical relationships may be expected between irregularities at different heights and have been reported by Thomas (1962) and others.

At least as complicated as the relationship between irregularities at different latitudes and at different heights is the relationship between the effects observed with different experimental techniques. International conferences, in fact, have been devoted to the results of particular observing techniques (Aarons, 1963). Obviously, much work

needs to be done on relating observations obtained with different techniques, at different places, and due to irregularities at different heights (when the height is known). In the meantime, there is need for work with specific observing techniques (or judiciously chosen combinations) at specific latitudes. Nowhere is the need for descriptive work more acute than in the auroral and polar regions. Not only are past observations scarcest in high-latitude regions, but also the phenomena are often more complicated there than at lower latitudes.

To a large extent, observations in the polar regions have been restricted to those obtained with ionosondes (ground-based and topside). Calvert and Schmid (1964), for instance, have reported on world-wide spread F as observed from above the F layer. Penndorf (1962, 1964), using bottom-side ionograms, has found permanent maxima of spread F in the northern and southern magnetic polar regions and travelling maxima which circulate around the boreal and austral auroral zones on the midnight meridian.

At auroral-zone latitudes, other observing techniques also have been used. In the present work, VHF observations of radio stars have been employed. Before proceeding to the specifics of this work, let us briefly review the results of possibly related previous work on ionospheric irregularities in the auroral zone. We shall not consider D region irregularities to any appreciable extent, for two reasons. First, far less is known about the auroral D region than about the higher layers of the auroral ionosphere. Second, due to the inherently lower ion density of the D region, its contribution to the scattering of extraterrestrial VHF waves is not likely to be competitive with the contribution of higher regions.

The relatively high collision frequency of the D region suggests the use of cosmic-noise absorption as an indicator of (at least large-scale) irregularities there, which may be related to higher irregularities detectable by radio-star techniques. Ansari (1964) for instance, has reported patches of absorption, using a narrow-beam riometer. In addition, information on smaller-scale irregularities in the auroral D region may be forthcoming in the next few years from application of VHF ionospheric scatter propagation to geophysical problems.

Results at middle latitudes lead first to consideration of the F layer as the likely location for scintillation-producing irregularities. In probably the earliest investigation of radio-star scintillation as a recognized ionospheric phenomenon, Ryle and Hewish (1950) found a definite association with spread F. In another early scintillation study, Little and Maxwell (1951) found a continuous but marked increase in the fluctuation of radio-star amplitude when the line of sight from the source to their mid-latitude observatory traversed the auroral zone. Later, Briggs (1958) performed an extensive study of spread F and scintillation at mid latitude and found his results consistent with the view that they are caused by the same irregularities.

An informative presentation of the characteristics of high-latitude spread F has been given by Penndorf (1962, 1964). For an auroral-zone station such as College, Alaska, which lies in the path of Penndorf's travelling spread-F maximum, the phenomenon shows clear-cut seasonal and diurnal variations. For the solar-maximum period which Penndorf analyzed, spread F at College exhibited a consistent nighttime maximum. In summer, the nightly maximum was simply the culmination of a gradual and deep 24-

hour variation. In winter, it spread for many hours before and after midnight, encroaching on the middle hours, which then showed a short sharp dip in spread-F occurrence. The equinoctial periods appeared as clear-cut transitions between summer and winter conditions. Shimazaki (1962) and other workers have found a decrease in high-latitude spread-F near solar minimum as compared with solar maximum, in contrast to lower-latitude spread F.

Herman (1964) has interpreted Penndorf's results in terms of a competition between photoionization and charged particle ionization in the F layer. In Herman's model, field-aligned irregularities are produced by proton flux. Homogeneous ionization by solar illumination would tend strongly to obscure the irregularities during the day, leaving a travelling maximum of irregular structure on the auroral-zone midnight meridian. Herman's model requires an unspecified magnetospheric mechanism to produce spatially irregular proton streams. This problem has existed for years, however, in regard to auroral electrons.

As pointed out by Shimazaki (1962), spread F as observed on vertical-incidence ground-based ionograms probably does not reveal the whole spread-F picture at high latitudes. For instance, Bates (1959, 1960a, 1960b) has observed oblique HF backscatter from F-layer irregularities. Due to aspect sensitivity, he concluded that the irregularities are field-aligned and he calculated their heights (1960a) to be in the region of 250 to 400 km. The irregularity backscatter was found to be primarily a nighttime phenomenon, with occasional patchy returns observed during the day (1960b). Transitional effects near sunrise and sunset were noted which prompted Bates to write, "It appears that during magnetically quiet periods solar

radiation eliminates the random irregularities - - -." This comment is of interest in regard to Herman's proposed model of spread F.

Another oblique-sounder HF return reported by Bates (1960b) and interpreted by him as being due to a (possibly irregular) field-aligned sheet of ionization is of interest in the light of certain topside sounder results. Muldrew (1963) has reported evidence of propagation via field-aligned sheets of ionization as the topside sounding satellite, Alouette, passed over the equatorial F region. Alouette has revealed a variety of apparently field-alinged spread F configurations (Calvert and Schmid, 1964). At least one type displays a strong latitudinal occurrence maximum at high latitudes along with a secondary but definite equatorial peak. Calvert, Knecht and VanZandt (1964) have interpreted certain auroral-zone returns from the fixed-frequency topside sounder Ionsopheric Explorer I (S-48) in terms of sheets of field-aligned irregularities extending from normal F-layer heights at least to the height of the satellite (about 950 km). The interpretation seems quite clear from their published ionograms.

A large collection of evidence for field-aligned irregularities in the auroral E layer has been secured over the years. The phenomenon known as radio aurora and detected by radar returns from aurorally associated ionization has provided a large portion of the evidence. A survey of experimental and theoretical work on the subject was given by Owren (1960), who concluded that auroral radar returns were produced by aspect-sensitive scattering from field-aligned irregularities. Both horizontal and vertical (upward as well as downward) motions of ionization in radio auroral forms have been reported by many workers on the basis of range changes and doppler shift and spread observations (Bowles, 1954; Nichols, 1957).

The obvious question of how closely visual and radio auroras are related (in particular, in regard to their positions) has been argued almost since the discovery of the latter. Early results often were ambiguous or else implied only a loose spatial relationship between radio and visual forms (Harang and Landmark, 1954). Recent work by Kelly (1965) using a narrow-beam (2.2 degrees) antenna in conjunction with a photometer of matching field of view directed along the radio line of sight shows close spatial and temporal relationships between specific radio and visual forms. Strength of radar returns also was found to be directly related to auroral brightness.

The radio aurora is believed to be very closely associated with sporadic E ionization in the auroral zone. In a survey of world-wide sporadic E characteristics, Thomas and Smith (1959) classified auroral-zone sporadic E into four types: so-called "flat, slant, retardation and auroral." They reported little seasonal variation for the overall phenomenon in the auroral zone but found that individual types show varying yearly patterns. All types show geomagnetic correlation. The authors could find no data available on correlation with radio-star scintillations. All types generally show spreading of the ionosonde returns, in common with equatorial sporadic E but in contrast with mid-latitude returns. Rapid vertical and horizontal motions and evidence for field-alingment were reported.

Work carried out both before and after the survey by Thomas and Smith suggested a close relationship between visual aurora and types of sporadic E other than the so-called "auroral" type. Knecht (1956) found "slant" type sporadic E to be related to remote auroras and concluded that there

was a close spatial relationship between visual auroral forms and the ionization responsible for his radio observations. He also found the highest frequency present in aurorally associated sporadic E returns to be directly related to auroral brightness.

Bates (1961) later found slant sporadic E to occur only during magnetic disturbance and thought it to be simply the HF manifestation, on vertical-incidence ionosondes, of certain VHF auroral radar returns. Hunsucker and Owren (1962) also pointed out that so-called "auroral" type sporadic E was not the only type related to visual aurora. They found it to be the type usually present on vertical-incidence ionograms obtained in the presence of zenithal auroras but also found "flat" sporadic E returns under such conditions. They found a correlation coefficient of 0.5 between the upper cutoff frequency of sporadic E and a zenithal auroral index. Under conditions of pulsating aurora, they reported almost inevitable strong absorption or complete blackout on HF vertical soundings.

The one type of sporadic E in the auroral zone which does not appear to be related to visual auroral displays is the so-called "retardation" type. An unpublished study by Ansari revealed some similarities in the behavior of retardation sporadic E and spread F in the auroral zone near solar maximum. The similarities did not exist for other types of sporadic E. Ground-based ionosondes, however, cannot be considered reliable indicators of relationships between irregular structure at different ionospheric altitudes. All too often, ionization at low levels obscures the situation at higher levels at times of most interest.

The advent of topside sounders and their coordinated use with ground-

based ionosondes is improving our knowledge of trans-ionospheric conditions, although limitations still exist under disturbed conditions. Evidence is starting to come in for the existence of field-aligned structure extending through great altitude ranges. For instance, du Castel and Vila (1964) have reported being able to trace such structure from sporadic E levels up to 1000 km. They raised the conjecture that "such fronts might turn out to be responsible for some oblique-reflection spread F echoes at the polar latitudes - - -." Bates' field-aligned sheets come to mind. It is of interest that Bates (1960b) differentiated between aspect-sensitive backscatter from field-aligned irregularities in the F layer and returns attributed to the field-aligned "sheet." The comment of du Castel and Vila, quoted above, continued "- - - we should not confuse their isolated discontinuous pattern of travelling disturbances with the regular steady periodic structure responsible for spread F." The latter authors, however, concluded that normal spread-F irregularities also are manifestations of very high-latitude structure, stating that "spread F is thus understood as the bottom extension of exospheric sheets of ionization."

According to du Castel and Vila, field-aligned structure in the upper F layer is very widespread. They postulate that special magnetic conditions may be necessary for it to become detectable by ionosondes exploring the bottom of the F layer. They describe the structure as being "ripply" in character, with spatial wavelengths of the order of a kilometer. In one particular case, such ripples with spatial wavelengths estimated at 5 km were observed over England. This is in remarkable agreement with the scales obtained for mid-latitude F-layer structure from early radio-star scintillation measurements (Ryle and Hewish, 1950; Hewish, 1951, 1952; Little and Maxwell, 1951).

In addition to the kilometer-scale structure, du Castel and Villa find a larger-scale "envelope." The envelope delineates the upper boundary of the smaller-scale structure, forming wedge-shaped groups. The sharp apices of the wedges point upward along the magnetic field and are separated by distances of the order of a few hundred kilometers. Lawrence, Jespersen and Lamb (1960) attributed slow angular variations of radio stars to "lens-like ionospheric irregularities having dimensions as large as 200 kilometers."

It would appear that many of the interpretations given to mid-latitude observations of radio-star scintillations are on the verge of corroboration by the powerful techniques of topside sounding. The topside sounders also may be able to fill in descriptive detail of structures which radio-star observations were able to suggest only in idealized fashion. A major point which seems to be emerging is that the F-layer irregularities responsible for mid-latitude radio-star scintillations are intimately related to heretofore little known structure in exospheric ionization. Exospheric irregularities were detected with satellite scintillation techniques in the northern auroral zone as early as 1959 (Basler and DeWitt, 1962), but they seemed to be sporadic. The relative consistency of the topside-sounder observations makes the manner in which such exospheric structure relates to the ionospheric-magnetospheric interface a question of particular interest, especially in the auroral zones. For instance, the theory offered by Axford and Hines (1961) to explain a large number of high-latitude geophysical phenomena relies heavily on the latitudinal dependence of diurnal maximization in high-latitude ionospheric irregularity occurrence.

To some extent, the statistical data used by Axford and Hines could be misleading as regards the morphology of specific events. Akasofu (1964), for instance, has shown that the instantaneous "auroral belt" shows significant departures from the statistical auroral zone. The same situation may be expected for radio auroras. Some radio methods may produce statistical results which in fact are biased against major magnetospheric agitations because of the effects of absorption. Sporadic-E and bottomside spread-F studies are among these.

Observations of radio-star and satellite scintillations at frequencies above about 50 MHz offer unbiased data. The possibility that these techniques could contribute to understanding of high-latitude geophysical phenomena through application at particularly disturbed times has been relatively unexplored. Surveys of world-wide satellite scintillation (e.g. Yeh and Swenson, 1964; Aarons, 1964) imply that such studies might be profitable. The satellite surveys have shown the existence of an often sharply defined zone of enhanced scintillation at auroral and (statistically) subauroral latitudes. This zone seems to coincide closely with that found for certain topside spread-F structure (Calvert and Schmid, 1964). In the case of scintillations, for which there are more observations, the equatorial boundary of the irregular zone is found to be related to geomagnetic K index. These and other observational facts have prompted Aarons (1964) to state, "It is inescapable that the moment to moment variations of irregularity regions are under as strong a control by the state of solar disturbance as are the visible aurora but the physical linking mechanism is nearly completely unknown."

Observations of radio-star scintillation at Saskatoon, Saskatchewan,

over a four-year period (1955-58) have been interpreted by Forsyth and Paulson (1961) in terms of a high-latitude region of enhanced irregularities whose southern boundary migrated southward with increasing solar activity. Fremouw (1963), working with periods of particular disturbance (visibility fades observed at College during the IGY) found a dependence on local magnetic K index which is consistent with a southward shift also of the northern boundary of the scattering zone during periods of high magnetic activity. Thus, he found the "importance" (a measure of both duration and severity) of severe scatter events to be directly related to local K index up to an index of 3 but to be inversely related for greater K indices. This is in contrast to lower-latitude observations of similar events (but at different phases of the solar activity cycle), which have shown more direct relationships (Nichols, 1960; Moorcroft and Forsyth, 1963).

In view of the observations mentioned above relating irregularities to high-latitude disturbance phenomena, the presence of high-latitude irregularities also as a normal ionospheric feature is a befuddling - but persistent - fact. Yeh and Swenson (1964) have stated, "scintillation occurs much more frequently than any of these other phenomena, and may provide a more sensitive indication of the (particle) 'dumping' process." This conjecture has not been demonstrated experimentally, although Hook and Owren (1962) have reported one observation of E-layer irregularities beneath a satellite which simultaneously detected an influx of electrons.

Aarons has pointed out that in addition to simultaneous observations of particle flux, topside spread F, and scintillations, "We need more

measurements on the strength of the irregularities and their height and size variation with latitude and geophysical disturbance and the lifetime of individual irregularities as well as cloud regions." The primary goal of the present work is to provide some of these measurements at times of enhanced irregular structure in the auroral zone near solar minimum.

Within the present context, "enhanced irregular structure" refers to the relatively strong, small-scale structure responsible for radio-star visibility fades. Visibility fades occur when the flux from a radio star becomes sufficiently scattered to reduce the correlation between signals received at two nearby antennas. They also have been called "long duration fades" (Little et al, 1962) and "radio-star fadeouts" (Flood, 1963; Moorcroft, 1963).

Besides representing an observed phenomenon asking for explanation in its own right, the visibility fade offers itself as a recognizable discrete event against the background of essentially omnipresent auroral-zone scintillations. In addition, it provides an opportunity for quantitative measurement of certain parameters of small-scale ionospheric structure with radio-interferometric techniques, as we shall see in later chapters. The strong direct dependence of auroral-zone ionospheric scattering on the solar activity cycle (Owren, Fremouw and Hunsucker, 1964) suggests solar minimum as the opportune time for an attempt at sorting out "disturbances" from "normal" irregular structure in the auroral zone.

CHAPTER II

INTERFEROMETRIC RECEPTION OF RANDOMLY SCATTERED WAVES

IIA INTRODUCTORY CONCEPTS

A1 Descriptions of Scattering

When a plane wave passes through a region of irregular refractive index, it emerges as a distorted version of itself - no longer plane but rather containing spatial variations in phase. Suppose, for instance, that a plane wave of light from a distant point source encounters a sheet of glass having irregular thickness. On the source side of the glass, the surfaces of constant phase are parallel planes, and the direction of travel of the wave is easily identified with the perpendicular to these planes. On the opposite side of the glass, the surfaces of constant phase contain ripples as a result of the differential phase retardation caused by the irregular glass.

The manner in which we commonly describe the effect of the irregular glass on the penetrating wave depends on how large a portion of the wavefront we are interested in at a given time. If all of our information comes from a small portion of a single phase ripple or irregularity, the wavefront still appears as approximately a plane. The perpendicular to this quasi-plane is still identified with the direction of travel of light rays, and to the extent that this direction is different from the original propagation direction, we say the wave has been refracted by the glass. Lacking any information from elsewhere in the wavefront, we are apt to conclude that the glass has the not very irregular shape of a simple wedge.

If now we explore a plane near the glass (on the "output" side),

successively examining the phase of the wave on small adjacent segments of the same irregularity, we begin to sense that the surfaces of constant phase are not planes. Still identifying the "light rays" with the direction of propagation, we measure a change in direction as we move. After we have explored one phase irregularity in this fashion, the glass seems to us to have the shape of a lens. If we continue to explore the irregular wavefront in this fashion, taking note of the differential refraction imposed by the glass, we think of the glass as a collection of positive and negative lenses.

So long as, at any one time, we receive information from a portion of the wavefront which is small compared with one irregularity, we are content to think of the effect of the glass as refraction. We have no trouble assigning an instantaneous direction of propagation to that portion even if we note that the direction changes with time. If, however, we consider the nature of the wavefront over many irregularities, we no longer can find a unique direction defined by the direction of "rays" which lie perpendicular to the surfaces of constant phase. Indeed, the rays so defined are travelling in a multiplicity of directions, and we refer to the light as having been scattered by the glass rather than refracted.

A2 The Angular Spectrum

We should like to find a means of describing scattering which will be valid over our whole wavefront region of interest. If our instantaneous interest is confined to a small portion of one irregularity, the concept of rays will suffice, and we can explore a larger portion of the wavefront over a period of time. If, however, our instantaneous interest

is over many irregularities, another more useful concept has been made available to us by Booker and Clemmow (1950), the concept of an angular spectrum of plane waves. We shall not review in detail the fundamentals of angular spectra but rather move directly to apply them to our observational problem. The fundamentals have been discussed on several levels.

An elementary discussion has been given by Sokolnikoff and Redheffer (1958), in which it is shown how Fourier transformation of the field existing at the aperture of an antenna gives a plane-wave expansion of the field. The usefulness of this expansion, which constitutes the angular spectrum, arises from the fact that the plane-wave components can be taken as propagating independently away from the antenna - or from a piece of rough glass, or from an irregular ionosphere - and then synthesized by an inverse Fourier transformation to produce the field at any other plane. This was shown rigorously by Booker and Clemmow as well as by Booker, Ratcliffe and Shinn (1950). The correspondence of the field so produced to the Fresnel diffraction pattern also was shown by Booker and Clemmow, who related the concept to diffraction and antenna problems. All these considerations were reviewed with relative brevity and clarity by Ratcliffe (1956).

Booker and Clemmow showed that the angular spectrum is identical to the polar diagram of a spatially limited antenna at sufficiently great distance. It is in this case that the concept of rays becomes useful. The concept of an angular spectrum is valid at any distance from an antenna of any size. It is to be noted that while sequential observation of small portions of a wavefront will allow us eventually to determine the angular spectrum, the sum of rays from all portions is not identical

to the angular spectrum. Rays are defined only over very restricted regions of space while components of the angular spectrum are infinite in spatial extent, just as components of a frequency spectrum are infinite in temporal extent. For a number of important special cases, however, the angular spectrum may be thought of as a collection of rays. In particular, at sufficient distance from a random scattering screen, the width of the angular spectrum can be closely approximated by the angular extent of rays emanating from a typical irregularity.

A3 Amplitude and Phase of Random Signals

For application of the angular-spectrum formalism to a particular problem, such as ionospheric scattering, it is convenient to look for valid simplifications of the general approach. Before we even mentioned the term angular spectrum, in describing the scattering of light by an inhomogeneous glass, we utilized some simplifications of reality. For instance, we talked about a plane wave. A plane wave has a unique direction of propagation and, rather obviously, it has therefore an angular spectrum made up of a single unique component. Beyond this, however, the discussion of wave propagation involves the concept of phase, and we must ask what we really mean by phase and under what conditions it is a meaningful concept.

Our most common encounters with the concept of phase are with time-varying quantities. For instance, suppose we observe the temporal variation of voltage at the terminals of an antenna. If the voltage is varying sinusoidally with time about a mean of zero, we can completely specify the voltage by noting its frequency, its amplitude, and its phase at some

reference time. Further, by noting the reference-time phase of the voltage produced by antennas at other positions, we can determine phase as a function of position and ascertain the propagation of an electromagnetic wave with considerable conceptual ease.

If, in the present work, we were dealing with signals from man-made earth satellites, the monochromatic concept of phase alluded to above would be quite adequate. We shall be dealing, however, with signals from natural radiators - radio stars. In this case, the voltage which we observe at the terminals of an antenna has the character of noise. That is, the voltage is a random function of time, where by "random" we simply mean unpredictable. In the monochromatic case, the time-varying real voltage can be specified for all time by a single complex number giving its (real) amplitude and phase. (The complex number may be referred to as the complex amplitude.) In the noise case, no single number can provide us with such a complete description of the voltage. What then can we mean if we talk of "amplitude" and "phase" and how can we describe the propagation of a "wave"?

A straight-forward development of "a complex representation of real polychromatic fields" is given by Born and Wolf (1959, section 10.2). We shall concern ourselves here with one of the resulting concepts of that development. The concept is that of the envelope of a random signal, and we shall demonstrate it empirically rather than analytically. Consider the oscillograms shown in figure 1. At the left is displayed the (amplified) output voltage from a random noise generator. We note the unpredictable nature of the voltage and, referring to its Fourier transform, we are apt to call it "white noise." By this we mean that the

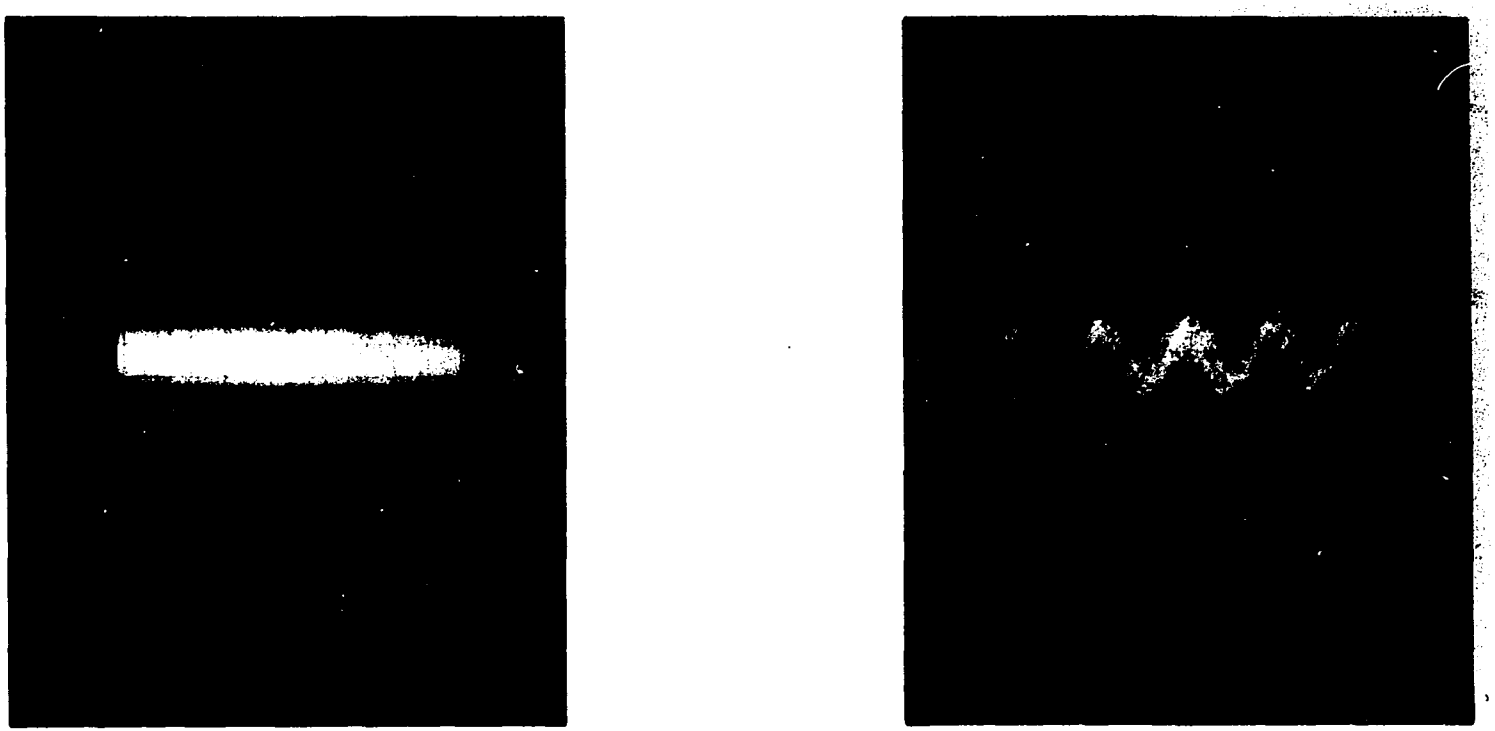

Fig. 1. Left, white noise; right, band-limited noise. Illustrating the meaning of the envelope amplitude and phase of a noise signal.

power spectrum of the signal contains equal contribution from all frequencies. We seldom venture beyond the concept of a power spectrum to consider what might be the relationship between the phases of the Fourier components. This we shall do later, in a different context, but for now we are concerned with the time domain. In looking at the left oscillogram, we can see no quantities which we might term the amplitude or phase of the time-varying signal. The best we can do is to note the fluctuation of instantaneous voltage as a function of time.

In the right-hand oscillogram is shown the output of the same noise generator, after the signal has been passed through a band-limiting filter. In this case, the "filter" was in fact an amplifier of the type employed at intermediate frequency in our radio-star observations. The amplifier passband was centered at 30 MHz and had a half-power bandwidth of about 250 kHz. The oscilloscope sweep rate and the photographic exposure time were equal to those in the left oscillogram. The observed voltage, while still having the general character of noise, is now seen to have some element of predictability, characterized by what we might call its "envelope." The envelope appears as a sort of fuzzy sine wave with a frequency of 30 MHz. To the envelope, we can assign a nebulous amplitude and phase.

If we stop to consider the manner in which the fuzzy sine wave is produced by the oscilloscope, we can give analytic definition to the envelope. The oscillogram is produced by repetitive sweeps of the scope's electron beam, each sweep lasting a few cycles of a 30 MHz oscillation. If the amplitude and phase of the 30 MHz signal vary with time, randomly but slowly compared with the basic 30 MHz oscillation, then successive sweeps of the elctron beam produce the fuzzy sine wave observed.

Thus, the observed signal could be described analytically as a sine wave at the center frequency of our band-limiting filter, with the amplitude and phase themselves being functions of time. Born and Wolf arrived at this result rigorously. Our intent here is to establish some intuitive feeling for what is meant by the amplitude and phase of a random noise signal. Note that these terms and their unifying concept of an "envelope" have meaning only when the bandwidth of the noise signal is limited. We shall make use of this idea of "band-limited white noise" later.

It is important to note that in most observations of natural noise radiators such as radio stars - including the present observations - the signal of the type shown in the oscillogram is detected and averaged. The averaging is over times very long compared with the characteristic times of the signal shown. These characteristic times are the period of the fundamental oscillation (0.033 microseconds in this case) and the longer time of variations in amplitude and phase. This latter characteristic time is determined by the filter bandwidth, being comparable with its reciprocal. It is called the coherence time of the signal and, in the present example, is about four microseconds.

For averaging times very long compared with the coherence time, what we finally deal with are the average amplitude and phase of the signal envelope. These are very well defined quantities, as can be appreciated by considering a smoothed version of the trace shown in the right-hand oscillogram. The ionospheric effects with which we shall be concerned produce deviations from these averages, which are slow compared with all the times we have thus far considered - on the order of many hundreds of

milliseconds or a few seconds, in fact. Thus, although we shall be dealing with random noise signals, the concepts of amplitude and phase will continue to be useful and well defined.

From the above rather intuitive introduction to the concepts of angular spectrum and random-noise envelope and the references to rigorous treatments of these subjects, let us proceed to the problem of ionospheric scattering. Along our route, we shall introduce another important concept, that of random phasing in the angular spectrum. This idea will be fundamental to our theoretical considerations and is not in such widespread use as the general concept of an angular spectrum or the envelope parameters of a noise signal. Accordingly, we shall have to explore the meaning and consequences of random phasing rather completely - although only within the context of our particular problem.

IIB RELATION BETWEEN ANGULAR SPECTRUM AND FREQUENCY SPECTRUM

Let us begin from an observational point of view, considering the reception of an ionospherically scattered signal by a radio interferometer. We are not concerned whether the original signal is deterministic, as from a satellite, or noiselike, as from a radio star, so long as the latter is bandwidth limited in the sense that the signal envelope is well defined. In either case, we shall be concerned with amplitude and phase modulations of the signal imposed by the ionosphere. In accord with what actually is observed for the most part, we shall take the modulation itself to be random. Departures from this condition, which in fact also are observed on occasion, represent interesting exceptions and will be discussed in Chapter V. In much of the present chapter, we shall follow

closely the work of Bramley (1951), generalizing on and adding to his development where appropriate to our observational situation.

Let the observing frequency be $\omega/2\pi$ and suppose that the randomly modulated signal is Fourier analyzed. Thus, let the voltage at the terminals of one antenna be described as

$$v_1 = \sum_{n=1}^{N} c_n \cos [\omega t + (\omega_n - \omega)t + \phi_n] \qquad 2\text{-}1$$

where N is some large integer. Each Fourier component in the above expression has the nature of a sinusoid at the observing frequency, whose phase is changing linearly with time at the rate $(\omega_n - \omega)$. Let us denote the time-varying phase by $\psi_n(t)$ and investigate how it might be produced in the wavefield impinging on the antenna.

Consider a plane wave at the observing frequency approaching the antenna from a direction making an angle α_n to the vertical. In a coordinate system with origin at the antenna where the z-axis is vertical and the wave's propagation direction is in the xz plane, such a wave could be expressed as

$$e_n = d_n \cos [\omega t + \phi_n + (\omega/c)(x \sin \alpha_n + z \cos \alpha_n)] \qquad 2\text{-}2$$

where c is the velocity of light. For any α_n, such a wave would produce at the antenna ($x = z = 0$) a voltage of the form

$$v_{1n} = c_n \cos (\omega t + \phi_n) \qquad 2\text{-}3$$

This corresponds to the n^{th} Fourier component of equation 2-1, with the time-varying phase $\psi_n(t)$ equal to zero.

If, now in addition to propagation along the wave normal, the wave-

front is moving in the x direction with an additional (and relatively very small) velocity u, then $\psi_n(t)$ becomes a non-zero function of α_n. This is seen readily by considering that in this case the third term in the argument of equation 2-2 would be

$$(\omega/c)\,[(x - ut)\sin\alpha_n + z\cos\alpha_n] \qquad 2\text{-}4$$

so that at the antenna terminals, we get

$$v_{1n} = c_n \cos[\omega t + \phi_n - (\omega/c)(ut\sin\alpha_n)] \qquad 2\text{-}5$$

Comparison with equation 2-1 reveals at once that

$$\psi_n(t) = -\omega t\,(u/c)\sin\alpha_n = -(2\pi/\lambda)\,ut\sin\alpha_n \qquad 2\text{-}6$$

where λ = the observing wavelength, and that

$$\omega_n = \omega[1 - (u/c)\sin\alpha_n] = (2\pi/\lambda)(c - u\sin\alpha_n) \qquad 2\text{-}7$$

Thus, the total output v_1 of equation 2-1 could be produced by an angular spectrum of plane waves propagating toward the antenna and simultaneously drifing horizontally. Each Fourier frequency component of v_1 would arise from a single component of the angular spectrum. This view corresponds to drift past the antenna of an irregular wavefront produced by a drifting but otherwise unchanging irregular ionosphere. It is, of course, not the only manner in which the voltage v_1 could be produced.

The frequency components ω_n could be produced by a purely temporal modulation by a smooth ionosphere. In this case, a neighboring antenna always would produce an output identical to v_1, which is inconsistent with a vast collection of observational material from the past, as

reviewed in Chapter I, and from the present work. Such a situation would not correspond to ionospheric scattering at all. Combinations of drift and temporal modulation also could occur. In this case each component of the angular spectrum would have a frequency spectrum associated with it. At the observing frequencies used in this work and with the techniques employed, we are not concerned with components which might be introduced by temporal modulation.

Aside from pure drift at a single velocity, there is another kind of wavefront motion to be considered. This is a wavefront which changes its spatial structure as it drifts, which would arise if the various angular components drifted at different velocities. With interferometer techniques alone it is impossible to differentiate between these two kinds of motion, and we shall not concern ourselves with the relationship between angle and velocity. Our experimental results will be unaffected so long as we suitably restrict our conclusions. Attempts to describe wavefront motion in detail would be futile.

IIC OUTPUT VOLTAGES OF NEIGHBORING ANTENNAS

Equation 2-1 and the ensuing discussion relate to the output voltage of a single antenna, one of a pair of antennas used in a radio interferometer. Now suppose the second antenna is located on the x axis at a distance d from the first. Due to the separation between antennas, a given component of the angular spectrum will arrive with different phases at the two antennas. To account for this effect, we can write the output voltage of the second antenna as in equation 2-1, adding a fourth term in the argument. In order to preserve symmetry, let us also shift the origin

of our coordinate system midway between the antennas. Then the two output voltages are

$$v_1 = \sum_{n=1}^{N} c_n \cos(\omega t + \psi_n + \phi_n + \chi_n) \qquad 2\text{-}8$$

$$v_2 = \sum_{n=1}^{N} c_n \cos(\omega t + \psi_n + \phi_n - \chi_n)$$

where ψ_n is the time varying phase given by equation 2-6 and

$$\chi_n = (\pi d/\lambda) \sin \alpha_n \qquad 2\text{-}9$$

The antenna voltages also can be written as

$$v_1 = A_1 \cos(\omega t + \theta_1) \qquad 2\text{-}10$$

$$v_2 = A_2 \cos(\omega t + \theta_2)$$

The amplitudes A and phases θ will in general be different for the two antennas owing to the fourth terms in equation 2-8. They will be functions of time owing to the time variations of the ψ_n. Bramley (1951) assumed the ψ_n to be independent random functions of time and did not consider the explicit relationship between them and the angular spectrum.[1] As discussed above, an irregular wavefront drifting at a constant velocity will produce ψ_n's which are linear functions of time. Bramley's assumption corresponds to time varying drift velocities and was made in order to account for the statistical distributions thought to describe ionospheri-

[1] To avoid confusion, it is prudent to point out that Bramley's ψ_n are equivalent to the sum of ψ_n and ϕ_n in the present notation, which was chosen to allow explicit separation of time varying and static quantities.

cally scattered radio signals, namely those associated with band-limited white noise. We shall see shortly that the assumption of independence is sufficient to ensure the same distributions.

IID SIGNAL STATISTICS FOR A RANDOMLY PHASED ANGULAR SPECTRUM

D1 The Special Case of Completely Scattered Waves

1a Single Antenna: Let us denote the complex amplitudes of the antenna voltages by V_1 and V_2 and those of their Fourier components by C_{1n} and C_{2n}. Then we have, from equations 2-8 and 2-10

$$V_1 = A_1 \exp(i\theta_1) = \sum_{n=1}^{N} C_{1n} = \sum_{n=1}^{N} c_n \exp(i\gamma_{1n})$$

2-11

$$V_2 = A_2 \exp(i\theta_2) = \sum_{n=1}^{N} C_{2n} = \sum_{n=1}^{N} c_n \exp(i\gamma_{2n})$$

where $\gamma_{1n} = (\psi_n + \phi_n + \chi_n)$ and $\gamma_{2n} = (\psi_n + \phi_n - \chi_n)$

Equations 2-11 show that the complex amplitudes V_1 and V_2 are the phasor sums of the component complex amplitudes C_{1n} and C_{2n}, respectively. The summations represent random walk processes if the component phases are "random."

Now the ψ_n and χ_n are defined by equations 2-6 and 2-9, respectively. We have said nothing about the ϕ_n thus far, however. We now assume them to be random variables[1] which are uniformly distributed between zero and 2π and independent. This is what is meant by a "randomly phased angular spectrum," and for sufficiently large N it is the sole assumption necessary to produce A's and θ's distributed as the envelope amplitudes and

---

[1] Random functions of angle, α, but temporal constants.

phases of band-limited white noise, as we shall now see. The ionospheric requirements for random phasing will be explored in Chapter III.

Note that if the ϕ_n are uniformly distributed and independent, the γ_{1n} and γ_{2n} are also. The summations in 2-11 then are random walks, and the central limit theorem can be evoked to show that the real and imaginary components of V_1 and V_2 approach normal distributions as N increases without limit. For our purposes, the descriptive treatment of the central limit theorem given by Munroe (1951) and the somewhat more rigorous one by Middleton (1960) are enlightening.

It is pertinent to point out that while independence of the component phasors in 2-11 is neither a necessary nor a sufficient condition for the central limit law to hold, it does allow statement of the central limit theorem in the relatively simple form attributed to Liapounoff and in the less restricted Lindeberg formulation. In this formulation, the most important restriction on the component phasors, from a physical point of view, is that no one of them dominates the aggregate. The detailed density distribution of the components is not specified by the theorem and may take a wide variety of forms. Note that in the present situation, we have not assumed any particular distribution for the c_n.

Let us define the real and imaginary components of V_1 respectively as

$$A_{1c} = A_1 \cos \theta_1$$

and 2-12

$$A_{1s} = A_1 \sin \theta_1$$

and similarly for the real and imaginary components of V_2. Since A_{1c} and

A_{ls} are normally distributed for a randomly phased angular spectrum, as discussed above, then under this sole assumption we can follow Rice (1945) in his treatment of the envelope of band-limited white noise and establish the statistical characteristics of the envelope amplitude A_l and θ_l. We begin with the joint density distribution of A_{lc} and A_{ls}. Since each of these variables is normally distributed, their joint distribution will be the product of two gaussians if they are statistically independent. That they are independent is shown in Appendix 1a.

In view of the result of Appendix 1a, the joint distribution for A_{lc} and A_{ls} can be written as the product of two one-demensional normal distributions. Taking into account the zero means of the A's, we have for the joint probability density distribution function[1]

$$f(A_{lc},A_{ls}) = \frac{p(A_{lc},A_{ls})}{dA_{lc}\,dA_{ls}} = \frac{1}{2\pi\,\sigma_c\sigma_s}\exp\left[-\left(\frac{A_{lc}^2}{2\sigma_c^2}+\frac{A_{ls}^2}{2\sigma_s^2}\right)\right] \qquad 2\text{-}13$$

where $p(A_{lc},A_{ls})$ denotes the probability that A_{lc} and A_{ls} lie in the elementary rectangle $(dA_{lc}\ dA_{ls})$, and the σ's are the standard deviations of the A's.

Appendix 1a deals with the cross-products of the real and imaginary components of A_l. Straight-forward application of the same development to the squares of the real and imaginary components yields the variances of the components. Thus, it is easily shown that

$$\sigma_c^2 = \sigma_s^2 = \tfrac{1}{2}\sum_{n=1}^{N} c_n^2 \qquad 2\text{-}14$$

---

[1] We shall work throughout with (differential) probability density distribution functions, denoted by f. For brevity, we shall often use the term "distribution" to mean functions of this sort. In no case will we be referring to the corresponding (integral) probability distribution function.

In view of equation 2-14, let us denote both the standard deviations by σ. Then the probability in equation 2-13 becomes

$$p(A_{1c},A_{1s}) = \frac{dA_{1c}\, dA_{1s}}{2\pi\sigma^2} \exp\left\{ - \frac{A_{1c}^2 + A_{1s}^2}{2\sigma^2} \right. \qquad 2\text{-}15$$

Equations 2-12 show that $(A_{1c}^2 + A_{1s}^2) = A_1^2$ and that $(dA_{1c}dA_{1s}) = (A_1 d\theta_1 dA_1)$. Making these changes of variables in equation 2-15 we obtain

$$p(A_1,\theta_1) = \frac{A_1 d\theta_1 dA_1}{2\pi\sigma^2} \exp\ (-A_1^2/2\sigma^2) \qquad 2\text{-}16$$

Equation 2-16 shows that A_1 and θ_1 are independent random variables since $p(A_1,\theta_1)$ can be expressed as the product of $p(A_1)$ and $p(\theta_1)$. Integration of $p(A_1,\theta_1)$ with respect to θ_1 over the range zero to 2π yields

$$p(A_1) = \frac{A_1 dA_1}{\sigma^2} \exp\ (-A_1^2/2\sigma^2) \qquad 2\text{-}17$$

Division of 2-17 into 2-16 then shows that

$$p(\theta_1) = d\theta_1/2\pi \qquad 2\text{-}18$$

Thus the joint distribution function $f(A_1,\theta_1)$ is given by the product of $f(A_1)$ and $f(\theta_1)$, where $f(A_1)$ is the Rayleigh distribution given by

$$f(A_1) = (A_1/\sigma^2) \exp\ (-A_1^2/2\sigma^2) \qquad 2\text{-}19$$

and $f(\theta_1)$ is the uniform distribution between zero and 2π, given by

$$f(\theta_1) = 1/2\pi \qquad 2\text{-}20$$

Equations 2-19 and 2-20 show that the envelope amplitude and phase of the fluctuating voltage produced at the terminals of an antenna by the constant horizontal drift of a randomly phased angular spectrum obey

the same statistical laws as do the envelope amplitude and phase of band-limited white noise. In arriving at this result we have relaxed the assumption made by Bramley regarding the angular spectrum. No assumption need be made about the drift velocity of the component waves in the angular spectrum, other than that it be nonzero. The assumption of random phasing is sufficient.

1b Two antennas: Obviously the developemnt of equations 2-19 and 2-20 holds for A_2 and θ_2 as well as for A_1 and θ_1. We now open the question of the relationship between the voltages at the two antennas. Important quantities are the product of voltages v_1v_2, the product of amplitudes A_1A_2, and the difference of phases $\theta_2 - \theta_1$. In particular, we shall be concerned with the means of these quantities and with the variance of the phase difference.

The mean $\overline{v_1v_2}$ of the product of voltages is the covariance of voltages and is important to observations with phase-switch interferometers, as we shall see. It is shown in Appendix 1b that this quantity is given by

$$\overline{v_1v_2} = \tfrac{1}{2} \sum_{n=1}^{N} c_n^2 \cos 2\chi_n \qquad 2\text{-}21$$

under the assumption of random phasing, where χ_n is the phase angle defined in equation 2-9.

Since equation 2-21 gives the covariance of the voltages, it provides a measure of the correlation between them. The relations we seek between the A's and θ's also involve the correlation between the signals received at the two antennas. Since there are four variables, the situation may be expected to be more complicated, however. To find the desired relation-

ships, we must investigate the joint probability density distribution of the variables. We begin by considering the joint distribution of the four gaussian random variables A_{1c}, A_{1s}, A_{2c}, and A_{2s}.

Since we are dealing with gaussian variables, the joint distribution will be a four-dimensional gaussian. It will not, in general, be simply the product of four one-dimensional gaussians since we have not established independence of all four A's. Fundamentally, the multi-variate normal (or gaussian) distribution if that function resulting from the multi-variate central limit law. It can be derived from consideration of the n-dimensional random walk, as has been done by Middleton (1960), for instance.

A convenient form of the n-dimensional normal distribution function for variables with zero means is given without rigorous development by Bendat (1958). In our present quadri-variate case, the n-dimensional form reduces to

$$f(A_{1c},A_{1s},A_{2c},A_{2s}) = \frac{|M|^{-\frac{1}{2}}}{(2\pi)^2} \exp\left(\frac{-1}{2|M|} \sum_{\substack{i=1 \\ j=1}}^{4} M_{ij}A_iA_j \right) \qquad 2\text{-}22$$

where the numerical suscripts refer successively to the four double subscripts, 1c, 1s, 2c, and 2s; and M_{ij} denotes the cofactors of the determinate $|M|$, whose matrix is

$$M = \begin{pmatrix} \mu_{11} & \mu_{12} & \mu_{13} & \mu_{14} \\ \mu_{21} & \mu_{22} & \mu_{23} & \mu_{24} \\ \mu_{31} & \mu_{32} & \mu_{33} & \mu_{34} \\ \mu_{41} & \mu_{42} & \mu_{43} & \mu_{44} \end{pmatrix} \qquad 2\text{-}23$$

The elements of the matrix are the second moments of the random variables, and M is known as the moment matrix.

The elements of the moment matrix are discussed in Appendix 1c, and it is shown there that under the condition of random phasing M can be reduced to

$$M = \begin{pmatrix} \sigma^2 & 0 & \mu_c & -\mu_s \\ 0 & \sigma^2 & \mu_s & \mu_c \\ \mu_c & \mu_s & \sigma^2 & 0 \\ -\mu_s & \mu_c & 0 & \sigma^2 \end{pmatrix} \qquad 2\text{-}24$$

where

$$\sigma^2 = \tfrac{1}{2} \sum_{n=1}^{N} c_n^2 \qquad 2\text{-}25$$

$$\mu_c = \tfrac{1}{2} \sum_{n=1}^{N} c_n^2 \cos 2\chi_n \qquad 2\text{-}26$$

$$\mu_s = \tfrac{1}{2} \sum_{n=1}^{N} c_n^2 \sin 2\chi_n \qquad 2\text{-}27$$

All the information we require concerning the antenna voltages, v_1 and v_2, is contained in equation 2-21 and the elements of the moment matrix M. For a randomly phased angular spectrum, it is more appropriate to consider a spectral continuum than discrete spectral components. Thus, let us now replace equations 2-25 through 2-27 and equation 2-21 with their corresponding integral representations. Noting that $\tfrac{1}{2} c_n^2$ is the power which would be dissipated in a unit resistance by the n^{th} component wave of the angular spectrum, we see that equation 2-25 gives P, the total power (per unit resistance) contained in the spectrum. Let us denote by $p(\alpha)$ the (unitary resistance) angular power density in the spectrum. Then, upon recalling the definition of χ_n from equation 2-9, we obtain the

following:

$$\sigma^2 = \int_{-\pi}^{\pi} p(\alpha)\, d\alpha \qquad 2\text{-}28$$

$$\mu_c = \int_{-\pi}^{\pi} p(\alpha) \cos [(2\pi d/\lambda) \sin \alpha]\, d\alpha \qquad 2\text{-}29$$

$$\mu_s = \int_{-\pi}^{\pi} p(\alpha) \sin [(2\pi d/\lambda) \sin \alpha]\, d\alpha \qquad 2\text{-}30$$

$$\overline{v_1 v_2} = \int_{-\pi}^{\pi} p(\alpha) \cos [(2\pi d/\lambda) \sin \alpha]\, d\alpha = \mu_c \qquad 2\text{-}31$$

Now equations 2-22 and 2-24 show that the joint distribution of A_{1c}, A_{1s}, A_{2c}, and A_{2s} is given by

$$\frac{1}{4\pi^2[\sigma^4-(\mu_c^2+\mu_s^2)]} \exp\left\{\frac{-1}{\sigma^4-(\mu_c^2+\mu_s^2)}\left[\sigma^2(A_{1c}^2+A_{1s}^2+A_{2c}^2+A_{2s}^2)\right.\right.$$

$$\left.\left.-2\mu_c(A_{1c}A_{2c}+A_{1s}A_{2s})-2\mu_s(A_{1s}A_{2s}-A_{1s}A_{2c})\right]\right\} \qquad 2\text{-}32$$

To find the joint distribution of A_1, A_2, θ_1, and θ_2, we now transform to these coordinates from the four A's. The result, as is easily shown, is

$$\frac{A_1 A_2}{4\pi^2[\sigma^4 - (\mu_c^2 + \mu_s^2)]} \exp\left\{\frac{-1}{2[\sigma^4 - (\mu_c^2 + \mu_s^2)]}\left[\sigma^2(A_1^2 + A_2^2) - 2\mu_c A_1 A_2 \cos(\theta_2 - \theta_1) - 2\mu_s A_1 A_2 \sin(\theta_2 - \theta_1)\right]\right\} \qquad 2\text{-}33$$

It is to be noted that the distribution 2-33 cannot be represented as the product of an amplitude distribution and a phase-difference distribution. Thus, while the amplitude and phase at a single antenna are statistically independent, the amplitude at each of a pair of antennas is statistically dependent upon the amplitude at the other and upon the phase difference between the two antennas.

To find the joint distribution of the amplitudes, it is necessary to integrate over all possible phases. Similarly, to find the distribution of $\theta_2 - \theta_1$, integrations must be carried out over A_1 and A_2. Rice (1945) gives the joint distribution of A_1 and A_2 as

$$\frac{A_1 A_2}{\sigma^4 - (\mu_c^2 + \mu_s^2)} I_o\left[\frac{A_1 A_2 (\mu_c^2 + \mu_s^2)^{\frac{1}{2}}}{\sigma^4 - (\mu_4^2 + \mu_s^2)}\right] \exp\left\{-\frac{\sigma^2 (A_1^2 + A_2^2)}{2[\sigma^4 - (\mu_c^2 + \mu_s^2)]}\right\} \qquad 2\text{-}34$$

where I_o represents the zero-order modified Bessel function of the first kind for the argument in brackets. The integration over amplitudes has been carried out by MacDonald (1949), with the following result for the distribution of $\theta_2 - \theta_1$.

$$f(\theta_2-\theta_1) = \frac{\sigma^4 - (\mu_c^2 + \mu_s^2)}{2\pi\sigma^4} \quad \frac{(1-\beta^2)^{\frac{1}{2}} + \beta(\pi - \cos^{-1}\beta)}{(1-\beta^2)^{3/2}} \qquad 2\text{-}35a$$

where $\beta = [\mu_c \cos(\theta_2-\theta_1) - \mu_s \sin(\theta_2-\theta_1)]/\sigma^2$ 2-35b

Now, we are interested in certain moments of the distributions 2-34 and 2-35. In the case of amplitudes, we are particularly interested in the mean of their product $\overline{A_1A_2}$. For some applications, for instance a space-diversity receiving system employing square-law detectors and post-detection correlation techniques, the quantity $\overline{A_1^2A_2^2}$ is of interest also. Middleton (1960) outlines the development of these moments, with the following results:

$$\overline{A_1A_2} = \frac{\pi\sigma^2}{2} F(-\tfrac{1}{2},-\tfrac{1}{2},1,R^2) = \sigma^2[2E(R) - (1 - R^2)K(R)] \qquad 2\text{-}36$$

$$\overline{A_1^2A_1^2} = 4\sigma^2(1 + R^2) \qquad 2\text{-}37$$

where F is the gaussian hypergeometric function, E is the complete elliptic integral of the second kind, K is the complete elliptic integral of the first kind, and

$$R = \frac{(\mu_c^2 + \mu_s^2)^{\frac{1}{2}}}{\sigma^2} \qquad 2\text{-}38$$

It is pointed out in Apendix 1c that the μ's are covariances between components of signal at the antennas, while σ^2 is the variance of the signal voltage at a single antenna. Thus R is a kind of correlation

coefficient between the signals at the two antennas. In the special case where the spectrum is an even function (in our case, a symmetrical angular spectrum centered on $\alpha = 0$), μ_s vanishes (Rice, 1945, p. 78; Middleton, 1960, p. 352). In this case R is identical to the correlation between the voltages v_1 and v_2, as is evident from equation 2-31 and 2-38. In the more general case with which we must deal, the two are not identical but still are closely related. We shall find that R is a parameter of ionospheric interest which can be determined experimentally.

Now, in general, the correlation between two variables is defined as the ratio of their covariance to the geometric mean of their variances. If the variances are equal, then obviously the correlation is given by the ratio of the covariance to the variance of either. It is easy to show, then, that the correlation between the amplitudes at the two antennas is given by

$$\rho_A = \frac{\overline{A_1 A_2} - \bar{A}_1^2}{\overline{A_1^2} - \bar{A}_1^2} \qquad 2\text{-}39$$

and that between the square of the amplitudes by

$$\rho_{A^2} = \frac{\overline{A_1^2 A_2^2} - \bar{A}_1^2}{\overline{A_1^4} - \overline{A_1^2}^2} \qquad 2\text{-}40$$

The various terms appearing in 2-39 and 2-40 are given by equations 2-36 and 2-37 and the distributions of A_1 and A_1^2. The distribution of A_1 is the Rayleigh distribution, given by equation 2-19. A simple change

in stochastic variable[1] gives the distribution of A_1^2 as follows

$$f(A_1^2) = \frac{f(A_1)}{2A_1} = (1/2\sigma^2) \exp(-A_1^2/2\sigma^2) \qquad 2\text{-}41$$

The distributions of $f(A_1)$ and $f(A_1^2)$ yield the following:

$$\overline{A_1}^2 = (\pi/2)\,\sigma^2 \qquad 2\text{-}42$$

$$\overline{A_1^2} = 2\,\sigma^2 \qquad 2\text{-}43$$

$$\overline{A_1^2}^2 = 4\,\sigma^4 \qquad 2\text{-}44$$

$$\overline{A_1^4} = 8\,\sigma^4 \qquad 2\text{-}45$$

Combination of the above with equations 2-36 and 2-37 yields, from equations 2-39 and 2-40, the following:

$$\rho_A = \frac{4[E(R)-\frac{1}{2}(1-R^2)K(R)] - \pi}{4 - \pi} \qquad 2\text{-}46$$

$$\rho_A{}^2 = R^2 \qquad 2\text{-}47$$

Series solutions for the complete elliptic integrals are given in standard tables of integrals (Hodgman, 1955, integrals no. 459 and 460).

---

[1] See Bendat (1958), section 3.4-3, for a discussion of change of variable in density distributions.

Using these, it is easily shown that equation 2-62 reduces to

$$\rho_A = 0.91 \left(R^2 + \frac{1}{16}R^4 + - - - - - - - \right) \qquad 2\text{-}48$$

This gives the approximate (and equation 2-46 the exact) relation between the wavefront correlation function R and the cross-correlation coefficient ρ_A between the amplitudes at the two antennas, for the case of a randomly phased angular spectrum in which no component predominates.

The degree of relation between the amplitudes at the two antennas is given in a meaningful fashion by the correlation coefficients ρ_A and $\rho_A 2$. These quantities are simply related to the wavefront correlation function R as described above. Now, the phase difference between the signals at the two antennas also is related to R. This fact is evident from the distribution function for $(\theta_2 - \theta_1)$ as derived by MacDonald (1949) and given in our equations 2-35 upon recalling the definition of R given in equation 2-38. It is difficult, however, to extract a physically meaningful relationship with the degree of generality retained to this point. Let us, therefore, simplify our considerations and return later to a discussion of the phase characteristics.

Recalling that all the physical information we require about the antenna voltages is contained in the elements of the moment Matrix M, let us return to the integrals which define the elements, equations 2-28 through 2-31. From physical considerations, the integration limits in these equations were set at $-\pi$ and $+\pi$. This allows signal reception from all directions, and we can as well set the limits at $-\infty$ and $+\infty$. The physical information concerning the directional distribution of received signal is contained in the angular power density function $p(\alpha)$, more

commonly called the "angular power spectrum."

For an ionospherically scattered satellite or radio-star signal, we expect the flux to be received in a narrow cone centered on the direction of the source.[1] It is reasonable to assume also that the angular power spectrum is an even function about the center direction,[2] without specifying the shape of the spectrum in detail. Thus let the center direction be denoted by α_o and make the following change of variables:

$$\alpha = \alpha_o + \delta \qquad 2\text{-}49$$

$$p(\alpha) = F(\delta) = F(-\delta) \qquad 2\text{-}50$$

A physically reasonable assumption which is persistently verified by observation is that F is appreciable only for values of δ which are sufficiently small that $\cos\delta$ may be approximated by unity and $\sin\delta$ by δ. The above set of assumptions means that we are assuming a narrow, symmetrical angular spectrum.

It is shown in Appendix 1d that a narrow, symmetrical angular spectrum leads to the following expressions for the signal covariances μ_c and μ_s and the wavefront correlation R:

---

[1] The "direction of the source" may be only an apparent direction due to refraction by ionospheric structure of a scale larger than that producing the scattering presently under consideration.

[2] It has been pointed out by K. W. Philip (private communication) that one might expect some skewing of the angular spectrum to result from the non-isotropic nature of a magneto-ionic medium. The possible effect of the geomagnetic field on the shape of the angular spectrum produced by ionospheric scattering has not been considered here, except insofar as it might influence the shape of ion-density irregularities.

$$\mu_c = \cos 2\chi_o \int_{-\infty}^{\infty} F(\delta) \cos \left(\frac{2\pi d}{\lambda} \delta \cos \alpha_o\right) d\delta \qquad 2\text{-}51$$

$$\mu_s = \sin 2\chi_o \int_{-\infty}^{\infty} F(\delta) \cos \left(\frac{2\pi d}{\lambda} \delta \cos \alpha_o\right) d\delta \qquad 2\text{-}52$$

$$R = \frac{\int_{-\infty}^{\infty} F(\delta) \cos [(2\pi d/\lambda) \delta \cos \alpha_o] d\delta}{\sigma^2} = \frac{\int_{\infty}^{\infty} F(\delta) \cos [(2\pi d/\lambda) \delta \cos \alpha_o] d\delta}{\int_{-\infty}^{\infty} F(\delta) d\delta} \qquad 2\text{-}53$$

Now, equations 2-21 and 2-26 show that the covariance of the voltages at the two antennas is equal to μ_c. Therefore, under the assumption of a narrow symmetrical angular spectrum, we have

$$\overline{v_1 v_2} = \cos 2\chi_o \int_{\infty}^{\infty} F(\delta) \cos [(2\pi d/\lambda) \delta \cos \alpha_o] d\delta \qquad 2\text{-}54$$

so

$$\overline{v_1 v_2} = \sigma^2 (R \cos 2\chi_o) \qquad 2\text{-}55$$

This relates the covariance of voltages to the wavefront correlation function R and shows that the correlation of voltages is simply R cos $2\chi_o$.

The correlation of amplitudes at two antennas receiving a narrow symmetrical angular spectrum is given by equation 2-48 with R evaluated according to equation 2-53. For the square of amplitudes, the correlation is given by R^2.

When the angular spectrum is narrow and symmetrical, it becomes possible to obtain a meaningful description of the phase difference

between the two antennas. In this case, MacDonald's general expression for the distribution of $\theta_2 - \theta_1$, given by equations 2-35, can be reduced as follows. With μ_c, μ_s, and R given respectively by equations 2-51, 2-52 and 2-53, MacDonald's parameter β from our 2-35b becomes

$$\beta = R\,[\cos 2\chi_o \cos(\theta_2 - \theta_1) - \sin 2\chi_o \sin(\theta_2 - \theta_1)]$$

$$= R\,[\cos(\theta_2 - \theta_1 + 2\chi_o)] \qquad 2\text{-}56$$

Substitution of this expression for β into 2-35a gives the following distribution for $\theta_2 - \theta_1$:

$$\frac{1-R^2}{2\pi}\left(\frac{1}{1-R^2\cos(\theta_2-\theta_1+2\chi_o)} + \frac{R\cos(\theta_2-\theta_1+2\chi_o)}{[1-R^2\cos(\theta_2-\theta_1+2\chi_o)]^{3/2}}\left\{\pi - \cos^{-1}[R\cos(\theta_2-\theta_1+2\chi_o)]\right\}\right) \qquad 2\text{-}57$$

The distribution 2-57 is still rather complicated, but two facts are evident upon direct inspection. First the distribution of the phase difference $\theta_2 - \theta_1$ is highly dependent upon the wavefront correlation function R. Second, the distribution is even about $2\chi_o$. It can be seen also that the limiting values of zero and unity for the correlation R yield a uniform distirbution over a range of 2π and a Dirac delta fuction at $2\chi_o$, respectively. For any R, the average value of $\theta_2 - \theta_1$ is $2\chi_o$.

As pointed out by Bramley (1951), the variance and higher moments of the phase-difference distribution would be difficult to calculate. Bramley did calculate the mean absolute phase difference, obtaining for this observational parameter

$$\overline{|\theta_2 - \theta_1|} = \cos^{-1} R \qquad 2\text{-}58$$

However, the entire development to this point contains a physically severe restriction demanded by the Lindeberg formulation of the central limit theorem. Before discussing observational parameters, as such, let us remove this restriction.

D2 The Special Case of Weakly Scattered Waves

The Lindeberg formulation of the central limit theorem requires that no component in our angular spectrum dominates the spectrum. If we were discussing backscatter, for instance, this condition would preclude consideration of a spectrum containing a strong component due to specular reflection. In the forward scatter case we might expect an analagous "nondeviated" or nonscattered component. In Chapter III we shall discuss such a component within the context of ionospheric structure. For now, let us assume its existence and ask how we can handle it in our present observational discussion. Again we shall follow Bramley's application of Rice's work. In order to describe conditions observed in the auroral zone, however, we shall have to extend Bramley's analysis and its mathematical foundation due to Rice. Unfortunately, we shall have to resort to numerical techniques.

In the foregoing sections of this chapter we have been dealing with a signal received on the ground after scattering in the ionosphere. We began in equation 2-1 with a Fourier sum of scatter components, with the general component of angular frequency ω_n presumed to be the result of ionospheric modulation. Suppose now that in addition to the scatter, or modulation, components there is a unique component at the angular frequency $\omega_o = \omega$. The relationship between the unique component and the

remainder of the spectrum is that of a carrier and modulation-produced sidebands.

In the absence of ionospheric modulation by scattering, there would be no sidebands and the entire flux from the source would be contained in the unique component. In the foregoing, we were forced by the central limit theorem to consider the opposite case of complete scattering, where all power is contained in the scatter spectrum. We shall now consider the case of weak scatter in which both the nonscattered and scattered components exist but where the former dominates the overall angular spectrum.

For the case of weak scatter, the expression corresponding to equation 2-1 is identical to 2-1 with the addition of a term outside the summation, giving the contribution of the nonscattered component. Since the phases, ϕ_n, in 2-1 are assumed to be random, we are free to reference them in such a way that $\phi_o = 0$. In addition, for $\omega_o = \omega$, the second term in the argument of 2-1 vanishes, and the contribution of the nondeviated component is simply $c_o \cos \omega t$. That is, the time varying phase ψ_o is zero. It is only in this case that the concept of "carrier" and "sidebands" can be retained strictly.

It is to be noted that one could take account of large-scale refractive effects by allowing the "nondeviated" component to have a time-varying phase $\psi_o(t)$. In this case, small-scale scatter effects would be described in the frequency domain and large-scale refractive effects in the time domain of the same Fourier pair. If this were done, we would find that we would have to have one foot in each domain of the spatial-angular Fourier pair also. This approach has potential for describing

multiple-scaled ionospheric structure, but it becomes somewhat complicated analytically. We shall concern ourselves only with effects which, in the present context, can be assigned to "small-scale scattering."

Whatever the nature of the angular spectrum, the voltages v_1 and v_2 at the two antennas can be represented by (time-varying) amplitudes A_1 and A_2 and phases θ_1 and θ_2, as in equations 2-10. We are interested in relations between these quantities for the case of a nonscattered component, which we shall denote by S cos ωt, accompanied by a scatter spectrum. The situation is mathematically equivalent to a sinusoidal signal in the presence of a noise spectrum. It is the scatter or "noise" component which was described in section D1 of this chapter.

All of the foregoing results can be taken over with a slight change in notation. We can no longer equate the antenna amplitudes and phases with those of the scatter-component resultant alone. We shall retain A's and θ's for the former and use B's and ϕ's for the latter. With this notation in mind and taking into account the separation between antennas, the antenna voltages can be written as

$$v_1 = A_1 \cos(\omega t + \theta_1) = S \cos(\omega t + \chi_o) + B_{1c} \cos \omega t - B_{1s} \sin \omega t \quad 2\text{-}59$$

$$v_2 = A_2 \cos(\omega t + \theta_2) = S \cos(\omega t - \chi_o) + B_{2c} \cos \omega t - B_{2s} \sin \omega t \quad 2\text{-}60$$

where the four B's represent components of random-walk resultants as discussed in section D1a of this chaper.

The relations between the various quantities above are easily seen in the phasor diagrams of figure 2, where it is to be remembered that the B's and ϕ's are random variables.

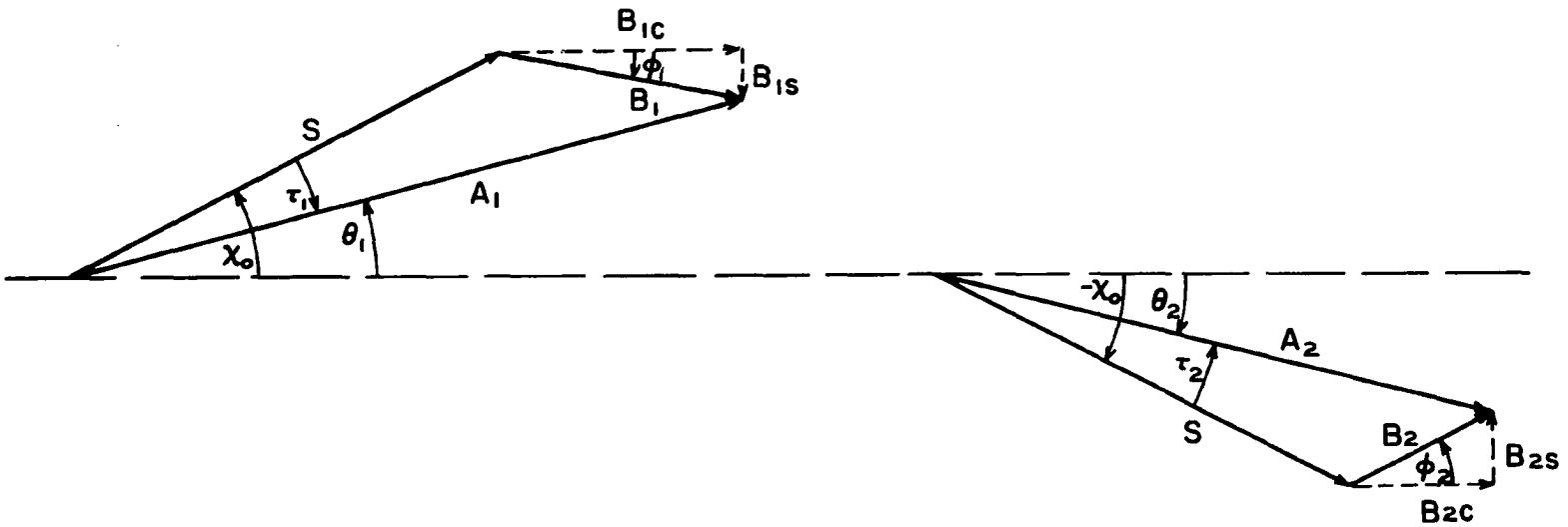

Fig. 2. Phasor relations of scattered and nonscattered signal components at two antennas of an interferometer.

From the phasor diagrams or from equations 2-59 and 2-60, it is obvious that

$$A_1^2 = S^2 + 2S(B_{1c} \cos \chi_o + B_{1s} \sin \chi_o) + B_{1c}^2 + B_{1s}^2 \qquad 2\text{-}61$$

$$A_2^2 = S^2 + 2S(B_{2c} \cos \chi_o - B_{2s} \sin \chi_o) + B_{2c}^2 + B_{2s}^2 \qquad 2\text{-}62$$

The last two terms in each of the above, when averaged, each give the variance σ^2 of the scatter components. Further, since B_{1c}, B_{1s}, B_{2c} and B_{2s} have zero means in accord with the results of section D1a, we get the following upon averaging equations 2-61 and 2-62:

$$\overline{A_1^2} = \overline{A_2^2} = S^2 + 2\sigma^2 = 2P \qquad 2\text{-}63$$

where P is the (average) total power (per unit resistance) received from the source. At the frequencies with which we are concerned, where ionospheric absorption may be ignored, the total power is constant.

From equations 2-59 and 2-60 we can find also the covariance of the voltages v_1 and v_2. It is shown in Appendix 1e that the result is

$$\overline{v_1 v_2} = \tfrac{1}{2}S^2 \cos 2\chi_o + \mu_c \qquad 2\text{-}64$$

For a narrow scatter spectrum which is symmetrical about the direction of the nonscattered component, μ_c is found from equations 2-51 and 2-53 to be

$$\mu_c = R\,\sigma^2 \cos 2\chi_o \qquad 2\text{-}65$$

Thus equation 2-64 becomes

$$\overline{v_1 v_2} = (\tfrac{1}{2}S^2 + R\sigma^2) \cos 2\chi_o \qquad 2\text{-}66$$

Since the correlation ρ between the voltages is given by the ratio of the covariance to the power P, we have from 2-66 and 2-63

$$\rho = \frac{S^2 + 2R\sigma^2}{S^2 + 2\sigma^2} \cos 2\chi_o \qquad 2\text{-}67$$

It can be seen that if S goes to zero, the variance reduces to that given in equation 2-55 for the complete scattering case and ρ to the corresponding value of correlation, R cos $2\chi_o$.

Equations 2-66 and 2-67 hold for all values of the variables and so are quite general. To discuss the correlation of amplitudes and the phase-difference characteristics of the signals in this general case, however, is difficult. We shall restrict our considerations here to the case of weak scatter, following the example of Bramley (1951). In section D3 we shall extend Bramley's considerations to the more general case, using numerical techniques.

Weak scatter is characterized by the condition that σ is small compared with $S/\sqrt{2}$. In this case, according to Bramley, we have approximately

$$A_1 = S + B_{1c} \cos \chi_o + B_{1s} \sin \chi_o + \frac{1}{2S}(B_{1c} \sin \chi_o - B_{1s} \cos \chi_o)^2 \qquad 2\text{-}68$$

$$A_2 = S + B_{2c} \cos \chi_o - B_{2s} \sin \chi_o + \frac{1}{2S}(B_{2c} \sin \chi_o + B_{2s} \cos \chi_o)^2 \qquad 2\text{-}69$$

These approximations can be verified by squaring and comparing with 2-61 and 2-62. If this process is carried out, it is found that the approximation involves ignoring the effect of terms containing factors of order σ/S and σ^2/S^2. From 2-68 and 2-69 we find that

$$\overline{A_1} = \overline{A_2} = S + \frac{\sigma^2}{2S} \qquad 2\text{-}70$$

and

$$\overline{A_1}^2 = \overline{A_2}^2 \approx S^2 + \sigma^2 \qquad 2\text{-}71$$

As in the complete scatter case, we shall find that important quantities are the mean product of amplitudes $\overline{A_1 A_2}$ and the corresponding quantity for the squares of the amplitudes $\overline{A_1^2 A_2^2}$. If, again, we ignore terms of high order in σ/S, we obtain approximately from 2-68 and 2-69

$$\overline{A_1 A_2} = S^2 + \sigma^2 + \mu_c \cos 2\chi_o + \mu_s \sin 2\chi_o \qquad 2\text{-}72$$

and from 2-61 and 2-62

$$\overline{A_1^2 A_2^2} = S^4 + 4\sigma^2 S^2 + 4S^2 (\mu_c \cos 2\chi_o + \mu_s \sin 2\chi_o) \qquad 2\text{-}73$$

The details are given in Appendix 1f.

Now equation 2-39 shows that we can obtain the correlation coefficient for amplitudes from 2-70, 2-71 and 2-72. Thus

$$\rho_A = \frac{\mu_c \cos 2\chi_o + \mu_s \sin 2\chi_o}{\sigma^2} \qquad 2\text{-}74$$

But comparison with equations 2-51 and 2-52 and 2-53 shows that, for a narrow symmetrical spectrum, this gives simply

$$\rho_A = R \qquad 2\text{-}75$$

In order to find the correlation coefficient for the squares of the amplitudes from equation 2-40, we still need $\overline{A^2}^2$ and $\overline{A_1^4}$. The former we get simply from 2-63. Thus we have approximately

$$\overline{A_1^2}^2 = \overline{A_2^2}^2 = S^4 + 4S^2 \sigma^2 \qquad 2\text{-}76$$

The latter is obtained from 2-61 and 2-62 with the approximate result

$$\overline{A_1^4} = \overline{A_2^4} = S^4 + 8S^2\sigma^2 \qquad 2\text{-}77$$

Combining these along with 2-73, we get from 2-40

$$\rho_{A^2} = \frac{4S^2 (\mu_c \cos 2\chi_o + \mu_s \sin 2\chi_o)}{4S^2 \sigma^2} \qquad 2\text{-}78$$

Again this reduces, for the case of a narrow symmetrical scatter spectrum, to

$$\rho_{A^2} = R \qquad 2\text{-}79$$

Thus in the weak scatter case the correlation coefficient for amplitudes and that for the square of amplitudes are equal and both are given directly by the wavefront correlation function.

From the phasor diagrams of figure 2, we obtain the following:

$$\tan \theta_1 = \frac{S \sin \chi_o + B_{1s}}{S \cos \chi_o + B_{1c}} \qquad \tan \theta_2 = \frac{-S \sin \chi_o + B_{2s}}{S \cos \chi_o + B_{2c}} \qquad 2\text{-}80$$

Now, we should like the distribution of the random variable $(\theta_2 - \theta_1)$. Accordingly, we need the distributions of θ_1 and θ_2. Since χ_o is constant, the desired distributions will be identical, except for a shift in mean, to the distributions of τ_1 and τ_2, where the latter two random variables are defined as

$$\tau_1 = \theta_1 - \chi_o \quad \text{and} \quad \tau_2 = \theta_2 + \chi_o \qquad 2\text{-}81$$

Combining 2-80 and 2-81, we find

$$\tan \tau_1 = \frac{\frac{S \sin \chi_o + B_{1s}}{S \cos \chi_o + B_{1c}} - \tan \chi_o}{1 + \frac{S \sin \chi_o + B_{1s}}{S \cos \chi_o + B_{1c}} \tan \chi_o} \; ; \; \tan \tau_2 = \frac{-\frac{S \sin \chi_o - B_{2s}}{S \cos \chi_o + B_{2c}} + \tan \chi_o}{1 + \frac{S \sin \chi_o - B_{2s}}{S \cos \chi_o + B_{2c}} \tan \chi_o} \qquad 2\text{-}82$$

It is easily shown that 2-82 reduces to

$$\tan \tau_1 = \frac{B_{1s} \cos \chi_o - B_{1c} \sin \chi_o}{S + B_{1c} \cos \chi_o + B_{1s} \sin \chi_o} \; ; \tan \tau_2 = \frac{B_{2s} \cos \chi_o + B_{2c} \sin \chi_o}{S + B_{2c} \cos \chi_o + B_{2s} \sin \chi_o} \qquad 2\text{-}83$$

In the weak scatter case where S dominates the angular spectrum, τ_1 and τ_2 will be small and the above can be approximated by

$$\tau_1 = S^{-1}(B_{1s} \cos \chi_o - B_{1c} \sin \chi_o) \; ; \; \tau_2 = S^{-1}(B_{2s} \cos \chi_o + B_{2c} \sin \chi_o) \qquad 2\text{-}84$$

Equations 2-84 show that, in the weak scatter case, τ_1 and τ_2 are the sums of two independent gaussian random variables. Accordingly, they themselves have gaussian distributions. Their means and variances will be given by the sums of the means and variances of the corresponding B's. Thus both τ_1 and τ_2 have means of zero and, taking into account the constants $S^{-1} \cos \chi_o$ and $S^{-1} \sin \chi_o$, variances of $\sigma^2 S^{-2}$.

From equations 2-84, we obtain

$$\overline{\tau_1\tau_2} = S^{-2}\left(\overline{B_{1s}B_{2s}}\cos^2\chi_o - \overline{B_{1c}B_{2c}}\sin^2\chi_o + \overline{B_{1s}B_{2c}}\sin\chi_o\cos\chi_o\right.$$

$$\left. - \overline{B_{2s}B_{1c}}\sin\chi_o\cos\chi_o\right)$$

$$= S^{-2}[\mu_c(\cos^2\chi_o - \sin^2\chi_o) + 2\mu_s(\sin\chi_o\cos\chi_o)]$$

$$= S^{-2}(\mu_c\cos 2\chi_o + \mu_s\sin 2\chi_o) \qquad 2\text{-}85$$

and

$$\overline{\tau_1^2} = \overline{\tau_2^2} = S^{-2}\sigma^2 \qquad 2\text{-}86$$

From equations 2-85 and 2-86 we see that the correlation coefficient between τ_1 and τ_2, and therefore between θ_1 and θ_2, is given by

$$\rho_\tau = \frac{\mu_c\cos 2\chi_o + \mu_s\sin 2\chi_o}{\sigma^2} \qquad 2\text{-}87$$

Again, for the case of a narrow symmetrical scatter spectrum, this reduces to

$$\rho_\tau = R \qquad 2\text{-}88$$

Thus in the case of weak scatter and a narrow symmetrical randomly phased scatter spectrum, the correlation coefficients for all pertinent envelope parameters are given directly by the wavefront correlation R.

The characteristics of τ_1 and τ_2 established above may be summarized by a two-dimensional normal distribution with zero means, variances of σ^2S^{-2}, and correlation R. Thus (Bendat, 1958, section 3.4.4)

$$f(\tau_1,\tau_2) = \frac{S^2}{2\pi\sigma^2\sqrt{1-R^2}} \exp\left[-\frac{S^2(\tau_1^2 - 2R\tau_1\tau_2 + \tau_2^2)}{2\sigma^2(1-R^2)}\right] \qquad 2\text{-}89$$

More important, the characteristics of τ_1 and τ_2 allow us to establish the distribution of $\tau_2 - \tau_1$. Middleton (1960, section 7.5-1) shows that the distribution of the sum of two gaussian random variables is always gaussian, even if the two variables are not independent. He also shows that the mean of the sum is equal to the sum of the means and gives a very general expression for the variance of the resulting distribution. In our particular case, the resulting mean is zero and the resulting variance is given by $(2\sigma^2/S^2)(1 - R)$. Hence the distribution of $\tau_2 - \tau_1$ is

$$f(\tau_2 - \tau_1) = \frac{S}{2\sigma[\pi(1-R)]^{\frac{1}{2}}} \exp\left[\frac{-S^2(\tau_2 - \tau_1)^2}{4\sigma^2(1-R)}\right] \qquad 2\text{-}90$$

Now equations 2-81 show that

$$\tau_2 - \tau_1 = \theta_2 - \theta_1 + 2\chi_o \qquad 2\text{-}91$$

Thus equation 2-90 gives the distribution of the phase difference $\theta_2 - \theta_1$ with the mean shifted by $2\chi_o$. Therefore the moments of the distribution 2-90 give directly the central moments of $\theta_2 - \theta_1$. In addition, if we define

$$\eta = \tau_2 - \tau_1 \qquad 2\text{-}92$$

we also see that $\overline{|\eta|}$ gives the mean deviation of $\theta_2 - \theta_1$ from its mean value of $2\chi_o$. This observational quantity is given, from the

distribution 2-90, by

$$\overline{|\eta|} = \frac{S}{\sigma[\pi(1 - R)]^{\frac{1}{2}}} \int_0^\infty \eta \exp\left[\frac{-S^2 \eta^2}{4\sigma^2(1-R)}\right] d\eta \qquad 2\text{-}93$$

The integral is of the form $\int_0^\infty \eta\, e^{-a^2\eta^2}\, d\eta$, which by a change of variable to $x = a\eta$, is found to be $1/2a^2$ or $2\sigma^2(1-R)/S^2$. Thus we obtain

$$\overline{|\eta|} = \frac{\sigma}{S}\, 2\left(\frac{1 - R}{\pi}\right)^{\frac{1}{2}} \qquad 2\text{-}94$$

which is the weak scatter expression corresponding to equation 2-58 in the complete scatter case.

D3 The General Case of Arbitrary Degree of Scatter

3a The coherence ratio: In sections D1 and D2 of this chapter we have discussed the statistical characteristics of two types of signals. The first was assumed to be totally scattered during transmission through the ionosphere. In the second case it was assumed that only a very small portion of the total flux was scattered, the major portion arriving at the ground without any ionospherically introduced characteristics. This condition of weak scatter corresponds to reality at middle latitudes. The condition of complete scatter was treated by Bramley (1951) largely to provide an analytical foundation for the weak-scatter case. In the auroral zone, ionospheric conditions are such that the complete scatter case also is met occasionally in observations. More often, conditions are intermediate between the two extremes of weak and complete scatter. Thus it is necessary to treat the general case.

In section D2 we introduced an ionospherically nondeviated component of the angular spectrum whose amplitude is S and whose average power

therefore is $S^2/2$. The nondeviated component was added to a noiselike spectrum of scatter components of average power σ^2. Obviously the ratio of the two contributions to total received power can be used as a measure of the degree of scattering. Now, when there is no scattering the received wavefront is fully coherent, and when there is complete scattering the wavefront has the noncoherent or random character of noise. As a measure of the degree of scattering, therefore, let us define the "coherence ratio" b as

$$b = S^2/2\sigma^2 \qquad 2\text{-}95$$

It was pointed out in section D2 that the nondeviated component is mathematically equivalent to a sinusoidal signal buried in noise, the latter arising from the scatter spectrum. Thus the coherence ratio is mathematically equivalent to a (power) signal-to-noise ratio. It is immediately evident that the complete scatter case of section D1 corresponds to a coherence ratio of zero while the weak scatter case of section D2 corresponds to large coherence ratio. Full coherence is achieved as the flux in the scatter spectrum vanishes, forcing the coherence ratio to increase without limit.

The importance of the coherence ratio in describing the effect of ionospheric scattering is obvious. It is a direct measure of the degree to which scattering is taking place during a given observation. This has been recognized for some time and put to use in observations with radiometers and other simple receivers. In analysis of such observations it was possible to make direct use of the work of Rice (1945) on the mathematical analysis of a sinusoidal signal buried in noise (McNicol,

1949). Rice's work, however, stopped short of providing a mathematical basis for analyzing interferometric observations. When two antennas are used and phase coherence between them is retained, one must deal with the correlation which exists between the signals received at the two antennas. The mathematical analogies dealing with the temporal autocorrelation function of a signal were developed by Rice for the case of pure noise but not for the case of a sinusoid buried in noise.

Now Bramley (1951) was able to adapt Rice's work to the case of weak scatter as observed with an interferometer. He did not treat the general case however. His work was adequate for observations at middle latitudes. At equatorial (Koster, 1958) and auroral (Little et al, 1962) latitudes, however, significant reductions are observed in the correlation of voltage at the two antennas of an interferometer. These reductions, which we shall call "visibility fades," can occur only if the coherence ratio decreases to finite values. In the extreme, the coherence ratio may decrease to zero so that complete scatter takes place, but any finite value is possible and indeed a wide range is observed.

Studies of visibility fades to date either have effectively ignored the quantitative ionospheric information available in them or else have treated the phenomenon approximately. The approximate approach precludes direct experimental determination of the coherence ratio. In some of the work which has appeared in the literature, the significance of the coherence ratio and of Bramley's approach to the problem does not appear to have been fully appreciated. It is our intent in this section to extend Bramley's approach to include the general case of arbitrary coherence ratio.

3b Covariance of voltages and fringe visibility: It is widely known that the output of a phase-switch radio interferometer gives directly the covariance of its antenna voltages (Bracewell, 1958; Fremouw, 1963). We have already established (equation 2-66) that this quantity is given for arbitrary b, by

$$\overline{v_1 v_2} = (\tfrac{1}{2}S^2 + R\sigma^2) \cos 2\chi_o \qquad 2\text{-}96$$

Now, in the absence of ionospheric scatter, σ vanishes and all power is contained in the nondeviated component of the angular spectrum. Thus, under disturbed ionospheric conditions the covariance of antenna voltages, and therefore the averaged output of a phase-switch interferometer, becomes $P \cos 2\chi_o$. But P, the total flux received from the source, is independent of scatter conditions and in general is given, according to equation 2-63, by $\tfrac{1}{2}S^2 + \sigma^2$. Therefore the ratio of the averaged output of a phase-switch interferometer under conditions of scatter to that under undisturbed conditions is given by

$$\frac{\tfrac{1}{2}S^2 + R\sigma^2}{\tfrac{1}{2}S^2 + \sigma^2} = \frac{b + R}{b + 1} \qquad 2\text{-}97$$

Comparison of 2-97 with equation 2-67 shows that

$$\frac{b + R}{b + 1} \cos 2\chi_o = \rho \qquad 2\text{-}98$$

where ρ is the correlation coefficient for voltages.

Now, the covariance is inherently an average quantity, so that identification of it with the output of any instrument implies some sort of averaging of that output. In our case, where we are dealing with a radio interferometer observing a radio star whose signal has been

scattered by the ionosphere, our averaging period must be long compared with the scintillations produced by motion of the scattering region. Typically this requires averaging over at least many tens of seconds and preferably over a few minutes.

Statistical stationarity requires that b and R remain constant over the averaging period. In the case of a radio star, however, its direction α_o and the phase angle χ_o derived therefrom vary with time due to the earth's rotation. We shall see later that a convenient and meaningful averaging period, which turns out in practice to be on the order of minutes, is that during which $2\chi_o$ varies from $-\pi/2$ to $+\pi/2$. Let us denote by $\bar{\rho}$ the average value of ρ during this period. Now χ_o is approximately a linear function of time so, during the same period, we have $\overline{\cos 2\chi_o} = 2/\pi$. Thus, over such an averaging period, we have

$$\frac{b + R}{b + 1} = \frac{\pi\bar{\rho}}{2} \qquad 2\text{-}99$$

Equation 2-99 relates the coherence ratio b and the wavefront correlation R to the average mathematical correlation coefficient between the voltages at the antenna outputs. The right side of the equation has little physical significance and in fact depends strongly upon our choice of averaging period. The physical parameters we desire are b and R. For simplicity, let us replace $\pi\bar{\rho}/2$ with the symbol r, where

> r = the ratio of the average output of a phase-switch interferometer under conditions of scatter to that under undisturbed ionospheric conditions, with the period of averaging in each case corresponding to one-half cycle on the instrument's output pattern.

With this definition, the disturbed coherence ratio b and wavefront

correlation R are related observationally by

$$r = \frac{b + R}{b + 1}. \qquad 2\text{-}100$$

The parameter r has strict mathematical meaning through its relation to $\bar{\rho}$, but its physical meaning is obscure from this point of view.[1] It will be given more obvious meaning later when we discuss observational scaling procedures. For now let it suffice to say that r is a quantity which is readily determined from phase-switch interferometer observations. We shall call it "visibility." Its importance lies in its relationship to the physically meaningful quantities b and R. The relation of b and R to ionospheric parameters will be developed in Chapter III.

3c The analytical approach to amplitude and phase characteristics and its limitations: Equation 2-96 gives the covariance of antenna voltages for arbitrary coherence ratio. In order to obtain equally general relations for the amplitude and phase characteristics analytically, we must obtain the appropriate joint probability density functions. Several successors of Rice in the field of signal statistics and communication theory have dealt with the problem of a signal buried in noise. Notable among these is Middleton, who developed the quadri-variate joint distribution for amplitudes and phases and carried out the integrations necessary to obtain the joint distributions for amplitudes and for phases independently (Middleton, 1947).

---

[1] For the reader familiar with radio-astronomy terminology, consideration of equations 2-98 and 2-100 will show that r is the fringe visibility of the interferometer record.

The distributions which Middleton developed are directly applicable to our situation if we include the reasonable assumption of a narrow symmetrical angular spectrum centered on the nondeviated component, with one additional assumption necessary, namely that the slowly varying phase χ_o is kept at zero. This "phase compensation" is produced and maintained electronically in the pertinent instrument of our experiment. Hence we are free to use Middleton's distributions directly.

Middleton's work is quite general and it includes provision for dealing with modulated signals. This provision could be used in our problem in order to account for refractive effects by large-scale ionospheric structure. Thus changes in apparent direction of the source would produce phase modulation of our nondeviated component and focusing or defocusing by ionospheric lenses would produce amplitude modulation. The same modulations, however, would be imposed on the scatter components, resulting in nonstationarity of the noiselike part of our total signal. Again we shall concentrate on small-scale scattering, having pointed out the potential of Middleton's formulation for dealing with multi-scaled ionospheric scattering.

For the case of small-scale scattering only, equation 5.18 of Middleton (1947) gives directly the joint distribution of amplitudes appropriate to our observations.[1] In our notation the distribution is

$$\frac{A_1 A_2}{\sigma^4(1-R^2)} \exp\left[\frac{-2b}{(1+R)} - \frac{A_1^2+A_2^2}{2\sigma^2(1-R^2)}\right] \sum_{m=0}^{\infty} \varepsilon_m I_m\left[\frac{RA_1A_2}{\sigma^2(1-R^2)}\right] I_m\left[\frac{SA_1}{\sigma^2(1+R)}\right] I_m\left[\frac{SA_2}{\sigma^2(1+R)}\right]$$

2-101

[1] The observations referred to here were obtained with a phase-sweep interferometer employing noncoherent detection and phase compensation. (The phase compensation feature has little practical significance in consideration of amplitudes but considerable importance for phase measurements).

where $\varepsilon_o = 1$, $\varepsilon_m = 2$ for $m \geq 1$, and I_m = the modified Bessel function of the first kind and order m.

While the distribution above is quite complicated, it is fairly easy to see that it reduces to the distribution given by Rice for pure noise, in the event that S and b vanish. In this case the second and third Bessel function arguments above vanish. The corresponding Bessel functions themselves then vanish except for order zero, in which order they have value unity (Watson, 1948, equation 2 in section 3.7 and Table II in the appendix). The distribution 2-101 then reduces to

$$f(A_1,A_2) = \frac{A_1 A_2}{\sigma^4(1-R^2)} \exp\left[-\frac{A_1^2 + A_2^2}{2\,\sigma^2(1-R^2)}\right] I_o\left[\frac{R\,A_1 A_2}{\sigma^2(1-R^2)}\right] \qquad 2\text{-}102$$

Upon recalling the definition of R from equation 2-38, it is readily seen that equation 2-102 is identical with equation 2-34, which is the distribution given by Rice for pure noise (our complete scatter case). In the opposite extreme of full coherence, where σ^2 vanishes and b increases without limit, the distribution becomes a Dirac delta function at $A_1 = A_2 = S$.

Now Middleton (1947) has developed expressions for second-order moments such as $\overline{A_1 A_2}$ and $\overline{A_1^2 A_2^2}$ from the distribution 2-101, from which we could derive the correlation coefficients for amplitudes and for the squares of amplitudes. The expressions are so complicated, however, as to preclude their usefulness for our observational problem.

Middleton's joint distribution for the phases θ_1 and θ_2 (equation 5.20 in his 1947 paper) is even more complicated than that quoted in our equation 2-101 for the amplitudes A_1 and A_2 under the same conditions. In his textbook on statistical communication theory (Middleton, 1960),

the author himself points out the limited applicability (due to complexity) of expressions for moments of the joint phase distribution. Further, it is not the joint phase distribution, per se, whose moments we desire for our observational problem, but rather observational parameters derived from the single-variate distribution of $(\theta_2-\theta_1)$. There appears to be no simple means of obtaining our desired distribution and observational parameters derived therefrom, even if we were to use Middleton's joint distribution for θ_1 and θ_2.

3d The numerical approach: In view of the above it appears necessary to abandon hope for an analytical treatment of the general scattering problem. Instead we shall develop a numerical technique which will allow us to compute observational parameters for arbitrary coherence ratio. The technique must produce results which agree with the analytical results of Rice and Bramley in the special cases where analytical solutions exist. In Chapters IV and V we shall use the results of the numerical analysis to reach observational conclusions.

Let us recall that the signals with which we must work in the general case consist of a nonscattered component whose amplitude is S and a spectrum of scatter components whose resultant amplitude is B_1 at one antenna and B_2 at the other. The phase angles of the nonscattered component are plus and minus χ_o, respectively, at the two antennas. The phase angles of the scatter components are independent of one another and uniformly distributed over a range of 2π.

Now χ_o is established purely by the position of the source and, for a radio star, is slowly varying and completely predictable. It contains

no information about the ionosphere or its scattering process (for the small-scale scattering under consideration here.) It can be (and is in our phase-sweep interferometer) maintained at the constant value of zero by instrumental introduction of time-varying phase compensation. The same phase retardation is introduced into each of the scatter components with the result that their statistical characteristics are unchanged. All the statistical results of section D1 of this chapter are applicable to the scatter spectrum and its resultant, with χ_o to be taken as zero throughout.

The relationships between the quantities of interest are those shown in the phasor diagrams of figure 2, except that χ_o is to be taken as zero. Thus we have the relations given in figure 3. It is to be recalled that the B's are random variables resulting from random-walk addition of a randomly phased angular scatter spectrum. Their statistical characteristics, along with the relative magnitude of S, determine the statistical characteristics of the A's and θ's. It is certain average characteristics of these latter random variables which we seek.

The independent variables which we wish to control as input parameters in our numerical technique are the relative magnitude of the non-scattered and scattered components and the correlation between the scatter resultants at the two antennas. That is, we wish to control the coherence ratio b (while maintaining the total power constant) and the wavefront correlation R. It will be recalled that the latter is identical to the correlation of voltage in the scatter spectrum when χ_o is zero.

Now the total power is given by $P = S^2 + \sigma^2$ and the coherence ratio by $b = S^2/2\sigma^2$. Combination of these two equations shows that

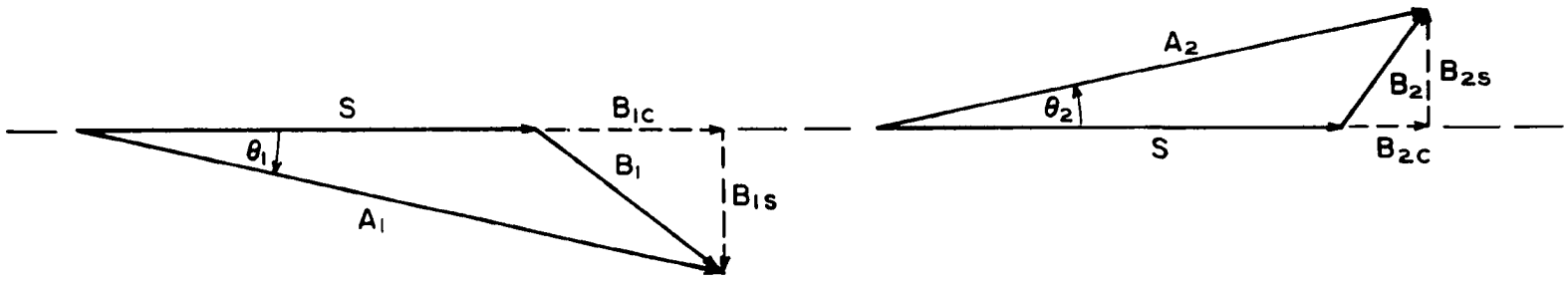

Fig. 3. Effective phasor relations of scattered and nonscattered signal components at two antennas of a phase-compensated interferometer.

$$S = [2bP/(b + 1)]^{\frac{1}{2}} \text{ and } \sigma = [P/(b + 1)]^{\frac{1}{2}} \qquad 2\text{-}103$$

For constant P, the magnitude of the coherent and nocoherent components are controlled by choice of b through equations 2-103.

The control of correlation is not so obvious but it turns out to be rather simple with digital computer techniques. Modern program libraries contain routines for generating fields of random numbers whose distributions are gaussian. We shall now show how four independent gaussian fields can be combined to produce two correlated gaussian fields in which the correlation coefficient is controllable as an input parameter. We shall find that the two correlated fields together with two of the original four independent fields possess the joint distribution which describes the scatter component of our angular spectrum.

First let us recall the distribution which must be satisfied. It is given in equation 2-32 for the case of general χ_o. Equations 2-51, 2-52 and 2-53 show that, for $\chi_o = 0$, μ_s vanishes and μ_c reduces to $R\,\sigma^2$. In this case, 2-32 becomes

$$f(B_{1c},B_{1s},B_{2c},B_{2s}) = \frac{1}{4\pi^2\,\sigma^4(1-R^2)}\,\exp\left\{\frac{-1}{\sigma^2(1-R^2)}\,[(B_{1c}^2+B_{1s}^2+B_{2c}^2+B_{2s}^2) - 2R(B_{1c}B_{2c}-B_{1s}B_{2s})]\right\} \qquad 2\text{-}104$$

This is the quadri-variate gaussian distribution appropriate to our case, namely a randomly phased, narrow and zero-center symmetrical angular spectrum of scatter components. The first and second moments are as follows:

$$\overline{B_{1c}} = \overline{B_{1s}} = \overline{B_{2c}} = \overline{B_{2s}} = 0$$

$$\overline{B_{1c}^2} = \overline{B_{1s}^2} = \overline{B_{2c}^2} = \overline{B_{2s}^2} = \sigma^2 \qquad 2\text{-}105$$

$$\overline{B_{1c}B_{2c}} = \overline{B_{1s}B_{2s}} = R\,\sigma^2$$

$$\overline{B_{1c}B_{1s}} = \overline{B_{2c}B_{2s}} = \overline{B_{1c}B_{2s}} = \overline{B_{2c}B_{1s}} = 0$$

Now suppose we have four independent random variables with gaussian distributions, namely B_{1c}, B_{1s}, x, and y, with the following first and second moments:

$$\overline{B_{1c}} = \overline{B_{1s}} = \overline{x} = \overline{y} = 0 \qquad 2\text{-}106$$

$$\overline{B_{1c}^2} = \overline{B_{1s}^2} = \overline{x^2} = \overline{y^2} = \sigma^2$$

Since we specified independence, the crossmoments are zero as follows:

$$\overline{B_{1c}B_{1s}} = \overline{xy} = \overline{B_{1c}x} = \overline{B_{1c}y} = \overline{B_{1s}x} = \overline{B_{1s}y} = 0 \qquad 2\text{-}107$$

Let us form the following linear combinations:

$$B_{2c} = RB_{1c} + (1-R^2)^{\frac{1}{2}}\,x \quad \text{and} \quad B_{2s} = RB_{1s} + (1-R^2)^{\frac{1}{2}}\,y \qquad 2\text{-}108$$

The means of B_{2c} and B_{2s} are simply the sums of the means of the two terms in their respective generating transformations, 2-108. In view of the first equation in 2-106, then, we have

$$\overline{B_{2c}} = \overline{B_{2s}} = 0 \qquad 2\text{-}109$$

Further, since B_{1c} and x are statistically independent and B_{2s} and y are also, the variances of B_{2c} and B_{2s} are the sums of the variances of the

terms in the generating transformations. In view of the second equation in 2-106, then, we have

$$\overline{B_{2c}^2} = \overline{B_{2s}^2} = R^2 \sigma^2 + (1-R^2)\,\sigma^2 = \sigma^2 \qquad 2\text{-}110$$

Forming other pertinent combinations from 2-106, 2-107 and 2-108 we get the following crossmoments:

$$\overline{B_{2c}B_{2s}} = R^2\overline{B_{1c}B_{1s}} + (1-R^2)\,\overline{xy} + R(1-R^2)^{\frac{1}{2}}\,(\overline{B_{1c}y} + \overline{B_{1s}x}) = 0$$

$$\overline{B_{2c}B_{1s}} = R\overline{B_{1c}B_{1s}} + (1-R^2)^{\frac{1}{2}}\,\overline{xB_{1s}} = 0$$

$$\overline{B_{2s}B_{1s}} = R\overline{B_{1s}^2} + (1-R^2)^{\frac{1}{2}}\,\overline{yB_{1s}} = R\sigma^2 \qquad 2\text{-}111$$

$$\overline{B_{2c}B_{1c}} = R\overline{B_{1c}^2} + (1-R^2)^{\frac{1}{2}}\,\overline{xB_{1c}} = R\sigma^2$$

$$\overline{B_{2s}B_{1c}} = R\overline{B_{1s}B_{1c}} + (1-R^2)^{\frac{1}{2}}\,\overline{yB_{1c}} = 0$$

Summarizing the first and second-order moments resulting from the four independent fields defined by 2-106 and the linear transformations 2-108, we get the following:

$$\overline{B_{1c}} = \overline{B_{1s}} = \overline{B_{2c}} = \overline{B_{2s}} = 0$$

$$\overline{B_{1c}^2} = \overline{B_{1s}^2} = \overline{B_{2c}^2} = \overline{B_{2s}^2} = 0$$

$$\overline{B_{2c}B_{1c}} = \overline{B_{2s}B_{1s}} = R\sigma^2 \qquad 2\text{-}112$$

$$\overline{B_{1c}B_{1s}} = \overline{B_{2c}B_{2s}} = \overline{B_{2c}B_{1s}} = \overline{B_{2s}B_{1c}} = 0$$

But the moments given in 2-112 are identical with those given in 2-105. Further, a gaussian distribution is defined uniquely by its first and second-order moments. Thus, starting with four independent gaussian random variables, we can transform two of them in such a way that the

resulting joint distribution defines voltages produced at two antennas by a randomly phased scatter spectrum with controllable correlation. The linear transformations involved are given in 2-108.

3e Results of the numerical approach: The preceding section describes a means of generating and relating the coherent and noncoherent component phasors shown in figure 3. With this accomplished, the trigonometry of the phasor diagrams allows straight-forward calculation of statistical characteristics of the resultant phasors as functions of b and R. For an extension of the work by Bramley, we should like to calculate the amplitude and amplitude-square correlation coefficients, ρ_A and $\rho_A 2$, and the mean absolute phase difference $\overline{|\eta|}$.

We saw in section D2 that ρ_A and $\rho_A 2$ are identical in the case of weak scatter and in section D1b that they are nearly so in the case of complete scatter. Thus, these two quantities are essentially equal throughout the range of b from zero to infinity and we shall concern ourselves only with ρ_A. Recalling that ρ_A is given by

$$\rho_A = \frac{\overline{A_1 A_2} - \overline{A_1}^2}{\overline{A_1^2} - \overline{A_1}^2} \qquad 2\text{-}113$$

it is easily seen from the phasor diagrams how ρ_A can be calculated once the phasors S, B_{1c}, B_{1s}, B_{2c}, and B_{2s} have been generated for a given combination of b and R, as described in section D3d.

Recalling also that $\overline{|\eta|}$ is given by

$$\overline{|\eta|} = \overline{|\theta_2 - \theta_1|} \qquad 2\text{-}114$$

when χ_o is zero, this quantity[1] too is easily found from the trigonometry. In performing this calculation, the phase difference is kept within the range of $-\pi$ to $+\pi$, corresponding to the observational fact that ambiguities are not resolved. This corresponds also to the fact that phase distributions in the work of Rice, MacDonald, and Middleton refer to a 2π range.

In figure 4 are given the results of numerical calculation of ρ_A and $|\eta|$ as functions of R for some finite values of b, along with the same quantities as obtained from Bramley's expressions for the limiting cases of large b and b = 0. These results are included to show how our numerical results relate to the analytical ones of Bramley. Certain other quantities are of more observational interest than ρ_A and $|\eta|$. Let us first explore the statistical characteristics of amplitude-related quantities and then examine the characteristics of phase.

Many scintillation studies have employed "scintillation indices" based on the fractional fluctuation of amplitude or power. These indices take no account of reductions in correlation between the signals received at two antennas of an interferometer. The most direct interferometric method of measuring amplitude or power fluctuations is with a phase-sweep (or "lobe-sweep") interferometer which employs simple rectification of the audio signal rather than coherent (or "phase-sensitive") detection at the sweep frequency. Aside from a constant of proportionality, the output of such a device is given in our notation by A_1A_2. This quantity,

---

[1] Sometimes called the "difference correlation coefficient" for phase (Ratcliffe, 1956, section 8.4).

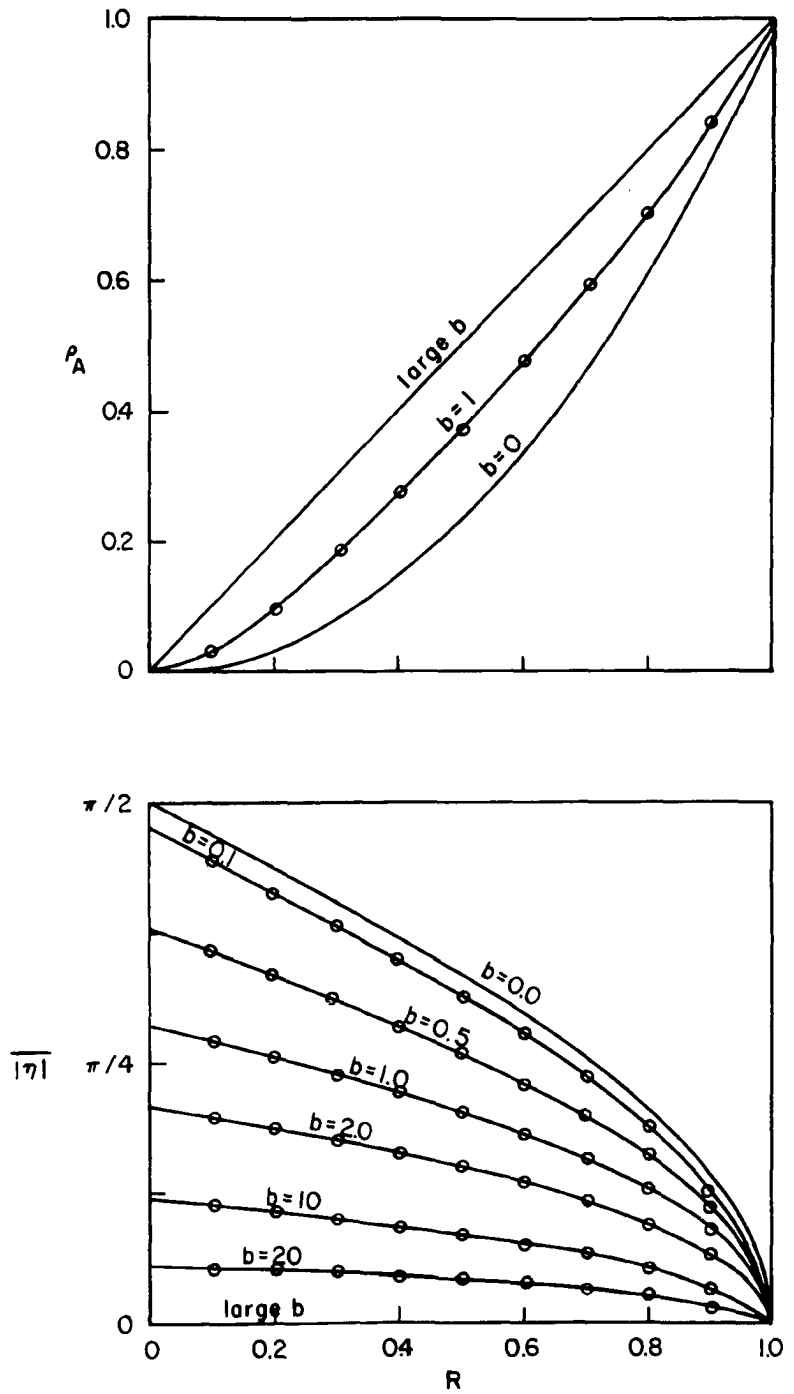

Fig. 4. Top, amplitude correlation coefficient computed numerically for b = 1 and analytically for limiting values of b; bottom, mean absolute phase difference computed numerically for finite values of b and analytically for limiting values of b.

or its square root, is of fundamental importance in scintillation indices as well as in the amplitude correlation coefficient ρ_A. Of interest, then, are the statistical distributions of A_1A_2 and $\sqrt{A_1A_2}$. The distribution of either of these quantities will suffice for our purpose, the other being easily obtained therefrom.

We shall concern ourselves with the distribution of $\sqrt{A_1A_2}$ because it can be compared directly to analytical results in a limiting case. This distribution can be obtained as a function of b and R by our numerical technique. Figure 5 gives the resulting histograms for twelve combinations of b and R. The histograms show that the average value of $\sqrt{A_1A_2}$, and therefore also the average value of A_1A_2, is not very strongly dependent on either b or R. Thus, these average quantities cannot be expected to yield much information about small-scale ionospheric scattering. Some workers have relied on $\overline{A_1A_2}$ in attempts to explain the nature of visibility fades. Others, notably Flood (1963) and Moorcroft (1963), have concentrated on phase characteristics during visibility fades.

While the average value of $\sqrt{A_1A_2}$ is not strongly dependent on b or R, figure 5 shows that the spread in the distribution is strongly controlled by b and to a lesser extent by R. The histograms clearly display the approach of the distribution toward a Dirac delta function as b is increased, which is to be expected from Bramley's analytical work. Less obvious, but nevertheless consistently displayed, is a sharper peaking of the distribution for a given b as R is decreased. This latter fact means that an interferometer record will show somewhat less fluctuation, for a given degree of ionospheric scatter, as amplitude scintillations at the two antennas become less correlated.

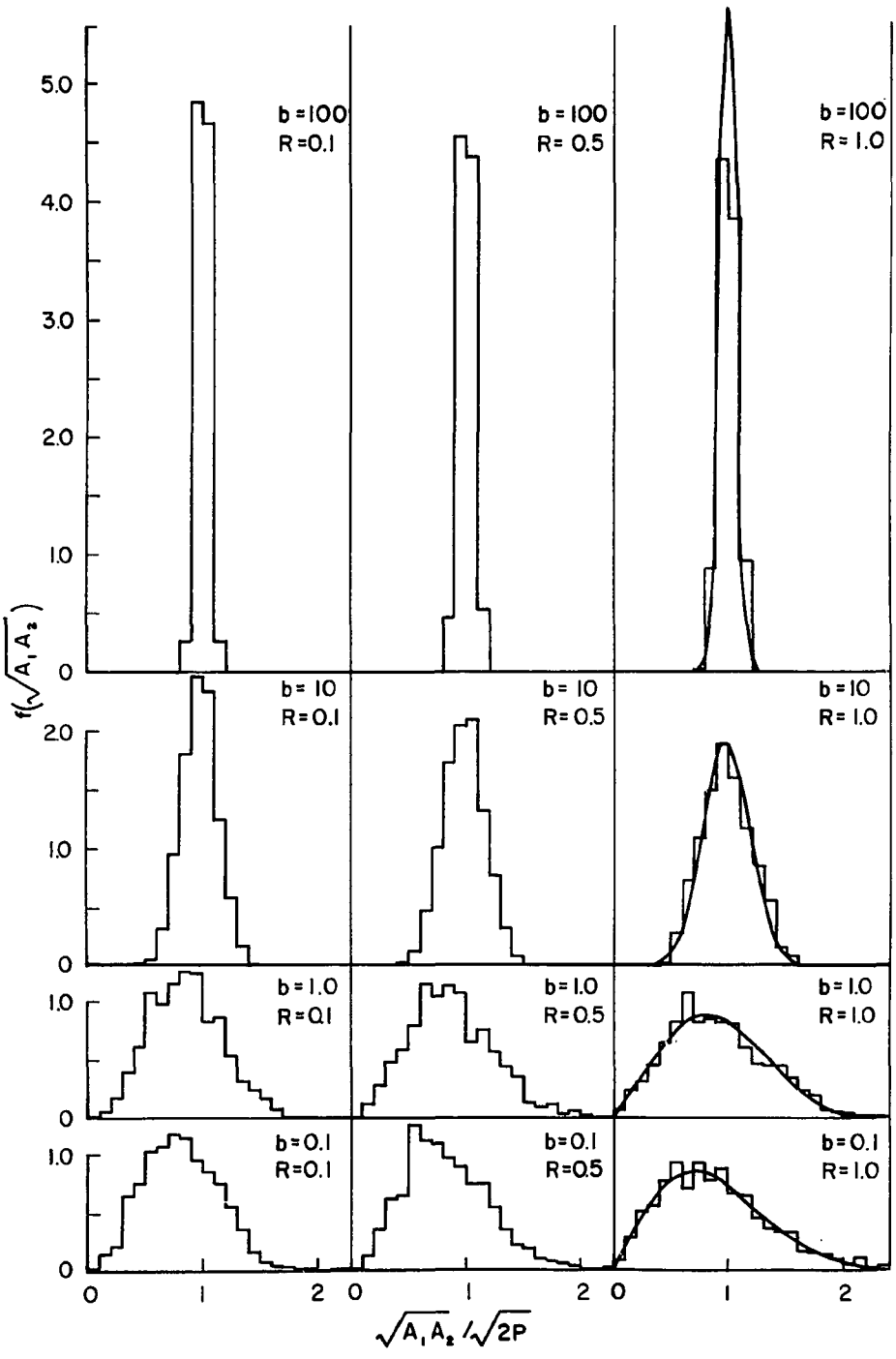

Fig. 5. Effective amplitude distribution for 12 combinations of coherence ratio, b, and wavefront correlation, R. Histograms computed numerically. Smooth curves computed from Rice distribution.

In section D2 it was pointed out that Rice's work on mathematical analysis of a sinusoidal signal buried in noise is directly applicable to observations of ionospheric scatter by single receivers. For the case of unity correlation, interferometric observations become identical with radiometric observations insofar as amplitude characteristics are concerned. Therefore, our distributions for unity correlation should agree with analytical results taken from Rice (1945). Under conditions of unity correlation, the output of a noncoherently detecting phase-sweep interferometer is simply proportional to received power and its square root is proportional to amplitude. The histograms of figure 5 under this condition must be consistent with the Rice distribution for amplitude, given in his equation 3.10-11. In our notation the Rice distribution is

$$f(A_1) = \frac{A_1}{\sigma^2} \exp\left[-\frac{A_1^2 + S^2}{2\sigma^2}\right] I_o\left(\frac{A_1 S}{\sigma^2}\right) \qquad 2\text{-}115$$

or

$$f(A_1) = \frac{(b+1)A_1}{P} \exp\left[-b - \frac{(b+1)A_1^2}{2P}\right] I_o\left(\frac{\sqrt{2b(b+1)}A_1}{\sqrt{P}}\right) \qquad 2\text{-}116$$

In the case $b = 0$, for which $P = \sigma^2$, the Rice distribution reduces to the Rayleigh distribution, given in equation 2-19.

The smooth curves given in the unity correlation column of figure 5 were calculated from equation 2-116. They show the degree of agreement between our numerically derived histograms and analytically derived distributions, where an analytical method is available. The fluctuations evident in the histograms resulted from the finite number (1000) of input data used in their generation. In computing observational quantities,

up to 10,000 input values were used for each of the four random variables B_{1c}, B_{1s}, x, and y. In addition, some graphical smoothing was employed. Thus, the results to be discussed shortly are relatively free of statistical fluctuations. We shall find later that most of our experimental data contain considerably fewer independent input values. In order to estimate errors due to statistical fluctuations, it was considered necessary to reduce such fluctuations to negligible levels in the theoretical computations.

In section D2 we defined the observational quantity r, called visibility. This quantity is obtained from phase-switch (or coherently detecting phase-sweep) observations by taking the ratio of the average output under scatter conditions to that under undisturbed conditions. Under conditions of severe scatter - i.e., during a visibility fade - the quantity r is observed to decrease below its undisturbed value of unity. Equation 2-100 shows that a sufficient condition for zero visibility is $b = R = 0$. The condition $b = 0$, it will be recalled, represents the condition of complete ionospheric scatter.

It was mentioned earlier in the present section that some attempts have been made to interpret visibility fades by their effect on the average output of a noncoherently detecting phase-sweep interferometer. Where this has been attempted, the observed effect has been less than obvious (fig. 14, Little et al, 1962). Figure 6 indicates quantitatively that this is to be expected, as was inferred qualitatively from the distribution of figure 5. The curves of figure 6 give the predicted ratio, $\overline{A_1 A_2}/2P$, of the average output of a noncoherently detecting phase-sweep interferometer during a visibility fade to that under undisturbed

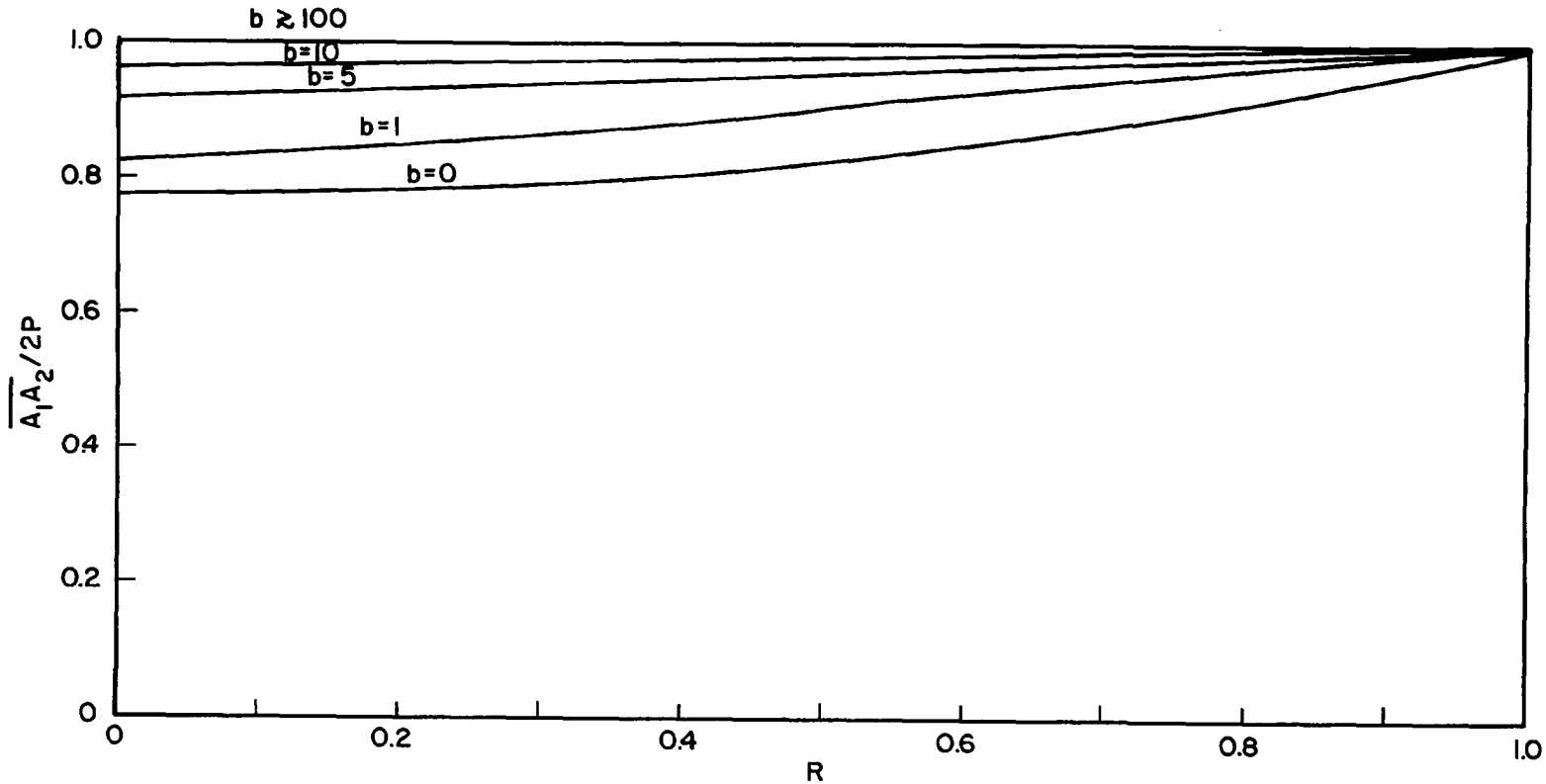

Fig. 6. Relative average output of a noncoherently detecting phase-sweep interferometer as a function of b and R.

ionospheric conditions. The ratio is given as a function of R and b. It is seen that a very severe visibility fade, one which produces the condition b = R = 0, results in only about a 22% decrease in the average output of a noncoherently detecting phase-sweep interferometer.

Whereas figure 6 displays the dependence of the average value of A_1A_2 on b and R, figures 7 and 8 display the dependence of the fluctuation of amplitudes on these two parameters. The ordinate in figure 7 is the fractional mean-square fluctuation of $\sqrt{A_1A_2}$, given by

$$\Delta_A = \frac{(\sqrt{A_1A_2} - \sqrt{\overline{A_1A_2}})^2}{(\sqrt{\overline{A_1A_2}})^2} \qquad 2\text{-}117$$

When R is near unity, the amplitudes are essentially identical, and the above reduces to the fractional mean-square amplitude fluctuation given by

$$\Delta_A = \frac{(A_1-\bar{A}_1)^2}{\bar{A}_1^2} = \frac{\overline{A_1^2} - \bar{A}_1^2}{\bar{A}_1^2} \qquad 2\text{-}118$$

Even at auroral latitudes, most scintillation observations are taken under conditions of near-unity wavefront correlation. The quantity Δ_A, or an amplitude "scintillation index" based on it, is then a direct measure of the coherence ratio b, corresponding to the relationship between Δ_A and b existing at the right-hand edge of figure 7. Under visibility-fade conditions, however, when R is reduced, the relationship between Δ_A and b is altered. Under such conditions, the apparent scintillation index is depressed. For instance, for b = 1.0 and R = 0, figure 7 shows that the interferometrically observed value of Δ_A, defined by equation 2-117, is 43% below the fractional mean-square amplitude fluctuation, defined by equation 2-118, which would be observed under the same conditions by a radiometer.

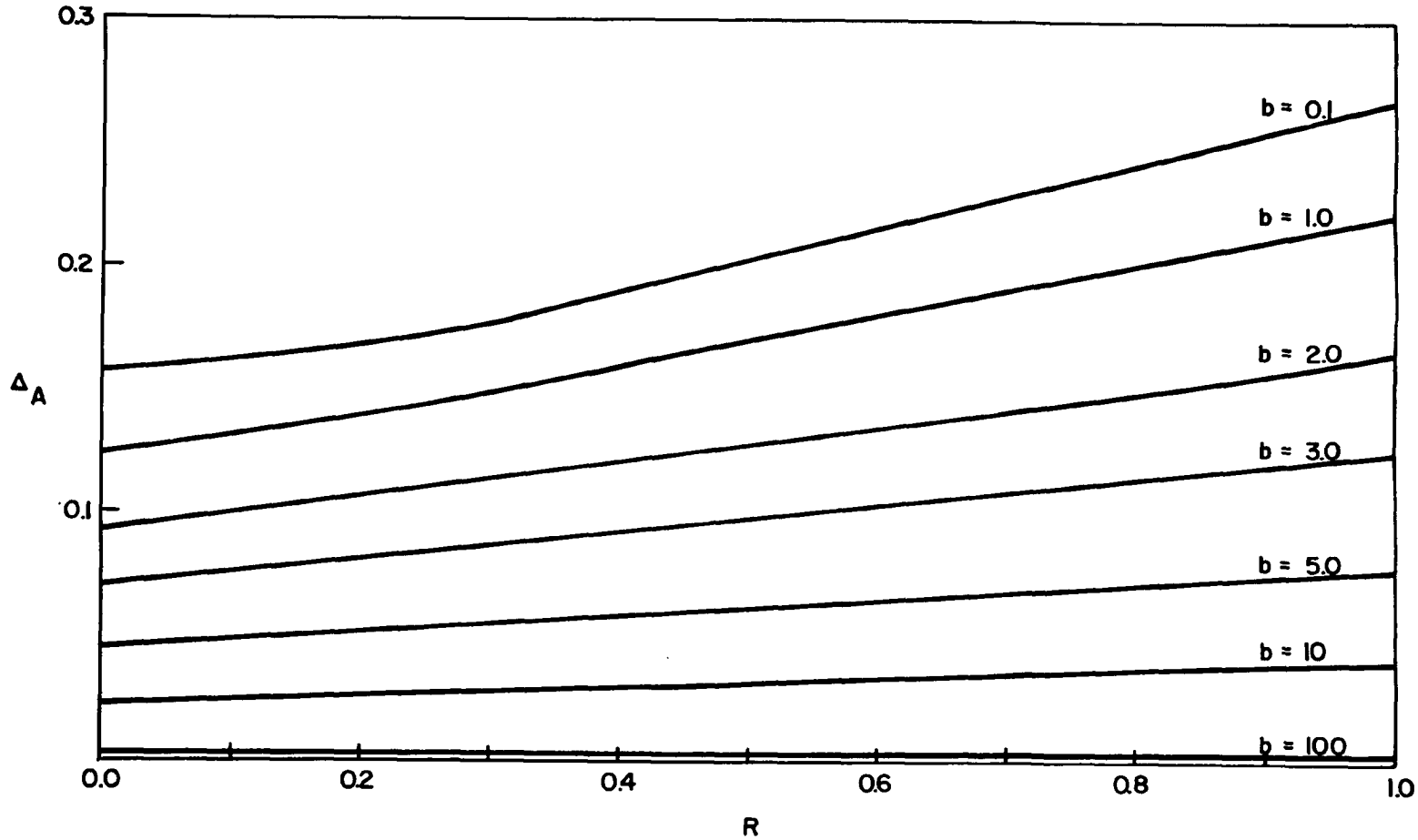

Fig. 7. Effective fractional mean-square amplitude fluctuation as a function of b and R.

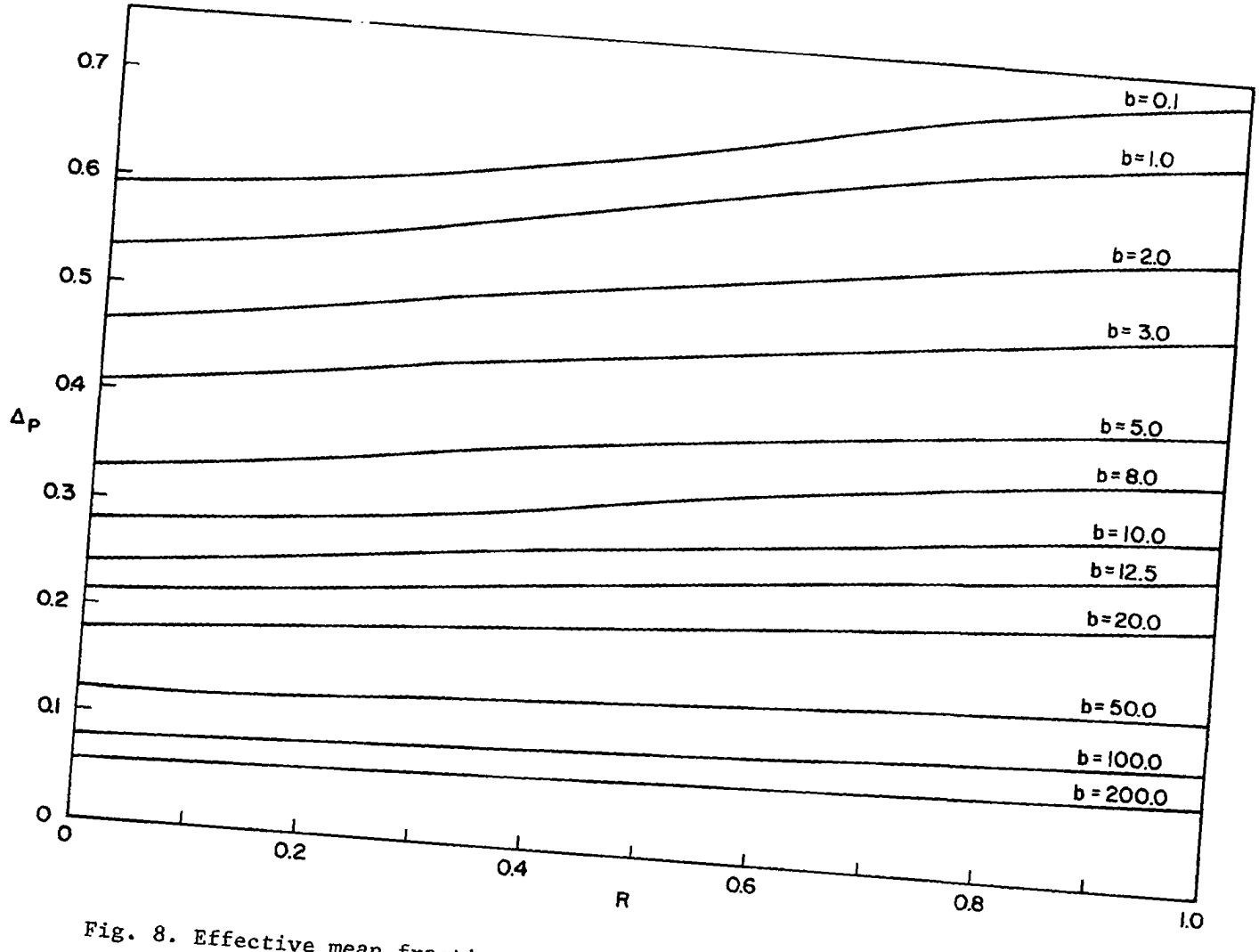

Fig. 8. Effective mean fractional power fluctuation as a function of b and R.

Another measure of amplitude scintillation sometimes used (Little, et al, 1962) is based on the mean fractional fluctuation in power received from the source. Under conditions of near-unity correlation, this latter quantity is given by

$$\Delta_P = \frac{\overline{|A_1^2 - \overline{A_1^2}|}}{\overline{A_1^2}} \qquad 2\text{-}119$$

Under visibility fade conditions, this generalizes to

$$\Delta_P = \frac{\overline{|A_1 A_2 - \overline{A_1 A_2}|}}{\overline{A_1 A_2}} \qquad 2\text{-}120$$

The quantity given in 2-120 is plotted as a function of b and R in figure 8, reducing to that given in 2-119 at the right-hand edge. Again the effect of reduced correlation on the apparent fluctuation is evident. For b = 1.0, zero correlation produces a 21% reduction as compared with the unity-correlation value.

Let us turn now to the characteristics of phase as calculated by our numerical technique. The quantity of observational interest is the phase difference η. The most complete description of η, of course, is given by its distribution function $f(\eta)$. In figure 9, $f(\eta)$ is plotted for twelve representative combinations of b and R. It is obvious that the technique yields the results predicted by the work of Rice (1944, 1945), MacDonald (1949), and Bramley (1951) in the limiting cases. In particular, for low b and R, $f(\eta)$ approaches a uniform distribution at the value $1/2\pi$ and is approximated by a Gaussian function for large b. The technique also yielded a Dirac delta function at zero for unity correlation and any value of b, although this fact is not shown in the figure.

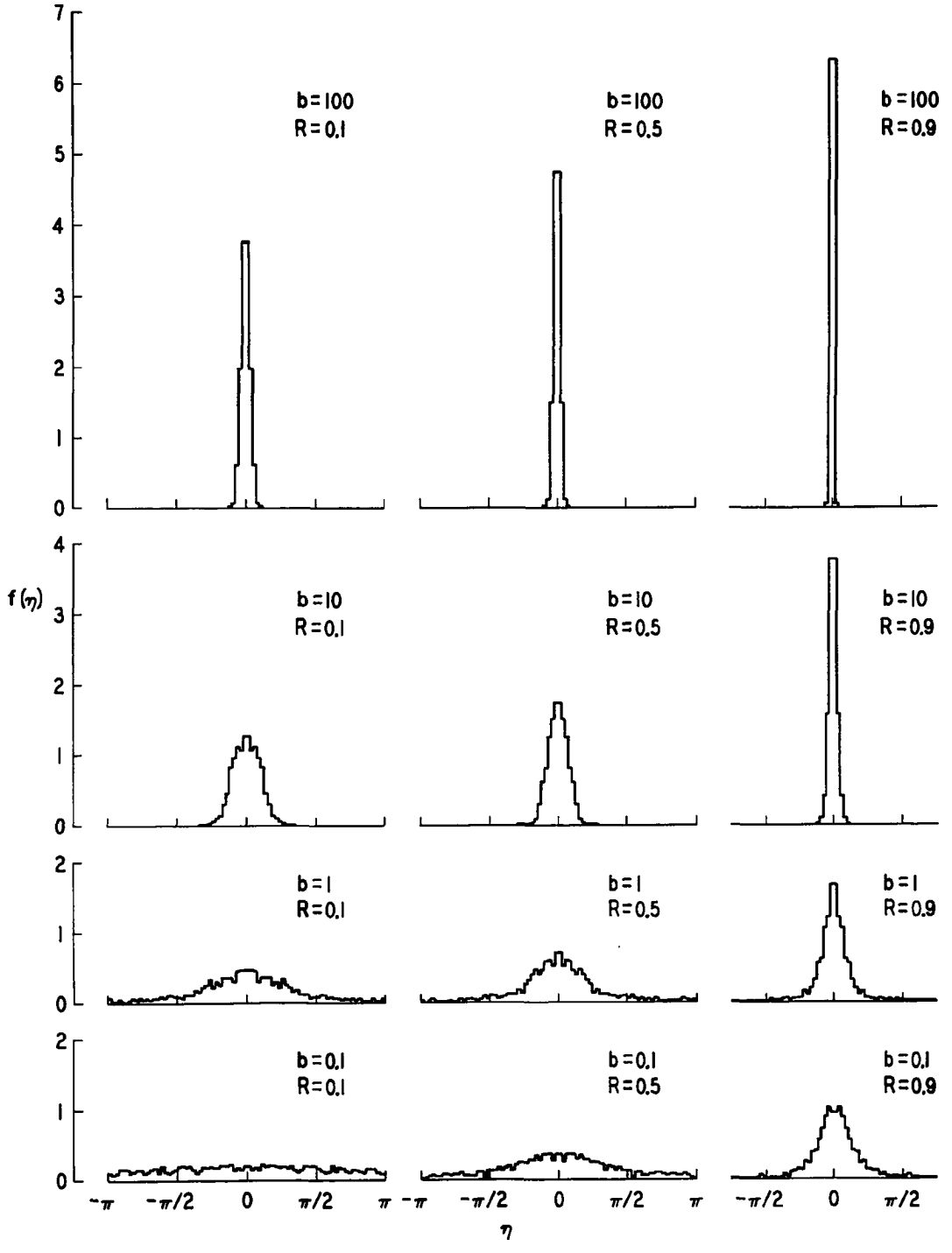

Fig. 9. Phase-difference distribution for 12 combinations of coherence ratio, b, and wavefront correlation, R.

It will be noted that for small b, the distribution departs from a delta function very quickly as the correlation R is decreased.

For actual use in observational analysis, what one desires rather than the full distribution of η is some average quantity derived therefrom. One possible choice is the variance $\overline{\eta^2}$, which is shown plotted as a function of b and R in figure 10. It will be found that the curves of figure 10 approximate $\overline{\eta^2} = \frac{(1-R)}{b}$ for sufficiently large b, in agreement with Bramley's results for the limiting case (Bramley, 1951, section 3). For b smaller than about 5, significant departures from the approximation are found.

IIE SUMMARY

The primary purpose of this chapter has been to provide a description of the observational results to be expected from interferometric observations of randomly scattered waves. The necessary concepts of the angular spectrum and the amplitude and phase of random signals were discussed briefly in section A. In section B, the relationship between the angular spectrum and the frequency spectrum of a signal received by a single antenna was explored and presented analytically for the case of a drifting but otherwise unchanging scattering layer. The discussion was extended to include a second antenna, thus introducing interferometric considerations, in section C.

The signal characteristics to be expected were developed and described in Section D, which was based on the assumption of random phasing in the angular spectrum. The meaning of this assumption as regards the received signal was explored in some detail in section D1a, which dealt with the signal statistics of single-antenna observations. The

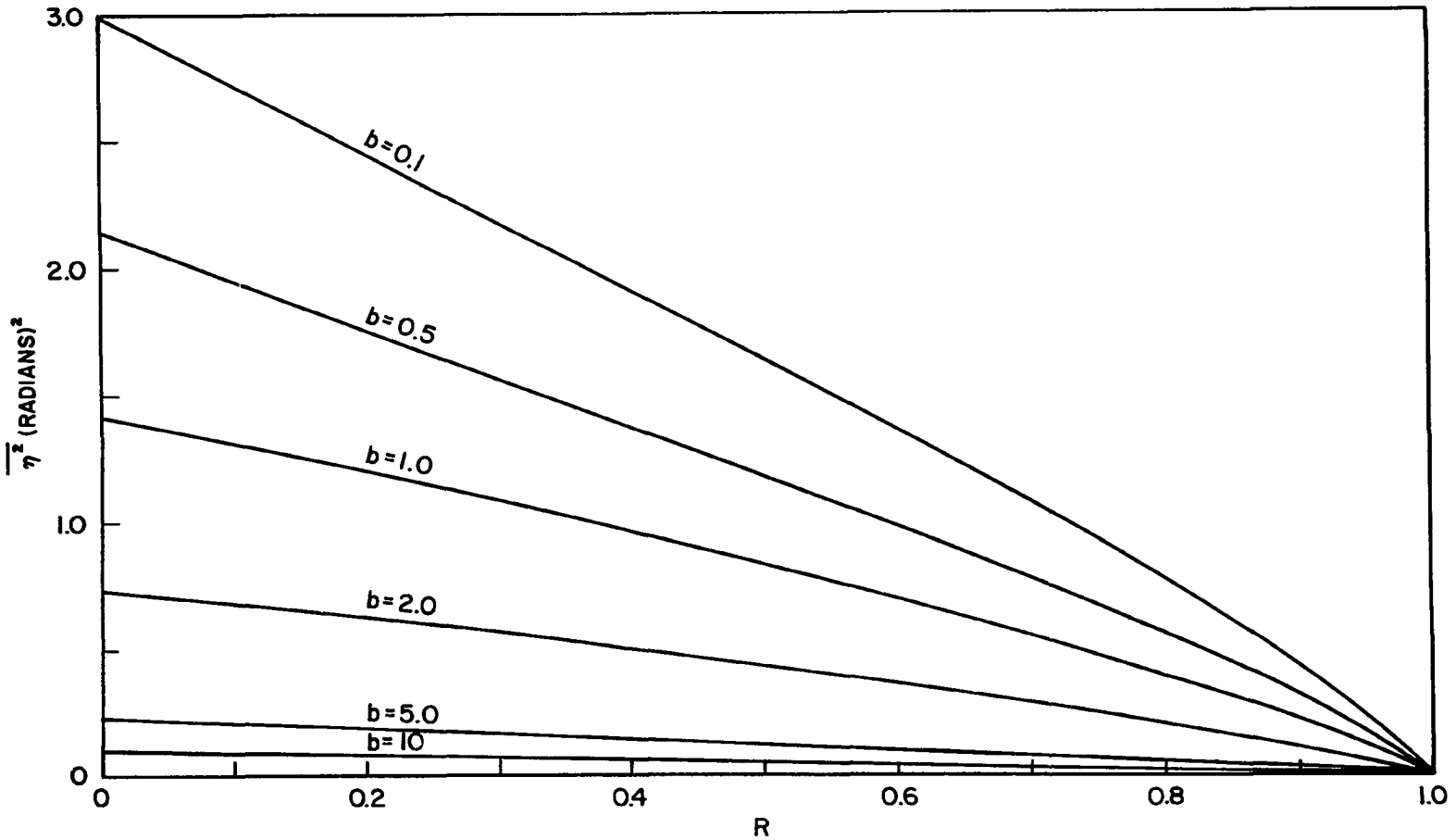

Fig. 10. Variance of the phase difference as a function of b and R.

discussion was extended to interferometric observations in section D1b. Sections D1 and D2 discussed the special cases of completely scattered and weakly scattered waves, respectively. The development followed closely the work of Bramley (1951), who applied the results of Rice (1944, 1945) to the problem of scattered-wave reception. The purpose of sections D1 and D2 was two-fold: to explore and relax slightly the assumption underlying Bramley's work and to lay the analytical framework for section D3.

The purpose of section D3 was to develop and present the signal statistics to be expected from random scattering for the general case of arbitrary degree of scattering. In section D3a, the coherence ratio b - being the ratio of nonscattered to scattered flux - was introduced as a measure of the degree of scattering. In section D3b, the covariance of voltages at two antennas of an interferometer was related to the coherence ratio and the wavefront correlation R, which was defined in section D1b. The observational parameter r, called the visibility, was related to the covariance of voltages and to b and R in section D3b. The resulting relationship, which is important to our experimental problem, was given in equation 2-100 as

$$r = \frac{b + R}{b + 1} \qquad 2\text{-}100$$

The covariance of voltages and the visibility are of importance because they are directly observable by means of a phase-switch or coherently detecting phase-sweep interferometer. When noncoherent detection is employed with a phase-sweep interferometer, pure amplitude information can be obtained. Such an interferometer also offers a means of obtaining

pure phase information. We shall see later that a combination of pure amplitude information with the complex information inherent in equation 2-100 allows measurement of certain ionospheric parameters related to b and R.

The graphical results of section D3e represent relations between b, R, and various statistical characteristics of the amplitude and phase of randomly scattered signals. The most complete description of the statistical characteristics is given in the density distribution histograms of figures 5 and 9. In our experimental problem, we shall use the information contained in the curves of figure 7, which relates to the fluctuation in the output of a noncoherently detecting phase-sweep interferometer as a function of b and R.

CHAPTER III

IONOSPHERIC PRODUCTION OF RANDOMLY SCATTERED WAVES

IIIA REQUISITES OF A RANDOMLY PHASED ANGULAR SPECTRUM

In Chapter II we discussed the statistical characteristics of an ionospherically scattered signal as received by an interferometer at the ground. Our point of view was observational with little consideration given to the manner in which the observed characteristics are produced. In this chapter we shall turn our attention from conditions at the ground to conditions at the ionospheric scattering layer and relate the two. It will be recalled that the fundamental assumption upon which the work of Chapter II was founded was that of random phasing in the angular spectrum. Our first job in the present chapter is to explore the feasibility and consequences of this assumption.

The scattering effect we are considering arises from the differential phase shift imposed on a plane wavefront as it passes through an irregular ionospheric layer. At the base of the layer the effect can be described in terms of the distribution of phase across a plane. For the scattering we are considering - as opposed to refraction in individual ionospheric lenses - we take the distribution to be continuous outside our range of interest. It does not die off in the manner of a wave packet but continues in the manner either of a periodic function or of a random function.

If the phase distribution is periodic, it can be represented as a Fourier series. If it is random, it can be represented as a Fourier integral. In either case, the simplest configuration is the limiting

one of a single Fourier component. More complicated periodic configurations then can be built up by adding harmonic components. Random configurations can be built by expanding the "bandwidth" limits on the Fourier integral. In the latter procedure, the resulting configuration is quasi-periodic for narrow fractional bandwidths in the manner of band-limited white noise. As the fractional bandwidth is increased, less and less ordered configurations result.

Let us begin by considering a simple cosinusoidal configuration of phase at the base of the scattering layer. That is, let the phase as a function of distance along one direction of a plane be

$$\theta(x) = \theta_o + \Delta\theta \cos (2\pi x/D) \qquad 3\text{-}1$$

In the above, θ_o represents the phase which the radio wave would have at the base of the layer if the layer had no irregular structure. $\Delta\theta$ represents the maximum phase deviation across the plane. The spatial period of the phase structure is D. θ_o is of little consequence, and we can reference our phase so that $\theta_o = 0$. In addition, we are not concerned with the amplitude of the radio wave at the base of the scattering layer. It is constant across the plane, and we shall take it as unity. With these simplifications, the "aperture distribution" describing the complex amplitude of the radio wavefront across the base plane is

$$V(x) = \exp [i\Delta\theta \cos (2\pi x/D)] \qquad 3\text{-}2$$

For the moment, let us consider the special case where $\Delta\theta$ is very small. In this case, equation 3-2 reduces approximately to

$$V(x) = 1 + i\Delta\theta \cos (2\pi x/D) \qquad 3\text{-}3$$

Now the angular spectrum associated with V(x), expressed as a function of the sine s of the propagation angle, is given by the Fourier transform of V(x) if distances are measured in units of the radio wavelength λ (Booker and Clemmow, 1950; Ratcliffe, 1956). The Fourier transforms of unity and cos $(2\pi x/D)$ are expressible in terms of the Dirac delta function. The former is a delta function at s = 0, and the latter is a pair of delta functions at $s = \pm 1/D$, or $s = \pm \lambda/D$ in unit measure rather than wavelength measure. Thus the angular spectrum of V(x) is made up of a nondeviated component wave of very nearly unit amplitude and two sidewaves of complex amplitude $i\Delta\theta/2$.

Ratcliffe (1956) has discussed the propagation of the angular spectrum described above. As the three waves propagate downward from the ionosphere, their relative phases change. The change in relative phase produces field distributions across lower planes which are different from that existing at the base of the scattering layer. The distributions may be thought of as Fresnel diffraction patterns. While the diffraction patterns differ at different levels, they are quite predictable owing to the small number of components in the angular spectrum and the simple phase relationship between them at all levels. The angular spectrum is far from being randomly phased. Under these simple conditions it is found that the diffraction patterns repeat themselves at periodic distances from the base of the scattering layer. Near the screen the field distributions are dominated by phase fluctuations, farther from it by amplitude fluctuations, still farther by phase fluctuations, and so forth.

If now the maximum phase deviation $\Delta\theta$ is allowed to be large, a more complicated angular spectrum is produced. The Fourier transform for the resulting waveform is well known in the theory of phase modulation. As pointed out by Ratcliffe (1956), the angular spectrum in this case is made up of discrete components at $s = \pm n\lambda/D$ where $n = 0, 1, 2, 3, - - -$. The amplitudes of the components are distributed as a series of Bessel functions of the first kind, with the amplitude of the n^{th} component being given by $J_n(\Delta\theta)$. The number of components with appreciable amplitude is approximately $\Delta\theta$. The phases of components at the base plane are simply related, with the phase of the n^{th} component being $n\pi/2$.

As the angular components propagate downward from the base of the scattering layer, again their relative phases change. If the normal to the base plane is taken as the z axis of the coordinate system and $\sin^{-1} s = \alpha$, then the propagation geometry shows that the phase of the n^{th} component varies along the z axis as $\frac{2\pi z}{\lambda} \cos \alpha_n$. It can be shown that nowhere beneath the base plane do the phases return to their initial interrelationship. Thus, at no plane is the Fresnel diffraction pattern identical to the aperture distribution.

Hewish (1951) has calculated the amplitude and phase distributions produced at various distances from the scattering layer by phase modulation having various values of maximum phase deviation $\Delta\theta$. He found that phase deviations predominate near the layer, as in the case of very small $\Delta\theta$. At greater distances from the screen, amplitude deviations are built up. At still greater distances the strengths of

amplitude and phase deviations remain roughly constant. The amplitude and phase deviations do not build and wane alternately as the distance is increased, as in the case of very small $\Delta\theta$.

The fact that the diffraction patterns do not show alternate phase and amplitude domination as a function of distance from the scattering layer is a consequence of the fact that the phases in the angular spectrum do not cyclicly repeat their interrelationship. This does not mean however, that, at any individual plane, the angular spectrum is randomly phased. At the base plane, all the phases are multiples of 2π. Obviously random phasing does not exist there. At lower planes, the phase of the n^{th} component is given by

$$\theta_n = \frac{n\pi}{2} + \frac{2\pi z}{\lambda} \cos \alpha_n \qquad 3\text{-}4$$

Due to the continuous variation of z, the second term above gradually distributes the component phases more uniformly in the range θ to 2π. However, this is not enough to produce random phasing. The definition of random phasing requires also that the component phases be independent of one another. Equation 3-4 shows that this is not the case for the angular spectrum under consideration. The n^{th} component phase bears a definite functional relationship to the $(n + 1)^{th}$ component phase, etc.

Suppose now that there is not just one sinusoidal component of phase structure in the wavefront at the base of the scattering layer, but many. Let the maximum radio phase deviation of the m^{th} component be $\Delta\theta_m$ and its spatial phase be ζ_m. Then, instead of equation 3-2, we have the following aperture distribution:

$$V(x) = \prod_{m=1}^{M} \exp \left\{ i\Delta\theta_m \cos \left[(2m\pi x/D) + \zeta_m \right] \right\} \qquad 3\text{-}5$$

where M is the number symbol $\prod$ components in the phase structure of the wavefront and the symbol $\prod_{m=1}$ represents an M-fold product.

The Fourier components of such a distribution can be obtained by carrying out the multiplication on the n components arising from the simpler distribution of equation 3-2, after accounting for the spatial phases ζ_m. This procedure produces the well-known components at $\pm nm\lambda/D$ and at sum and differences thereof. The amplitudes of the Fourier components are M-fold products of Bessel functions. If the ζ_m are taken to be zero, the phases of the Fourier components turn out to be integral multiples of $\pi/2$, as in the simpler case. The phases in the simple case arise as coefficients $(i)^n$ of the Bessel functions $J_n(\Delta\theta)$ in the Fourier series (Ratcliffe, 1956). For all the ζ_m equal to zero, the multiplication required by equation 3-5 simply adds integral exponents to these coefficients.

There is no reason that the ζ_m must be zero, however. Ratcliffe's equation 19, which gives the Fourier series representation of the simple distribution given in our equation 3-2, can be obtained by a method given by Starr (1953, Appendix 7). A generalization of Starr's procedure yields the following expansion for the distribution of equation 3-5:

$$V(x) = \prod_{m=1}^{M} \sum_{n_m=-\infty}^{\infty} e^{in_m \left(\frac{\pi}{2} + \zeta_m\right)} J_{n_m}(\Delta\theta_m) \exp\left(\frac{2\pi i m n_m x}{D}\right) \qquad 3\text{-}6$$

The individual Fourier components, which represent member waves of our angular spectrum with their phase measured at the point x = 0 in the base plane, are identified by a set of integers n_m. Thus

$$s = \sum_{m=1}^{M} m n_m \lambda / D \qquad n_m = 0, \pm 1, \pm 2, \text{ - - -} \qquad 3\text{-}7$$

The phases of the components are given by

$$\phi(s) = \sum_{m=1}^{M} n_m \left(\frac{\pi}{2} + \zeta_m\right) \qquad 3\text{-}8$$

It can be seen from equation 3-8 that any ordered relationship in the spatial phases ζ_m will result in an ordered - although possibly very complicated - relationship in the phases of the angular spectrum components. In this case, the angular spectrum is not randomly phased at the base plane. We have seen in the discussion of equation 3-4, that propagation downward from the ionosphere redistributes the phases in the angular spectrum but does not destroy correlation between them. Thus an angular spectrum corresponding to structure with ordered spatial phases will not be randomly phased at any plane. If, however, the spatial phases are independent, then the angular spectrum will be randomly phased at some distance beneath the base plane and beyond.

In order to achieve random phasing in the angular spectrum, then, we must have a number of spatial components in the radio phase distribution at the base plane, and the spatial phases must be independent of one another. They do not need to be uniformly distributed, however, since the phases of the angular spectrum are

redistributed during subsequent propagation in such a manner as to spread them between zero and 2π. It is to be noted also that the number of components in the angular spectrum is many times as great as the number of spatial components, except in the special case where the $\Delta\theta_m$ are very small. This is another "randomizing influence" on the angular spectrum.

In the above argument, we tacitly assumed that the components of spatial structure are harmonically related. This is of no consequence since we did nothing to restrict the fundamental spatial period. We are free to let it increase without limit so that we are dealing with Fourier integrals instead of Fourier series. In fact, to satisfy the random-phasing requirement that we have a large number of angular components, the basic period D must be large if s is to be restricted to physically meaningful values. Only angular components corresponding to s less than unity are capable of carrying radio energy away from the scattering layer. Greater values of s correspond to evanescent waves (Booker and Clemmow, 1950). A more stringent restriction on s was made in Chapter II, a restriction which is persistently verified observationally. We require s to be sufficiently small that it can be interchanged with its arcsine, α.

Let us summarize the implications of assuming random phasing in the angular spectrum. First, the requirement of a large number of independent angular components precludes strict periodicity or other steady-state structure within our region of interest. That is, there must be a degree of randomness in the wavefront phase at the base of

the scattering layer. In addition, the requirement of a uniform distribution of phase in the angular spectrum sets a minimum propagation distance between the base plane and our plane of observation for any given base-plane phase structure. These are the implications of the basic assumption of Chapter II. They are plausible but do not in themselves justify the assumption. The justification is observational, and we shall return to it in a later chapter.

It is to be noted that we have not specified the amplitudes of the angular spectrum components or the strengths $\Delta\theta_m$ of the spatial components of phase structure. The assumption of random phasing therefore is not seriously restricting from a physical point of view. It is true that we cannot deal with mathematically pure periodicity in ionospheric structure: a square-wave ionosphere or a sawtooth ionosphere, for instance. We can deal with quasi-periodic structure, however, in addition to completely random structure.

For a given degree of randomness in the structure, the condition of random phasing in the angular spectrum is more closely approximated the stronger the scatter, that is the larger the $\Delta\theta_m$. The distribution of $\Delta\theta$ within the spatial-frequency spectrum and the distribution of radio flux within the angular spectrum, however, are not specified. Thus the power spectrum of spatial structure in the wavefront at the base plane and the angular power spectrum still are quite arbitrary.

IIIB STATISTICAL DESCRIPTION OF THE POST-SCATTERING WAVEFRONT AND THE MEANING OF VISIBILITY

Any assumption we might have made about either the amplitude or the phase of the angular spectrum would have reduced the amount of ionospheric information we can hope to glean. It would take an uncompromised measurement of both to permit a full description of the ionospheric structure which produced the spectrum. Having made the assumption of random phasing, therefore, we cannot hope to reconstruct fully the phase structure at the base of the scattering layer. A full reconstruction would be practically impossible anyway because the phases of the angular spectrum change during subsequent propagation. The amplitudes of the spectral components do not change, however.

The angular power spectrum contains all of the amplitude and none of the phase information of the (complex) angular spectrum. Since only the phases change, it follows that the angular power spectrum remains constant during propagation from the base of the ionosphere. Booker, Ratcliffe and Shinn (1950) defined a generalized autocorrelation function for complex amplitude as follows:

$$\rho(\xi) = \frac{\overline{V^*(x)\ V(x+\xi)}}{\overline{V^*(x)\ V(x)}} \qquad 3\text{-}9$$

They showed that if V(x) denotes complex amplitude across the wavefront, $\rho(\xi)$ is proportional to the Fourier transform of the associated angular power spectrum and is therefore invariant during post-scattering propagation. In the case of ionospheric scattering, then, the autocorrelation function given by 3-9 is the same at the ground as at the

base of the scattering layer.

Now if $V(x) = A(x)\, e^{j\theta(x)}$ represents the complex amplitude of the wavefront across the ground (i.e., of the Fresnel diffraction pattern on the ground), then, aside from a constant of proportionality, the voltage at the output of an antenna located at x is

$$v_1 = \left\{ \text{Re} \quad V(x)\, e^{j\omega t} \right\} = A(x) \cos [\omega t + \theta(x)] \qquad 3\text{-}10$$

Similarly, the voltage at the output of an antenna located at $x+\xi$ is

$$v_2 = \left\{ \text{Re} \quad V(x+\xi)\, e^{j\omega t} \right\} = A(x+\xi) \cos [\omega t + \theta(x+\xi)] \qquad 3\text{-}11$$

Under conditions of ergodicity, we need not separate averages over t and over x, and we have

$$\begin{aligned} \overline{v_1 v_2} &= \overline{A(x)A(x+\xi) \cos [\omega t + \theta(x)] \cos [\omega t + \theta(x+\xi)]} \\ &= \tfrac{1}{2} \overline{A(x)A(x+\xi) \left\{ \cos [\theta(x+\xi)-\theta(x)] + \cos [2\omega t+\theta(x+\xi)+\theta(x)] \right\}} \\ &= \tfrac{1}{2} \overline{A(x)A(x+\xi) \cos [\theta(x+\xi)-\theta(x)]} \\ &= \tfrac{1}{2} \overline{\text{Re}\, [V^*(x)V(x+\xi)]} \end{aligned} \qquad 3\text{-}12$$

But $\overline{v_1 v_2}$ is just the temporal covariance of the antenna voltages, which is obtained directly from the output of a phase-switch interferometer, and $\overline{\text{Re}[V^*(x)V(x+\xi)]}$ is the spatial autovariance of complex amplitude. It was shown in section D2 of Chapter II that the temporal covariance of voltages is equal to $[\tfrac{1}{2}S^2 + R\sigma^2] \cos 2\chi_o$, where $\tfrac{1}{2}S^2$ is the power in the nondeviated component of the angular spectrum and σ^2 is the power in the scatter spectrum. It is easily shown also, by

letting ξ go to zero in the derivation of equation 3-12 and then using Parseval's equality, that $\frac{1}{2}\,\overline{\mathrm{Re}V^*(x)V(x)} = P$ where P is the total power in the angular spectrum, $\frac{1}{2}S^2 + \sigma^2$. Thus, we have

$$\frac{\overline{V^*(x)V(x+\xi)}}{\overline{V^*(x)V(x)}} = \frac{S^2 + 2R\sigma^2}{S^2 + 2\sigma^2} \cos 2\chi_o = \frac{\overline{v_1 v_2}}{P} \qquad 3\text{-}13$$

where the notation Re is to be understood in accordance with the usual convention.

The right side of equation 3-13 is simply the (temporal) cross-correlation coefficient for the antenna voltages, which we denoted by ρ in Chapter II. Equation 3-13 shows that ρ, expressed as a function of antenna spacing ξ, is identical to the generalized spatial autocorrelation function defined by Booker, Ratcliffe, and Shinn. According to the conclusions of Booker, Ratcliffe, and Shinn, $\rho(\xi)$ measured on the ground-level diffraction pattern is identical to the autocorrelation function of the aperture distribution at the base of the ionospheric scattering layer.

As it stands, $\rho(\xi)$ contains the factor $\cos 2\chi_o$ which arises solely from the angular position of the source under observation. The position factor contains no ionospheric information regarding small-scale scatter. Let us, therefore, concern ourselves with the interferometer fringe visibility r, defined in section D3b of Chapter II, instead of with ρ. Comparison of equations 2-98 and 2-100 of that section shows that

$r(\xi) = \rho(\xi)/\cos 2\chi_o$. Thus we have, from equation 3-13,

$$r(\xi) = \frac{S^2 + 2R\sigma^2}{S^2+2\sigma^2} \qquad 3\text{-}14$$

Upon recalling the definition of the coherence ratio b, equation 3-14 reduces to equation 2-100, Thus

$$r(\xi) = \frac{b + R}{b + 1} \qquad 3\text{-}14'$$

Now $r(\xi)$ is the same at the ground as at the base of the scattering layer. Since the angular power spectrum is invariant during post-scattering propagation, the coherence ratio also remains constant. Therefore R must be identical at all planes too. Now S and σ, and therefore b, are not functions of antenna position and therefore are independent of ξ. R, on the other hand, is a measure of the correlation existing between the scatter-component resultants at the two antennas. The ξ-dependence of $r(\xi)$, therefore, arises through R, which we may write $R(\xi)$.

Let us return to consideration of equation 3-6, whose terms are components of the angular spectrum for a general aperture distribution $V(x)$[1]. The 0^{th} component, for which all the $n_m = 0$, is the non-deviated component of the angular spectrum. If all the $\Delta\theta_m$ are zero, corresponding to no phase fluctuations at the base plane, all power is contained in the nondeviated component, since all the Bessel functions except that of zero order have zero magnitude for zero argument. The higher-order waves, then, represent the scatter spectrum. They are responsible for the phase fluctuations at the base plane and for the

[1]Note that V(x) is not, in general, identical at the ground and at the base plane.

fluctuations in amplitude and phase at lower planes.

The wavefront consists of a plane wave identical to the non-deviated component, upon which are superposed spatial fluctuations due to the scattered part of the signal. $R(\xi)$ represents the spatial auto-correlation function of the fluctuating part of the wavefront. It was for this reason that we referred to R in Chapter II as the wavefront autocorrelation. The visibility $r(\xi)$ is essentially the spatial auto-correlation function of the composite wave-field.

IIIC PHYSICAL MEANING OF THE PARAMETERS b AND R

C1 The Coherence Ratio b

The above discussion shows that the interference fringe visibility depends upon the strength of the phase fluctuations at the base of the ionospheric scattering layer - through b - and on the wavefront auto-correlation function $R(\xi)$. We should like to relate b and R to iono-spheric parameters. First let us relate b more explicity to the strength of the phase fluctuations. In order to simplify matters, we shall assume normal incidence of the nondeviated component relative to the ionosphere and to our antenna baseline at the ground. That is, we shall assume $\alpha_o = \chi_o = 0$, which will allow us to interchange $\rho(\xi)$ and $r(\xi) \cos 2\chi_o = r(\xi) \cos (\frac{2\pi d}{\lambda} \sin \alpha_o)$ and note that

$$\xi = d \cos \alpha_o \qquad 3\text{-}15$$

Equation 3-15 takes account of the fact that for off-normal incidence, the observing interferometer has a foreshortened baseline. That is ξ

is a measure of distance along the wavefront, which is equal to distance along the ground only for normal incidence.

The assumption of normal incidence here is not physically restricting, being only a convenient simplification of geometry which can be retracted at will by employing the mathematical relation between $\rho(\xi)$ and $r(\xi)$, together with equation 3-15. We shall now make a more basic assumption, akin to and consistent with that of random phasing in the angular spectrum. The assumption of random phasing requires that the phase of the wavefront at the base of the scattering layer be treated as a random variable. We shall need a distribution function with which to describe the wavefront phase. Following Bramley (1955), let us choose the normal distribution, which is reasonable on physical grounds.

The normal distribution in this instance is not demanded, a priori, by the central limit theorem since we know very little about the manner in which the wavefront phase fluctuations are built up. On the other hand, it does not seem unlikely that the fluctuations are built up by a large number of scatterings by independent ion-density irregularities. In this case, a normal distribution for the wavefront phase may be expected, whatever the origin and detailed distribution of the irregularities themselves.

It is to be noted that, while we are assuming a normal distribution for the wavefront phase at the base plane, we are making no restricting assumptions about the moments which describe either the first or the second-order distribution. In particular, we are putting no restrictions on the variance of the phase nor on its spatial autocorrelation function.

We shall, for convenience and without loss of generality, assume that the average, θ_o, of the phase is zero.

Bramley (1955) has developed, under the assumptions mentioned above, the relationship between $r(\xi)$ and the variance and autocorrelation function of the phase distribution. The result is given in his equation 28, which in our notation is

$$r(\xi) = \exp\left[-\overline{\theta^2}\,(1-\rho_\theta)\right] \qquad 3\text{-}16$$

where $\overline{\theta^2}$ is the variance of the phase and ρ_θ is its autocorrelation function.

Now, according to the results of Booker, Ratcliffe and Shinn (1950), the Fourier transform of $r(\xi)$ is the normalized angular power spectrum, expressed as a function of $s = \sin\alpha$. For small angles we can replace s with α, and we have

$$p(\alpha) = \frac{P}{\lambda}\int_{-\infty}^{\infty} \exp\left[-\overline{\theta^2}\,(1-\rho_\theta)\right] \exp\left(-j2\pi\alpha\xi/\lambda\right) d\xi \qquad 3\text{-}17$$

where $p(\alpha)$ represents the flux per unit angle in the spectrum, P is the total flux, and the wavelength λ appears explicitly because we choose to use unit measure rather than wavelength measure. Equation 3-17 can be written also as

$$p(\alpha) = \frac{P}{\lambda} e^{-\overline{\theta^2}} \int_{-\infty}^{\infty} e^{\overline{\theta^2}\rho_\theta(\xi)} \exp\left(-j2\pi\alpha\xi/\lambda\right) d\xi \qquad 3\text{-}18$$

Upon expansion of the real exponential in the integrand into its

series representation, the above becomes

$$p(\alpha) = \frac{P}{\lambda} e^{-\overline{\theta^2}} \int_{-\infty}^{\infty} \exp(-j2\pi\alpha\xi/\lambda)\, d\xi + \frac{P}{\lambda} e^{-\overline{\theta^2}} \int_{-\infty}^{\infty} \sum_{n=1}^{\infty} \frac{[\overline{\theta^2}\rho_\theta(\xi)]^n}{n!} \exp(-j2\pi\alpha\xi/\lambda) d\xi \qquad 3\text{-}19a$$

The first integral results in a delta function at $\alpha=0$. Further, for any physically reasonable autocorrelation function, $\rho_\theta(\xi)$, the infinite series in the second term is uniformly convergent and therefore may be integrated term by term. Thus equation 3-19 becomes

$$p(\alpha) = P\, e^{-\overline{\theta^2}}\, \delta(\alpha-0) + \frac{P}{\lambda} e^{-\overline{\theta^2}} \sum_{n=1}^{\infty} \frac{\overline{\theta^2}^n}{n!} \int_{-\infty}^{\infty} [\rho_\theta(\xi)]^n \exp(-j2\pi\alpha\xi/\lambda)\, d\xi \qquad 3\text{-}19b$$

Now the integral of $p(\alpha)$ over the whole angular spectrum must equal P. From the definition of the Dirac delta function, it is easily seen that the integral of the first term above is $P\, e^{-\overline{\theta^2}}$. The integral of the second term, then, must be $P(1-e^{-\overline{\theta^2}})$. Thus, the first term represents a wave travelling in the original propagation direction and carrying all of the flux in the event of no phase fluctuations ($\overline{\theta^2} = 0$). It is the nondeviated component of the angular spectrum. The second term carries whatever flux is not contained in the nondeviated component, for any degree of phase fluctuation across the base plane (i.e., for arbitrary $\overline{\theta^2}$). It is the scatter spectrum. The ratio of flux in the two terms, which is the coherence ratio, is given by

$$b = e^{-\overline{\theta^2}} / (1 - e^{-\overline{\theta^2}}) \qquad 3\text{-}20$$

The above expression relating the coherence ratio to the variance of phase at the base of the scattering layer was derived by Bramley (1955) for the special case of a Gaussian autocorrelation function. We have shown here that no such restriction is required

C2 The Wavefront Autocorrelation Function R(ξ)

Equation 3-20 relates b to conditions at the base of the scattering layer. Let us turn now to the relationship between R(ξ) and conditions at the base plane. It is easily seen from equation 3-20 that

$$b + R = \frac{e^{-\overline{\theta^2}} + R(1 - e^{-\overline{\theta^2}})}{1 - e^{-\overline{\theta^2}}} \qquad 3\text{-}21$$

and

$$b + 1 = 1/(1 - e^{-\overline{\theta^2}}) \qquad 3\text{-}22$$

Combination with equation 3-14 produces

$$r = e^{-\overline{\theta^2}} + R(1 - e^{-\overline{\theta^2}}) \qquad 3\text{-}23$$

Equating 3-16 with 3-23 results in

$$e^{-\overline{\theta^2}}\, e^{-\overline{\theta^2}\rho_\theta} = e^{-\overline{\theta^2}} + R(1 - e^{-\overline{\theta^2}}) \qquad 3\text{-}24$$

which produces, in view of 3-20

$$\overline{\theta^2}\,\rho_\theta = \ln\left(1 + \frac{R}{b}\right) \qquad 3\text{-}25$$

It is easily shown from equation 3-20 that

$$\overline{\theta^2} = \ln\left(1 + \frac{1}{b}\right) \qquad 3\text{-}26$$

Hence the autocorrelation function $\rho_\theta(\xi)$ of the base-plane phase distribution is given in terms of the wavefront autocorrelation function $R(\xi)$ by

$$\rho_\theta(\xi) = \frac{\ln\left[1 + \frac{R(\xi)}{b}\right]}{\ln\left[1 + \frac{1}{b}\right]} \qquad 3\text{-}27$$

Equation 3-27 can be expressed as

$$\rho_\theta = \sum_{n=1}^{\infty} n^{-1} \left[\frac{R/b}{1 + (R/b)}\right]^n \Big/ \sum_{n=1}^{\infty} n^{-1} \left[\frac{1/b}{1 + (1/b)}\right]^n \qquad 3\text{-}28$$

For large coherence ratio, b, the series can be approximated by their initial terms with the result that

$$\rho_\theta \approx \frac{1 + (1/b)}{1 + (R/b)} R \approx R \qquad 3\text{-}29$$

Thus, for weak scattering, the wavefront autocorrelation function is nearly identical to the autocorrelation function of the phase distribution across the base plane. This result was obtained by Bramley (1955) for the special case of a Gaussian autocorrelation function. Again, the result holds for arbitrary autocorrelation function.

The general expression, equation 3-27, shows that for moderate and strong scattering (ie, for moderate and small coherence ratio), the phase-distribution autocorrelation function ρ_θ can be obtained only from a knowledge of both b and R. In Chapter IV, we shall describe an experiment for determining b and R, based on the development of Chapter II. Now we must turn to the problem of relating b and R, through their dependence on $\overline{\theta^2}$ and ρ_θ, to parameters of ionospheric structure.

Again we shall base our procedure on the work of Bramley(1955), generalizing where possible.

IIID SCATTERING OF VHF WAVES BY ION-DENSITY IRREGULARITIES

D1 The Variance of Phase at the Base of the Scattering Layer

The operating frequencies in our experiment are well above the gyro, collision, and plasma frequencies of the auroral E and F layers. Under these conditions, the refractive index μ encountered by our observing wave of frequency $\omega/2\pi$ in passing through a region which may contain scattering irregularities can be obtained from

$$\mu^2 = 1 - (Ne^2/m\varepsilon_o\omega^2) \qquad 3\text{-}30$$

where N = the electron density in the region, e = the electronic charge, m = the electronic mass, and ε_o = the permitivity of free space. In passing through an elemental thickness dz of such a region, the wave undergoes a phase shift of $(2\pi/\lambda)\mu dz$, where λ is its free-space wavelength.

Let us suppose now that the region does in fact contain electron-density irregularities and that the electron density in the dz element under consideration is $\bar{N} + \Delta N$, where $\bar{N}$ is the average value of N in the region. The departure of the refractive index in the element from the average value in the region will be given by

$$\Delta\mu = \int_o^{\Delta N} (d\mu/dN)\, dN \qquad 3\text{-}31$$

From equation 3-30, $d\mu/dN$ is seen to be

$$\frac{d\mu}{dN} = \frac{-e^2}{2\mu m \epsilon_o \omega^2} \qquad 3\text{-}32$$

If the deviation of N in the element is sufficiently small, μ may be taken as a constant when equations 3-31 and 3-32 are combined. If this is done, then $d\mu/dN$ can be placed outside the integral in 3-31, and obviously$(\Delta\mu/\Delta N) = (d\mu/dN)$.

Then we have, from 3-32

$$\Delta\mu = \frac{-e^2 \Delta N}{2\mu m \epsilon_o \omega^2} \qquad 3\text{-}34$$

The approximation involved in obtaining equation 3-34 has been tested for the observing conditions of our experiment. At the lowest frequency used in the majority of the observations (68 MHz), the approximation results in less than a 2% error in $\Delta\mu$ even for a 50% modulation in electron density in the most dense region of the ionosphere. Thus, even under disturbed conditions in the auroral zone, the approximation is considered acceptable. Furthermore, at the observing frequencies used, the ionospheric refractive index may be expected to depart from unity by at most a few percent. Accordingly,μ in equation 3-34 will be taken as unity.

As a result of the above considerations, it is easily seen that the magnitude of the excess phase shift $(2\pi/\lambda)\Delta\mu dz$ suffered by the wave because of the deviation in electron density in the dz element is

$$d\theta = \frac{\pi e^2 \Delta N}{m \epsilon_o \omega^2 \lambda} \, dz \qquad 3\text{-}35$$

For purposes of quantitative calculation, it is convenient to express the constants in equation 3-35 in terms of the plasma frequency and average electron density of the irregular region. If we denote the plasma frequency by $f_o = \omega_o/2\pi$, then $\frac{d\theta}{dz}$ becomes

$$\frac{d\theta}{dz} = \frac{\pi}{\lambda} \frac{\omega_o^2}{\omega^2} \frac{\Delta N}{N} \qquad 3\text{-}36$$

Now ΔN represents the deviation from the mean of the electron density in an element of depth dz in the irregular region. All the other quantities in 3-36 are constants or relatively very slowly varying functions of z. Therefore, whatever the statistical distribution of electron density in the region, the variance $\overline{(d\theta/dz)^2}$ of $d\theta/dz$ is obtained from the variance $\overline{(\Delta N)^2}$ of the electron density as follows:

$$\overline{\left(\frac{d\theta}{dz}\right)^2} = \frac{\pi^2}{\lambda^2} \left(\frac{\omega_o^2}{\omega^2}\right)^2 \frac{\overline{(\Delta N)^2}}{\overline{N}^2} \qquad 3\text{-}37$$

The last factor in 3-37, of course, is the mean-square fractional fluctuation in electron density in the irregular region. Note that we have not assumed a distribution function for the electron density. It can be Gaussian as might be expected if the irregularities are produced by a large number of independent ionizing particles. On the other hand, it can be quite different as might result from some more ordered process.

As the wave propagates through the irregular region, the excess elemental phase shift $\frac{d\theta}{dz}(z)$ along the z axis (or along any other representative path of constant x and y) varies in proportion to $\Delta N(z)$.

The function $\frac{d\theta}{dz}(z)$ is a particular sample function of the random process represented by the ensemble of similar functions along all possible paths of constant x and y. If the total thickness of the irregular layer is t, then the phase at the intersection of the z axis and the bottom of the irregular layer is

$$\theta = \int_0^t \frac{d\theta}{dz}(z)\, dz \qquad 3\text{-}38$$

Hence θ/t is just the finite-interval spatial average of $d\theta/dz$.

In sampling theory, θ/t would be called the sample mean of $d\theta/dz$. The integral in 3-38 taken along some other path of constant x and y would, in general, be different from that taken along the z axis. If we now inspect the sample mean along the x axis, we obtain $\theta(x)/t$, where $\theta(x)$ is the spatially fluctuating wavefront phase. We can now obtain the variance of the wavefront phase from the well-known expression for the variance of the sample mean (Davenport and Root, section 5-3 and section 4-8). Thus

$$\overline{\theta^2} = 2t \left(\overline{\frac{d\theta}{dz}}\right)^2 \int_0^t \left(1 - \frac{\tau}{t}\right) \rho_z(\tau) d\tau \qquad 3\text{-}39$$

where ρ_z is the spatial autocorrelation function[1] of $d\theta/dz$ and therefore of the electron-density variation[2] in the z direction.

---

[1] In the present context, the term "autocorrelation function" refers to what is sometimes (inaccurately) called the "normalized autocorrelation function." The quantity termed "autocorrelation function" by Davenport and Root is equal to the product of our autocorrelation function and the variance and may aptly be called the autovariance function. Accordingly the variance of $d\theta/dz$ appears explicitly in our equation 3-39, whereas the corresponding quantity is contained implicitly in Davenport and Root's equations 4-83 and 5-13. There are several terms used interchangably by various authors to define what we are calling autocorrelation and to define closely related but not identical quantities. Care must be exercised to avoid confusion even in the case of ergodic processes, which we are considering. For nonergodic processes, still more inconsistencies in nomenclature arise.

[2] See page 123 for the mathematical definition of $\rho_z(\tau)$.

In accord with our assumption that the ionosphere's irregular structure is not strictly periodic, $\rho_z(\tau)$ must approach zero for very large values of τ. For a thick layer in which t is very large compared with the largest value of τ for which $\rho_z(\tau)$ makes a significant contribution to the integral, equation 3-39 can be replaced by

$$\overline{\theta^2} = 2t \overline{\left(\frac{d\theta}{dz}\right)^2} \int_0^t \rho_z(\tau)\, d\tau \qquad 3\text{-}40$$

D2 Phase Variance for a Scattering Layer with a Gaussian Structural Autocorrelation Function

The approximation involved in obtaining equation 3-40 has a somewhat different meaning depending upon whether the ion-density structure is strictly random or quasi-periodic in the z direction. In the former case, the layer simply must be several irregularities thick. In the latter case, the layer thickness must be great compared with the spatial wavelength of the basic periodicity and compared with the (larger) distance over which the periodicity is maintained with essentially constant phase. In both cases, the layer must be thick compared with what we might call "the correlation depth" of the scattering layer. In the random case, the correlation depth gives directly a measure of the average size of an irregularity. In the quasi-periodic case, the correlation depth may be many times greater than the size of a single irregularity, how much greater depending upon how well defined the periodicity is.

Bramley (1955) treated the random-layer problem in the special case where the autocorrelation function of the ion-density irregularities in the z direction is given by the ("denormalized") Gaussian function.

That is, he treated the case where

$$\rho_z = \exp(-\tau^2/\tau_o^2) \qquad 3\text{-}41$$

The assumption of the so-called Gaussian autocorrelation function yields for the integral of equation 3-40

$$I = \frac{\sqrt{\pi}\,\tau_o}{2}\,\mathrm{erf}(t/\tau_o) \qquad 3\text{-}42$$

where $\mathrm{erf}(t/\tau_o)$ stands for the error function, which has value zero for zero argument and tends to unity as t increases. Thus, for t much larger than τ_o, the variance of phase fluctuations at the base of the scattering layer is given by

$$\theta^2 = \sqrt{\pi}\,\tau_o\, t\,\overline{\left(\frac{d\theta}{dz}\right)^2} \qquad 3\text{-}43 \text{ (Gaussian)}$$

In the above, τ_o represents the distance at which the autocorrelation function falls to e^{-1}, thus being a measure of the size of the irregularities.

D3 Phase Variance for other Autocorrelation Functions

Another autocorrelation function sometimes assumed in scattering problems is the exponential function, $\exp(-\tau/\tau_o)$. For the exponential case, I is given by $\tau_o(1 - e^{-t/\tau_o})$, and the phase variance for large t is

$$\overline{\theta^2} = 2\tau_o\, t\,\overline{\left(\frac{d\theta}{dz}\right)^2} \qquad 3\text{-}43 \text{ (Exponential)}$$

Let us investigate the phase variance for some other simple autocorrelation functions. One of the simplest of which we might conceive is the rectangular function, which has value unity up to $\tau=\tau_o$ and value

zero for larger τ. In this case, equation 3-40 produces

$$\overline{\theta^2} = 2\tau_o \, t \, \overline{\left(\frac{d\theta}{dz}\right)^2} \qquad \text{3-43 (Rectangular)}$$

The rectangular autocorrelation function produces a result identical in form to that obtained from the exponential autocorrelation function. It must be remembered that the correlation depth τ_o is necessarily defined differently for the two cases, however. In the rectangular case, τ_o is the value of τ at which the autocorrelation function drops abruptly from unity to zero. In the exponential case, τ_o is the value at which the autocorrelation reaches e^{-1}.

Another simple autocorrelation function is that which drops linearly as $1 - \tau/\tau_o$ until $\tau = \tau_o$ and remains at zero for larger values of τ. In this case, equation 3-40 produces

$$\overline{\theta^2} = \tau_o \, t \, \overline{\left(\frac{d\theta}{dz}\right)^2} \qquad \text{3-43 (Linear)}$$

It is easily shown that autocorrelation functions which follow a positive integral power law of the form $1 - (\tau/\tau_o)^n$, so that they drop off more slowly than the linear function, produce

$$\overline{\theta^2} = \frac{2n}{n+1} \, \tau_o \, t \, \overline{\left(\frac{d\theta}{dz}\right)^2} \qquad \text{3-43 (Integral powe}$$

Similarly, positive fractional power law functions of the form $1 - (\tau/\tau_o)^{1/n}$, which drop off faster than the linear autocorrelation function, yield

$$\overline{\theta^2} = \frac{2}{n+1} \, \tau_o \, t \, \overline{\left(\frac{d\theta}{dz}\right)^2} \qquad \text{3-43 (Fractional power)}$$

All of the autocorrelation functions considered above describe random scattering layers. Their Fourier transforms, which would represent the power spectrum of electron-density structure in the z direction, could be likened to the frequency response characteristics of low-pass filters. As one last example of a random-layer autocorrelation function, let us arbitrarily choose one-quarter of an ellipse. That is, let us choose

$$\rho_z = \tau_o^{-1} \sqrt{\tau_o^2 - \tau^2} \qquad 0 \leq \tau \leq \tau_o$$

$$\rho_z = 0 \qquad \tau > \tau_o \qquad \text{3-44}$$

In this case, we have

$$I = \int_0^{\tau_o} \tau_o^{-1} \sqrt{\tau_o^2 - \tau^2}\, d\tau = \pi\tau_o/4 \qquad \text{3-45}$$

and

$$\overline{\theta^2} = \frac{\pi}{2} \tau_o\, t\, \overline{\left(\frac{d\theta}{dz}\right)^2} \qquad \text{3-43 (Elliptical)}$$

A glance at the equations 3-43 shows that for all the autocorrelation functions considered, the variance of phase at the base of the scattering layer is given by

$$\overline{\theta^2} = k\, \tau_o\, t\, \overline{\left(\frac{d\theta}{dz}\right)^2} \qquad \text{3-46}$$

where t represents the thickness of the scattering layer, τ_o the scale of irregularities in the layer, and k is a dimensionless constant determined by the detailed shape of the autocorrelation function. In most cases, k will be smaller the more sharply the autocorrelation function falls off at small values of τ, although it depends also on the precise definition of τ_o.

Let us turn now to an example of a quasi-periodic scattering layer. Such a layer is characterized by an oscillating autocorrelation function, whose oscillations die out rapidly or slowly depending on whether the periodicity is ill-defined or well-defined. The power spectrum of the electron-density structure could be likened to the response characteristic of a bandpass filter, centered on the frequency corresponding to the quasi-period. The envelope which defines the decay of the autocorrelation-function oscillation is the Fourier transform of the band-limiting function. The shape of the envelope is unimportant for our purpose, the feature of interest being the oscillatory nature of the autocorrelation function. Let us examine the case of a Gaussian envelope, so that the auto-correlation function is given by

$$\rho_z = \exp(-\tau^2/\tau_o^2) \cos(\tau/l_z) \qquad 3\text{-}47$$

In the above autocorrelation function, τ_o is again the correlation depth. The size of irregularities, however, is on the order of l_z, which is $(2\pi)^{-1}$ times the quasi-period of the structure.

To evaluate the integral in equation 3-40 for the autocorrelation function of equation 3-47, let us make the following changes in variable:

$$\text{let } x = \tau/\tau_o \text{ and let } g = \tau_o/l_z$$

Then the integral becomes

$$I = \tau_o \int_o^{t/\tau_o} \exp(-x^2) \cos gx \, dx \qquad 3\text{-}48$$

Using integral 313-6 of Grobner and Hofreiter (1961), we find that

$$I = \frac{\sqrt{\pi}\,\tau_o}{4e^{g^2/4}} \left\{ \left[\operatorname{erf}\left(\frac{t}{\tau_o} - \frac{ig}{2}\right) + \operatorname{erf}\left(\frac{t}{\tau_o} + \frac{ig}{2}\right] - \left[\operatorname{erf}\left(-\frac{ig}{2}\right) + \operatorname{erf}\left(\frac{ig}{2}\right)\right] \right\} \qquad 3\text{-}49$$

The error function is odd, so the second term in curly brackets is zero.

If the quasi-periodicity of the scattering layer in the z direction is too well defined, τ_o and g are large, and we must deal with complex arguments in the error functions of the first term in curly brackets. Further, if τ_o is allowed to become too large, only unrealistically large values of t safeguard the assumption we made in deriving equation 3-40. On the other hand, for weakly defined quasi-periodicity, the real parts of the error-function arguments dominate, and equation 3-49 becomes approximately

$$I = \frac{\sqrt{\pi}}{\alpha}\,\tau_o\, e^{-g^2/4} \operatorname{erf}(t/\tau_o) \qquad 3\text{-}50$$

Thus, for sufficiently large t, we obtain

$$\overline{\theta^2} = \sqrt{\pi}\,\tau_o\, t\, e^{-g^2/4} \overline{\left(\frac{d\theta}{dz}\right)^2} \qquad 3\text{-}51$$

Equation 3-51 is identical to equation 3-43 (Gaussian) except for addition of the factor $e^{-g^2/4}$. The ratio g of correlation depth to quasi-period is a measure of the degree of periodicity in the scattering layer structure. For well-defined quasi-periodicity g is large and l_z represents the size of the dominant structure. For ill-defined quasi-periodicity g is small. Equation 3-51 approaches identity with equation 3-43 (Gaussian) as the structure approaches strict randomness,

in which case τ_o becomes a statistical measure of the structural scale.

On the basis of the above discussion for Gaussian quasi-periodicity, it seems reasonable to generalize equation 3-46 to the following:

$$\overline{\theta^2} = kG\tau_o t \overline{\left(\frac{d\theta}{dz}\right)^2} \qquad 3\text{-}52$$

where G represents a factor which is a measure of the quasi-periodicity in the scattering layer's structure in the z direction. The factor G is unity for a strictly random layer, in which case τ_o is the statistical scale of irregularities. For weakly defined quasi-periodicity, G departs from unity and also depends upon the scale of the structure. The derivation of equation 3-52 does not hold for well-defined quasi-periodicity.

Substituting from equation 3-37, we have finally for the variance $\overline{\theta^2}$ of the phase at the base of a scattering layer whose autocorrelation function in the z direction may take a variety of forms

$$\overline{\theta^2} = kG\ \tau_o\ t\ \left(\frac{\pi}{\lambda}\right)^2 \left(\frac{\omega_o}{\omega}\right)^4 \frac{\overline{(\Delta N)^2}}{\overline{N}^2} \qquad 3\text{-}53$$

The special case of a Gaussian autocorrelation function, considered by Bramley (1955), is simply a case in which $kG = \sqrt{\pi}$.

D4 Relation Between the Structural Autocorrelation Function and the Phase-Distribution Autocorrelation Function

Equation 3-53 relates $\overline{\theta^2}$ to ionospheric parameters. We still must relate the autocorrelation function ρ_θ of the phase at the base of the scattering layer to ionospheric parameters. Bramley (1955) showed that for the special case of isotropic irregularities having a Gaussian

autocorrelation function, ρ_θ also is Gaussian. Although Bramley's development contains an error[1], we shall show that ρ_θ is identical to the x-direction autocorrelation function ρ_x of the scattering layer structure under rather general conditions. Bramley's special-case result follows correctly as an application of our general one.

First let us note the definition of ρ_θ under our choice of phase reference, which sets θ_o (the mean value of phase at the bottom of the layer) equal to zero. We have

$$\rho_\theta(\xi) = \overline{\theta(x)\theta(x+\xi)} / \overline{\theta^2} \qquad 3\text{-}54$$

where the bars denote averages over all values of x. From equation 3-38, it is seen that 3-54 can be written as

$$\rho_\theta(\xi) = \frac{1}{\theta^2} \overline{\int_o^t \int_o^t \frac{d\theta}{dz_1}(x,z_1) \frac{d\theta}{dz_2}(x+\xi,z_2)\, dz_1\, dz_2} \qquad 3\text{-}55$$

Substituting from equation 3-36, we obtain

$$\rho_\theta(\xi) = \frac{1}{\theta^2} \left(\frac{\pi}{\lambda}\right)^2 \left(\frac{\omega_o^2}{\omega^2}\right)^2 \frac{1}{\overline{N}^2} \overline{\int_o^t \int_o^t \Delta N(x,z_1)\, \Delta N(x+\xi,z_2)\, dz_1\, dz_2} \qquad 3\text{-}56$$

Now let us denote the double integral under the x-averaging bar as J. The geometry involved in evaluating J is shown in figure 11. The basic

---

[1] In going from his equation (13) to equation (14), Bramley incorrectly replaced a one-dimensional autovariance function with a two-dimensional autovariance function. His result (under a subsequent approximation) followed only as a result of the special transformation properties of the Gaussian function, and his procedure would not lead to a valid result in more general considerations.

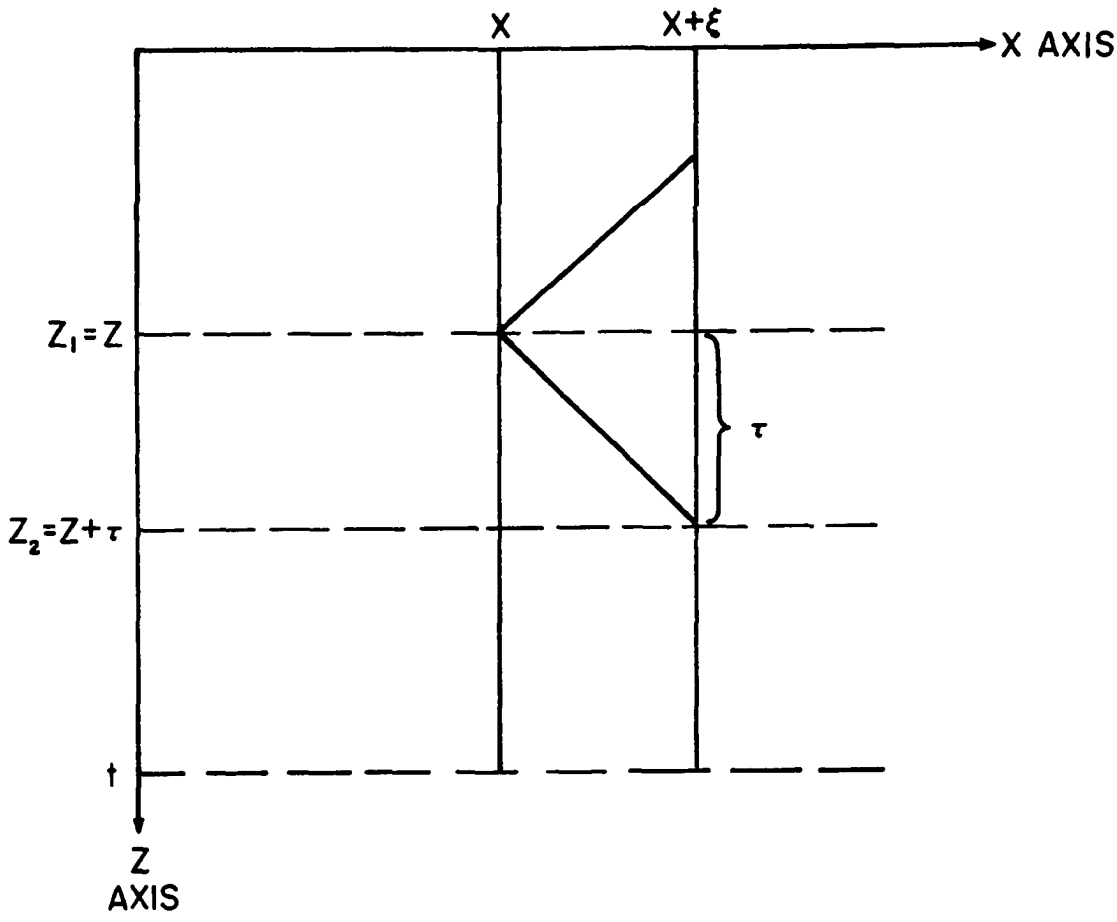

Fig. 11. Integration geometry for evaluating J.

coordinate system involved is indicated by the general x and z axes, with the origin at the upper left corner of the figure. The integrations are taken through the thickness t of the irregular scattering layer, along the z paths located at x and x+ξ. The integrand is the product of ΔN at each pair of points z_1 and z_2 located on the two paths. Now let us denote z_1 by z and z_2 by z+τ. Then the double integration can be taken over z and τ as follows:

$$J = \int_0^t \left[\int_0^{t-\tau} \Delta N(x,z)\Delta N(x+\xi,z+\tau)dz + \int_{\tau}^{t} \Delta N(x,z)\Delta N(x+\xi,z-\tau)dz \right] d\tau \qquad 3\text{-}57$$

Consider the first term in equation 3-57. The integrand is the product formed at the ends of the lower diagonal line in figure 11. The integral over z is obtained as the line moves down through the scattering layer. There is no contribution for z less than zero because ΔN(x,z) is then zero. There is no contribution for z greater than t-τ because ΔN(x+ξ,z+τ) is then zero. The first term, with the limits as shown, thus contains the total contribution of products between the general point z on the path at x and points at a distance τ lower on the path at x+ξ. Similarly, the second term contains the total contribution of products between the general point z and points a distance τ above it. There is no contribution for z less than τ or z greater than t because in each case one end or the other of the product path (the upper diagonal line) is outside the irregular layer. Integrating over τ from zero to t collects all the non-zero contributions to conclude the evaluation of the double integral J.

A simple origin shift in the second term of equation 3-57 produces

$$J = \int_0^t \left[\int_0^{t-\tau} \Delta N(x,z)\Delta N(x+\xi,z+\tau)\, dz + \int_0^{t-\tau} \Delta N(x,z+\tau)\Delta N(x+\xi,z)\, dz \right] d\tau \qquad 3\text{-}58$$

Now it is $\overline{J}$, the x-average of J, which we desire for use in equation 3-56. We are free to interchange the order of averaging over x and integrating over z and τ since the limits and integration variable in the averaging process are independent of those in the explicit integrations We have, therefore,

$$\overline{J} = \int_0^t \left[\int_0^{t-\tau} \overline{\Delta N(x,z)\Delta N(x+\xi,z+\tau)}\, dz + \int_0^{t-\tau} \overline{\Delta N(x,z+\tau)\Delta N(x+\xi,z)}\, dz \right] d\tau \qquad 3\text{-}59$$

Aside from a factor of $t-\tau$, the inner integrals of equation 3-59 each represent an average over x and z of the product of ΔN at points in the xz plane separated by a distance ξ in the x direction and τ in the z direction. If the range of z averaging is sufficiently large, then, each of the inner integrals is the two-dimensional autovariance function of the electron density N in the scattering layer. Recalling that the variance of N in the layer is $\overline{(\Delta N)^2}$ and denoting the two-dimensional spatial autocorrelation function of N by $\rho_N(\xi,\tau)$ we find that $\overline{J}$ becomes

$$\overline{J} = \overline{(\Delta N)^2} \int_0^t 2\,(t-\tau)\,\rho_N(\xi,\tau)\, d\tau = 2t\,\overline{(\Delta N)^2} \int_0^t \left(1-\frac{\tau}{t}\right)\rho_N(\xi,\tau)\, d\tau \qquad 3\text{-}60$$

Let us assume now that ρ_N can be expressed as the product of two independent but otherwise arbitrary one-dimensional autocorrelation functions $\rho_x(\xi)$ and $\rho_z(\tau)$, where

$$\rho_x(\xi) = \frac{\overline{\Delta N(x,z)\Delta N(x+\xi,z)}}{\overline{[\Delta N(x,z)]^2}}$$

and

$$\rho_z(\tau) = \frac{\overline{\Delta N(x,z)\Delta N(x,z+\tau)}}{\overline{[\Delta N(x,z)]^2}}$$

Then, equation 3-60 can be written as

$$\overline{J} = [2t\ \overline{(\Delta N)^2} \int_0^t (1 - \tfrac{\tau}{t})\ \rho_z(\tau)\ d\tau]\ \rho_x(\xi) \qquad 3\text{-}61$$

But the integral in equation 3-61 is just that which appears in equation 3-39. Hence $\overline{J}$ is given by

$$\overline{J} = [\overline{\theta^2}\ \overline{(\Delta N)^2} / \overline{(\tfrac{d\theta}{dz})^2}]\ \rho_x(\xi) \qquad 3\text{-}63$$

Let us now replace the averaged double integral in equation 3-56 with $\overline{J}$ from 3-62 and substitute the right-hand side of equation 3-37 for $\overline{(\frac{d\theta}{dz})^2}$. Upon doing so, we obtain

$$\rho_\theta(\xi) = \rho_x(\xi) \qquad 3\text{-}63$$

Equation 3-63 states that the spatial autocorrelation function of the phase distribution at the base of the scattering layer is identical to the parallel component of the autocorrelation function of structure in the scattering layer. The prime assumption upon which this simple result is based is that the ion-density autocorrelation function can be expressed as the product of mutually independent component functions in the directions of the coordinate system. The assumption does not appear very restrictive. We have considered only two dimensions for simplicity and because the experiment we shall describe in Chapter IV is not dependent upon conditions in the third dimension (and, of course, cannot therefore yield information concerning structure in the third

dimension). Generalization to three dimensions is straight-forward.

Along the route to equation 3-63, we made another incidental assumption, that of a "sufficiently large" range of z integration. This assumption means that the layer thickness t is large compared with the largest value of τ for which there is significant contribution to the integrals. This is the same assumption made earlier in approximating equation 3-39 by equation 3-40. Consequently, we could make the same approximation in equation 3-61. Nothing would be gained however, and our result would be the same.

The assumption that the layer is thick compared with the z-direction correlation distance (which we termed the "correlation depth" earlier) also means that our result does not depend explicitly on the upper limit placed on the τ integration in evaluating J. The careful reader may have felt uneasy about the choice of t as a limit since there is no a priori reason for this choice contained in the geometry. The justification lies in the thick-layer assumption. Any limit equal to or greater than t would produce the same result, as it would in equation 3-40, since the contribution outside the range 0 to t is negligible under the assumption.

IIIE SUMMARY AND DISCUSSION

E1 Assumptions and Results

Let us summarize the important results of this chapter. First, it was shown that our assumption in Chapter II that we are dealing with a randomly phased angular spectrum means that we must exclude certain simple kinds of ionospheric structure from consideration. In

particular, we are not here considering refraction in one or a few ionospheric lenses or scattering by strictly periodic ionospheric structure. Although both of these problems can be attacked using the concept of the angular spectrum, the assumption of random phasing excludes them. The simple refraction problem is more conveniently attacked from the ray point of view anyway. Strict periodicity of ionospheric structure is not likely in practice, and quasi-periodicity is not excluded by the assumption of random phasing.

Another assumption, which we made in the present chapter, is that the scattering layer under consideration is thick compared with the correlation depth of its structure. For purely random structure the thick-layer assumption means that the layer is several irregularities deep. For quasi-periodic structure along the radio line of sight, the layer must be deep also compared with the distance over which the quasi-periodicity is sustained with approximately constant phase. Any given layer thickness therefore sets a limit on the degree to which the quasi-periodicity can be defined.

A third assumption, also made in the present chapter, is that the phase at the base of the scattering layer has a normal distribution, such as might result from a large number of independent scatterings. Under the second and third assumptions and two others of less physical importance, the following major results were obtained:

$$\overline{\theta^2} = \ln\left(\frac{1}{b} + 1\right) \qquad \text{(from equation 3-20)} \qquad 3\text{-}64$$

$$\rho_\theta(\xi) = \frac{\ln\left[1 + \frac{R(\xi)}{b}\right]}{\ln\left[1 + \frac{1}{b}\right]} \qquad \text{(from equation 3-27)} \qquad 3\text{-}65$$

$$\overline{\theta^2} = K\,\tau_o\,t\,\frac{\pi^2}{c^2}\,\frac{f_o^4}{f^2}\,\frac{\overline{(\Delta N)^2}}{\overline{N}^2} \qquad \text{(from equation 3-53)} \qquad 3\text{-}66$$

(where c = velocity of light and K = kG)

$$\rho_\theta(\xi) = \rho_x(\xi) \qquad \text{(from equation 3-63)} \qquad 3\text{-}67$$

The first two expressions above relate the variance $\overline{\theta^2}$ and autocorrelation function $\rho_\theta(\xi)$ of the phase distribution at the base of the ionospheric scattering layer to the observational quantities b and $R(\xi)$. The second pair of equations relates $\overline{\theta^2}$ and $\rho_\theta(\xi)$ to ionospheric parameters. Thus, the set of four equations provides a route to evaluation of certain ionospheric parameters from interferometric observations at the ground.

Each of the above four equations either is identical to a corresponding result given by Bramley (1955) for the special case of isotropic ionospheric structure having a Gaussian autocorrelation function or is readily reduced thereto. We have not, however, assumed isotropy or a Gaussian autocorrelation function in the present work. In addition, there is no restriction on the magnitude of the coherence ratio b or the variance $\overline{\theta^2}$ of the base-plane phase. Therefore, the results hold for strong as well as weak scatter.

E2 Ionospheric Optical Thickness and Scattering Coefficient

Bramley (1954) pointed out that the analysis contained in his 1955 paper (carried out earlier but delayed relatively in press) afforded a means of relating the supposed thin diffracting screen of Booker, Ratcliffe and Shinn (1950) and other workers to a more realistic thick scattering layer. The terms "strong" and "weak" scatter which we have used from time to time above are directly applicable only to the equivalent thin diffracting screen. It is not to be supposed that a thin layer of the terrestrial ionosphere is capable of strong single scatter of waves in the frequency range we are considering.[1] It would take a more highly ionized or denser medium to do so. A succession of weak scatterings in a thick layer, however, can result in a decreased coherence ratio and produce a resultant field identical to that produced by a single strong scattering in the equivalent thin screen.

Fejer (1953) specifically analyzed the process of multiple weak scatterings - ie, scatterings for each of which the Born approximation[2] holds - in a thick irregular medium. In his analysis, Fejer assumed an isotropic scattering layer with a Gaussian autocorrelation function. Bramley (1954) demonstrated the equivalence of his own and Fejer's results for this special case, insofar as the final resultant field is concerned. Owren (1962) extended Fejer's analysis to a nonisotropic Gaussian scattering layer and showed that the procedure amounts to a technique for solving the equation of radiative transfer, treated more generally by Chandrasekhar (1960).

---

[1] A possible exception is the small number of observations at 26.3 MHz.

[2] Also known as Born's first approximation and stating that the scatter field is weak compared with the incident field.

The radiative transfer approach has the great conceptual advantage of allowing description of the wave-field within the scattering medium itself. On the other hand, when one can observe only the resultant wave after emergence from the medium - as is the case in most ionospheric experiments, including ours - the relative simplicity of Bramley's approach renders it the more useful. Thus, for the most part, we shall use Bramley's results as generalized herein.

Based on the demonstrated equivalence of Bramley's and Fejer's results in the special case of a Gaussian autocorrelation function, however, we shall freely use the descriptive terminology employed by Fejer and by Owren. In particular, for all of our VHF observations (where the Born approximation may safely be assumed to hold), we shall take a measurable decrease in coherence ratio to indicate the occurrence of multiple scatter.

Now Fejer (1953) and Bramley (1954) agreed that the "effective depth of scattering" of the thick layer is equal to the variance $\overline{\theta^2}$ of phase at the base of the layer. It is evident from the work of Owren (1962) that Fejer's "effective depth of scattering" is identical to the optical thickness of a purely scattering layer. Thus $\overline{\theta^2}$ represents the optical thickness of our scattering layer. The plausibility of this result for a general autocorrelation function can be seen by comparing the integral over angles of our equation 3-19b with the formal solution of the equation of radiative transfer, as given for instance by Chandrasekhar (1960) in equation 50 of his Chapter I.[1]

---

[1] The source function $\tilde{J}(s')$ which appears in the integral of Chandrasekhar's expression is given, for a scattering atmosphere, in his equation 41. The latter equation involves an integral over all (scatter) angles of the "phase function" of the scattering process, which is essentially our angular power spectrum. An arbitrary phase function or angular power spectrum implies an arbitrary spatial autocorrelation function.

Equation 3-64 shows that determination of the coherence ratio b measured at the ground allows direct calculation of the optical thickness of the ionospheric scattering layer. The combination of equations 3-65 and 3-67 shows that the additional measurement of the wavefront autocorrelation function $R(\xi)$ at the ground allows calculation of the spatial autocorrelation function of the scattering layer in the direction parallel to the interferometer baseline.

Equation 3-66 relates the optical thickness to other physical parameters of the scattering layer. The optical thickness of the layer can be defined as

$$\overline{\theta^2} = \int_0^t \ell \, dz \qquad 3\text{-}68$$

where ℓ is the (linear) scattering coefficient of the layer, defined as the flux scattered per unit path length from an incident beam of unit flux density.[1] If the scattering coefficient is constant through the geomagnetic thickness of the layer, then obviously the optical thickness is simply the product of the scattering coefficient and the geometric thickness. Comparison with equation 3-66, then, shows that the scattering coefficient of the layer is given by

$$\ell = K \tau_o \frac{\pi^2}{c^2} \frac{f_o^4}{f^2} \frac{\overline{(\Delta N)^2}}{\overline{N}^2} \qquad 3\text{-}69$$

---

[1] The equivalent quantity in Chandrasekhar's work is $\kappa\rho$ where κ is the mass scattering coefficient and ρ is the mass density of the scattering constituent of the atmosphere. (See equation 51 of his Chapter I.)

The assumption that ι is constant holds under our tacit assumption that the scattering layer is statistically uniform (ie, displays spatial stationarity) in the z direction, which ensures that all the quantities on the right of equation 3-69 can be treated as constants. Moderate departures from the assumed condition mean that equation 3-69 must be interpreted as giving a weighted average scattering coefficient for the layer.

The scattering coefficient given by equation 3-69 is analagous to the absorption coefficient of the magneto-ionic theory (Ratcliffe, 1959, section 4.4). The absorption coefficient determines the exponential rate of attenuation suffered by a wave in traversing an absorbing region. The scattering coefficient determines the exponential rate of attenuation suffered by the nondeviated component of a wave in travelling through a scattering region. In the case of absorption, electromagnetic energy from the wave-field is transformed into heating of the medium by collisions, decreasing the strength of the wave. In the scattering case, energy is transferred from the nondeviated component into the scatter spectrum, decreasing the coherence ratio while maintaining constant total wave-field energy.

Reinserting the explicit expression for critical frequency into equation 3-69 produces

$$\iota = \left(\frac{e^2}{4\pi c \epsilon_o m}\right)^2 f^{-2} K \tau_o \overline{(\Delta N)^2} \qquad 3\text{-}70$$

Equation 3-70 shows that the scattering coefficient displays a wavelength-squared frequency dependence and depends on the structure of the scattering

layer through K, τ_o and $\overline{(\Delta N)^2}$. It will be recalled that K is a dimensionless constant determined by the line-of-sight spatial autocorrelation function of the layer. It was developed as the product kG, where k depends upon the overall shape of the autocorrelation function (the envelope in the quasi-periodic case) and G depends upon the degree to which quasi-periodicity is developed, reducing to unity for a strictly random layer. The correlation depth of the layer is given by τ_o, which reduces to the statistical scale of irregularities in the line-of-sight direction for the case of a strictly random layer. The final factor, of course, gives the strength of the irregularities as the variance of electron density in the layer. The elements of the first factor have their usual meaning in rationalized MKS units, so that the factor has the numerical value 4.53×10^{17} meter^4/second^2.

CHAPTER IV

EXPERIMENTAL DETERMINATION OF THE IONOSPHERIC AUTOCORRELATION FUNCTION AND OPTICAL DEPTH

IVA INTRODUCTION

The major results of Chapter III are embodied in equations 3-64 through 3-67. In section III E1, it was stated that this set of equations provides a means of evaluating certain parameters describing ionospheric structure from interferometric observations at the ground, namely the ionospheric structural autocorrelation function and the optical depth. The "observational quantities" which are the inputs to the evaluation are the coherence ratio b and the wavefront autocorrela-function $R(\xi)$. It must now be pointed out that the two so-called observational quantities are not observed directly as the outputs of any measuring instrument. Rather they are derived from more directly observed quantities in a manner based on the development of Chapter II.

The primary experimental problem at hand, then, is to determine b and $R(\xi)$ from interferometric observations. Recalling that the independent variable ξ represents interferometer spacing, it appears that the experiment will involve a number of spacings. Such is the case, although the number must be small for practical reasons. In the present experiment, several frequencies were employed also, in order to test the frequency dependence of the observed scattering process. First, let us explore the means at our disposal for determining b and R at a single frequency and spacing.

The basis of our method lies in the observed fact (Little, Reid,

Stiltner and Merritt, 1962) that in the auroral zone the average amplitude of the interference pattern produced at the output of a phase-switch interferometer occasionally decreases in a manner which cannot be explained by ionospheric absorption. Observations by Flood (1963) have implied that such decreases are due to reductions in the correlation coefficient between the voltages produced at the outputs of the interferometer antennas. According to discussions in Chapter II and Chapter III, decreases in voltage correlation can be described quantitatively as reductions in the source visibility r, measured on the output record of a phase-switch interferometer. We shall refer to such events as visibility fades.

The visibility r, as an observational quantity, was defined in Chapter II, and it was shown there that, under the sole assumption of a randomly phased angular spectrum,

$$r = \frac{b + R}{b + 1} \qquad 4\text{-}1$$

Equation 4-1 holds for any value of b and R. A second equation of equal generality, relating b and R to another observational quantity, would allow direct solution for b and R. Unfortunately, explicit relations have been derived only for special cases. For instance, in the case of large coherence ratio, we have from equations 2-94 and 2-95

$$\overline{|n|}^2 = \frac{1 - R}{2\pi b} \qquad 4\text{-}2$$

where n represents the output of an independent phase channel, obtainable from a phase-sweep interferometer.

A number of other observational quantities, involving either independent phase or independent amplitude information, could be used

to supplement equation 4-1 in the special cases of large coherence ratio (weak scatter) or zero coherence ratio (complete scatter). For the general case of arbitrary coherence ratio which we wish to attack, no available explicit relations will suffice. However, we can combine equation 4-1 with results of the numerical technique described in section D3 of Chapter II to obtain a graphical solution for b and R in the general case.

The quantities obtained by the numerical technique relate directly to the outputs of a phase-sweep interferometer. The graphical solution provides a single value of $R(\xi)$ and the value of b, which is not a function of ξ. Once b is established, application of equation 4-1 to the visibility obtained from phase-switch interferometers on other spacings allows determination of the wavefront spatial autocorrelation function $R(\xi)$. Details of data reduction, graphical solution, and quantitative calculation will be discussed in sections IVC and IVD. Let us now turn to a description of the observations and instrumentation.

IVB INSTRUMENTATION AND OBSERVATIONS

B1 Antennas and Field-site Layout

Visibility fades had first been observed in the auroral zone by Dr. C. G. Little and several coworkers during the International Geophysical Year (Little, Reid, Stiltner and Merritt, 1962). Their observations had been carried out at 223 and 456 MHz, using 28-foot parabaloids on an east-west baseline of 100 yards. They termed the fades which they observed "long-duration fades" because they took place over the period of many individual scintillations.

At the close of the IGY, the College radio interferometers were shut down and lay idle most of the time for almost three years. Late in 1961, the original instruments were reactivated under the direction of Dr. Leif Owren. During 1962 it became obvious that the post-IGY decline in solar activity had been accompanied by a drastic reduction in auroral-zone scintillation. At 223 MHz, the amplitude scintillation index devised by Little et al (1962) on a scale from zero to four displayed a decrease in its most frequently observed value from three during the IGY to one during 1962 (Owren, Fremouw, and Hunsucker, 1964). At 456 MHz, measurable scintillation was hardly ever observed in 1962. Visibility fades were very rare on both frequencies with the existing baseline of 91.4 meters.

In view of the decreased scintillation and fade activity, a decision was made to extend the observations to lower frequencies and wider baselines. During 1963 there ensued a period of instrument development designed to allow multi-spacing, multi-frequency observations. In addition to the original frequencies, two lower frequencies were chosen and antennas purchased. A prime consideration in choice of frequencies was freedom from interference.

The first new frequency chosen was 137 MHz. This frequency was chosen for several reasons, one of which was the potential usefulness of observations to evaluation of propagation in NASA's satellite band of 136.0 to 137.0 MHz. By using antennas cut for 137.0 MHz, it was possible to operate just within or just outside of the satellite band. This capability proved very helpful. Early observations with the 137 MHz antennas were carried out at 136.5 MHz, in the center of the protected

satellite band. This ensured virtually complete freedom from interference other than at times of known satellite passes. As the density of satellite transmissions increased, observations were moved to 137.5 MHz, which also proved to be a satisfactory frequency.

The other new frequency chosen was 68 MHz, which turned out to be the prime observing frequency. There were two basic reasons for choosing a frequency between 50 and 100 MHz. First, this band is low enough that considerable scintillation activity could be expected. On the other hand, it is high enough that absorption effects could be neglected. The tentative choice of 68 MHz was made because of its convenient numerical relationship to 136 MHz. In addition, it is in a television band, with no immediately local station in operation on the channel in question. An interference check showed no contamination from remote television stations or any other source. The frequency has proven to be quite free of interference. The only persistent source of interference experienced has been from one of the Geophysical Institute's own sounders at a nearby field site. The sounder has a very low duty cycle and its transmissions are readily identified on the interferometer records, causing no scaling difficulties.

On each of the four observing frequencies - 68, 137, 223, and 456 MHz - it was planned to construct tri-spacing interferometers. For each of the two new frequencies, three antennas were purchased from Telrex Corporation. They consist of quad-stacked, four-bay yagi arrays, with eight elements per bay at 137 MHz and six elements per bay at 68 MHz. The gain is 18 db at 137 MHz and somewhat less at 68 MHz. The 28-foot parabaloids were to be supplemented by long yagis for 223 and 456 MHz

observations. Equipment limitations and lack of scintillation activity at 456 MHz resulted in abandonment of observations at this frequency. The antenna purchased for 223 MHz observations also was obtained from Telrex. It is a quad-stacked array of four 16-element yagis, with an overall length of 5 1/2 meters. The gain is approximately 23 db, which equals the gain of the previously existing parabaloids at the same frequency.

While a sound basis for choice of observing frequencies and selection of antennas was available, there was little a priori information upon which to base choice of baselines. Essentially all that was known was that if visibility fades were to be observed at 223 MHz, one would require a baseline considerably longer than about 100 meters. Accordingly, the 223 MHz yagi was placed to give the greatest spacing which was readily available along an extension of the existing parabaloid baseline. This position turned out to be approximately 218 meters west of the east parabaloid. The yagi and two dishes thus made available east-west baselines of 91.4 meters (68 wavelengths), 126.9 meters (95 wavelengths), and 218.3 meters (162 wavelengths). It had been planned to mount the yagi on a van to allow variation of spacing between 127 and 218 meters. This proved infeasible, however, due to the length and fragile nature of the antenna. Furthermore, it was found desirable to operate with the greatest available 223 MHz spacing.

As a result of initial 223 MHz observations, it was decided to make 220 meters the prime observing baseline for 68 and 137 MHz. Accordingly, a new east-west baseline was laid out to the north of the existing one.

One 68 MHz yagi and one 137 MHz yagi were placed approximately due north of the instrument building. A pair of antennas then was erected 220.1 meters to the east, giving spacings of 50 and approximately 100 wavelengths at 68 and 137 MHz, respectively. In order to provide one longer and one shorter baseline at each of the new frequencies, it was decided to place a third pair of antennas to the west of the first pair. To allow some adjustment of baseline, this third pair was placed on a wooden track.

The track allows adjustment from about 6 to about 31 wavelengths at 68 MHz and from about 12 to 63 wavelengths at 137 MHz when the movable antennas are operated in conjunction with the center fixed antennas. When the movable antennas are operated in conjunction with the east fixed antennas, adjustment ranges from about 56 to 82 wavelengths at 68 MHz and from about 112 to about 164 wavelengths at 137 MHz.

After a period of trial observations at various spacings, it was found that the convenient tri-spacings of 110, 220 and 330 meters produced useful visibility-fade and scintillation observations at 68 and 137 MHz. For the visibility-fade observations, with which we are concerned here, tri-spacing was employed at 68 MHz. In addition, 137 MHz observations were carried out with the 220-meter spacing, and 223 MHz observations were performed with 218 meters spacing. Table 1 summarizes the antenna and baseline characteristics of the interferometers used in the experiment.

TABLE 1

INTERFEROMETER ANTENNAS

Frequency	Antennas	East-West Baselines
68 MHz	4-bay yagi arrays, 6 elements per bay	110 meters = 25 wavelengths 220 meters = 50 wavelengths 330 meters = 75 wavelengths
137 MHz	4-bay yagi arrays, 8 elements per bay	220 meters = 101 wavelengths
223 MHz	A 4-bay yagi array, 16 elements per bay, and 8.5-meter parabaloid	218 meters = 162 wavelengths

Figure 12 is an aerial view of the Ballaine Lake field site, at which the instruments were located. The top of the photograph is north. The diamond shaped clearing near the lower left-hand corner of the photograph is the College minitrack station. The long east-west clearing is the location of the interferometer baselines. The two parabaloids, with the main instrument building between them, are most readily found by their long north-extending shadows. To the west of the dishes, at the end of the clearing, can be seen the 223 MHz yagi hut. The yagis had not been installed at the time the photograph was taken.

The 68 and 137 MHz baseline extends along the northern edge of the clearing. The center antennas were placed approximately due north of the main building. The east antennas were placed in the rectangular

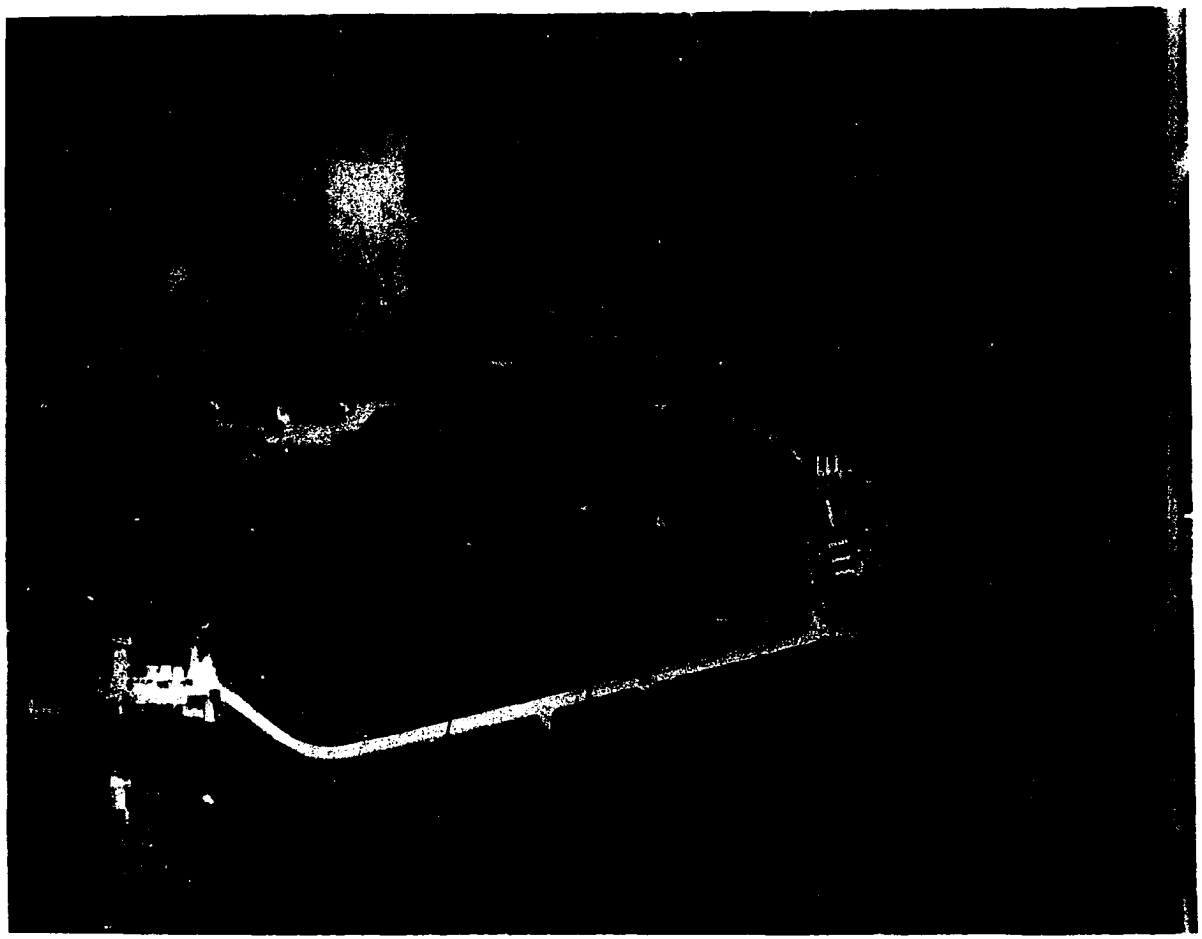

Fig. 12. Ballaine Lake field site including interferometer baselines and College minitrack station.

area at the east end of the baseline. The wooden track for the movable pair of antennas was laid out approximately from the center yagis to near the west end of the clearing. Figure 13 gives the baseline survey information for all instruments.

The pre-existing parabaloids are on polar mounts and are equipped with sidereal drives as well as fast-slew drives in declination and right ascension. (For details concerning the dishes, see Geophysical Institute Report UAG R88.) Polar mounts and drives for the new yagis were built in the Geophysical Institute machine shop. In right ascension, the mounts are equipped with fast-slew drives and interchangeable solar and sidereal tracking drives. Declination is manually adjustable by means of a pivot and mechanical lock in conjunction with a declination-reading protractor attached to each mount. Access for declination adjustment is by attached ladder, and adjustment can be carried out within a minute. Figure 14 shows the moveable 137 and 68 MHz yagis and mounts, complete except for ladders. The elevated boxes at right are switching and plug-in stations for local oscillator and i-f signals, regulated and nonregulated power, and antenna control circuits.

Since continuous observations were desired from all instruments, the yagi drives were designed with rotating radio-frequency couplers, which allowed uninterrupted tracking of circum-polar sources. The pre-existing parabaloids were outfitted with a recycling device which allows them to "unwind" their cables upon reaching a limit switch near lower transit of a circum-polar source. The device was constructed in such a manner that the source is reacquired and tracking resumed after a seven-

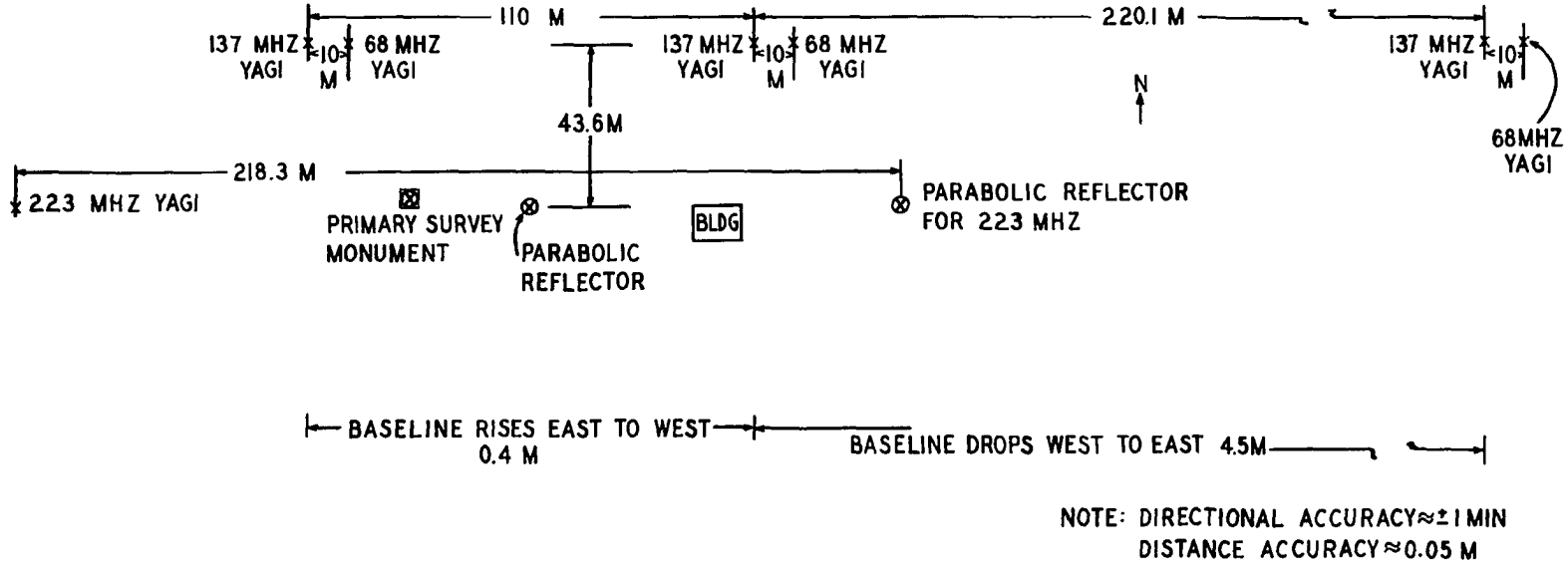

Fig. 13. Interferometer baseline survey information.

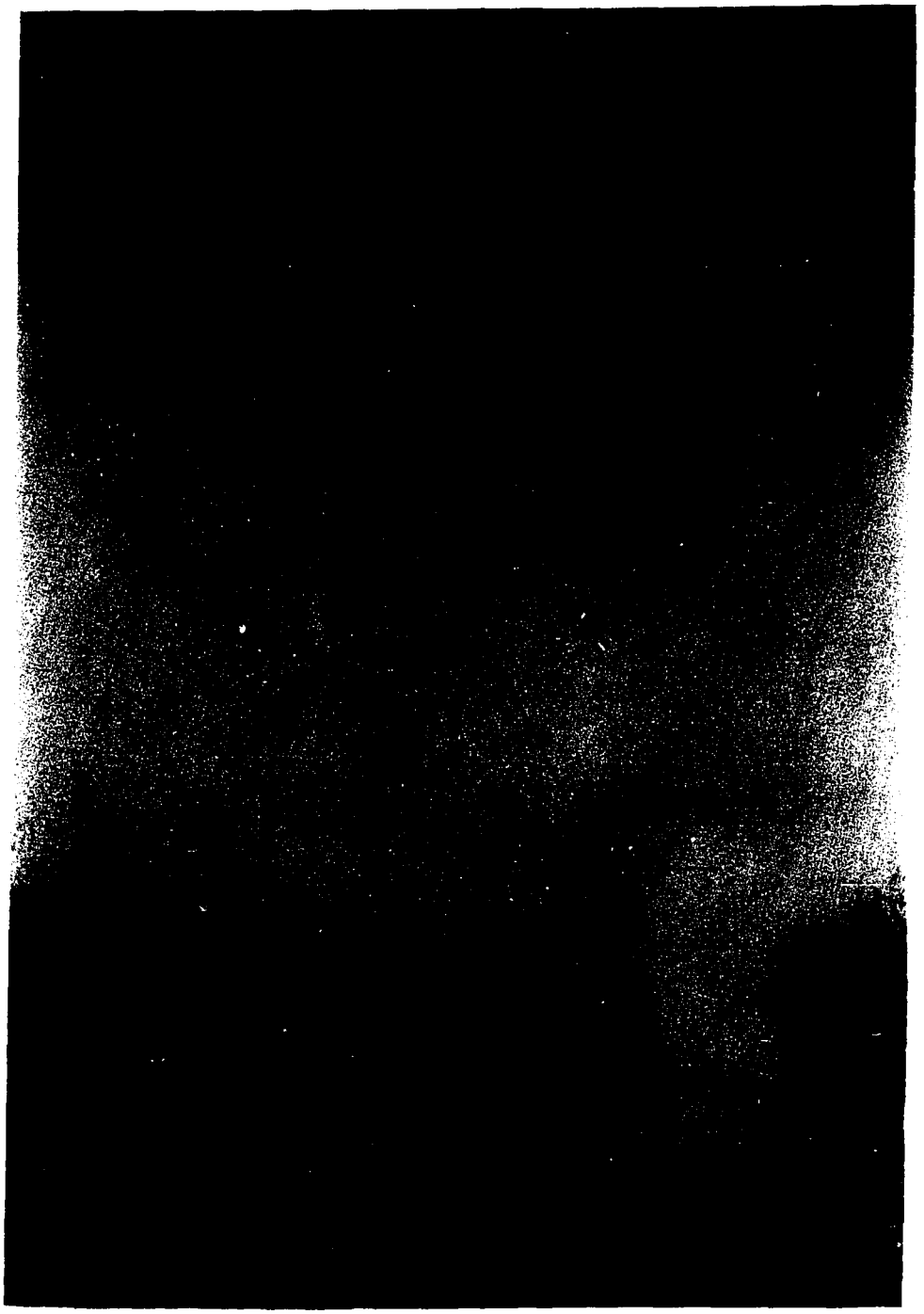

Fig. 14. View eastward along 68 and 137 MHz interferometer baseline.

minute recycle period. The recycle device was incorporated into the dish control consoles located in the main building. Thus no modification was required in the parabaloid mounts or in the control circuits running underground from the building to the mounts.

Control circuits to the yagi drives were run in armored cable on top of the ground, allowing tracking and right-ascension slewing control from the main building. For cold-weather operation, the drives required internal heaters. In addition, heat, light and maintenance outlets were required in each anntenna hut since radio-frequency amplification and frequency conversion were carried out in the field. Temperature in the huts was thermostatically controlled by means of electric heaters and fans. Nonregulated power for heat, lights, maintenance outlets, and antenna drives plus regulated power for electronic circuits was run underground from the main building. The cable trenches are located at the south edge of the baselines, cables emerging to junction stations near each antenna location.

B2 Interferometric Receivers

Along with the two 28-foot parabaloids, there existed two phase-switch and two phase-sweep interferometric receivers. The instruments had been used in the earlier 223 and 456 MHz observations of Little and his coworkers. After several years of idleness, they were found in a state of considerable disrepair. Nevertheless, all of the phase-switch circuits were renovated and placed back in operation, with the exception of the local oscillators and the 456 MHz r-f amplifiers and mixers. The intermediate-frequency circuits were modified to operate at 30 MHz

rather than at their original 32 MHz in order to make them compatible with plans for new instruments. New local oscillators were constructed. Aside from the small change in intermediate frequency and a narrowing of the i-f bandwidths[1], the basic instruments are essentially as described in Geophysical Institute report UAG R88. They will not be described in detail here.

For the experiment with which we are concerned, it was desired to have the equivalent of five phase-switch interferometers. Two new instruments were constructed. They incorporate features of the two pre-existing receivers and features of a design made available by Dr. Owren plus innovations. The result is a considerable simplification and decrease in size as compared with the pre-existing receivers. The fifth instrument, a phase-sweep interferometer, was purchased from Boeing Scientific Research Laboratories.

Figure 15 is a simplified block diagram which corresponds to either of the two new phase-switch interferometers. Circuit diagrams are given in Appendix 2 for one of the instruments, the other being essentially identical following frequency conversion. The operation of phase-switch interferometers is well-known, first having been described by Ryle (1952). It will not be repeated here. The primary difference between the two receivers built for the present experiment and the two previously existing at College is use of a lumped-circuit "Mills" switch rather than a distributed-circuit cable switch as the phase-reversing element. The main advantages are a saving in space and greater freedom from residual sensitivity to noncoherent inputs

[1]Necessary to avoid white-noise blurring on the lengthened 223 MHz baseline and to escape interference on frequencies near 223 and 68 MHz.

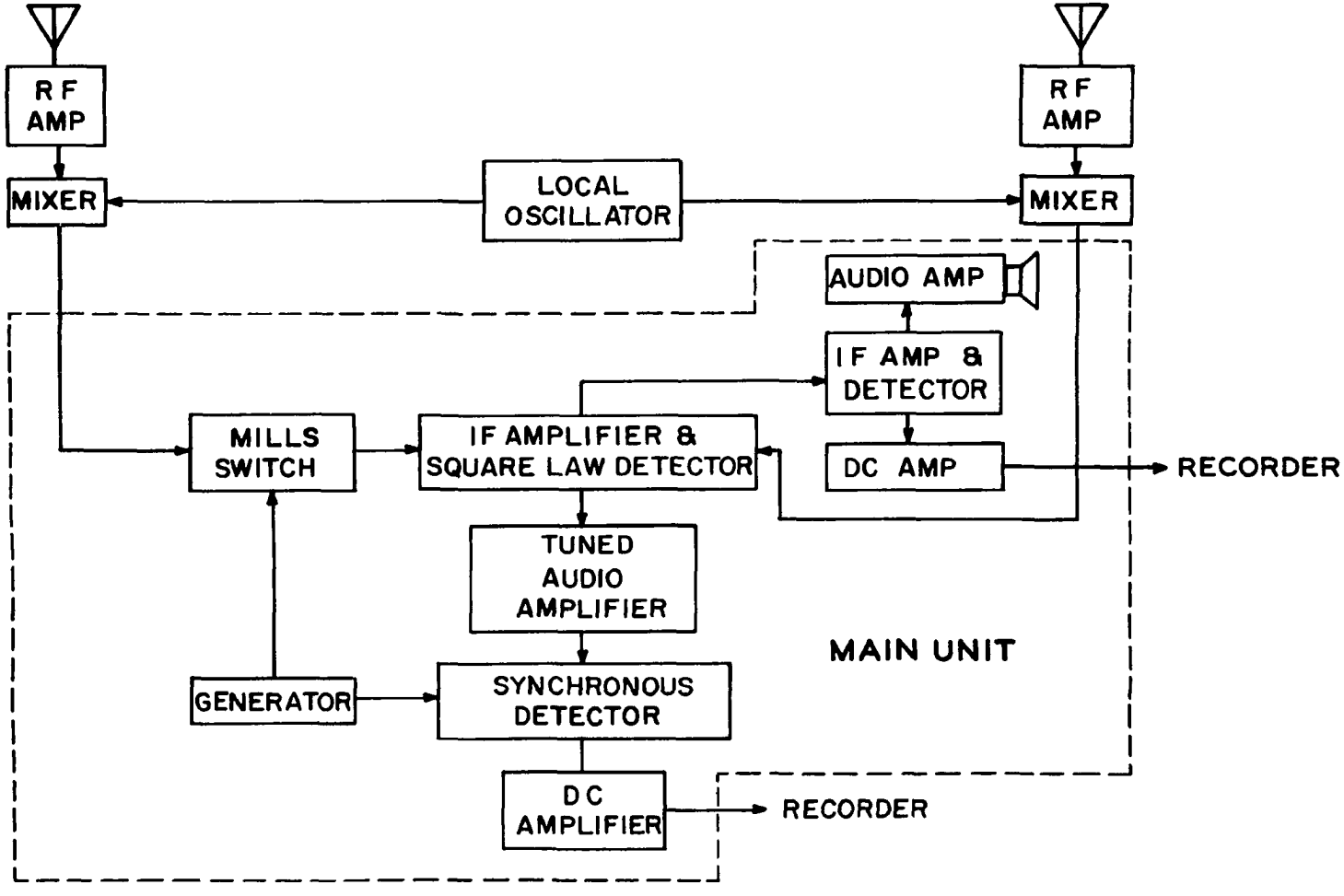

Fig. 15. Simplified block diagram of new phase-switch interferometers, built for 68 and 137 MHz observations.

due to imbalance in the switch circuit. Figure 16 is a photograph of the instrument section labeled "main unit" in the block diagram.

Now, in section IVA it was pointed out that for determination of the coherence ratio b and the wavefront autocorrelation R for a single frequency and antenna spacing, a combination of observations is required. One needs independent phase or amplitude information[1] in addition to the complex information available from a phase-switch interferometer. Independent phase and amplitude information are available from a phase-sweep interferometer, in a manner described in part by Little et al (1962). A phase-sweep interferometer also can supply the complex information available from a phase-switch interferometer, if a synchronous detector is used with the former, as is evident from the work of Hanbury Brown, Palmer and Thompson (1955)[2].

Phase-sweep interferometers had been used in the early 223 and 456 MHz scintillation observations at College. An attempt was made to reactivate one of them, but serious difficulties were encountered. As a result of the meeting of the American Astronomical Society held at the University of Alaska in the summer of 1963, it was learned that a much

---

[1] We shall see later that independent amplitude information is preferable to independent phase information.

[2] A means of obtaining independent amplitude and phase information from a modified phase-switch interferometer has been described by Penfield (1958). It is perhaps worth noting that alternate names for various types of interferometers exist. Further, several hybrid instruments have been developed. A certain degree of confusion seems to have arisen in the literature on this account.

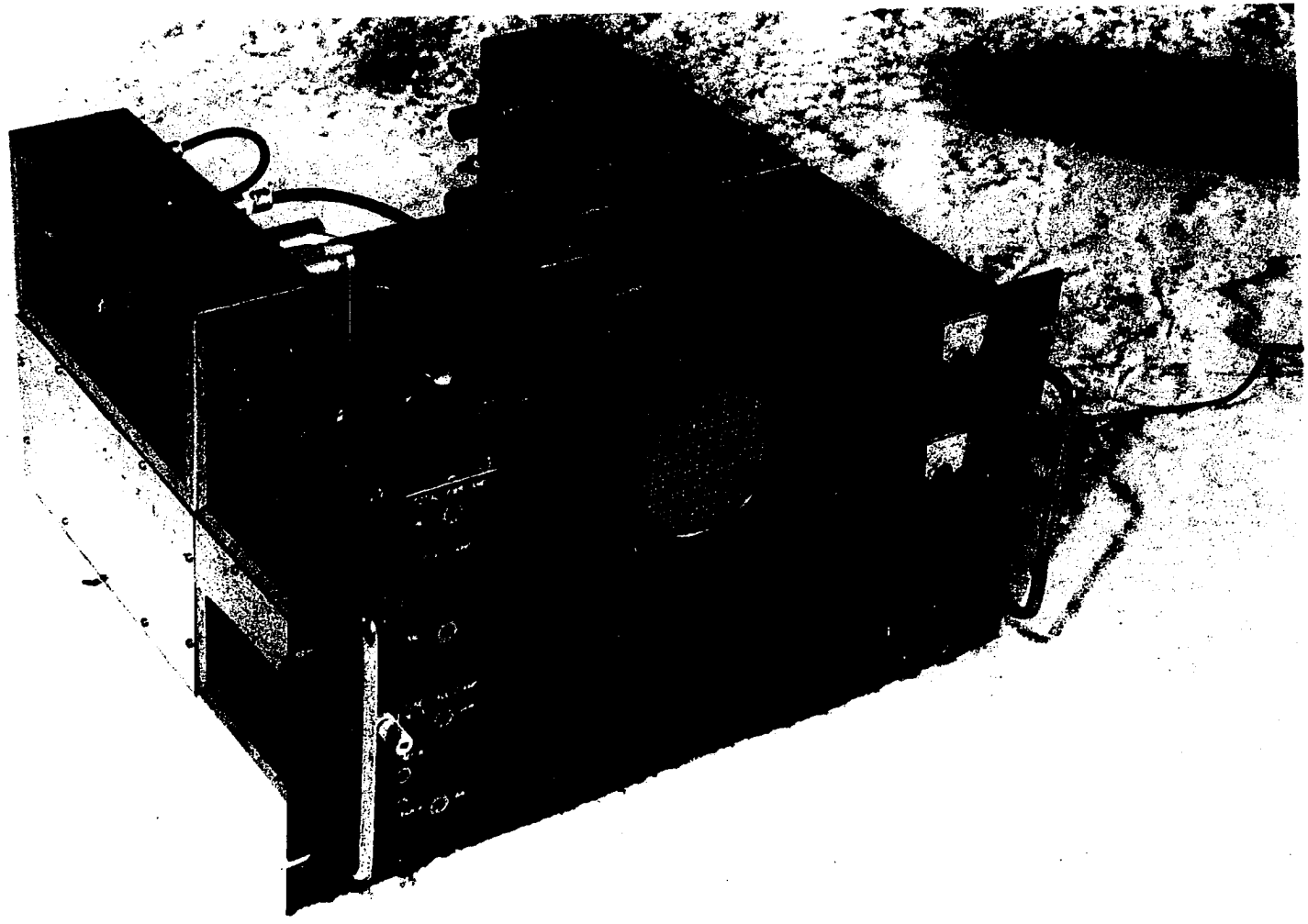

Fig. 16. Main unit of one of the two new phase-switch interferometers.

improved phase-sweep interferometer had been developed at Boeing Scientific Research Laboratories. It has been designed and built under the supervision of Mr. John Lansinger, who had previously had experience with the old College instruments.

As part of a joint IQSY study of auroral-zone scintillation by the Geophysical Institute and Boeing Scientific Research Laboratories, a BSRL phase-sweep interferometer was installed at the Ballaine Lake field site. The instrument was purchased from BSRL by the institute, which carried out the observations, data reduction being performed by the Boeing group. The interferometer features a phase-compensating circuit, which subtracts the phase difference predicted on the basis of source position from the observed phase difference. The output of the phase-recording channel thus records phase scintillation directly, without superposition of the sawtooth wave which otherwise would arise from source motion. For the duration of the joint observing program, BSRL supplied an analogue-to-digital converter for use with the phase-sweep interferometer.

The BSRL phase-sweep interferometer and phase compensator have been described by Lansinger and Gagnon (1961). Details will be omitted here. In the present experiment, the interferometer, phase compensator, and A/D converter were operated at 68 MHz on the 220-meter baseline.

In addition to the instruments described above, a fifth phase-switch interferometer was used for a small number of transit observations at 26.3 MHz. The antennas for this instrument consist of eleven full-wave dipoles with half-wave separation, giving a fixed east-west fan beam. They were placed on an east-west baseline of 215 meters (18.9

wavelengths), which was laid out just to the north of the 220-meter baseline used for 68 and 137 MHz observations. The antennas were supplied by Dr. W. C. Erickson of the University of Maryland and were installed at College for joint observations of two lunar occultations of the Crab Nebula (Gotwols, Erickson, Fremouw and Owren, 1966), which took place in the summer of 1964. For the present experiment, the antennas were used in conjunction with a phase-switch interferometer made up of a communications receiver and essential circuits from the design shown in Appendix 2. Later, an improved version of the entire interferometer shown in the appendix was built for other 26 MHz observations.

A schematic layout of all interferometers used in the present experiment is given in figure 17. The outputs labeled "complex" refer to the mixture of phase and amplitude information obtained from the phase-switch interferometers and from the coherently detected output of the phase-sweep interferometer. The independent phase and amplitude outputs from the phase-sweep interferometer are so labeled. In addition to the outputs shown, total power was recorded from phase-switch receivers 1 through 4 for interference monitoring and trouble-shooting. The total-power records were not used in analysis. All the interferometers, per se, were operated at the intermediate frequency of 30 MHz except that used for the 26 MHz observations.

All the instrument outputs shown in figure 17 were recorded on Esterline-Angus recorders at a chart speed of 12 inches per hour after integration through output time-constants of approximately one second. For the most part, these records were not used in the present experiment but in associated research on scintillations. Concerning the visibility-

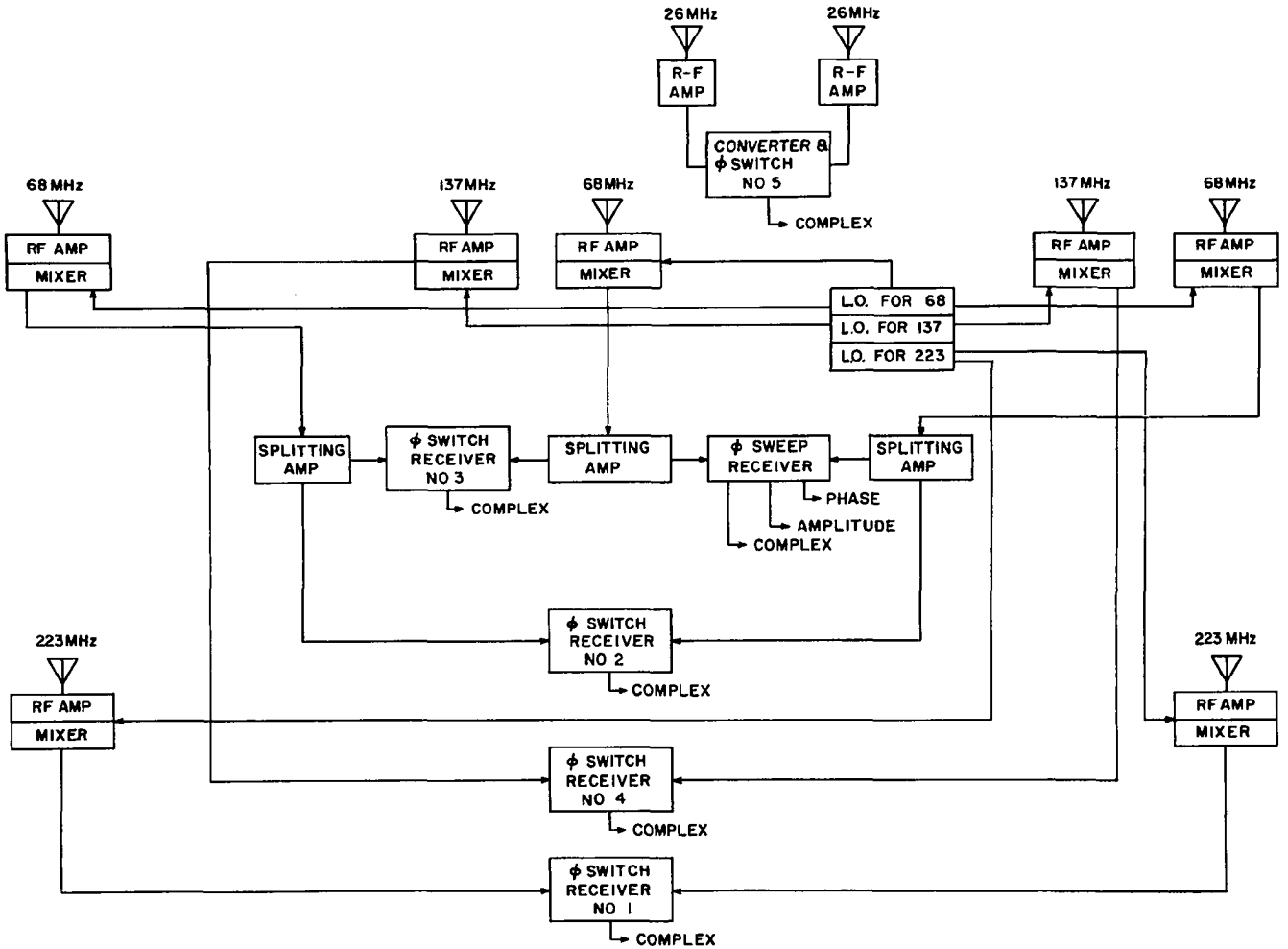

Fig. 17. Schematic layout of all interferometers employed.

fade experiment, they were used only as event indicators. The prime fade data were collected by other means.

As pointed out in section IIIA, the quantity desired from the complex-information channels during visibility fades is essentially the correlation of antenna voltages. Since correlation is by definition an average quantity, the measurements required averaging over periods of many individual scintillations, as is obvious from the development of Chapter II. The scintillations which accompany visibility fades have periods on the order of a few seconds. In order to obtain complex-channel records convenient for scaling of fade parameters, therefore, separate recordings were made after passing the signal through an additional time constant on the order of one minute. An exception was the 223 MHz channel, whose time constant was set at eleven seconds because of the relatively fast fringe rate of the basic interference pattern. Because it was desired to scale all complex channels together a multi-channel recorder was required. The need was filled by a 6-channel Sanborn, run at the rate of 0.25 mm/sec.

In contrast to the complex channels, a high information rate was required from the independent phase and amplitude channels. We shall see that the parameter of interest here is the fluctuation of the amplitude-recording channel. The only feasible means of reducing the amplitude information at the required rate was an automatic one. For this purpose, the A/D converter supplied by Boeing was used. The overall data recording setup used in the visibility-fade experiment and in the associated scintillation observations is shown schematically in figure 18. During the auroral observing season, an additional 6-channel

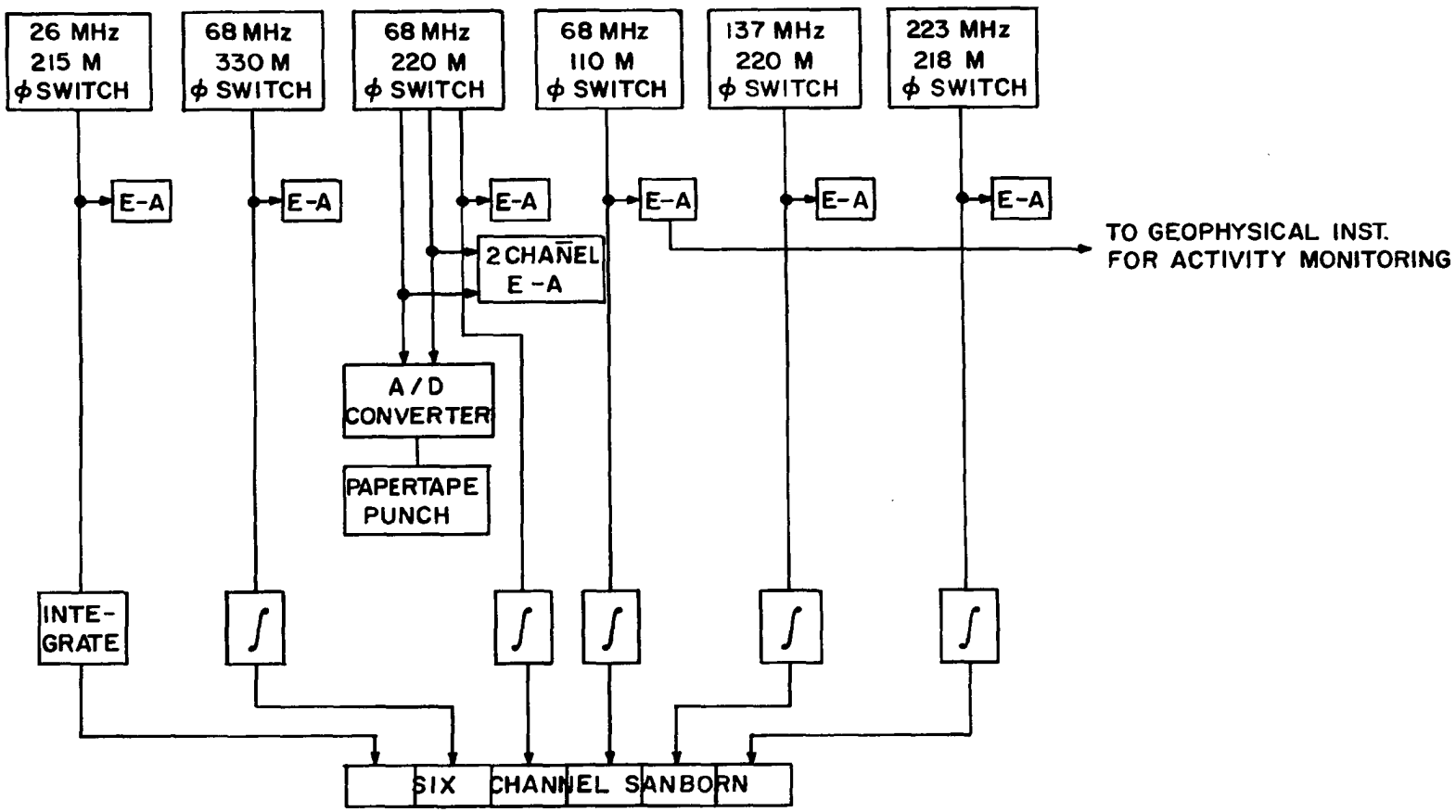

Fig. 18. Recording arrangement.

Sanborn was used to record line-of-sight auroral luminosity in two colors and four selected interferometer channels without smoothing.

IVC DATA REDUCTION AND SCALING

The first step in data reduction after almost any kind of observation, of course, is event identification. In the present case, the events are visibility fades of the radio source Cassiopeia A. For identification purposes, the records obtained from the 68 MHz, 330-meter spacing, phase-switch interferometer were used, this being the most consistently fade-sensitive channel. Since previously observed fades (Little et al, 1962; Moorcroft, 1962; Fremouw, 1963) had been obtained from instruments with output time-constants of one or a few seconds, identification in the present experiment was made from a similar record initially.[1] Figure 19 shows five such records. The top strip was obtained under quiet ionospheric conditions. The center strips were obtained under scintillation conditions. The bottom strips show two visibility fades, the left one short and uncomplicated, the right one longer and more involved. Minute ticks appear at the top of each strip, the time prints referring to 150° WMT in 12-hour notation.

Now, the scaled quantity desired from the complex-channel records is the visibility r during fades. In section D3b of Chapter II, r was defined as the ratio of the interference-pattern amplitude during a fade to that during an undisturbed period. Scaling for determination

---

[1] After some experience had been gained with the longer time-constant records, it was found that they could be used directly for identification purposes as well as for scaling.

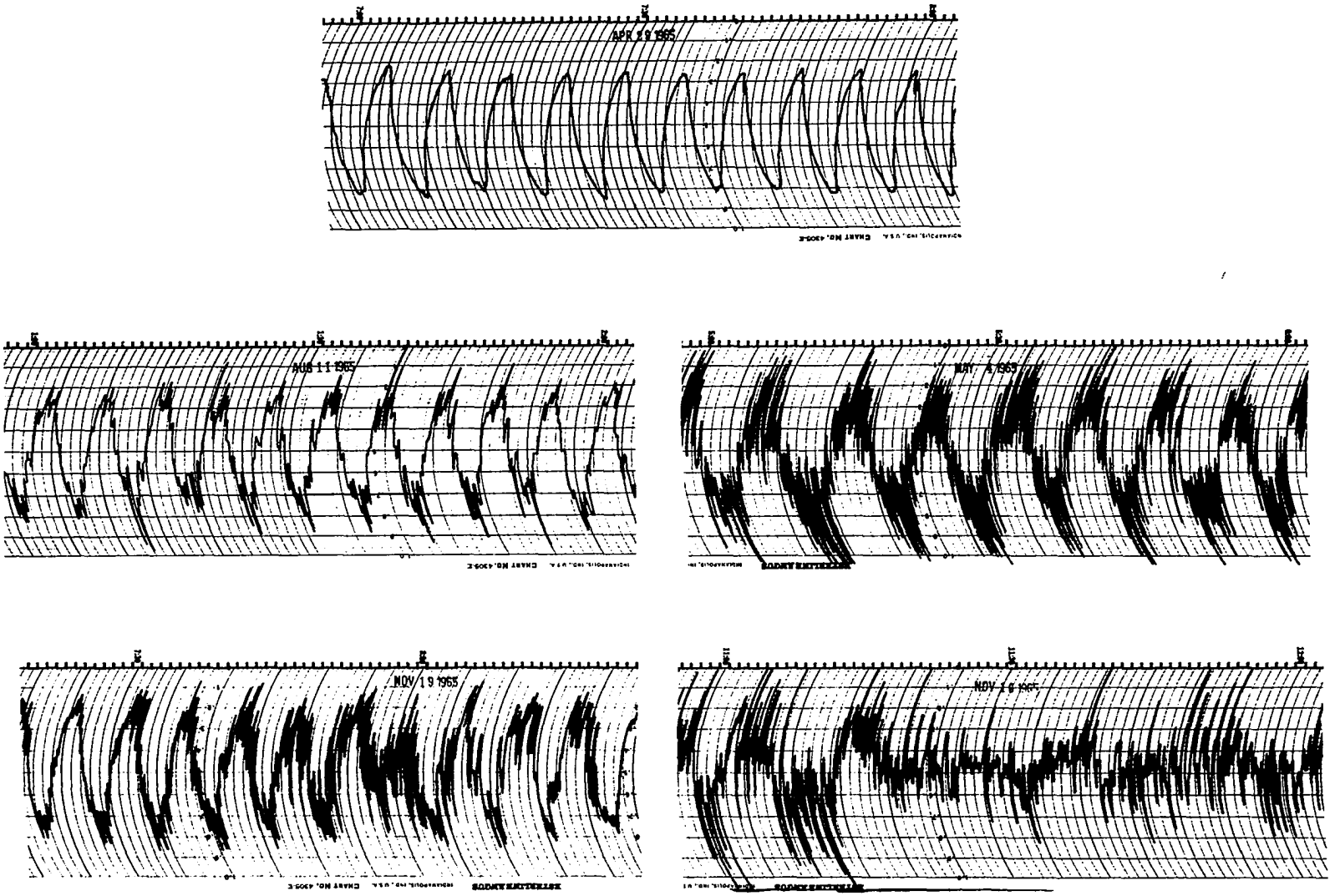

Fig. 19. 68 MHz, 330-meter phase-switch interferometer records. Top, quiet ionosphere; center, two levels of scintillation; bottom, two visibility fades.

of r was carried out from smoothed versions of records such as those at the bottom of figure 19. Figures 20 through 24 show the smoothed records obtained during the observing periods in figure 19, with corresponding dates marked. The 68 MHz, 330-meter record appears in the second channel from the top in each figure. The lower channels are respectively the 68 MHz, 220-meter record; the 68 MHz, 110-meter record; the 137 MHz, 220-meter record; and the 223 MHz, 218-meter record. The top channel is the 26 MHz, 115-meter record. Observations at 26 MHz were of low priority in the experiment and were carried out near either upper or lower transit of Cas A during part of the year only. Hence, a signal is present on channel one only in figures 20 and 21. Minute ticks appear at the bottom of each six-channel record strip, with 150° WMT hours marked in 24-hour notation.

As is evident in figure 19, the normal complex-channel records are comprised of the quasi-sinusoidal interference pattern characteristic of radio interferometers. The period of each pattern varies somewhat during the day due to the inherent observing geometry. The amplitude, however, is constant except for small instrumental effects, such as ground reflections, which are easily compensated for in scaling. Variations in the amplitude and phase of the pattern represent amplitude and phase scintillations of the source being observed. Net decreases in the amplitude over periods long compared with individual scintillations constitute the visibility fades with which we are concerned.

An example of a well developed visibility fade is shown in figures 25 and 26. Figure 25 shows the five unsmoothed complex-channel records, with the frequency and baseline marked beneath each record.

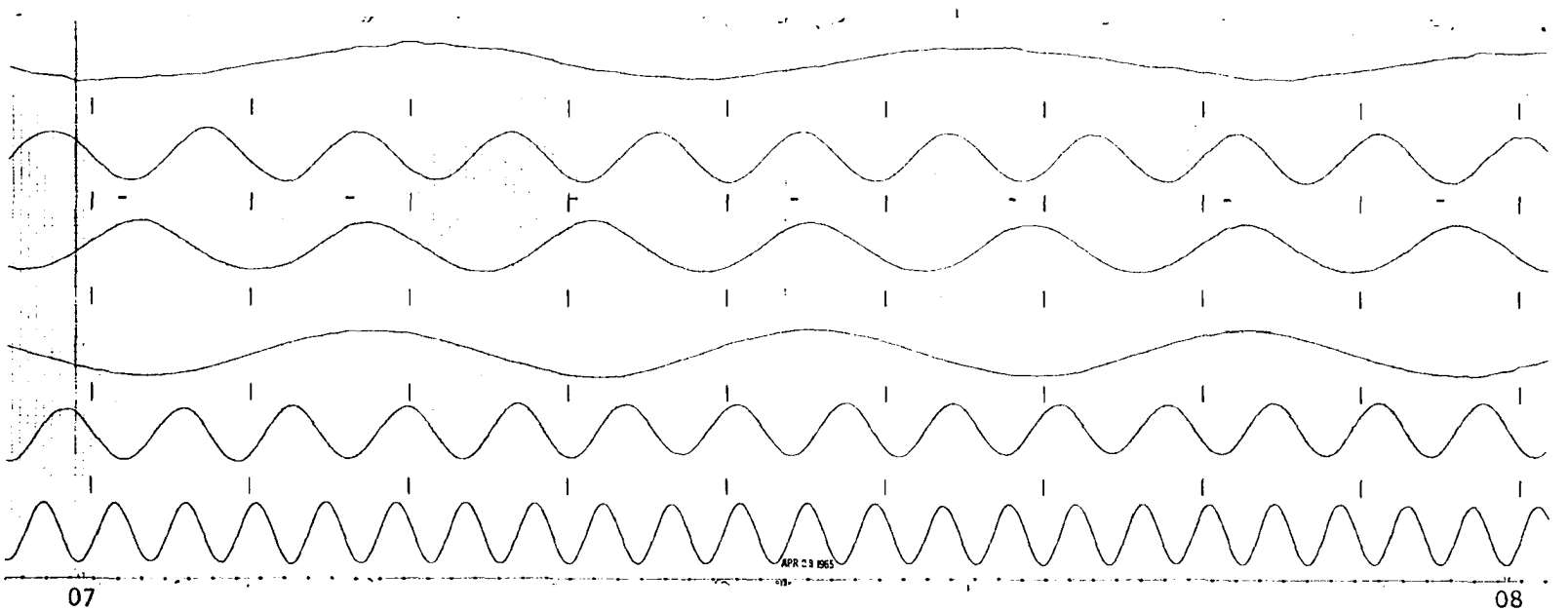

Fig. 20. Smoothed complex-channel interferometer records for quiet period of figure 19. Top to bottom: 26 MHz, 215 meters; 68 MHz, 330 meters; 68 MHz, 220 meters; 68 MHz, 110 meters; 137 MHz, 220 meters; 223 MHz, 218 meters.

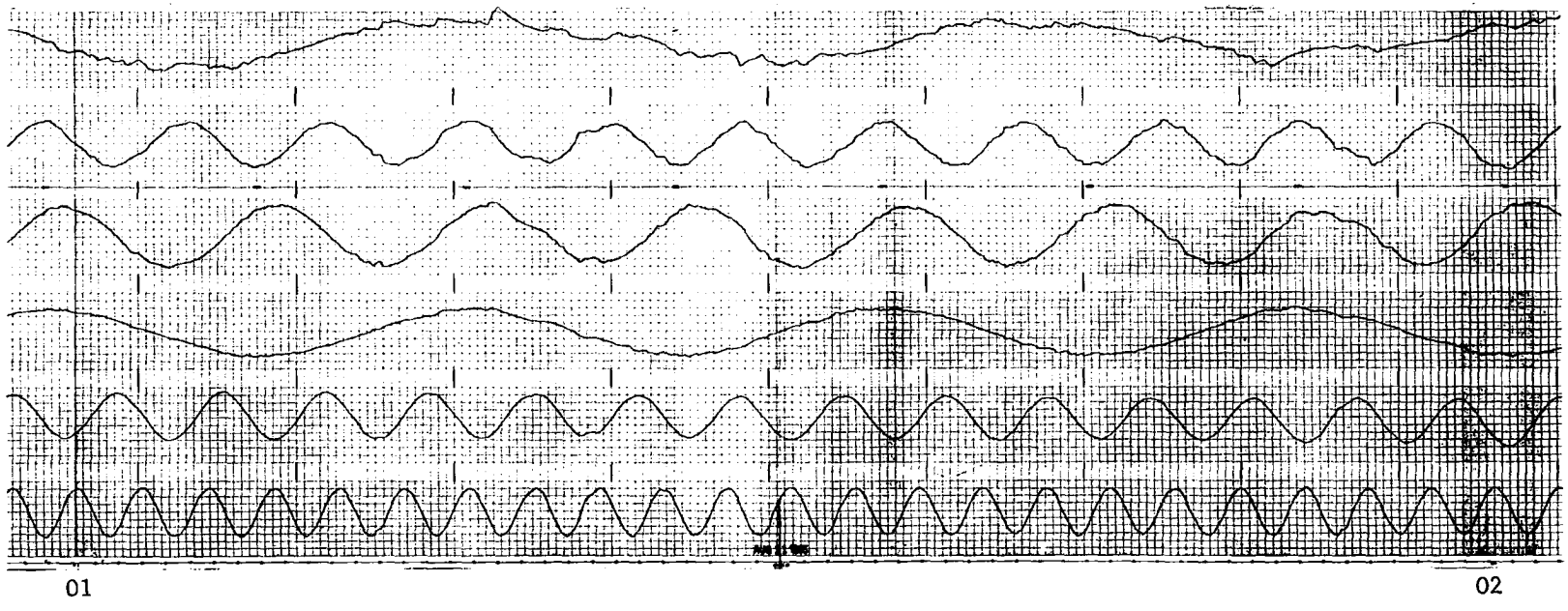

Fig. 21. Smoothed interferometer records for left scintillation period of figure 19.

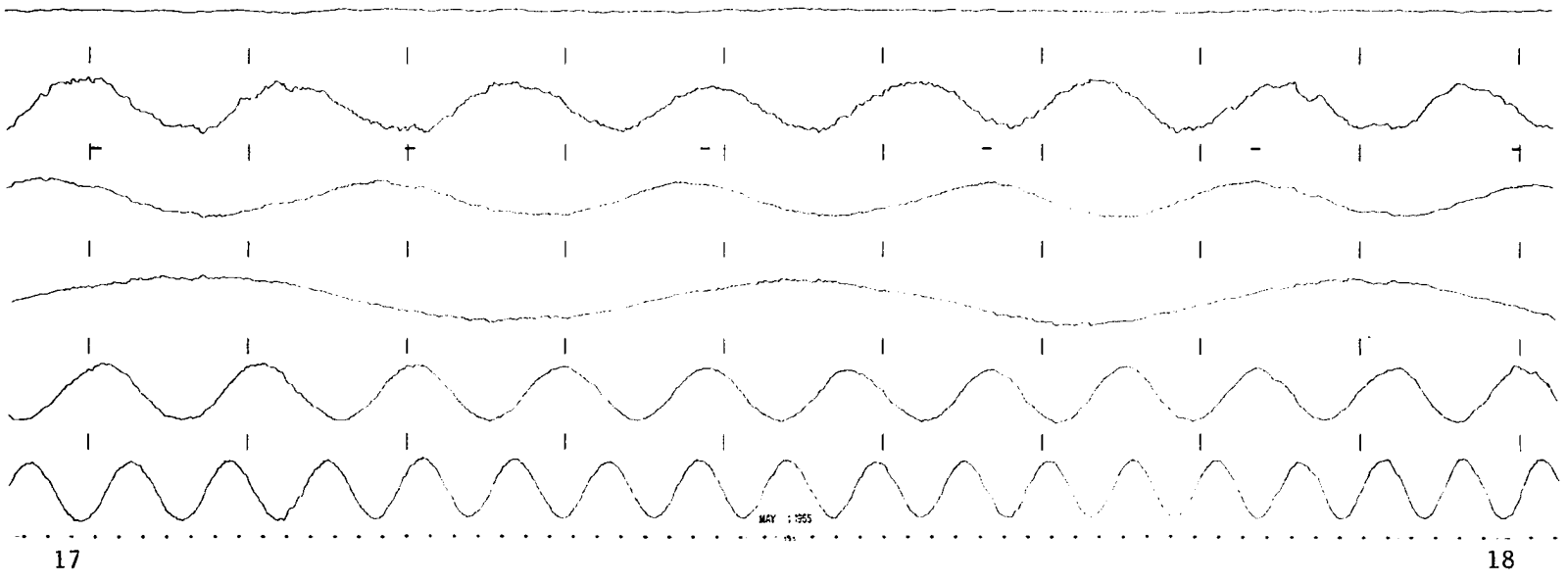

Fig. 22. Smoothed interferometer records for right scintillation period of figure 19.

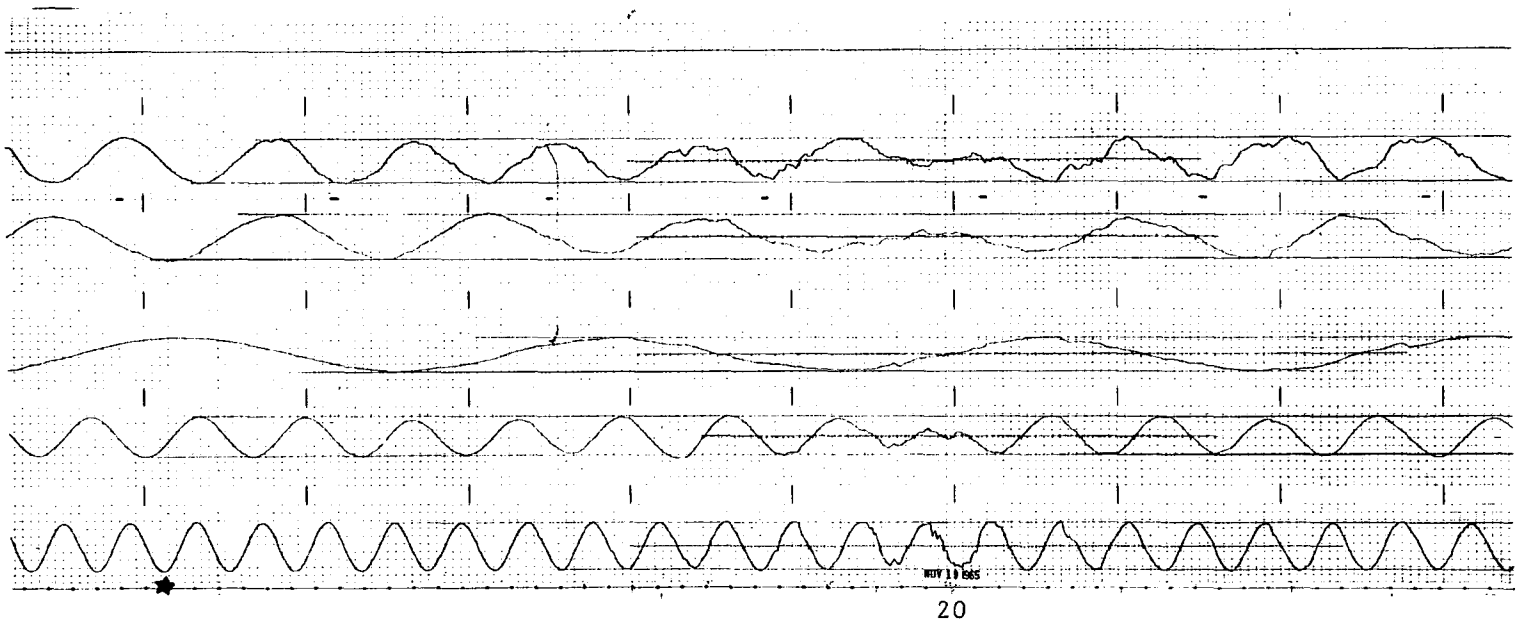

Fig. 23. Smoothed interferometer records for left visibility fade of figure 19.

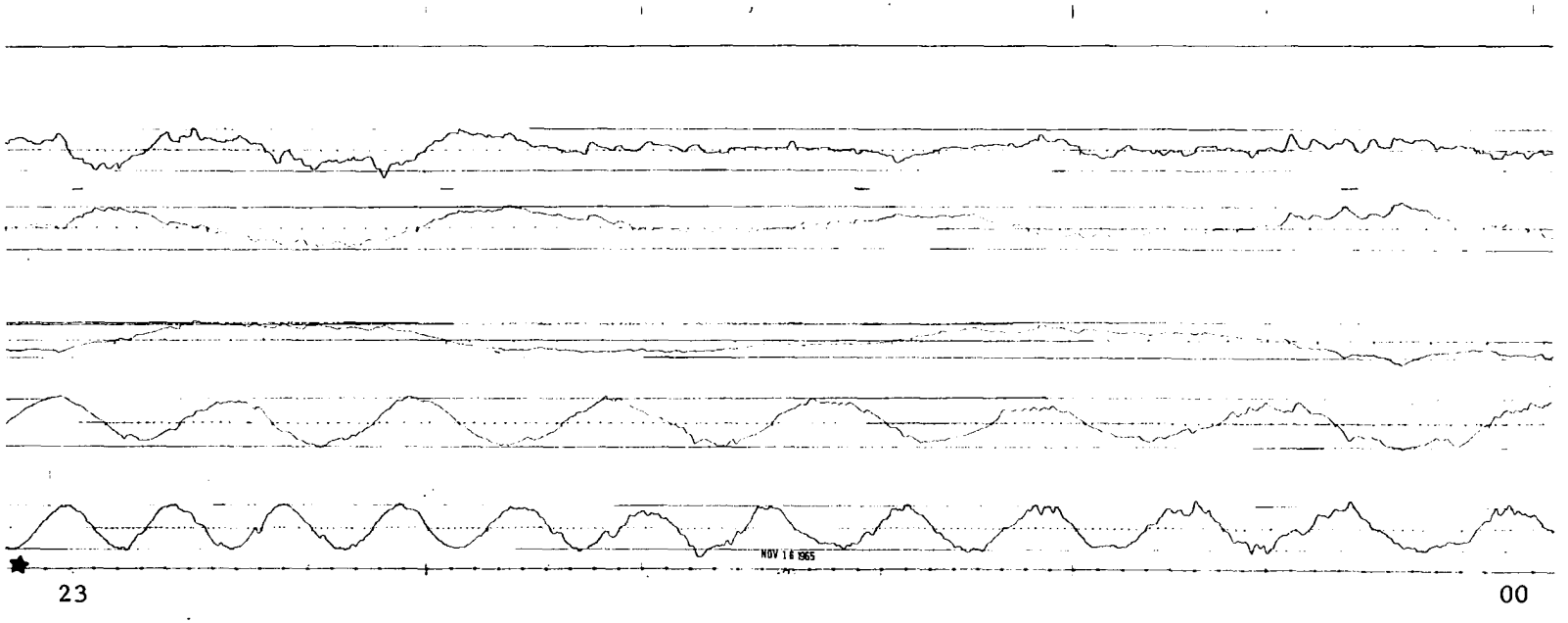

Fig. 24. Smoothed interferometer records for right visibility fade of figure 19.

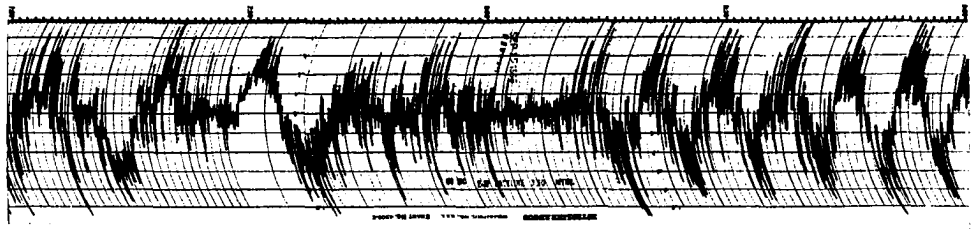

68 MHz 330 Meters

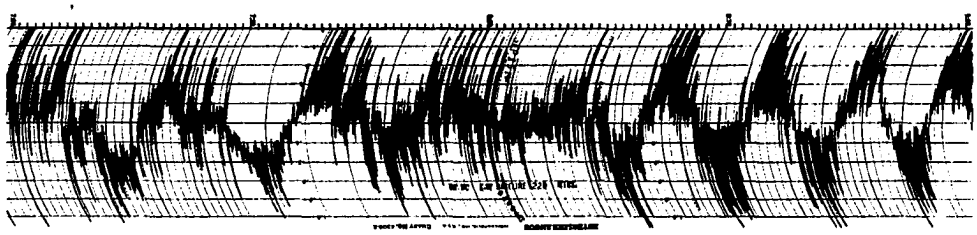

68 MHz 220 Meters

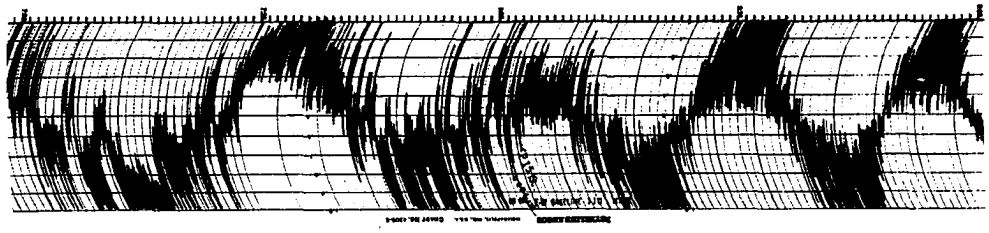

68 MHz 110 Meters

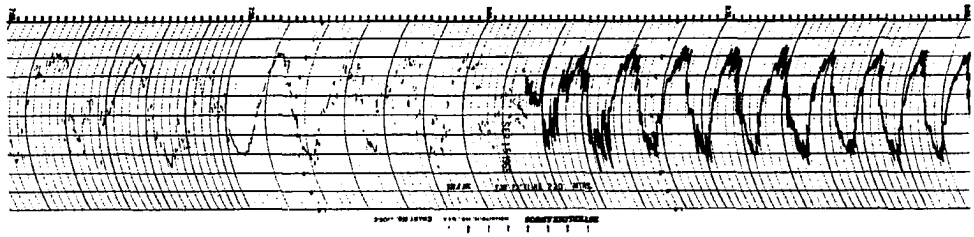

137 MHz 220 Meters

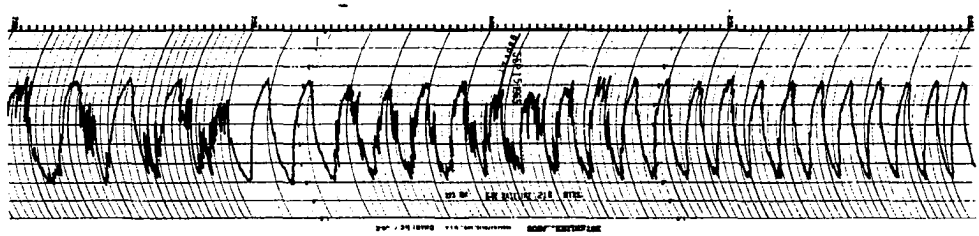

223 MHz 218 Meters

Fig. 25. Interferometer records of a well developed visibility fade.

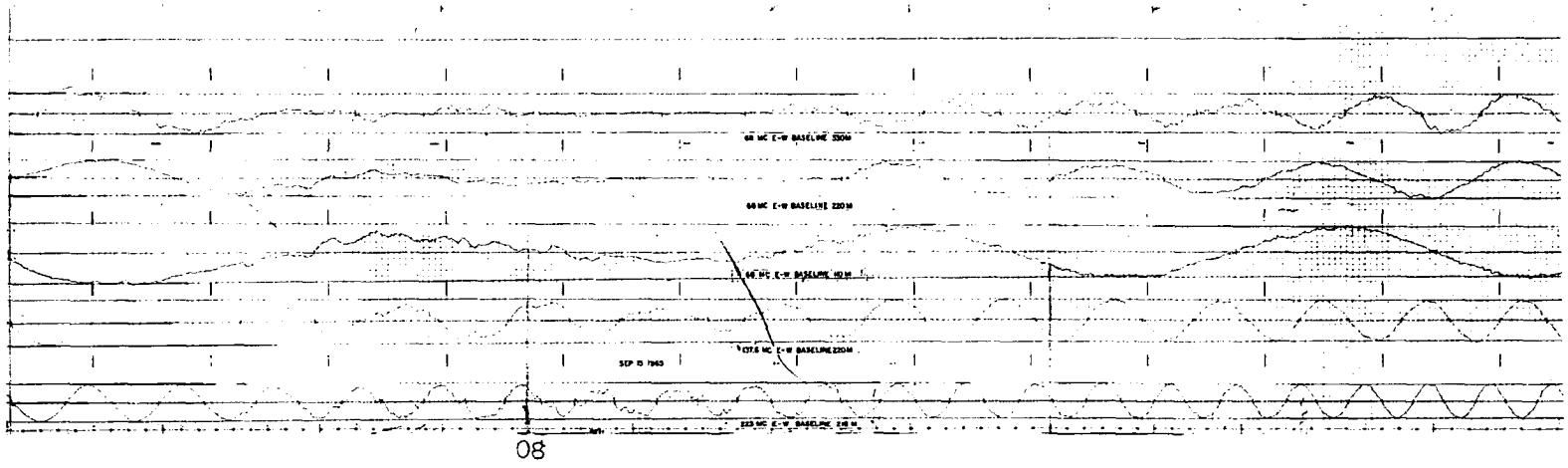

Fig. 26. Smoothed interferometer records for the visibility fade of figure 25.

(Unfortunately, the 137 MHz pen was clogged until it was discovered and cleared near the middle of the event. This was of no consequence in analysis of the fade since only the smoothed records were used for this purpose.) The smoothed records for the event are shown in figure 26. A more typical visibility fade is shown in figures 27 and 28.

Except for two short periods each day (near "elongation" of the interference pattern, when the source has little east-west apparent motion), each fringe of the undisturbed pattern very closely approximates a cycle of a constant-frequency sinusoid. If the ordinate value of the pattern is averaged between two center-line crossovers, therefore, the result is $2/\pi$ times the pattern amplitude. Accordingly, during a visibility fade, the average amplitude over a pattern half-period can be obtained by determining the average ordinate value of the pattern and multiplying by $\pi/2$. The visibility is given by the ratio of the result to the undisturbed amplitude.

In scaling the smoothed complex-channel records, the first job was to establish the undisturbed amplitude for each channel. The procedure was simple owing to the fact that the radio star under observation provided essentially a continuous calibration source during undisturbed periods. Thus continuous observations of Cas A and Cyg A over several weeks showed that short-term gain stability of the receivers was acceptable.

Slow variations in output pattern amplitude arose from a number of sources. First, tube aging and other effects caused drifts over periods of many days or weeks. Second, residual white-noise blurring

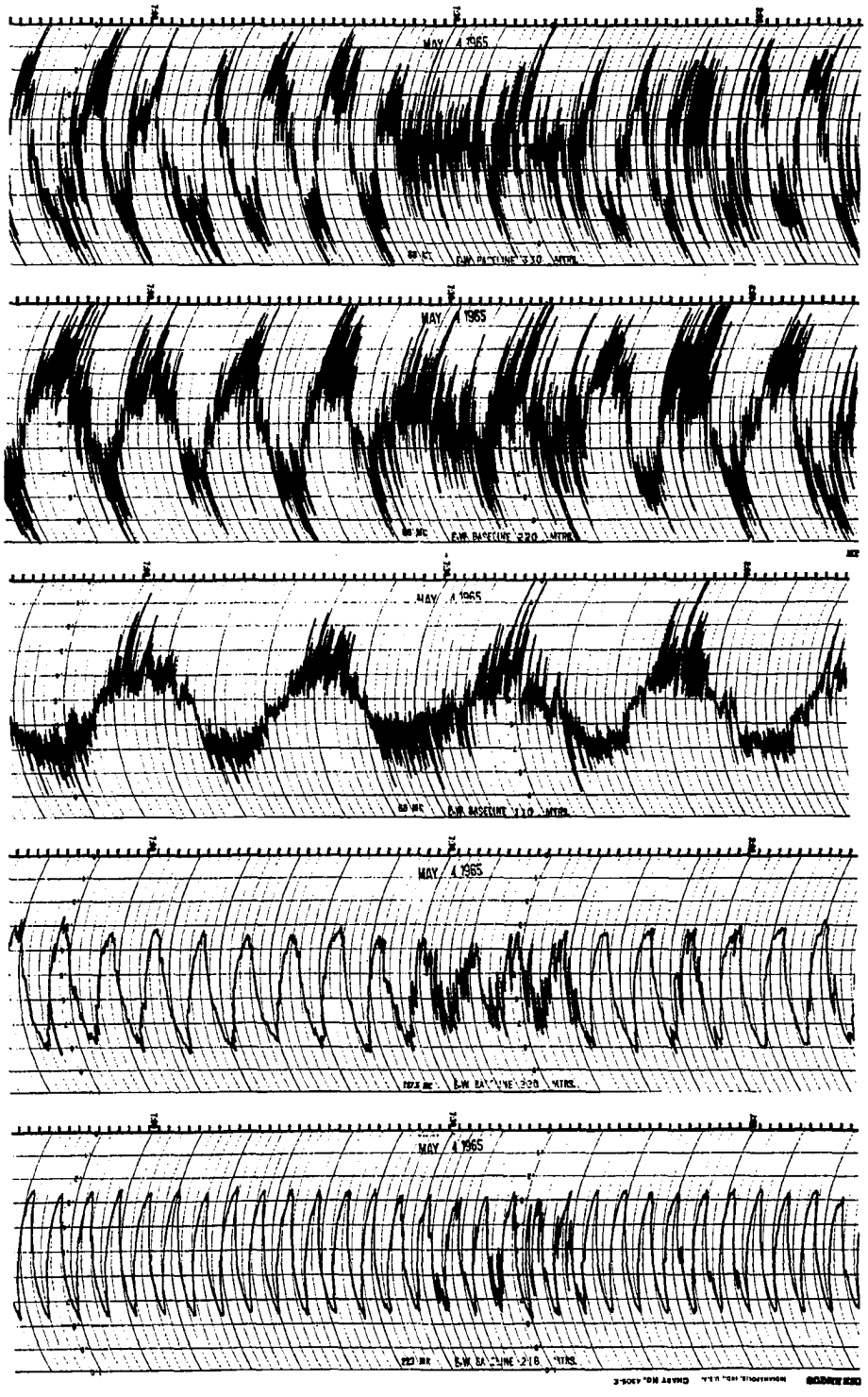

Fig. 27. Interferometer records of a typical visibility fade.

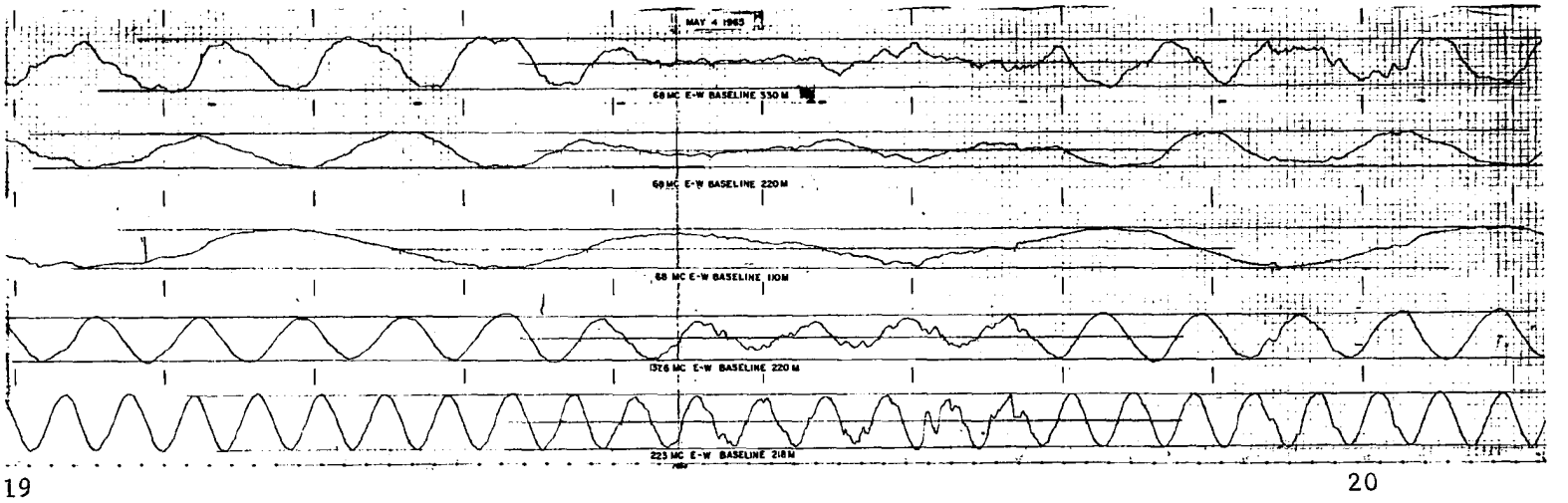

Fig. 28. Smoothed interferometer records for the visibility fade of figure 27.

caused daily amplitude variations of a few percent on the wider-baseline channels. Third, daily variations resulted also from ground reflections. The magnitude and phase of this last variation changed with local ground conditions - snow cover and to some extent moisture content of the ground in summer. Other effects were noted from time to time due to occasional antenna snow loading and possibly due to extreme temperature changes.

All of the above-mentioned effects were essentially negated by noting the output pattern amplitudes just before and just after each visibility fade which was scaled. In most cases, the undisturbed amplitude was the same before and after the event. In the case of some long fades, there was a detectable difference. In these cases, the undisturbed amplitude was assumed to change linearly during the event. In all cases, straight lines were drawn on the records connecting the pre-fade pattern peaks and nulls to the post-fade peaks and nulls. From these lines, the pattern center line during the event was established. Such maximum, minimum and center lines appear in figures 23, 24, 26, and 28.

In establishing the pre-fade and post-fade amplitude lines, several pattern fringes were inspected and their amplitudes averaged. This was necessary because of slow scintillations not smoothed out by the time-constant circuit. Scintillations long compared with the fringe rate represent a major source of uncertainty in the measurements, as we shall see later. Such scintillations are present to some extent much of the time at 68 MHz.

Once the undisturbed amplitudes for a given fade were established, the next step in scaling was to ascertain precisely the intervals over which the depressed amplitude was to be averaged. That is, the pattern crossover points had to be located during the event. In most cases, this step presented little or no difficulty. Still,in a great many instances, the crossovers did not occur in time where they would have under undisturbed conditions. Deviations in crossover times can arise from instrumental phase instability. However, in the present case, this was a negligible effect.

The crossover deviations observed during fades could be caused by either of two related ionospheric effects and, in fact, in most cases probably were caused by a combination of the two. First, large-scale refraction produces phase scintillations which are slow compared with the scintillation characteristic of visibility fades or in some cases compared even with the fringe rates. Second, during the approximately one-minute smoothing period introduced in the observations, only a finite number of fast scintillations occurs. Hence, there will be some statistical fluctuation in the smoothed record. Both effects are represented by scintillation components too long to be removed by the smoothing circuit. There is little hope of differentiating between the two effects or even of finding satisfactory definitions by which to classify them in all instances.

Phase scintillations slow compared with the electrical time constant but fast compared with the fringe rate usually represented a relatively minor source of uncertainty in the scaling of a given half-fringe. More troublesome were phase scintillations comparable to the undisturbed

half-fringes in period. A single scintillation can carry a disproportionate weight in the scaling of a particular half-fringe. Careful inspection of a large number of such instances led to the conclusion that the best scaling accuracy usually can be obtained by using actual crossovers rather than predicted crossovers in demarking scaling periods. In some instances, however, the scaling inaccuracy is aggravated by this choice.

Since a large number of visibility fades were to be scaled, it was necessary to decide upon a standard scaling procedure. As regards crossovers, it was decided to use the observed rather than the predicted times. This was the simpler choice from the point of view of scaling convenience and therefore the better from the point of view of efficiency. As mentioned above, it also appeared to produce the better accuracy in a majority of instances, although not always, as we shall see. In the final analysis, the only reliable means of suppressing the effect of slow scintillations (both phase and amplitude[1]) is to average the results of two or more half-fringes.

During deep fades, an additional problem arising from slow phase scintillations was encountered. In these cases, if appreciable scintillations longer than about a minute were present, more than the expected number of record crossovers sometimes occurred. In these instances, the crossovers of appropriate direction nearest the expected

---

[1]The amplitude effects of ionospheric focusing and defocusing will be discussed in section D3.

times were chosen to demark the limits of the scaling periods. In all cases, the deviation of the record trace from the center line was treated as a positive quantity in post-scaling computation. This means that if negative values of visibility occurred over short periods, the visibility for the half-fringe in question was overestimated. However, the procedure also discriminates against the effect of large, slow phase scintillations due to refractive effects. If was thought preferable to underestimate the effect for which we are looking rather than to allow extraneous effects a free rein which would result in overestimation.

Once the scaling periods were established, they were divided into ten equal segments and the ordinate value of the record in the center of each segment scaled. This procedure results in about a five percent overestimation of the visibility of a sinusoidal pattern. For an irregular pattern, short-term overestimations and underestimations tend to average out during a given scaling period. All record channels were scaled in identical fashion so that a large number of events could be handled. By dividing the scaling periods into ten parts, at least one scaling point was obtained for each independent point on each record. Exceptions occurred in a few events, observed near elongation, in which the scaling period for some channels exceeded ten times the instrumental output time constant.

Establishing of the undisturbed amplitudes and center lines of the five records scaled for most events, together with location of record crossovers and ten-fold division of scaling periods, represented the sum total of hand preparation for scaling of the complex-information records. Actual scaling then was done by semi-automatic means using the "Oscar F"

scaling machine. This machine performs analogue-to-digital conversion and data-card punching. The procedure involves simple positioning of crosshairs by an operator. In the present case, the prime data obtained were the ordinates of the record traces at the previously established ten points in time within each scaling period.

Besides the ten record values scaled within each period, several bits of auxiliary information were required. First, of course, the undisturbed amplitude was needed. This was obtained by scaling the ordinate of the maximum or minimum line, as the case may be for a particular scaling period. For each period, the ordinate at the beginning crossover time and that at the end crossover time were scaled. These ordinates were averaged in subsequent computations to allow for the possibility of slow changes in undisturbed amplitude.

For each fade, an identification card was punched containing the number of the event, the source under observation, the date, and a reference starting time.[1] Following this, a card containing the scaled information for each period within the fade was punched. Setting of the Oscar hairlines automatically punched out the ten scaled values, the undisturbed level, the ordinate of the center line, and appropriate abscissas referenced to the start time on the event identification card. The channel number was recorded by means of a punch keyboard on the Oscar, and other auxiliary information was inserted from a simple memory device internal to the Oscar. The information layout of the

---

[1] Due to the limited physical length of the Oscar scaling surface, a separate identification card was punched for each 27-minute segment of long fades.

identification and scaling cards is shown in figure 29.

From the scaled data described above were computed the visibility r for each interference pattern half-fringe of each of the five complex-information channels. The computation was straight-forward. Using the ordinate of the center line as a zero reference, the average of the ten scaled data values and the average of the two undisturbed amplitude scalings were calculated. The visibility then was obtained simply by multiplying the ratio of the two averages by $\pi/2$, as explained on page 174.

Due to the different fringe rates of the five complex-information interferometers, the periods over which the individual visibilities were computed were different. Since it was desired to compare results from the five channels, it was necessary to reduce them to common averaging intervals. Since the 68 MHz, 110-meter spacing, phase-switch instrument had the longest fringe period, it was used as the standard channel. The visibilities computed for the other channels then were averaged over the scaling periods of the standard channel.

The computer programs for initial visibility computation (pass 1) and for reduction to the standard averaging intervals (pass 2) are given in Appendix 3a. The programs provided both numerical and graphical outputs. Figures 30 and 31 are examples of the graphical outputs, corresponding respectively to the events of figures 25-26 and 27-28. The plots give visibility as a function of time for five complex-information channels. Channels one through three give the 68 MHz visibility for antenna spacings of 330, 220, and 110 meters, respectively. Channels four and five give the 137 and 223 MHz

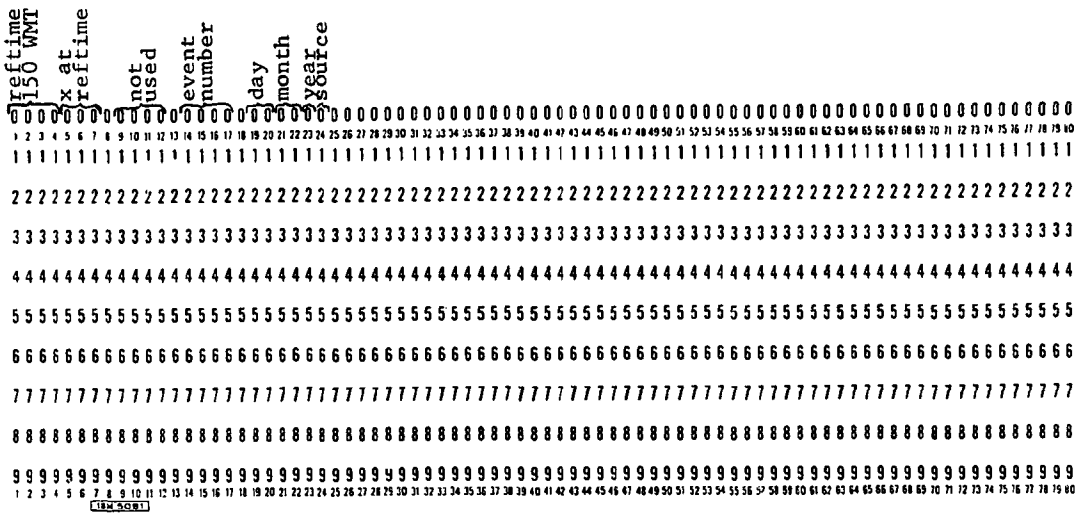

Identification Card

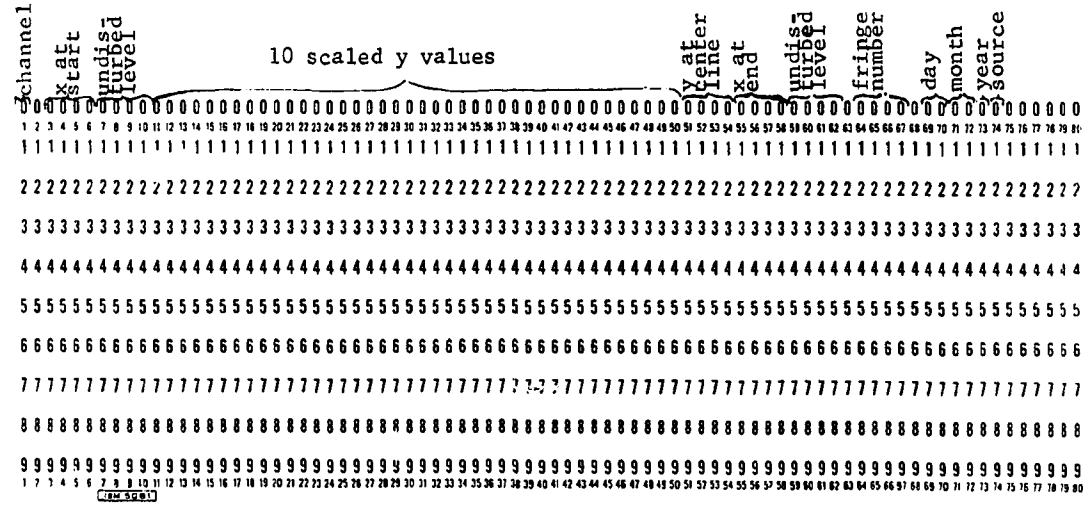

Scaling Card

Fig. 29. Information layout on data cards obtained from semi-automatic scaling of complex-channel interferometer records.

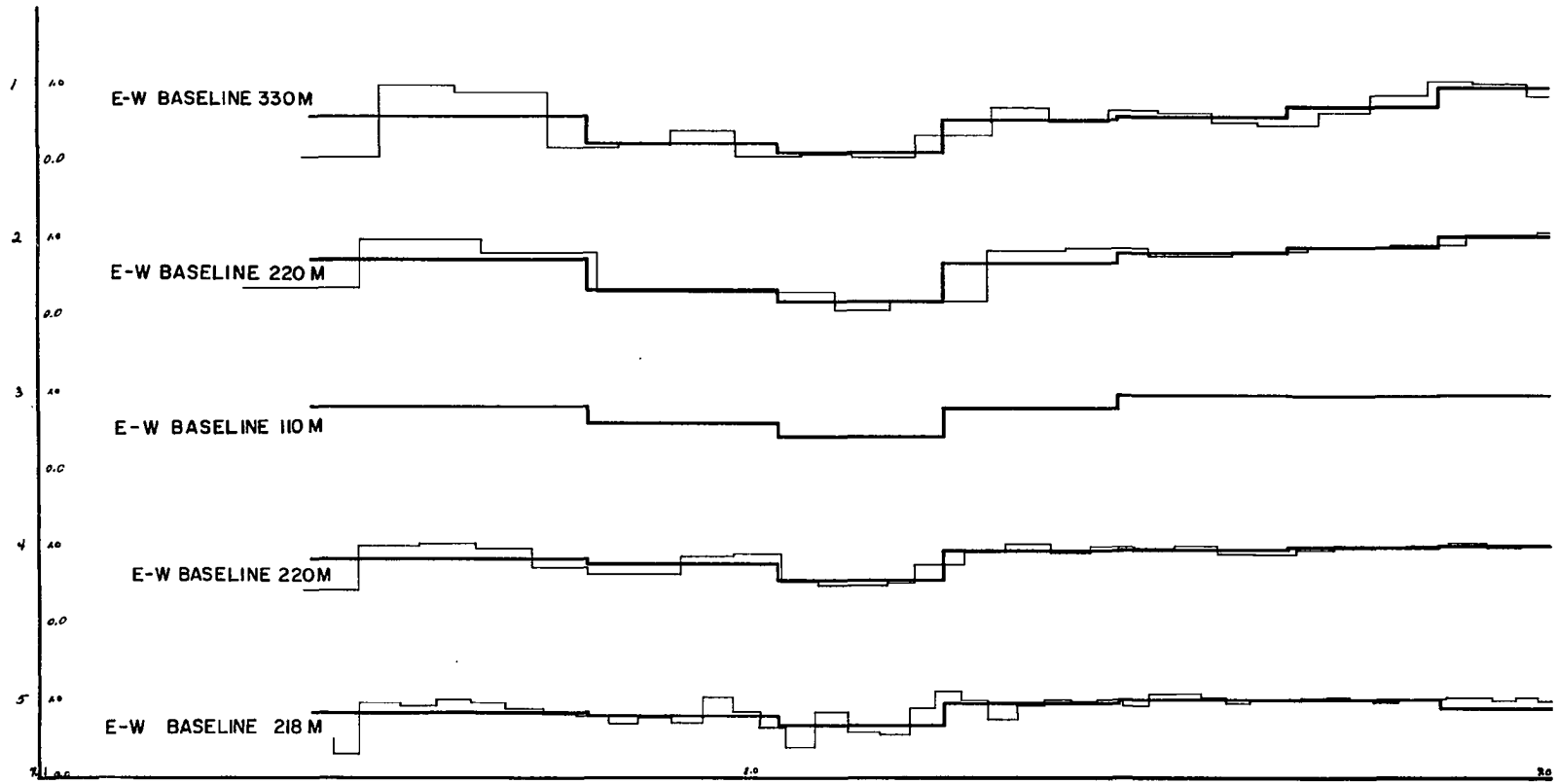

Fig. 30. Graphical computer outputs showing the variation in visibility as observed by five interferometers during the fade of figure 25.

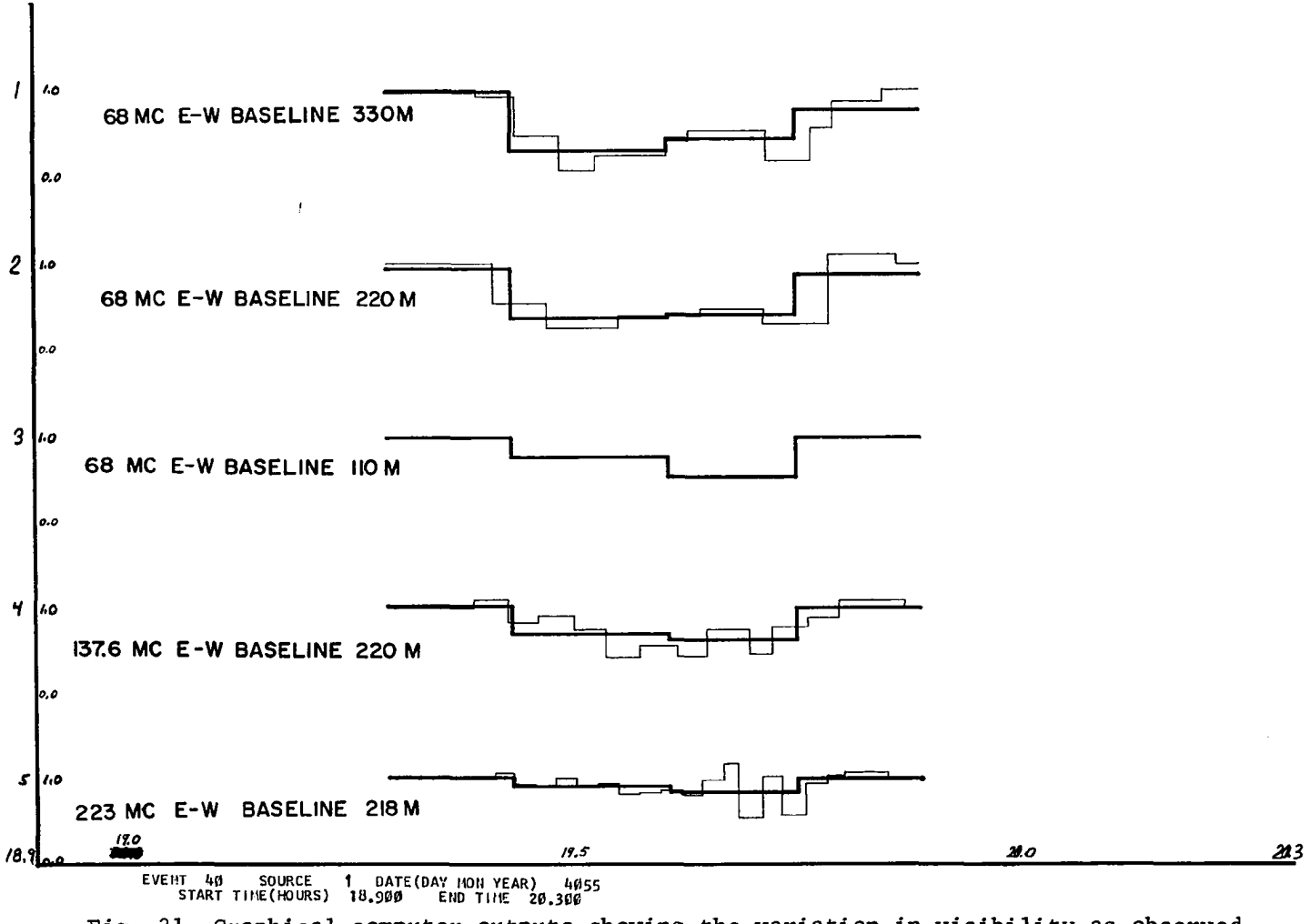

Fig. 31. Graphical computer outputs showing the variation in visibility as observed by five interferometers during the fade of figure 27.

visibility, respectively. The fine lines in all channels but number three represent the visibility obtained for each half-fringe of the respective records. The heavy lines in all channels represent the visibility averaged over the standard intervals corresponding to the 68 MHz, 110-meter, half-fringe periods. Time is reckoned in hours and decimals of 150° WMT, using 24-hour notation.

Most of the plots show systematic departures of the pass 1 outputs as compared with the pass 2 outputs. Thus it is possible to obtain better time resolution in visibility development than that present in the pass 2 outputs. However, there are also random departures between the two outputs, as is most evident in channel five of figure 31. The random fluctuations tend to be averaged out of the pass 2 outputs.

The apparent 223 MHz signal enhancement at about 19.67 hours in figure 31 resulted in part from a refractive phase effect which distorted the shape of the 223 MHz fringe in question. Despite the steps which were taken to suppress such effects by "riding with them" in selection of crossover times, they were sometimes noticeable in the pass 1 outputs, especially in cases where the fringe period was short. The only means of negating such effects is averaging over a number of fringes, accepting the consequent loss of ability to detect true changes in visibility over shorter periods.

Unlike the phase-switch and coherently detected phase-sweep interferometer records discussed above, the pure-phase and pure-amplitude outputs of the phase-sweep interferometer are straight lines under undisturbed conditions. Deviations from straight lines are directly

attributable to scintillations. We shall see in section D1 that the quantity desired therefrom for analysis of visibility fades is the mean square fractional fluctuation in the amplitude output. This quantity was computed by Boeing Scientific Research Laboratories at the computer facilities of the Boeing Company in Seattle. The necessary amplitude information was obtained from a BSRL analogue-to-digital converter located at the Geophysical Institute's Ballaine Lake field site near College. The punched tapes containing this and other information were flown to Seattle for data reduction and subsequent use in scintillation studies carried out jointly by the institute and BSRL. The reduced data pertinent to the visibility fade study were returned to College for analysis.

The amplitude data obtained from BSRL consisted of five-minute (or, in some cases, ten-minute) averages of fractional fluctuation. For use with the complex-channel data, it was desired to have averages over the varying half-fringe period of the 68 MHz, 110-meter, phase-switch interferometer. The necessary change in data presentation was carried out by treating the BSRL numerical results as a fifth input to the pass 2 computer program. Thus, the overall data reduction scheme resulted in time-varying evaluations of visibility as observed on five complex-information interferometers plus corresponding evaluation of amplitude fluctuations from a single interferometer, all averaged over the same time periods (typically on the order of ten minutes in length). The overall data reduction procedure is shown schematically in figure 32.

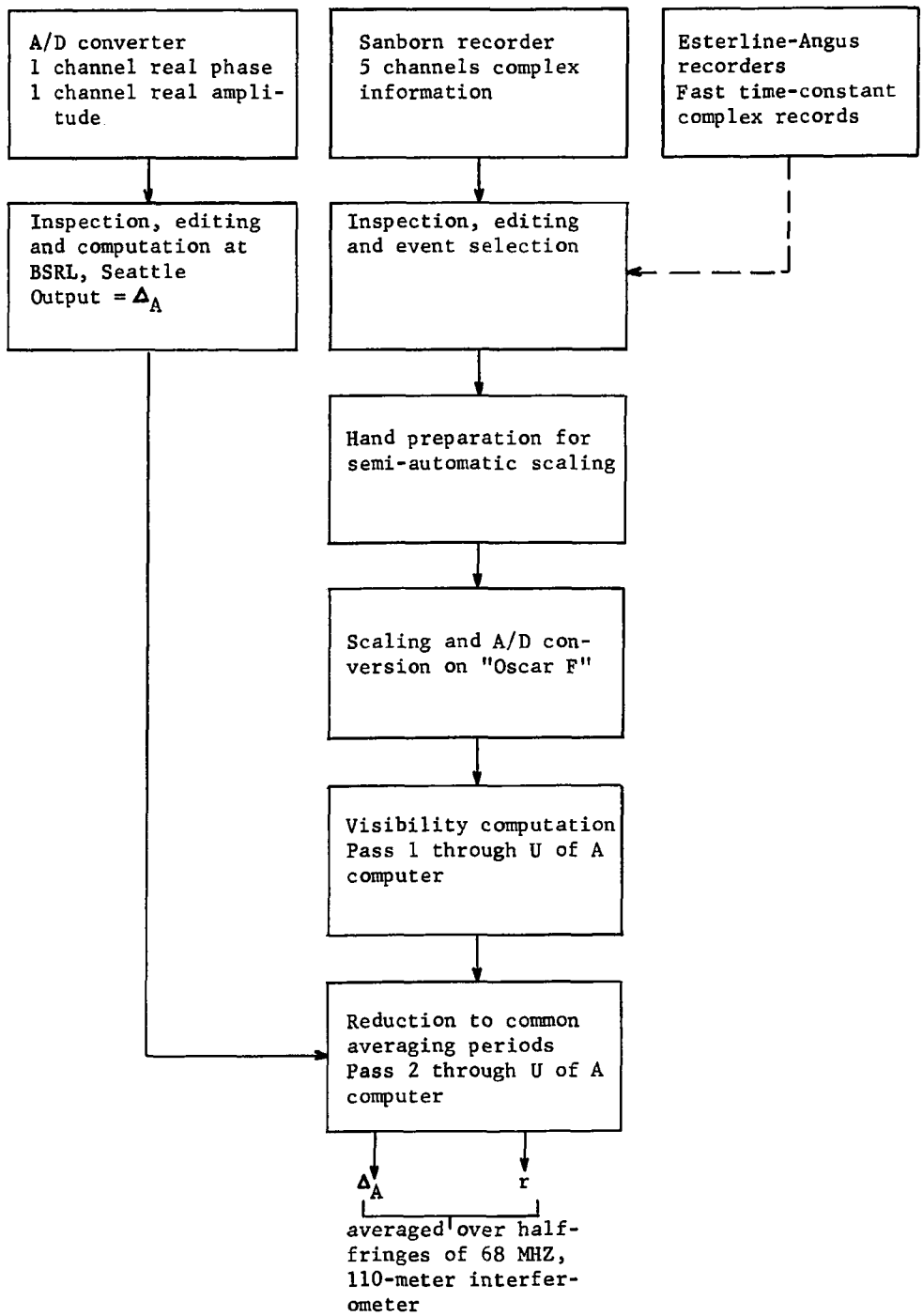

Fig. 32. Schematic representation of overall data reduction procedure for visibility fade analysis.

IVD DETERMINATION OF THE WAVEFRONT PARAMETERS b and R(ξ)

D1 Combination of Visibility and Real Amplitude Information

As pointed out in section IVA, the experimental problem in which we are involved is determination of the coherence ratio b and the wavefront autocorrelation function R(ξ), where ξ represents distance along the wavefront. The observational quantities made available by the data-reduction procedures described in section IVC are the visibility r(ξ) and the amplitude fluctuation Δ_A, defined by equation 2-117. In this section, we shall concern ourselves with analysis of observational results from a single frequency. Extension to additional frequencies is a matter of straight-forward calculation, which will be described in section D2.

For analysis of the observations obtained at our prime frequency of 68 MHz, we wish to find a single value of b and three values of R(ξ) for each averaging period within a given visibility fade for which r(ξ) and Δ_A are available. Each value of R corresponds to a single value of ξ, with each ξ representing essentially one of the interferometer spacings - 110 meters, 220 meters, or 330 meters. As pointed out in section IVA, equation 4-1 is one of the relations to be used for determination of b and R for a single spacing. Another relation is to be obtained from the independent amplitude information contained in Δ_A, as we shall now see.

Now, equation 4-1 was derived as equation 2-100 on the basis of a minor generalization of work done by Bramley (1951), and its essence is contained in his equation (42). The other major results of

Chapter II represent somewhat more extensive generalizations of Bramley's work, in particular of his special-case discussions of the independent amplitude and phase characteristics of ionospherically scattered signals. Our technique was a numerical one, and the results were presented in figures 4 through 10. Of these various figures, several relate to parameters directly observable by means of a phase-sweep interferometer. We shall be concerned here with figures 7 and 10.

Figure 7 relates the fluctuation in the amplitude-channel output of a phase-sweep interferometer to b and R. We shall want to discuss the relationship in detail. Before doing so, let us turn our attention to figure 10, which is concerned with the phase-channel output of a phase-sweep interferometer. Figure 10 shows the variance $\overline{\eta^2}$ of the phase-difference output of a phase-compensated, phase-sweep interferometer, such as that used in the present experiment, as a function of R for several values of b. Figure 33 shows $\overline{\eta^2}$ plotted instead as a function of b for several values of R. Alternatively, one can plot b as a function of R for various values of $\overline{\eta^2}$, as in figure 34.

Now, in principle, one could superpose on figure 34 a plot of b as a function of R for various values of r from equation 4-1. The intersections then would represent solutions of our experimental problem. That is, from observed values of visibility r and phase-difference variance $\overline{\eta^2}$ one could obtain values of coherence ratio b and wavefront autocorrelation R. There is a fundamental problem

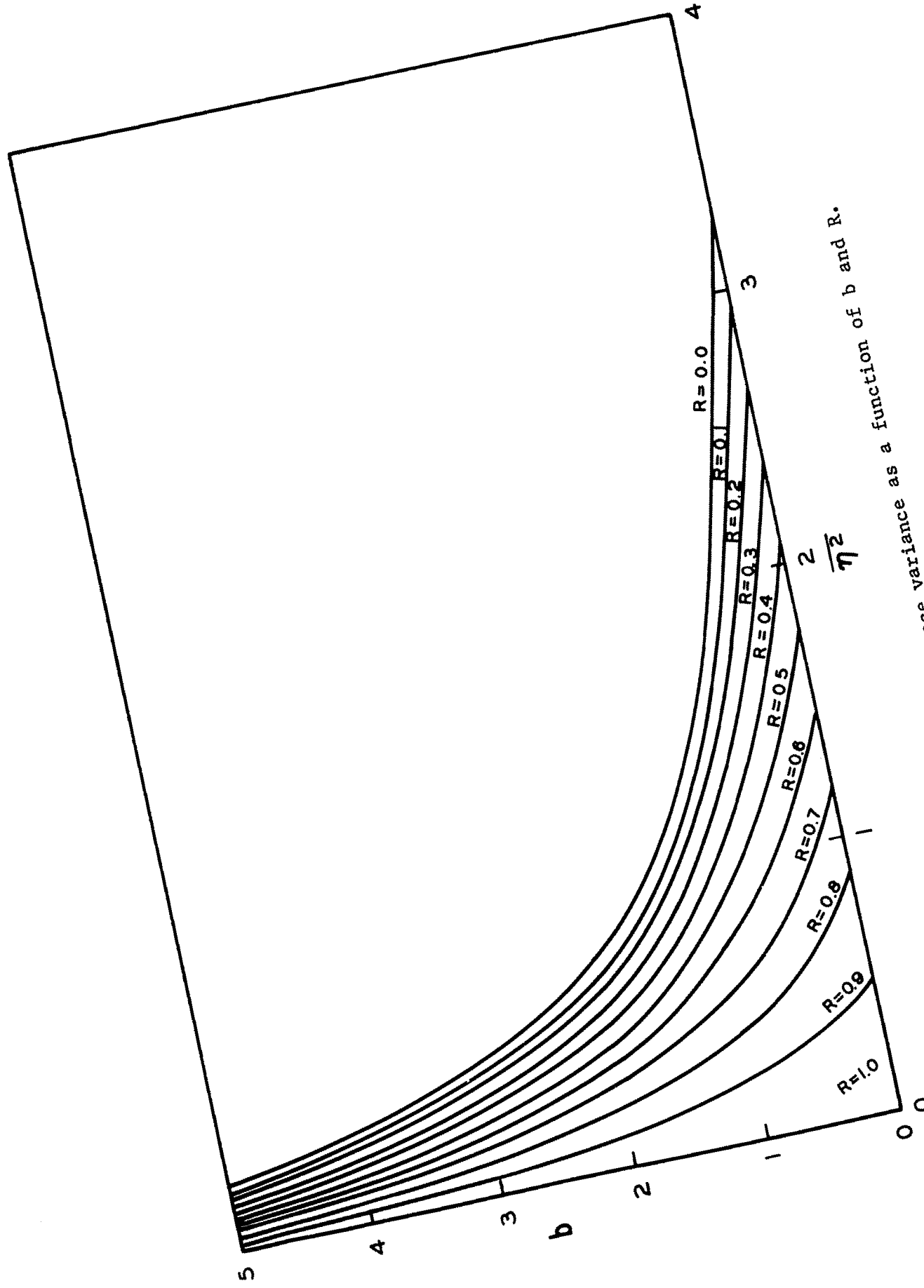

Fig. 33. Phase-difference variance as a function of b and R.

involved in such a procedure, however. The problem is apparent upon comparison of figure 34 with figure 35, which is the appropriate plot of equation 4-1. The two sets of curves have very similar slopes, precluding intersections sufficiently close to othogonal to be useful for experimental purposes.

The reason for lack of orthogonality in the $\overline{\eta^2}$ and r curves is rather apparent. The two quantities do not represent sufficiently independent information. That is, loss of visibility on a phase-switch or coherently detecting phase-sweep interferometer arises largely from the difference in phase of the signals received at the two antennas, even though the output of such a device contains complex information (i.e., a combination of phase and amplitude).

Let us now turn our attention to the pure amplitude information available from a phase-sweep interferometer. If the information contained in figure 7 is plotted in a fashion analogous to figure 34, a useful result is obtained. Figure 36 shows such a plot on an enlarged scale, superposed on the curves given in figure 35. The nearly orthogonal intersections of the two families of curves attest to the relatively high degree of independence of the information available from a complex-output interferometer and an amplitude-output interferometer during visibility fades.

To the extent that experimental data are consistent with the field of graphical intersections displayed in figure 36, the figure can be used to obtain values for the coherence ratio b and the wavefront autocorrelation R from a combination of interferometric observa-

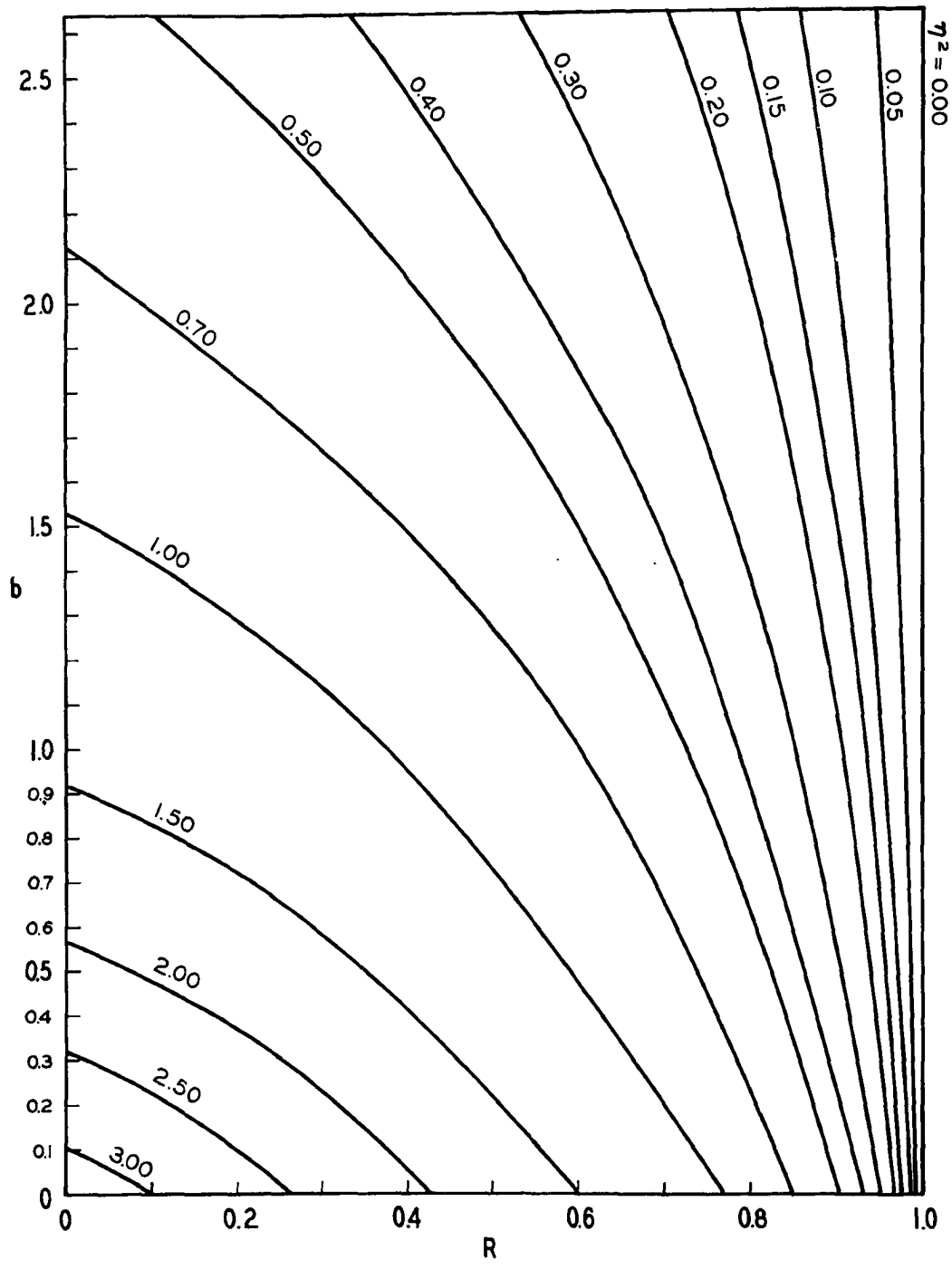

Fig. 34. Coherence ratio as a function of $\overline{\eta^2}$ and R.

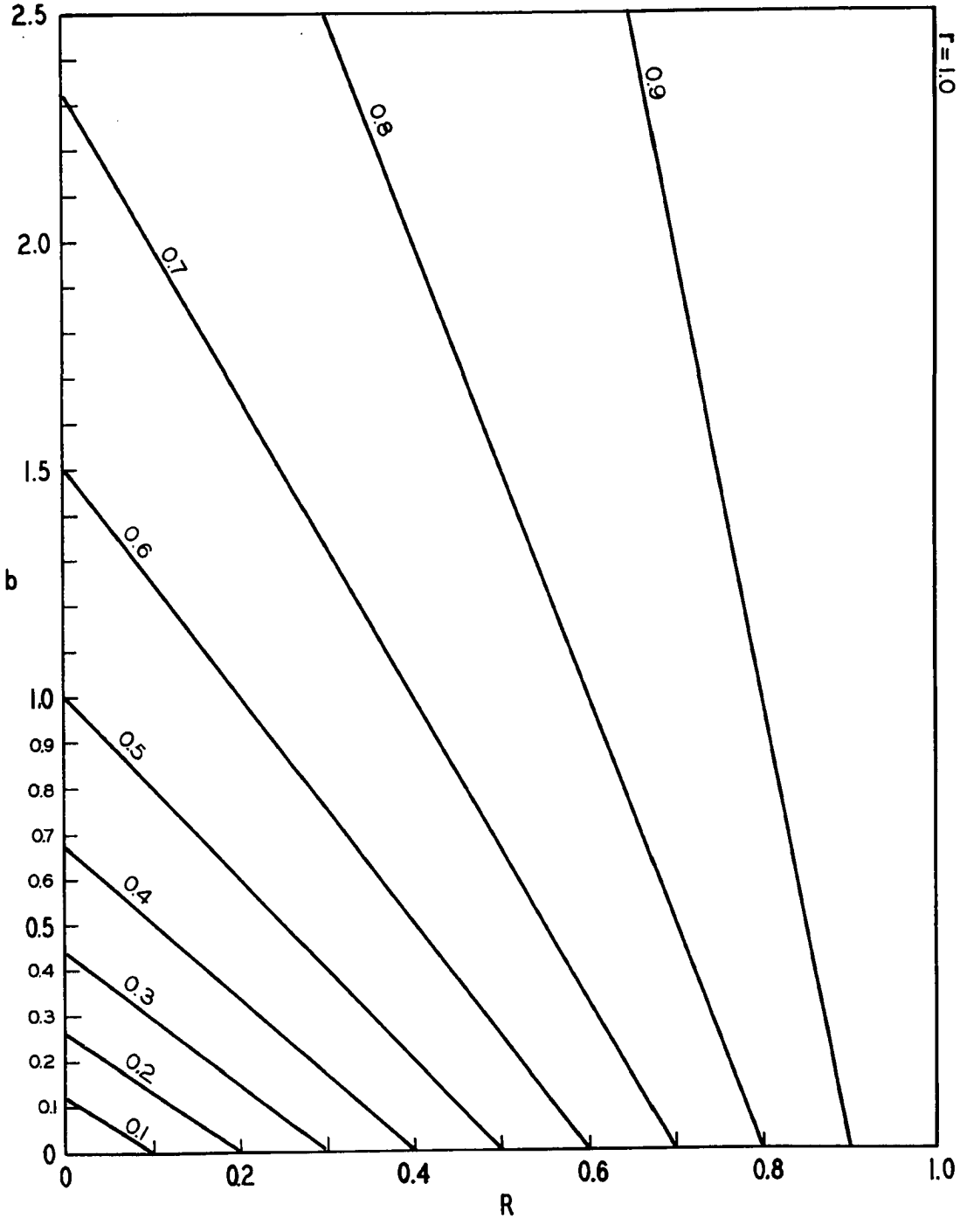

Fig. 35. The relationship of b and R to visibility, r.

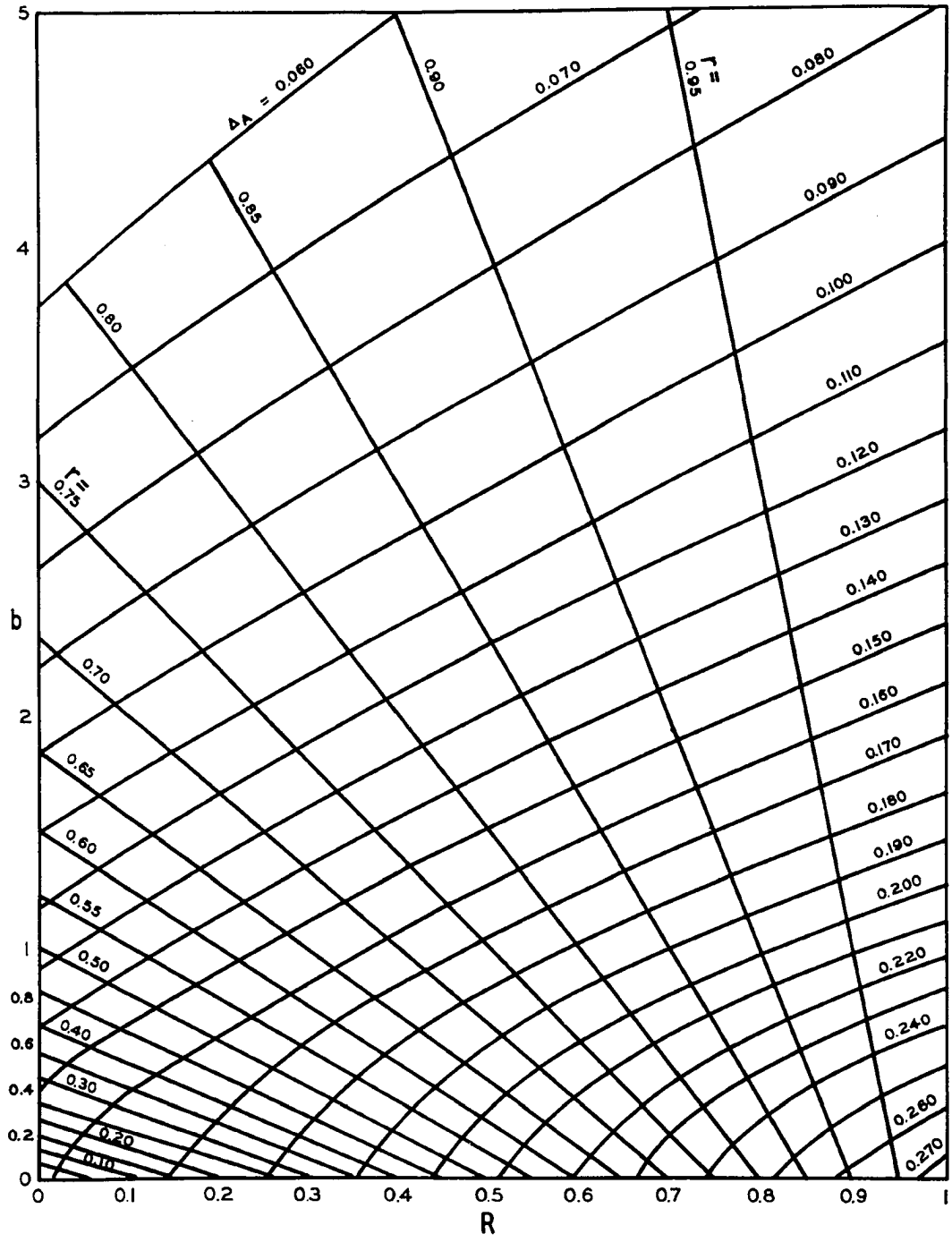

Fig. 36. Part of the field of graphical solutions for b and R which can be obtained from Δ_A and r during a visibility fade under conditions of random phasing in the angular spectrum.

tions. Inconsistent data would imply lack of validity of the assumptions made in the work leading to the two families of curves or at least contributions from factors not considered in the work. It will be recalled that the prime assumption made was that of random phasing in the angular spectrum, which underlies the development of Chapter II. In addition, certain tacit assumptions are involved in limiting the values of R and b displayed in figure 36. We shall discuss these limitations in section B2 of Chapter V.

The lines of constant Δ_A displayed in figure 36 were plotted from results of the numerical technique developed in Chapter II. Since the essence of the technique is a statistical model, there was some scatter in the results, and graphical smoothing was necessary. Along the right-hand border of figure 36 where R equals unity, Δ_A is given by equation 2-118 and can be calculated analytically on the basis of a Rice distribution. The analytical calculation was carried out and the result used as an aid in smoothing the numerical results, in view of the similarity of the distribution for general R to the Rice distribution. Such a similarity is evident in figure 5. The resulting curves of figure 36 are believed to be essentially free of statistical fluctuation. We shall return to this matter later in discussing estimated uncertainty in our observational data.

D2 Graphical Solution and Computations

Clearly, the curves of figure 36 allow us to determine b and R from a set of observations of r and Δ_A. For this purpose, the 68 MHz observations obtained with an interferometer spacing of 220 meters were

used. It will be recalled that the instrument employed was a phase-sweep interferometer. The visibility r was obtained from the coherent output by means of the data reduction procedures described in section IVC. The mean-square fractional fluctuation, Δ_A, in the output of the amplitude channel was obtained through the cooperation of Boeing Scientific Research Laboratories as also described in section IVC. A pair of values for r and Δ_A was computed for each half-fringe period of the 68 MHz, 110-meter spacing, phase-switch interferometer during a given visibility fade.

Once the 68 MHz coherence ratio b was established, then equation 4-1 was employed to calculate $R(\xi)$ from $r(\xi)$ obtained from the two 68 MHz phase-switch interferometers. Thus, the coherence ratio b and three values of the wavefront spatial autocorrelation function $R(\xi)$ were obtained for 68 MHz. It will be recalled that ξ represents distance along the wavefront and is related to interferometer spacing d, according to equation 3-15, simply by $\xi = d \cos \alpha_o$. Now α_o is given simply by the hour angle HA and declination δ of the source under observation, as follows:

$$\alpha_o = \sin^{-1} [\sin HA \cos \delta] \qquad 4\text{-}2$$

Hence the wavefront distance ξ is obtained from the interferometer spacing d by

$$\xi = d \sqrt{1 - \sin^2 HA \cos^2 \delta} \qquad 4\text{-}3$$

Since declination is constant for a given source and hour angle changes for any source at the constant rate of 15 degrees per hour, ξ was found

most conveniently and with completely sufficient accuracy from a graph of equation 4-3.

With b and three values of R (ξ) established, the single-frequency experimental problem is essentially complete. The ensuing procedure involves straight-forward calculation by means of equations 3-64 through 3-67. The procedure is best illustrated by means of an example, which will be presented in section IVE. Suffice it to say here that the next step in the work is to obtain the optical depth and spatial autocorrelation function of the ionospheric scattering layer from b and R(ξ).

It will be recalled that the optical depth is frequency dependent. According to equation 3-66, it ought to obey an inverse frequency-squared law. A test of this theoretical conclusion was devised and will be described in section E4.

D3 Probable Experimental Errors

The major source of error in establishing the visibility lay in slow variations of received flux. Slow amplitude scintillations, which may be thought of as ionospheric focusing and defocusing effects, having periods comparable to or longer than the half-fringe period of the interferometers, resulted in troublesome flux variations. The extent of their effect on the accuracy of visibility measurements was estimated from the amplitude record obtained from the phase-sweep interferometer.

The routine statistical computations carried out on the amplitude output by Boeing Scientific Research Laboratories included five-minute (or in some cases ten-minute) averages. In the absence of a visibility fade, these results represent the average flux received from the radio

star during the averaging period. It will be recalled that the half-fringe period of the 68 MHz, 110-meter interferometer was used as the standard averaging period in determination of visibility. This period is on the order of ten minutes except near the twice-daily times of fringe elongation, where it is greater.

As an estimate of the error caused by focusing and defocusing, the mean deviation in ten-minute amplitude averages for one hour preceding and one hour following each visibility fade was computed. In a few cases where fades occurred near each other, the error computation could be made only before and after the series of fades rather than before and after each individual fade.

The error due to slow flux variations showed itself as a percentage of the measured visibility, typically about $\pm$ 5%. On the other hand, the errors inherent in the semi-automatic scaling procedure used in visibility determination were independent of the actual visibility. Arising from limitations on operator and scaling-machine accuracy, they set an ultimate limit of about $\pm$0.05 on the accuracy of scaled visibility. Errors due to receiver response characteristics were negligible except in a few early observations. Small nonlinearities in the Sanborn recorder used for visibility-fade observations existed until the end of December 1964, whereupon they were corrected.

The prime source of error in determination of Δ_A arose from the limited number of independent samples available for its calculation during a given averaging period. The ultimate limit was set by the period of scintillations characteristic of visibility fades, which is on

the order of one or a few seconds. In the typical averaging period of ten minutes, one might expect to observe 300 to 600 independent values of amplitude-channel output, at the most. In practice, the data rate was set usually by the A/D converter. While some fades were observed with an A/D rate of 120 samples per minute, most were observed at a rate of 15 per minute. In this case, 150 samples were available for calculation of Δ_A during a ten-minute averaging period. In a few instances, the rate was five per minute, yielding only 50 samples in ten minutes.

In the numerical calculations performed in preparation of the curves of constant Δ_A given in figure 36, 10,000 independent data values were employed, and graphical smoothing still was required. In individual computer runs, 1000 values were used, ten runs then being averaged for preparation of the curves. An error analysis of the individual computer-run results was made. No significant systematic trends in the percentage errors was found as a function of b or R. The mean deviation from the finally accepted curves was $\pm 3\%$. On the assumption that the uncertainties in observational data obey the same statistics as the uncertainties in computed results and that uncertainty is proportional to the square root of the number of independent data samples, the following estimates for observational uncertainty in Δ_A were made: 4% at the fast A/D rate; 8% at the normal A/D rate; 13% at the slow A/D rate. These values were used as probable errors in data analysis.

IVE AN EXAMPLE

E1 Discussion of the Observation

In the remainder of this chapter, we shall be concerned primarily with a particular visibility-fade event. The purpose of the discussion is two-fold. First, it is intended to provide an example of the complete data analysis procedure used in the experiment. Second, it will be used to demonstrate the effects of the various sources of experimental error on the results. It was with the second purpose in mind that the event, number 42, was chosen. In order to display the effects of uncertainties, it was necessary to use an event involving several scaling periods, whose resulting values of b and R (for 68 MHz and 220 meters spacing) spread reasonably widely over the range included in figure 36.

Figure 37 shows the unsmoothed record obtained from the 330-meter-spacing interferometer at 68 MHz between 1430 and 1700 AST on June 4, 1965. A definite but not particularly severe visibility fade is evident, especially between about 1605 and 1630. Figure 38 shows, in two strips, the five smoothed interferometer records obtained between 1500 and 1700. The 68 MHz, 330 meter trace displays depressed fringes through much of the period, the 1605-1630 period being only the most well developed portion of the fade. The other two 68 MHz records show lesser degrees of fringe depression. Only slight fade effects are to be seen at 137 and 223 MHz, near the peak of the 68 MHz fade.

At 26 MHz, new circuits were being incorporated into the equipment when the fade began. Shortly after 1500, the 26 MHz instrument was put in operation and its center line adjusted approximately. However,

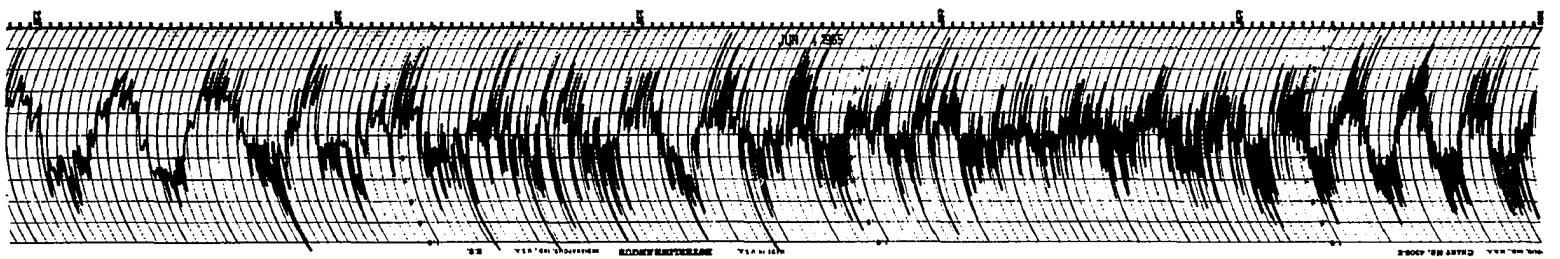

Fig. 37. 68 MHz, 330-meter, phase-switch interferometer record for event no. 42.

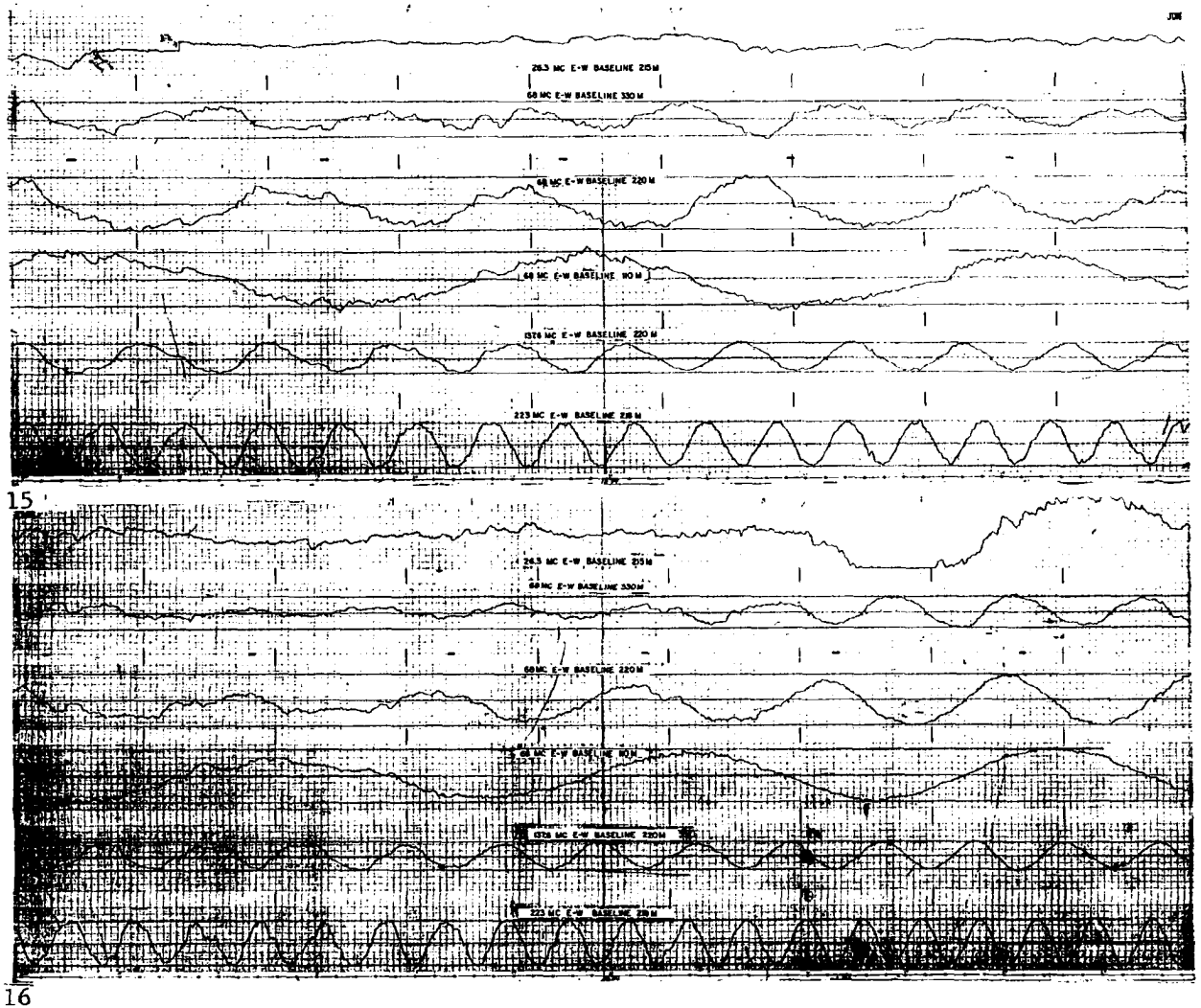

Fig. 38. Smoothed complex-channel interferometer records for event no. 42.

although Cassiopeia A was in the antenna beam, essentially no signal was observed due to the combined effects of absorption and visibility fading. Hence, it was not possible to make a gain adjustment. It will be noted that the end of the 68 MHz visibility fade was accompanied by a sudden return of the Cas signal at 26 MHz, between 1640 and 1645. Upon recovery, the interference pattern exceeded full scale in peak-to-peak amplitude. The source was near lower transit at the time of the observation, and no directly comparable absorption data are available. However, the College vertical riometer recorded less than one decibel of absorption at 30 MHz throughout the event. Between 1530 and 1545, the vertical absorption decreased only 0.1 db, from 0.8 to 0.7 db.

Figure 38 shows the undisturbed amplitude levels and zero lines established from the pre-fade and post-fade interference patterns recorded on channels 2 through 6. The pattern crossovers chosen to demark scaling periods are marked along the center lines, as are the scaling points obtained by ten-fold division of the periods. Event 42 was an uncomplicated one; in spite of some variation in the length of scaling periods, most crossovers are quite distinct.

In a few of the fringes shown in channels 2 and 3 of figure 38, there are multiple crossings of the center line. The most obvious example of this behavior occurred in channel 2 between 1523 and 1524. It will be recalled that the portion of the trace which appears "on the wrong side" of the center line, while being scaled as a negative value, actually was treated as positive by taking the absolute value in computations. Thus, there was an element of discrimination against the crossed over

portion of the trace. Inspection of all the other channels during the same time period shows that the crossover was almost surely caused by a single refractive effect rather than by a period of negative visibility on channel 2. The evidence is that all the other traces show slight bulges rather than depressions.

By using the absolute value of the scaled values, the extraneous refractive effect pointed out above was discriminated against to some extent, although to an extent which is not readily calculable for general error analysis. In deeper and more complicated fades, an unfortunate side effect of refraction discrimination arises. An example may be seen in channel 2 of figure 24. In the fringe which occurred between 2342 and 2349, there were two periods of negative trace values and no clear evidence that they were caused by isolated refractive effects. They may have been simply unsmoothed random fluctuations, representing short periods of negative visibility. If so, then visibility of the fringe was overestimated. Again, such underestimation of fading is considered preferable to the only other choice, which would be overestimation of fading in the presence of strong, isolated refractive effects.

The most serious adverse consequences of using the absolute values of the scalings is that it prevents the detection of negative average visibility over a given fringe, if it should occur. In a few instances, the records are suggestive of slightly negative visibility, although no systematic search was carried out. Some possible examples may be found in channel 2 of figures 24 and 28, but in both cases there is considerable fluctuation about the average. Also, in the event of figure 28, the error in placing the channel-two center line appears

greater than normal and probably contributed to the alleged negative visibility.

In the event of figure 26, the accuracy of center-line placement in channel 2 was greater. In the fringe which occurred approximately between 0808 and 0812, the trace is quite smooth and appears to display very slightly negative visibility. This and other such instances suggest that a systematic search and more accurate scaling of the existing visibility-fade records might reveal instances of negative visibility. However, none of the instances noted to date shows clear evidence of strongly negative visibility. Rarely has even slightly negative visibility been noticed for periods comparable with the standard averaging intervals used in the present experiment. Hence, the effect of such occurrences has been simply to produce a slight overestimation of visibility in deep fades.

E2 Determination of the 68 MHz Wavefront Parameters and Uncertainties

From the record shown in figure 38 the visibility during event 42 for the 68 MHz, 137 MHz, and 223 MHz traces was obtained by the procedure outlined in section IVC. Figure 39 shows the graphical output from the two computer passes, giving visibility for each fringe of each trace and for the standard averaging intervals. In comparing the visibility with the original records, note that time is given in hours and decimals in the former and in hours and minutes in the latter.

The numerical values of visibility given by the pass 2 computations were combined with the values of effective mean-square fractional fluctuations in amplitude, computed at Boeing Scientific Research

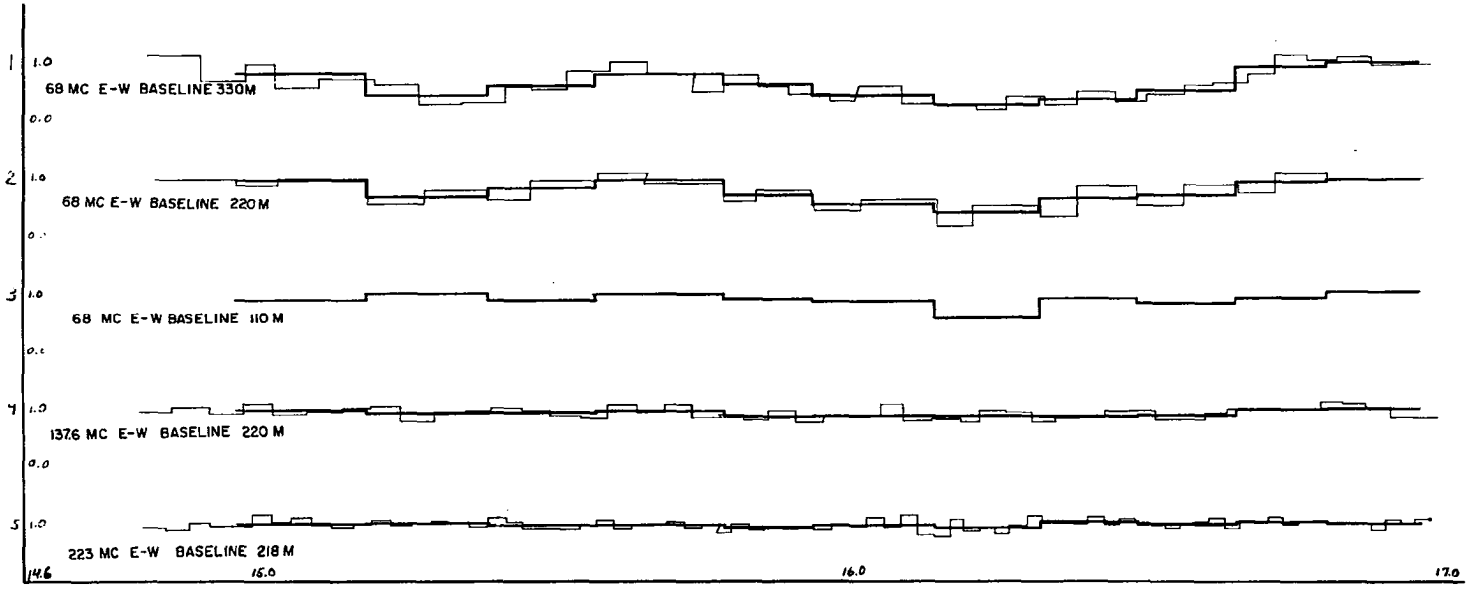

Fig. 39. Variation of 68, 137, and 223 MHz visibility during event no. 42.

Laboratories. From the combination of channel 3[1] visibility r and the corresponding amplitude fluctuation Δ_A, the coherence ratio b and channel 3 wavefront autocorrelation R were obtained by means of the set of curves given in figure 36. The graphical positions of the results are shown in figure 40 for the eleven standard averaging periods of the event.

The data points in figure 40 were placed on the r-Δ_A grid by linear interpolation, and the corresponding values of b and R were read from a rectilinear grid. The resulting wavefront autocorrelation R, of course, was the value corresponding to the effective spacing of the 220-meter interferometer. Since the lines of constant visibility on figure 40 represent equation 4-1, they were used to obtain values of R corresponding to the other two 68 MHz interferometer spacings. Figure 41 shows the resulting data points for three representative scaling periods, numbers 2, 4, and 6. In the case of period number 2, it was necessary to extend the lines of constant visibility into the region of negative wavefront autocorrelation. The significance of this fact and the validity of the extension will be discussed later.

In figure 41, the circled points represent data obtained from the 110-meter interferometer. The noncircled points and x's respectively represent data from the 220 and 330-meter interferometers. The effective spacings for the three instruments were obtained from a plot of equation 4-3, using the declination of Cas A for δ and its hour angle at the center of each scaling period of the event for HA. Table 2 gives the effective spacings, observed visibilities, observed amplitude

---

[1]Channel 3 of the original record, corresponding to channel 2 of the computer output.

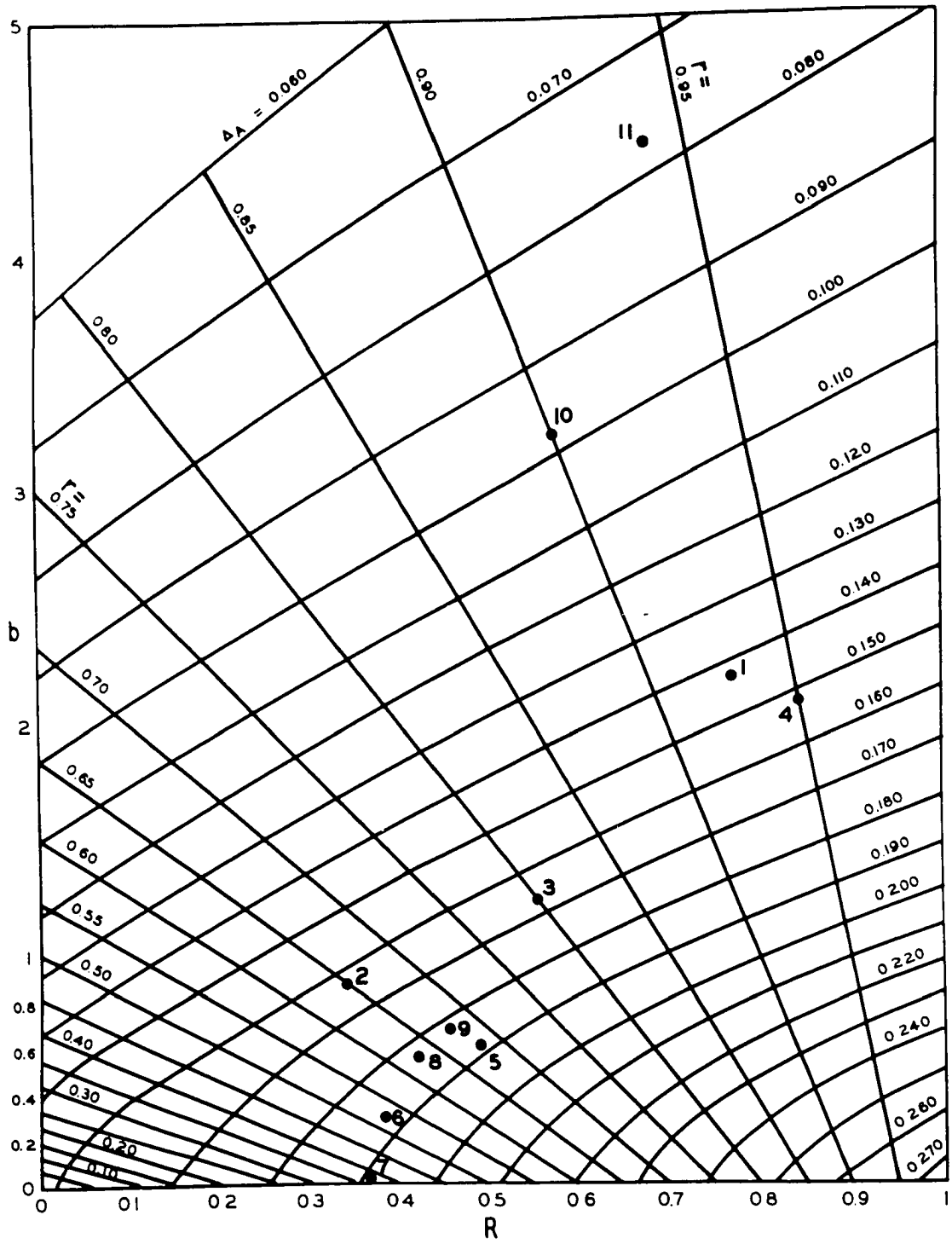

Fig. 40. Graphical solutions for the 68 MHz coherence ratio and the 68 MHz, 220-meter, wavefront correlation for event no. 42.

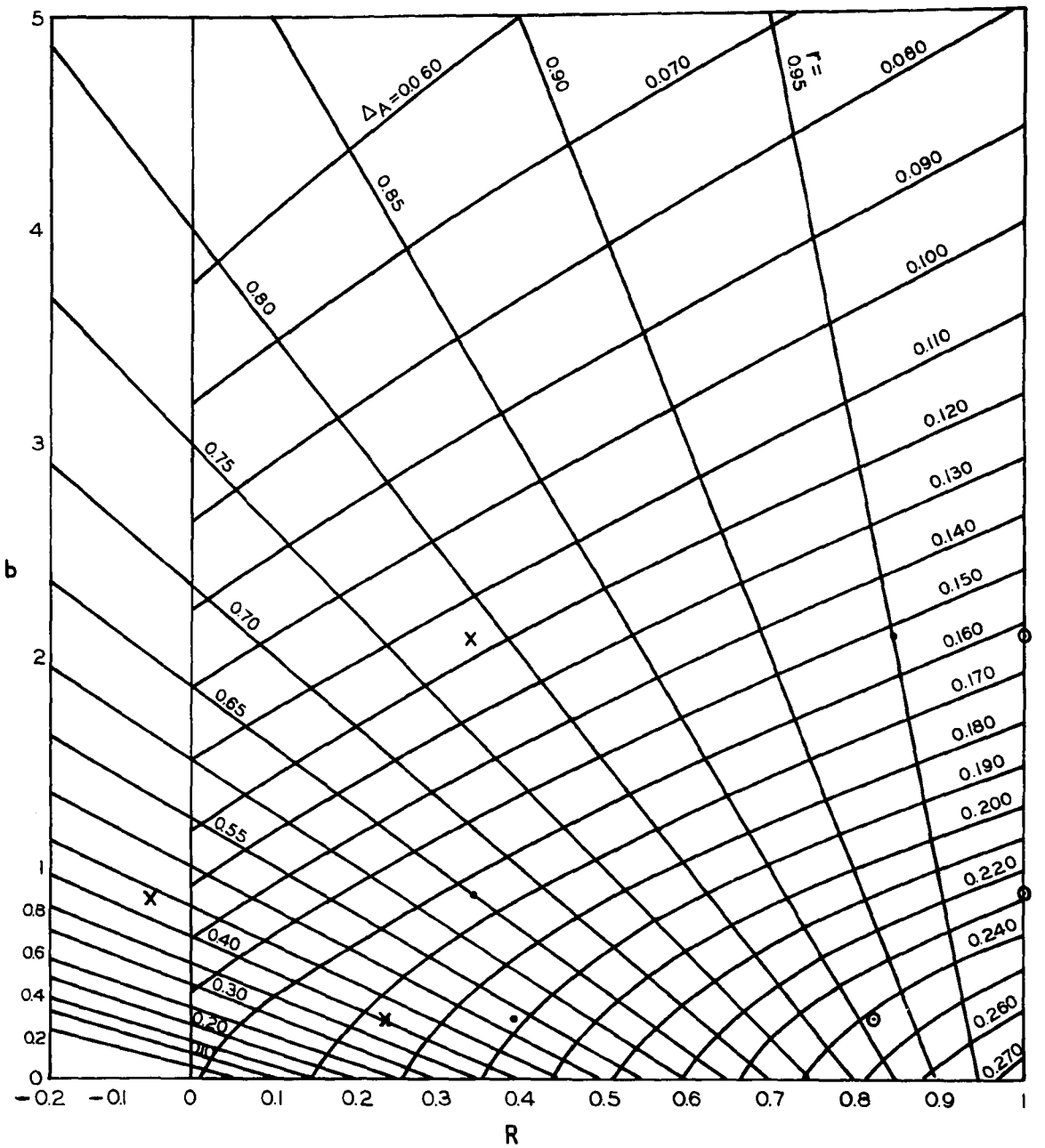

Fig. 41. Tri-spacing 68 MHz coherence ratio and wavefront correlation for three scaling periods of event No. 42. ∅ = 110 meter spacing; • = 220 meters spacing; x = 330 meters spacing.

fluctuation Δ_A, and resulting values of coherence ratio and wavefront autocorrelation for the eleven scaling periods of the event. The numerical subscripts refer to the three 68 MHz interferometers as follows: 1 for the 110 meter baseline, 2 for the 220 meter baseline, 3 for the 330 meter baseline. Δ_A, of course, was obtained from the 220 meter instrument, and b is independent of spacing.

TABLE 2

68 MHz DATA AND WAVEFRONT RESULTS FOR EVENT 42

68, 110 Fringe #	ξ_1	ξ_2	ξ_3	r_1	r_2	r_3	Δ_A	b	R_1	R_2	R_3
1	101 meters	202	303	0.89	0.93	0.80	0.142	2.21	0.65	0.78	0.36
2	102	204	306	1.00	0.65	0.43	0.164	0.87	1.00	0.34	-0.05
3	103	206	309	0.88	0.80	0.58	0.167	1.22	0.74	0.56	-0.02
4	104	208	311	1.00	0.95	0.78	0.152	2.07	1.00	0.84	0.34
5	104	209	312	0.91	0.69	0.60	0.188	0.61	0.86	0.50	0.36
6	105	210	315	0.86	0.52	0.41	0.187	0.29	0.84	0.38	0.24
7	106	212	317	0.58	0.38	0.26	0.192	0.02	0.57	0.37	0.25
8	106	213	319	0.91	0.63	0.35	0.183	0.56	0.86	0.42	-0.01
9	107	214	321	0.83	0.68	0.49	0.181	0.70	0.72	0.46	0.14
10	107	214	322	0.93	0.90	0.91	0.098	3.21	0.71	0.58	0.63
11	108	216	324	1.03	0.94	0.98	0.079	4.42	1.17	0.68	0.90

The last four columns of table 2 represent the solution of our single-frequency experimental problem for event 42. They describe the

68 MHz wavefront received at the ground during each of eleven approximately ten-minute periods during the visibility fade. This description will be used presently to calculate the optical depth and the structural autocorrelation function of the ionospheric scattering layer which produced the fade. First, however, let us explore the quantitative effect of experimental uncertainties on the results given in table 2. For this purpose, we shall obtain the uncertainties for eight of the eleven scaling periods. Periods number 4, 8, and 9 will be omitted because the calculations would be essentially repetitious of those carried out for other periods.

In event 42, the uncertainty in Δ_A was $\pm 4\%$. The uncertainty in r arising from slow variations in received flux was $\pm 3\%$. As in all events, the uncertainty in scaling r was taken as the constant value of ± 0.05. The error bars established by the above uncertainties are shown for the 220-meter baseline measurements in figure 42.

Obviously, for large values of b, the uncertainty in measurement of visibility greatly overshadows the uncertainty in Δ_A for this particular event. For very small b, the uncertainty in Δ_A dominates. For moderate values of b, the uncertainties from the two sources are roughly of equal importance. The b-axis projections of the error bars shown in figure 42 were added rms-wise for each scaling period in order to estimate the uncertainty in b, and similarly for the uncertainty in R. The results are shown in figure 43.

It will be noted that the lengths of the b and R error bars both increase with increasing b and would become excessive for b greater than

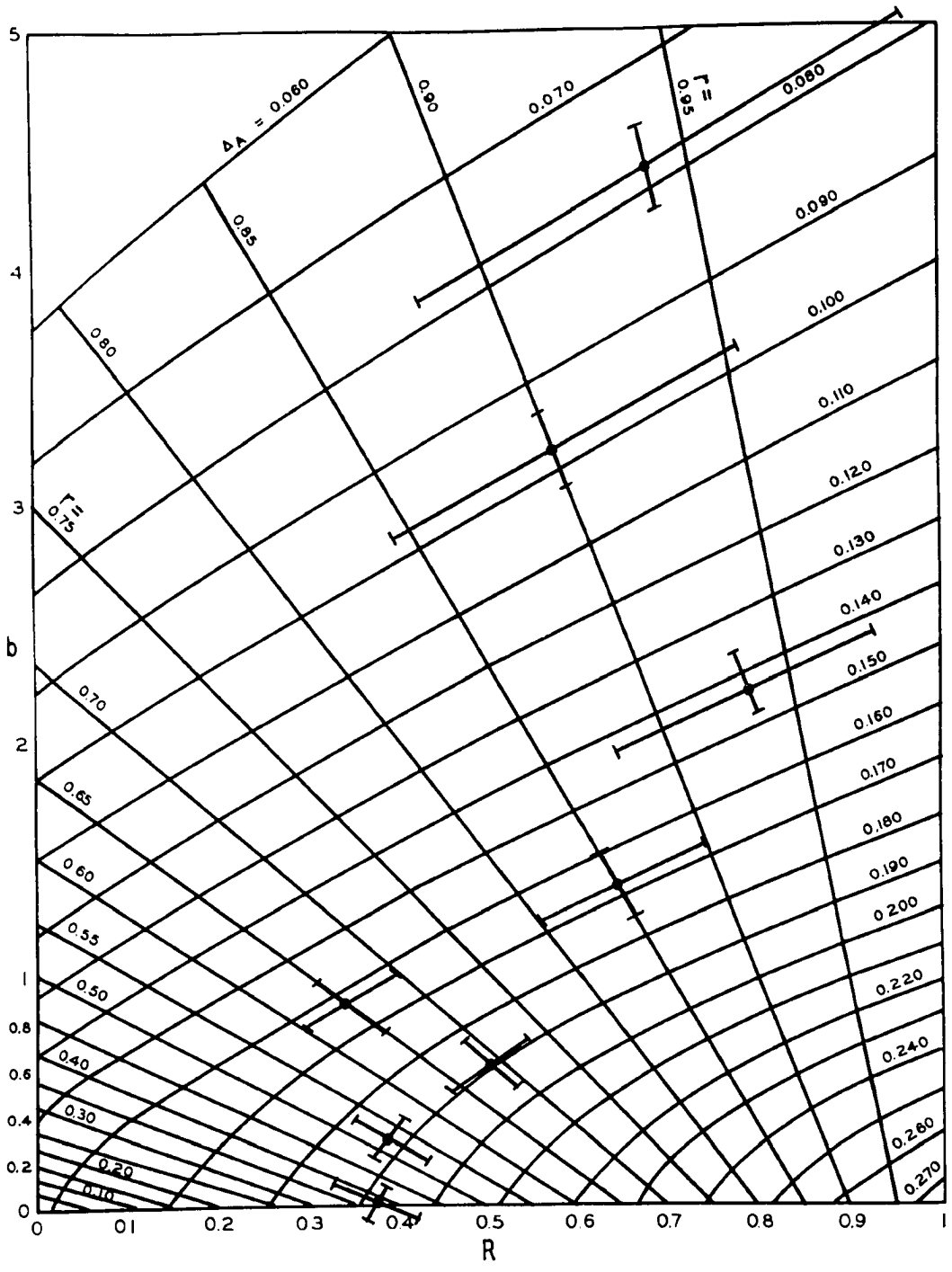

Fig. 42. Uncertainties in r and Δ_A for event 42.

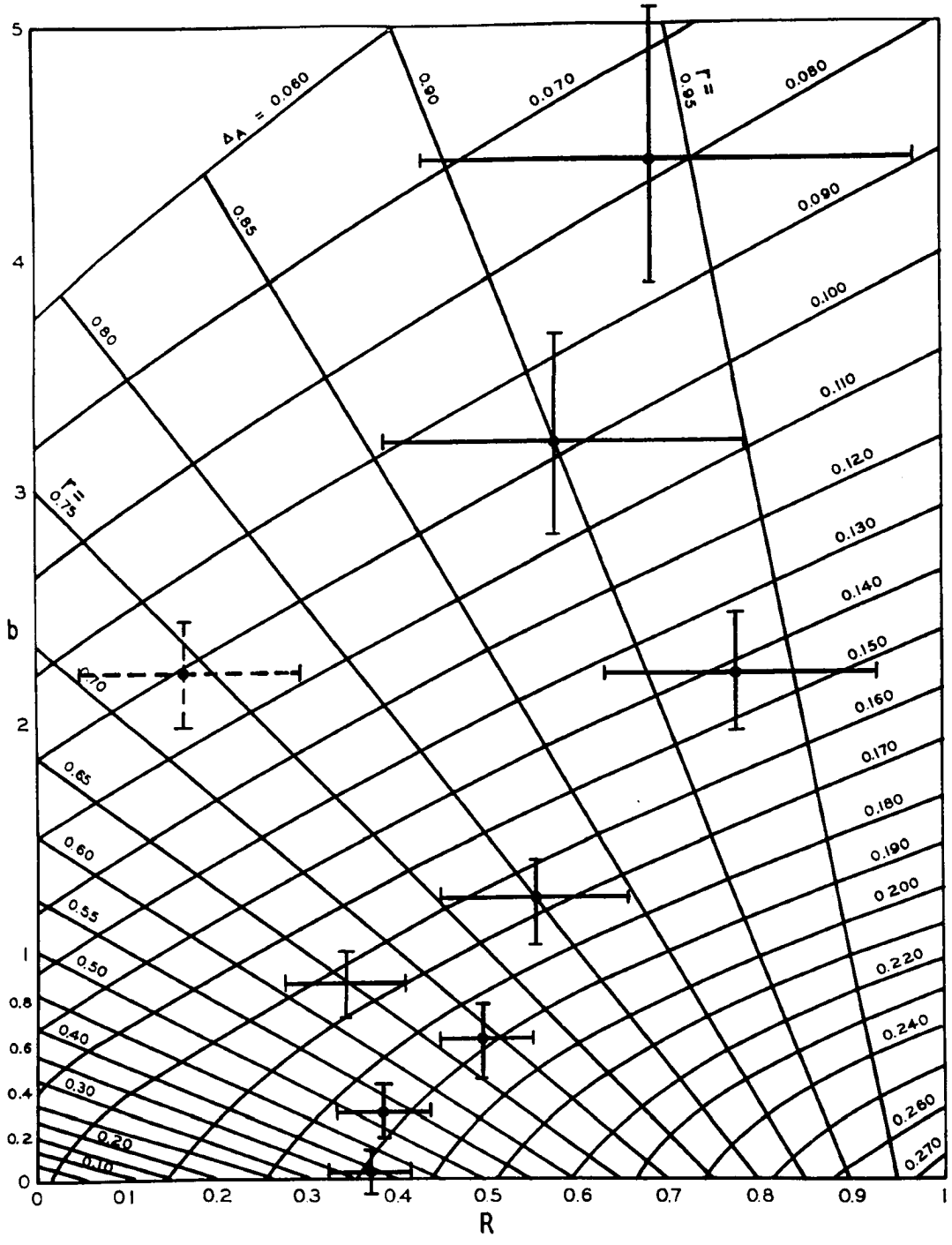

Fig. 43. Uncertainties in b and R for event 42.

about five. Accordingly, no attempts were made to perform measurements when b exceeded five. It will be recalled that for b greater than about five, Bramley's analytical results for large coherence ratio can be employed. This fact would in no way improve the accuracy of measurements in the large coherence ratio region. It does mean, however, that there would be no need to resort to our graphical techniques in any event.

In addition to the eight pairs of actual error bars from event 42, figure 43 shows also a pair of hypothetical bars, indicated by broken lines. The hypothetical error bars were calculated to show the dependence of uncertainties in b and R on the value of R. Comparison with the actual error bars for scaling period number one - at the right - shows essentially no R dependence of the b uncertainty and only a small R dependence of the R uncertainty. Accordingly, in all events, the uncertainties were taken to be independent of the value of R, and we shall look further at the dependence of the uncertainties on the value of b only.

Figure 44 shows the uncertainties in b and R for event 42 as functions of b. The points were obtained from the error bars in figure 43. The straight lines were drawn as convenient approximations to the functional relationships between the uncertainties and the value of b, for use in error analysis. That is, the uncertainties for event 42 were taken as

$$\text{uncertainty in } b = \pm(0.1 + 0.1b) \qquad 4\text{-}4$$

and

$$\text{uncertainty in } R = \pm(0.05 + 0.05b) \qquad 4\text{-}5$$

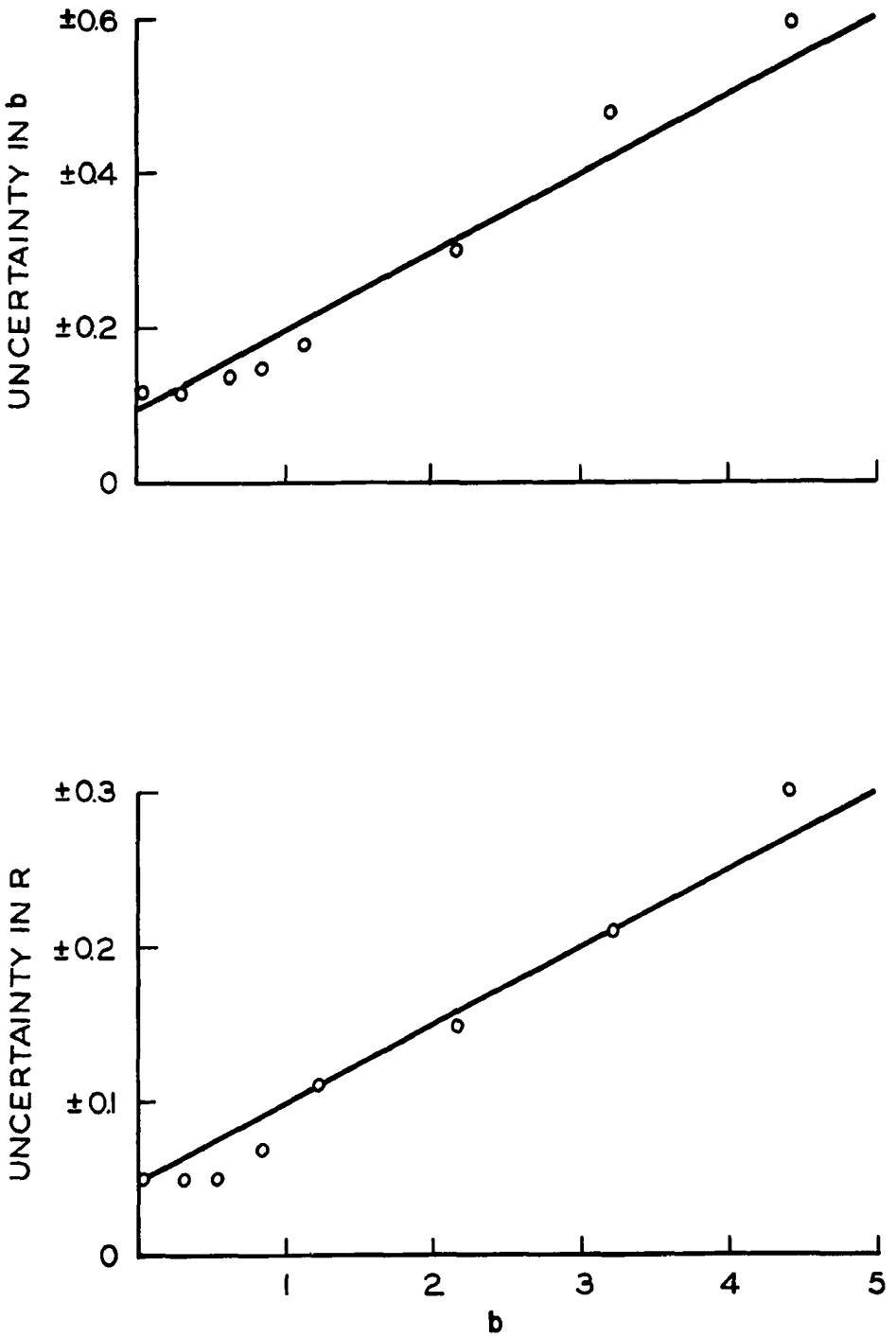

Fig. 44. Uncertainties in b and R for event 42 as functions of b.

It will be recalled that these uncertainties arose from experimental errors of ±4% in Δ_A and ±3% in r.

Now the uncertainty in Δ_A for most events was ±8% rather than ±4%, and in some events it was ±13%. In order to see the effect of increased uncertainty in Δ_A, hypothetical calculations were made using data points from event 42. The resulting approximate relations of the b and R uncertainties to the value of b are shown in figure 45 along with the results from figure 44. The effect of increased uncertainty in Δ_A is to increase the b uncertainty by an amount which depends weakly on b. The uncertainty in R changes considerably with uncertainty in Δ_A for small b but very little for large b.

The uncertainty in r varied over a considerable range from one observed visibility fade to another, owing to the variable effect of ionospheric focusing and defocusing. Let us now see how such variations in r uncertainty effect the uncertainties in b and R. In order to do so, additional hypothetical calculations were made using some of the data points from event 42. On the assumption of ±8% uncertainty in Δ_A, figure 46 shows the dependence of b and R uncertainty on b for three representative values of uncertainty in r due to focusing, namely 3, 5, and 7 percent. The uncertainty in both b and R is seen to vary somewhat with the focusing uncertainty in r for large values of b. For small values of b, both uncertainties are essentially independent of focusing because of the domination of the fixed scaling inaccuracy.

In figure 47, the curves of figures 45 and 46 have been combined in simple fashion. The curves of figure 47 are all straight lines

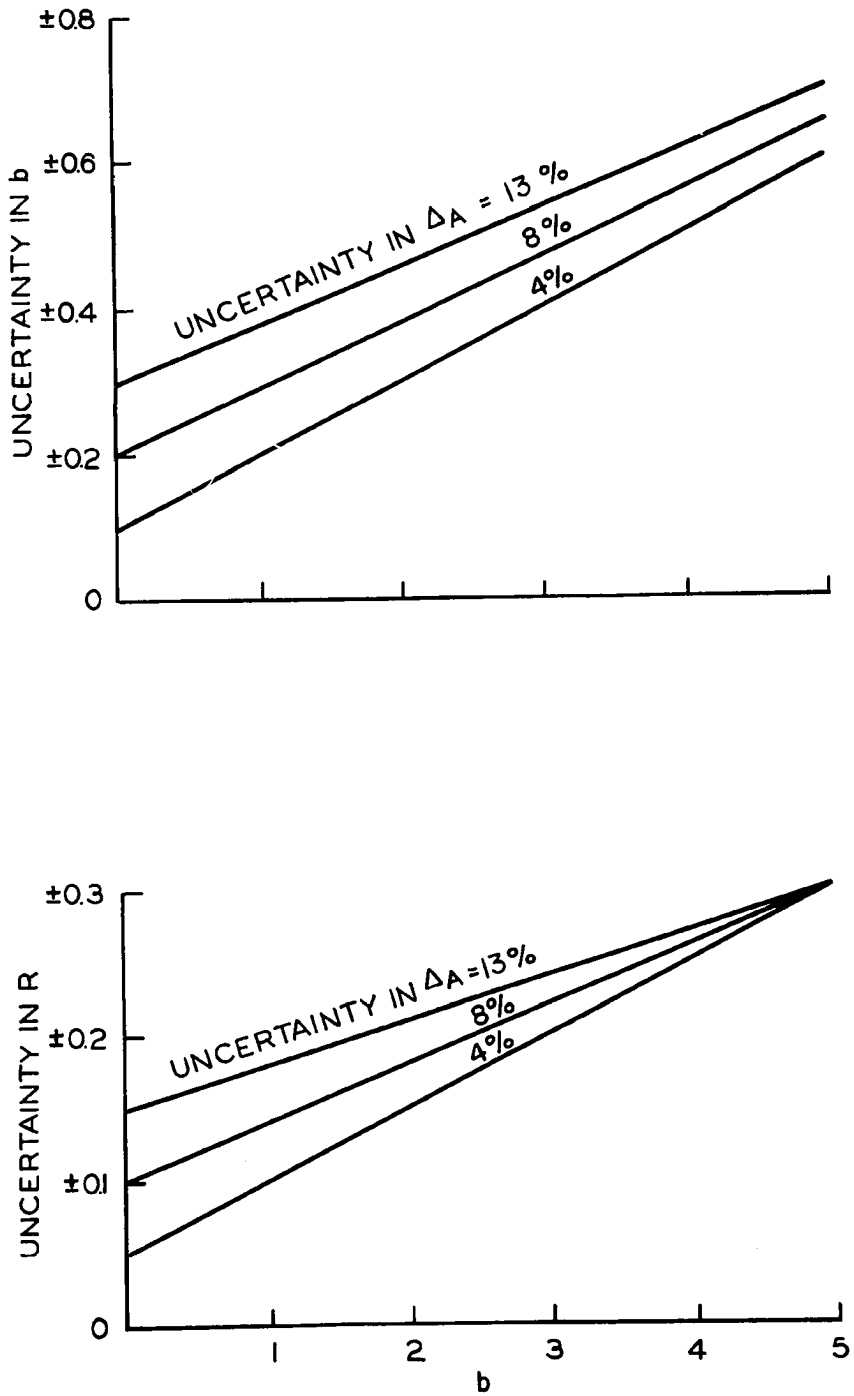

Fig. 45. The effect of uncertainty in Δ_A on the uncertainties in b and R.

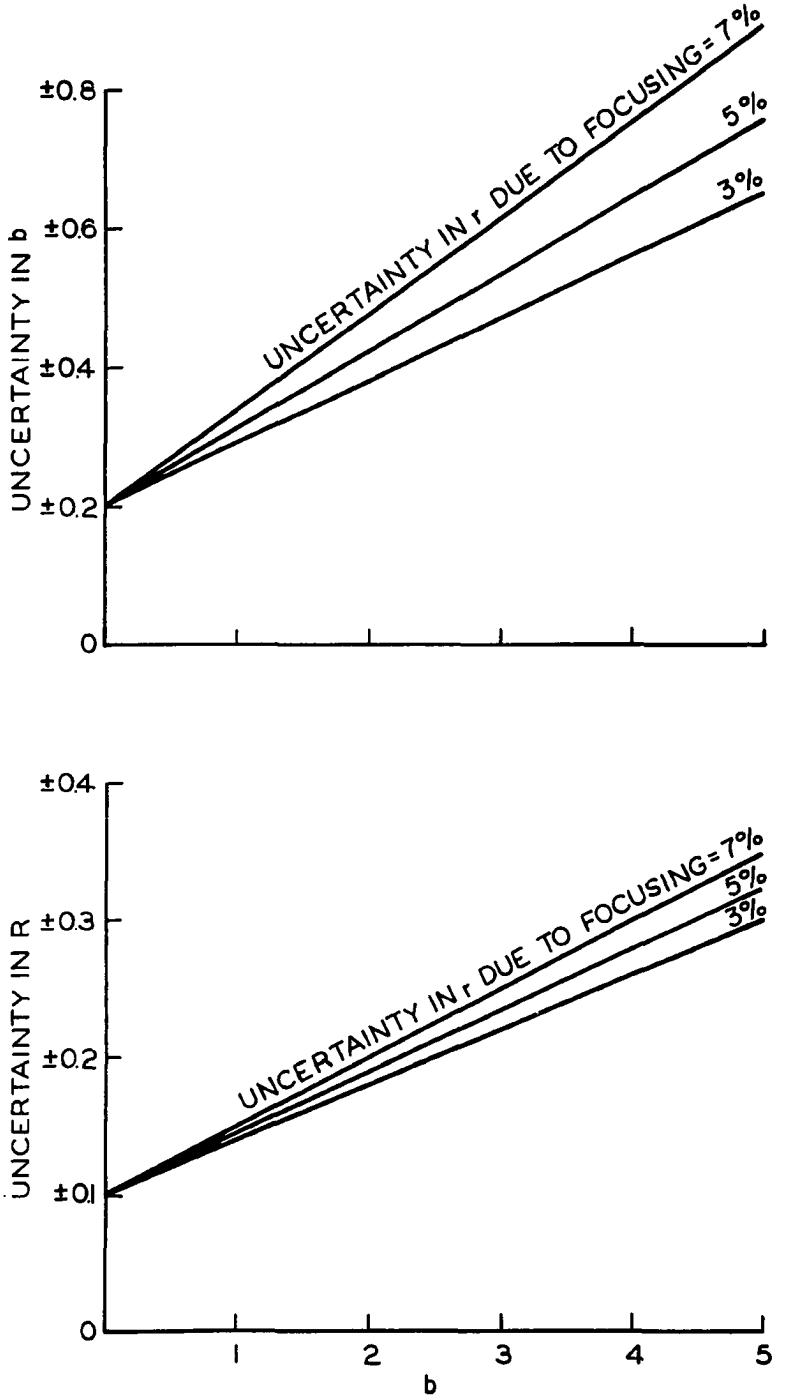

Fig. 46. The effect of focusing uncertainty in r on the uncertainties in b and R.

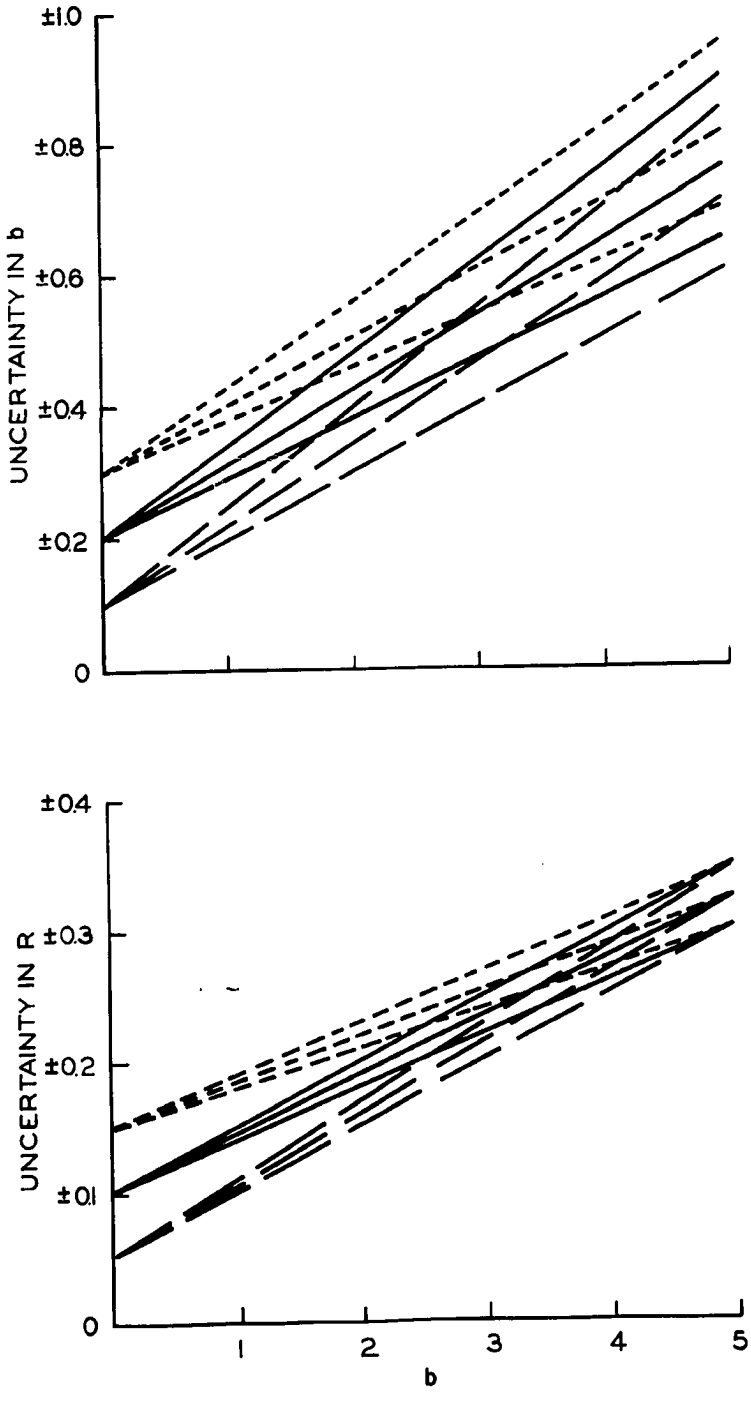

Fig. 47. The range of probable errors in b and R; composite of figures 45 and 46.

whose vertical intercept depends upon the uncertainty in Δ_A and whose slope depends upon both the uncertainty in Δ_A and the uncertainty in r due to ionospheric focusing.

As described in section D3, the focusing uncertainty in r was estimated by averaging the slow variations in output of the phase-sweep interferometer's amplitude channel for one hour before and one hour after each visibility fade event. The uncertainty was calculated for each event, and those for which the focusing uncertainty was greater than about 10% were discarded. The remaining events were divided into three groups according to their focusing uncertainty. Then the empirical equations for the curves of figure 47 were used to compute the uncertainties in b and R. While the equations were derived from consideration of the 220-meter baseline interferometer results, they were used also to estimate the uncertainties in R for the 110 and 330 meter baselines. Table 3 summarizes the equations used for calculating uncertainties in b and R for the various ranges of uncertainty in Δ_A and r.

TABLE 3a

UNCERTAINTY IN COHERENCE RATIO

Uncertainty in r due to focusing	Uncertainty in Δ_A		
	4%	8%	13%
2.2% - 3.5%	$\pm$(0.10 + 0.10b)	$\pm$(0.2 + 0.09b)	$\pm$(0.3 + 0.08b)
3.6% - 5.9%	$\pm$(0.10 + 0.12b)	$\pm$(0.2 + 0.11b)	$\pm$(0.3 + 0.10b)
6.0% - 10.4%	$\pm$(0.10 + 0.15b)	$\pm$(0.2 + 0.14b)	$\pm$(0.3 + 0.13b)

TABLE 3b

UNCERTAINTY IN WAVEFRONT AUTOCORRELATION

Uncertainty in r due to focusing	Uncertainty in Δ_A		
	4%	8%	13%
2.2% - 3.5%	$\pm$(0.05 + 0.050b)	$\pm$(0.10 + 0.040b)	$\pm$(0.15 + 0.030b)
3.6% - 5.9%	$\pm$(0.05 + 0.055b)	$\pm$(0.10 + 0.045b)	$\pm$(0.15 + 0.035b)
6.0 -10.4%	$\pm$(0.05 + 0.060b)	$\pm$(0.10 + 0.050b)	$\pm$(0.15 + 0.040b)

Table 4 gives the experimental results for visibility fade event number 42, from the last four columns of table 2, together with the uncertainties calculated from the equations of table 3.

TABLE 4

68 MHz WAVEFRONT RESULTS FOR EVENT 42

68, 100 fringe #	b	R_1	R_2	R_3
1	2.21 ± 0.32	0.65 ± 0.16	0.78 ± 0.16	0.36 ± 0.16
2	0.87 ± 0.19	1.00 ± 0.10	0.34 ± 0.10	-0.05 ± 0.10
3	1.22 ± 0.22	0.74 ± 0.11	0.56 ± 0.11	-0.02 ± 0.11
4	2.07 ± 0.31	1.00 ± 0.16	0.84 ± 0.16	0.34 ± 0.16
5	0.61 ± 0.16	0.86 ± 0.08	0.50 ± 0.08	0.36 ± 0.08
6	0.29 ± 0.13	0.84 ± 0.06	0.38 ± 0.06	0.24 ± 0.06
7	0.02 ± 0.12	0.57 ± 0.05	0.37 ± 0.05	0.25 ± 0.05
8	0.56 ± 0.16	0.86 ± 0.08	0.42 ± 0.08	-0.01 ± 0.08
9	0.70 ± 0.17	0.72 ± 0.08	0.46 ± 0.08	0.14 ± 0.08
10	3.21 ± 0.42	0.71 ± 0.21	0.58 ± 0.21	0.63 ± 0.21
11	4.42 ± 0.54	1.17 ± 0.27	0.68 ± 0.27	0.90 ± 0.27

E3 Ionospheric autocorrelation function and optical depth

From the results given in table 4, the optical depth and ionospheric autocorrelation were computed using equations 3-64 and 3-65 respectively. It will be recalled that the optical depth is numerically equal to the variance of phase across a plane at the base of the ionospheric scattering layer. To retain cognizance of the dual nature of this quantity, we shall retain the term optical depth and the mathematical notation $\overline{\theta^2}$. Now equation 3-65 yields directly the spatial autocorrelation function of the radio-frequency phase across the base plane. However, equation 3-67 states that the autocorrelation of phase is identical to $\rho_x(\xi)$ under the assumptions made in development of equation 3-63. $\rho_x(\xi)$ is the spatial autocorrelation function (parallel to the instantaneous interferometer baseline) of the ionospheric structure responsible for the observed visibility fade. The results of calculating optical depth and ionospheric autocorrelation for each of the eleven standard averaging periods of event 42 are given in table 5, along with calculated uncertainties. The computer program used for these calculations is given in Appendix 3b.

TABLE 5

IONOSPHERIC RESULTS FOR EVENT 42

68; 110 Fringe #	ξ_1	ξ_2	ξ_3	$\overline{\theta^2}$	$\rho_x(\xi_1)$	$\rho_x(\xi_2)$	$\rho_x(\xi_3)$
1	101 meters	202	303	$0.37^{+0.05}_{-0.04}$	$0.69^{+0.15}_{-0.16}$	$0.81^{+0.15}_{-0.09}$	$0.40^{+0.17}_{-0.17}$
2	102	204	306	$0.77^{+0.13}_{-0.11}$	$1.00^{+0.07}_{-0.06}$	$0.43^{+0.16}_{-0.11}$	$-0.08^{+0.16}_{-0.15}$
3	103	206	309	$0.60^{+0.09}_{-0.07}$	$0.79^{+0.10}_{-0.10}$	$0.63^{+0.11}_{-0.11}$	$-0.03^{+0.15}_{-0.15}$
4	104	208	311	$0.39^{+0.06}_{-0.04}$	$1.00^{+0.13}_{-0.14}$	$0.86^{+0.14}_{-0.14}$	$0.39^{+0.17}_{-0.18}$
5	104	209	312	$0.97^{+0.20}_{-0.14}$	$0.91^{+0.05}_{-0.07}$	$0.62^{+0.09}_{-0.10}$	$0.48^{+0.10}_{-0.11}$
6	105	210	315	$1.49^{+0.49}_{-0.27}$	$0.91^{+0.04}_{-0.05}$	$0.56^{+0.11}_{-0.10}$	$0.40^{+0.13}_{-0.11}$
7	106	212	317	$3.93^{+\infty}_{-1.83}$	$0.86^{+0.14}_{-0.13}$	$0.76^{+0.24}_{-0.20}$	$0.66^{+0.34}_{-0.21}$
8	106	213	319	$1.02^{+0.23}_{-0.15}$	$0.91^{+0.06}_{-0.07}$	$0.55^{+0.10}_{-0.11}$	$-0.02^{+0.15}_{-0.13}$
9	107	214	321	$0.89^{+0.17}_{-0.12}$	$0.80^{+0.07}_{-0.08}$	$0.57^{+0.09}_{-0.10}$	$0.21^{+0.12}_{-0.12}$
10	107	214	322	$0.27^{+0.04}_{-0.03}$	$0.74^{+0.19}_{-0.21}$	$0.61^{+0.20}_{-0.21}$	$0.66^{+0.20}_{-0.21}$
11	108	216	324	$0.20^{+0.03}_{-0.02}$	$1.15^{+0.23}_{-0.14}$	$0.70^{+0.26}_{-0.27}$	$0.91^{+0.24}_{-0.26}$

In addition to numerical results, the computer program for ionospheric parameters provided graphical outputs. Figure 48 shows the graphical results for event 42. In the top strip are shown the wavefront autocorrelation functions $R(\xi)$ and the coherence ratio b. The bottom strip shows the ionospheric autocorrelation functions $\rho_x(\xi)$ and the optical depth $\overline{\theta^2}$. The computer plotted one value of b and one value of $\overline{\theta^2}$, plus the associated error bars, for each standard averaging period during the event. Smooth curves then were drawn in by hand to indicate the development of coherence ratio and optical depth as functions of time. Time is given at the bottom of each strip in hours and decimals, 150° WMT.

Above and slightly to the left of each value of b, the wavefront autocorrelation function for the corresponding averaging period is shown. The computer plotted three values of R, corresponding to the three effective interferometer spacings, for each period plus the associated error bars. It also provided the reference value of unity for zero spacing. From the computer-plotted values of R, it was possible to sketch wavefront autocorrelation functions out to a few hundred meters, as shown in the figure.

Above and slightly to the left of each value of $\overline{\theta^2}$, the ionospheric autocorrelation function for the corresponding period is shown. Again, the computer plotted the data points and error bars, the suggested functions being drawn in by hand. Defining the scale, ξ_o, of ionospheric irregularities as that distance at which the structural autocorrelation function drops to e^{-1}, one can obtain the scale from the functions shown. Further, the error bars on the three values of $\rho_x(\xi)$ allow estimation of

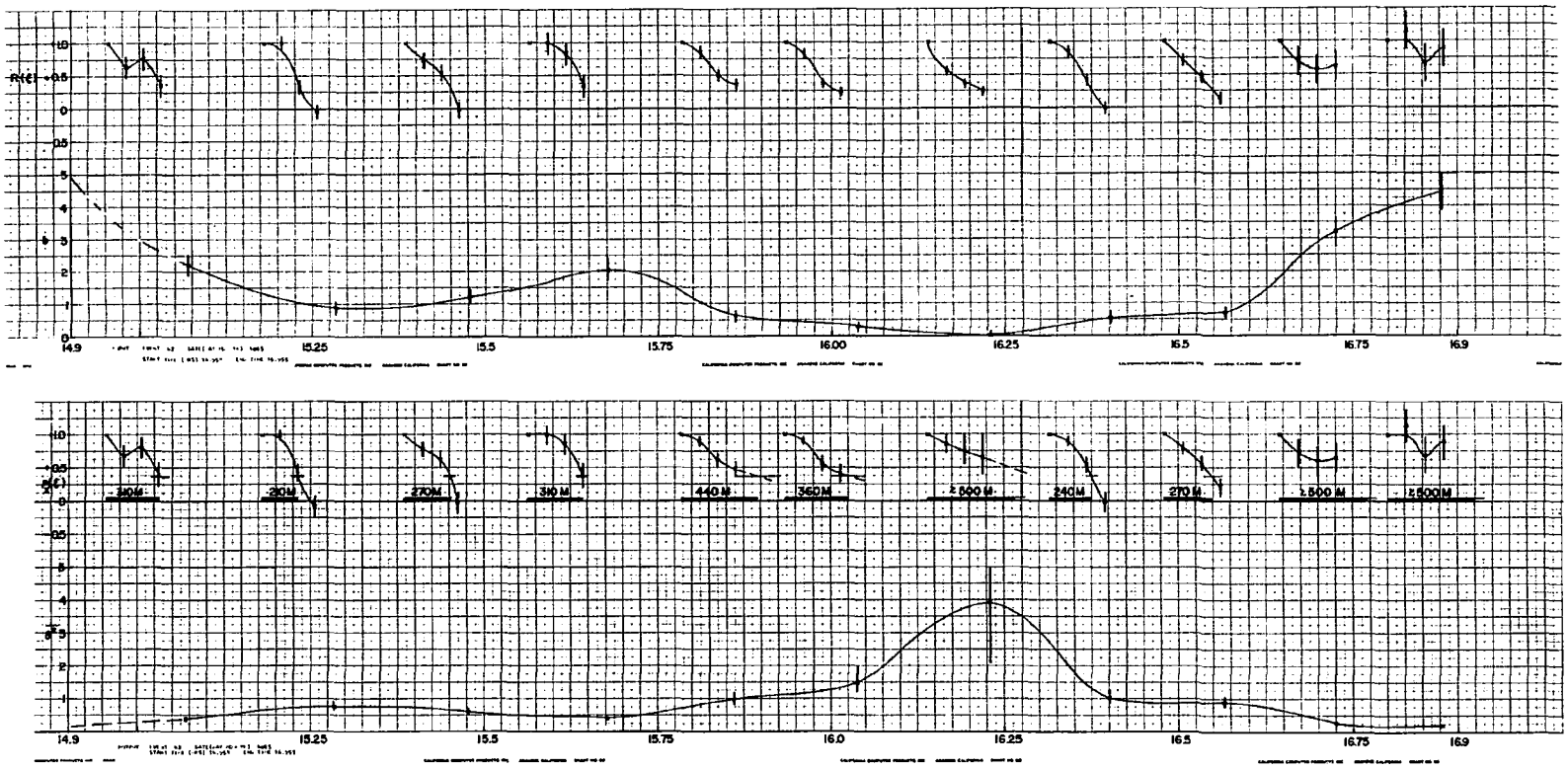

Fig. 48. Graphical computer results for event 42. Top, 68 MHz wavefront autocorrelation function and coherence ratio as functions of time. Bottom, ionospheric structural auto-correlation function and 68 MHz optical depth as functions of time.

the uncertainty in ξ_o. The error bars for ξ_o are shown in figure 48 as horizontal lines intersecting the ionospheric autocorrelation functions. The scale of irregularities for each averaging period is indicated by the heavy horizontal bar beneath the corresponding ionospheric autocorrelation function, with the numerical value in meters indicated.

E4 Frequency Dependence of the Scattering Process

With the 68 MHz optical depth determined, it becomes possible to test the frequency dependence of $\overline{\theta^2}$ by comparing visibility at the same spacing on several frequencies. According to equations 3-16 and 3-63, visibility is related to $\overline{\theta^2}$ and $\rho_x(\xi)$ as follows:

$$r = \exp\left[-\overline{\theta^2}\,(1 - \rho_x)\right] \qquad 4\text{-}6$$

The autocorrelation function ρ_x of the electron density, of course, is not dependent upon the observing frequency. The optical depth $\overline{\theta^2}$ is, however. Hence, the ratio of the logarithms of visibility at the same spacing on frequencies of f_1 and f_2 is as follows:

$$\frac{\ln r(f_1)}{\ln r(f_2)} = \frac{\overline{\theta^2(f_1)}}{\overline{\theta^2(f_2)}} \qquad 4\text{-}7$$

Now, if $\overline{\theta^2}$ is related to frequency by a power law, then equation 4-7 becomes

$$\frac{\ln r(f_1)}{\ln r(f_2)} = \left(\frac{f_1}{f_2}\right)^n \qquad 4\text{-}8$$

where n is the spectral index of the scattering process.

If equation 4-8 were plotted on log-log paper, the result of course would be a straight line with slope n. Figure 49 is essentially such

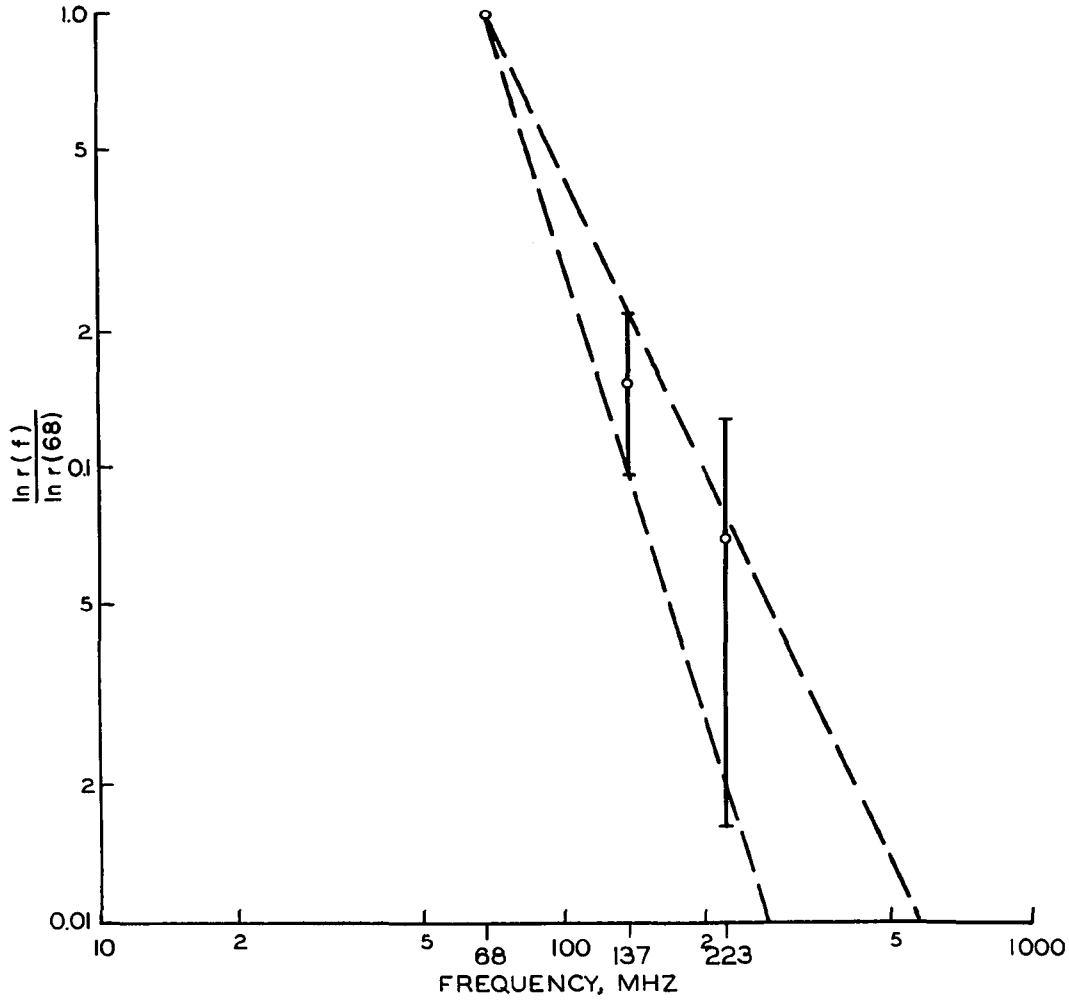

Fig. 49. Frequency dependence of the logarithm of equal-spacing visibility for one fringe of event 42.

a plot for a single fringe of event 42, with f_2 taken as 68 MHz and the abscissa representing the observing frequency f_1. The error bars were computed from the estimated uncertainty in scaling visibility at 137 and 223 MHz and do not take into account the uncertainty of scaling visibility at 68 MHz or the effects of ionospheric focusing at the higher frequencies. Within the limits of the indicated error bars, any spectral index from -2.1 to -3.4 is consistent with the observations.

Event 42 was not a favorable one for determing frequency dependence. Deeper fades provide a better opportunity for this determination. When the visibility on any frequency is near unity, taking the logarithm of visibility results in a small number. Small uncertainties in visibility then produce large uncertainties in the ratio of logarithms, which constitutes the ordinate of figure 49. Even in deep fades, it was found that the 223 MHz visibility seldom departed appreciably from unity for more than one or a few standard averaging periods during the event. In Chapter V, we shall return to the matter of frequency dependence, using only the most deeply faded fringes of selected events. Figure 49 is presented as an example of the procedure and corresponds to the most deeply faded standard fringe of event 42, namely fringe number seven.

E5 Discussion of the Results

Figures 37, 38, 39 and 48 demonstrate several points pertinent to the interpretation of radio-star visibility fades. First, compare figure 37 with channel two of figure 38. The unsmoothed record shows a complicated period of scintillation beginning about 1500. One could not say with certainty, however, that a sustained visibility fade began before

about 1544. From the smoothed trace, on the other hand, it is clear that the fringe visibility at 68 MHz on a spacing of 330 meters was depressed between about 1502 and 1531 in addition to the later period of well-defined fading. For a reasonable degree of accuracy in quantitative scaling of visibility, of course, the smoothed record is indispensible, but previous workers have not made use of this simple expedient.

Now, according to equation 4-1, there are two prerequisites to observation of a visibility fade on a complex-information interferometer: both the coherence ratio and the wavefront autocorrelation must decrease from their undisturbed values of infinity and unity, respectively. The experimental problem is to separate the effects of these two variables, which we have done by introducing essentially independent pure-amplitude information.

Note the variation of 68 MHz visibility on spacings of 330 and 220 meters, as given respectively in channels one and two of figure 39. Now compare the development of the averaged visibility (heavy lines) with the development of the coherence ratio b in figure 48. The developments are essentially identical. Thus, from a qualitative point of view, the variation of fringe visibility portrays the variation of coherence ratio (for values of b not too near zero). For quantitative determination of the coherence ratio, of course, the wavefront autocorrelation must also be found. If the coherence ratio becomes small, fringe visibility is essentially identical to wavefront autocorrelation at any given spacing. This condition holds, for instance, in fringe number seven.

Now, the coherence ratio is defined as the ratio of nonscattered to scattered flux. A record of coherence ratio versus time, then, yields information concerning ionospheric scattering which is analagous to the information concerning ionospheric absorption obtained from a riometer. A riometer records the fraction of total flux which escapes absorption in the ionosphere. By the same token, a plot of the quantity (b/b+1) would record the fraction of total flux which escapes scattering in the ionosphere. The optical depth of the ionosphere, considered as a purely scattering medium, is given by $\overline{\theta^2} = \ln (1 + b^{-1})$. Thus, the plot of $\overline{\theta^2}$ given in figure 48 is analagous to a plot of absorption in decibels. In fact, multiplying $\overline{\theta^2}$ by approximately four yields directly a quantity which might be termed "the scattering in db."

Let us turn our attention now to the autocorrelation functions shown in figure 48. With only four points available for drawing each curve, there is of course quite limited information contained in them. Still, at least in the seven center-most scaling periods of the event, the data allow drawing smooth autocorrelation functions with a considerable degree of confidence. While there are definite changes in shape of the curves from one scaling period to another, they all remain positive or very nearly so and are monotonically decreasing, except possibly near the ends of the event. For the most part, they could be approximated rather closely by either a gaussian or an exponential function.

The monotonic decrease of the ionospheric autocorrelation functions shown in the lower strip of figure 48 are characteristic of a random

scattering layer, devoid of quasi-periodicity.[1] The scale implied by the functions varied from about 210 meters to well beyond the greatest scale measurable, probably greater than 500 meters. Clearly the experimental limitation imposed by the use of only three interferometer spacings at 68 MHz was a serious one. Even with this limited experiment, however, an interesting fact is evident concerning the relationship between scale size and optical depth.

The dominant feature of the optical-depth development during event 42 was a sizeable increase during fringe number seven, which corresponds to the period between 1608 and 1619. Figure 37 shows that this period represents the most well-developed stage of the overall event. Now, reference to the top strip of figure 48 shows that the well-developed stage was brought on by a decrease in coherence ratio with very little change in the wavefront autocorrelation for spacings of 220 and 330 meters. Because of the manner in which the wavefront autocorrelation depends upon the optical depth and the structural autocorrelation function of the scattering layer, this set of circumstances must be accompanied also by an increase in structural autocorrelation. Such an increase is displayed in the ionospheric autocorrelation function $\rho_x(\xi)$ for fringe number seven.

The development of $\rho_x(\xi)$ in fringes six, seven, and eight of event 42, then, reveals the surprising result that the most obvious and well developed stage of the visibility fade was produced not by a decrease

---

[1] We shall see in Chapter V that positive, monotonic autocorrelation functions are the exception rather than the rule in the disturbed auroral ionosphere.

but rather by an increase in the size of ionospheric scatterers in the line of sight. That is, a short-term increase in the structural autocorrelation distance of the ionosphere in the direction parallel to the effective baseline of our interferometers actually was accompanied by a decrease in the autocorrelation distance of the overall complex wavefield received at the ground.

How can the above result be explained? The answer is contained in equation 3-66, the pertinent points of which are given by the following proportionality:

$$\overline{\theta^2} \propto K \tau_o t \overline{(\Delta N)^2} \qquad 4\text{-}9$$

In 4-9, t is the geometric thickness of the scattering layer, $\overline{(\Delta N)^2}$ is the variance of electron density in the layer, and K and τ_o are determined by the component of the ionospheric autocorrelation function in the direction of the line of sight. Now, the ionospheric autocorrelation functions given in figure 48 relate to a direction perpendicular to the line of sight. Without assuming isotropic irregularities, per se, let us suppose that the general shape of the x-direction functions is essentially the same as those for the z direction and that any growth or decrease in scale takes place isotropically.

Note that the function $\rho_x(\xi)$ for fringe six of event 42 displays no periodicities and can be approximated closely by a gaussian function. In this case, $K = \sqrt{\pi}$, as shown in section D2 of Chapter III. For fringe seven, there are no periodicities evident, and $\rho_x(\xi)$ can be approximated by an exponential function. In this case, K = 2, as shown in D3 of Chapter III. Since no periodicities are evident, τ_o is simply

the statistical scale of the irregularities along the line of sight. Now figure 48 shows that the statistical scale in the direction parallel to the effective baseline increased from about 380 meters to some value probably greater than 500 meters between fringe six and fringe seven. For isotropic growth, then, the factor $K\tau_o$ increased by a factor of at least $\frac{2 \times 500}{\sqrt{\pi} \times 380} = 1.5$ between fringes six and seven. This change, in itself, would produce a 50% increase in the optical depth of the layer, thus decreasing the coherence ratio and contributing to the development of the main stage of the visibility fade.

We see, then, that the increase in scale of the line-of-sight irregularities is not only consistent with the decrease in fringe visibility observed shortly after 1600 in figure 37 but that it actually contributed to that decrease. In fact, this contribution alone is sufficient to raise the value of $\overline{\theta^2}$ measured in fringe number six to the value indicated by the bottom of the uncertainty bar in fringe number seven of figure 48. In order to raise $\overline{\theta^2}$ to the value actually measured in fringe seven, an additional contribution is required from an increase in the factor $t\overline{(\Delta N)^2}$. That is, either the thickness of the scattering layer or the strength of the scattering irregularities - or both - also must have increased.

Excessive length of the $\overline{\theta^2}$ uncertainty bar, as in fringe seven of event 42, arises inevitably for small values of b, due to the relation between optical depth and coherence ratio. The uncertainty bars on $\rho_x(\xi)$ also are increased for small b for the same reason, but nowhere near so seriously. For $b = 0$, $\rho_x(\xi)$ is undefined, but its limit is

unity so long as $R(\xi)$ is not zero. It will be recalled that the condition $R = b = 0$ results in zero visibility. Thus, if visibility had gone to zero or had become negative during fringe seven for any spacing, the discussion above would be invalid. It did not, however, as can be seen readily be referring to the traces of figure 38 between 1608 and 1619.

It is important to note that negative visibility is precluded by equation 3-16, which was developed as equation 28 by Bramley (1955). This result is based on assumption of a gaussian distribution for phase at the base of the scattering layer (not, however, on assumption of a gaussian autocorrelation function). As pointed out in section E1, no clear-cut cases of significantly negative visibility have been noted in the present work. A systematic search ought to be carried out for such instances. If clearly negative visibility should occur, it would indicate violation of the assumption of a gaussian phase distribution and imply that the ionospheric process involved is probably of a more ordered nature than a large number of independent scatterings.

CHAPTER V

RESULTS

VA OBSERVATIONS AND SELECTION OF EVENTS

At the outset of this work, it was hoped that a year's observations would yield about 25 recognizable visibility fades. Actually, between 5 November 1964 and 27 December 1965, 133 such events were observed and scaled. Other visibility fades surely occurred during this period but were not scaled for one reason or another. There were, of course, data losses due to equipment failure and radio interference. A greater number of fades was omitted from scaling because of obviously excessive refractive effects. That is, there were times when visibility fades due to small-scale scattering were clearly discernible on the records but when quantitative scaling would have been futile because of focusing and defocusing by larger structure.

In the initial selection of fades for scaling, subjective criteria were used, and they were not very rigidly observed. The 68 MHz, 330-meter, phase-switch interferometer records were inspected visually for fades. The selection criteria were aimed at providing useable quantitative information and not at establishing the statistics of event occurrence, etc. Thus, in general, it was required that the visibility be depressed by at least about one-half (as estimated by inspection) at the peak of the event and that the overall event last for at least about ten minutes. Events which met these requirements but which were accompanied by large refractive effects were recorded but not scaled. On the other hand, particularly clear-cut fades were recorded and scaled even

if they failed to meet one of the criteria. These fades typically were short ones in which there was little or no complication due to focusing, such as the event of 19 November 1965, shown in figures 19 and 23.

Throughout the period of observation, all of the interferometers employed operated with gratifying reliability. Furthermore, interference was not a serious problem. Occasional discrete-frequency interference sources were observed. These were escaped either by slight changes in observing frequency or bandwidth or else through the cooperation of individuals transmitting the interfering signals. One unfortunate instance of interference occurred on 16 June 1965. On that day, Cassiopeia A was essentially lost at 68 MHz and 330 meters spacing for many hours, due to visibility fading. On that same day, a military field exercise began in the Fairbanks area. A communications channel set up for the exercise interferred with observations on our prime instrument - the phase-sweep interferometer operating at 68 MHz with 220 meters spacing. This instrument was wider in bandwidth than the 68 MHz phase-switch interferometers and thus more susceptible to interference. By the end of the day, the interference had been identified and eliminated, but by that time, the ionospheric condition which had produced the fading also had disappeared. On this occasion - as on all other occasions - prompt and willing cooperation was received from the U.S. Army, Alaska, in identifying and removing the source of interference.

More troublesome than discrete-frequency interference sources were occasional periods of broad-band radiation from the power-line

transformer installation serving the field site. This interference was easily removed but usually involved some delay in arrival of a power-line crew, and the condition usually recurred after a few months. More troublesome still were frequent, short power interruptions. While the interferometers recovered and operated normally after power failures, problems arose with the analogue-to-digital converter used for recording pure-amplitude information. Thus, when power failures occurred, useable amplitude data were lost until manual adjustments were made. Since most visibility fades occurred at night and the field site was not normally manned then, many fades were observed for which amplitude information was not recorded in useable form.

The output of the A/D converter was recorded on paper tape by means of a Tally digital punch. The punch proved to be the least reliable piece of equipment in the entire complex of instruments used in the experiment. Many hours of down time were suffered due to mechanical wear in the tape drive assembly. The same problems often recurred, and they were repairable with little complication, but each breakdown required several hours of repair effort, and occasionally it was necessary to wait for parts.

Due primarily to the short power interruptions, secondarily to the mechanical punch problems, and occasionally to other factors, reliable pure-amplitude information was available in useable form for only slightly more than half of the 133 visibility fades recorded on the complex-information interferometer channels. Thus, 70 events remained after data reduction. Inspection of the results of data reduction and

calculation of uncertainties revealed 12 additional events which were considered unreliable for quantitative determination of ionospheric parameters. Thus, the number of fades available for analyses was 58 - still more than twice the number hoped for at the onset of the work.

VB LIMITATIONS IMPOSED BY THE ASSUMPTIONS

B1 The Assumption of Stationarity

The development of Chapter II depends upon the assumption of stationary statistics. Since we are here determining spatial characteristics of the ionosphere from observations taken in time sequence, a rigorous discussion of the requirements of stationarity would be rather involved. We should have to be careful to distinguish spatial stationarity (or uniformity) from temporal stationarity and relate them both to the concept of ergodicity.

As a practical matter, we need only be concerned with the temporal stationarity of our records. Nonstationarity of the records implies either temporal nonstationarity or spatial nonstationarity (i.e. nonuniformity) of the ionospheric scattering layer whose effects are being observed. We cannot distinguish between these two possibilities any more than we can tell the difference between an ordered ionospheric drift and temporal changes in ionospheric structure.

The test for stationarity is simple. Stationarity requires that all statistical parameters which we measure remain essentially constant from one averaging period to the next. As a matter of observational fact, stationarity seldom existed over the duration of our standard averaging periods. (See, for instance, the discussion of figures 30

and 31 in section C of Chapter IV.) Now, what has been measured are spatial characteristics of the ionosphere - statistical in nature - in a certain region along the line of sight. Lack of stationarity means only that, during the course of a given observation, the spatial characteristics of the region changed somewhat and that our results include some time averaging.

B2 Agreement with the Assumption of Random Phasing

It will be recalled that the fundamental assumption underlying our experimental analysis technique is that the signal received by our interferometers after scattering by the ionosphere may be treated as a random noise signal. In particular, the modulation imposed by the ionosphere must itself be random in nature. According to the discussion of section A of Chapter III, the requisities of this assumption are that the ionospheric structure has a random character, although quasi-periodicity is allowed, and that the distance of propagation after scattering is sufficiently great. If these requisites are met, the received signal is comprised of a nondeviated component and an angular spectrum of scattered components, whose phases are independent and uniformly distributed. That is, we are dealing with a randomly phased angular scatter spectrum.

In Chapter II, we developed the density distributions and resulting average characteristics of the envelope amplitude and phase of a signal arising from a randomly phased angular spectrum. The most general results are the graphical ones given in section D3e of Chapter II. For our application, the most important results are those

summarized in figure 36 of section IV D1. Only interferometrically observed signals which are consistent with the field of graphical intersections displayed, in part, in figure 36 are consistent with the assumption of a randomly phased angular spectrum.

Note that the axes of figure 36 represent wavefront correlation R and coherence ratio b. Values of b are given between zero and five although any positive value of b is consistent with the assumption of random phasing. It was pointed out in section E2 of Chapter IV that experimental uncertainties become excessive for b greater than about five and that our graphical technique can be replaced by an analytical one in this case, anyway. It was for this reason that figure 36 was not extended to greater values of coherence ratio; observational points which fall beyond the top border of the figure are not inconsistent with our model. However, points which fall beyond the bottom border are inconsistent.

Now, in general, the wavefront correlation R is defined between plus and minus one. Hence, experimental points which fall beyond the left-hand margin of figure 36 are consistent with the assumed model so long as they do not correspond to values of R less than minus one. The curves of figure 36, for the most part, were used for establishing the 68 MHz coherence ratio and the value of the 68 MHz wavefront autocorrelation for an interferometer spacing of approximately 220 meters. Now, prior to the present work, considerations of ionospheric scattering nearly always involved assumption of either a gaussian or an exponential autocorrelation function to describe the

scattering structure. Under these assumptions, negative values of wave front autocorrelation would not occur.

No specific form for the various autocorrelation functions has been assumed in the present work. However, against the background of previous theoretical and experimental work, it was not expected that negative values of wavefront autocorrelation were likely - at least on spacings as small as 220 meters. Hence the numerical calculations performed to produce the curves of constant Δ_A in figure 36 were carried out only for values of R between plus one and zero. This turned out to be a mistake, although not an unduly serious one. We shall see in section C1 that negative values of ionospheric structural autocorrelation - and hence of wavefront autocorrelation - do indeed occur. They occur, in fact, for spacings as small as 110 meters and probably smaller.

When experimental points derived from 68 MHz observations with a spacing of 220 meters were found to lie beyond the left border of figure 36, a dilemma was encountered. On the other hand, the observations were fully consistent with the assumption of a randomly phased angular spectrum. On the other hand, means did not exist for accurate determination of the coherence ratio and wavefront autocorrelation. A compromise course of action was chosen. If the point lay close enough to the border that the uncertainty bars entered into the confines of figure 36, the observations were retained and the curves of Δ_A simply were extrapolated a short distance. If the uncertainty bars fell entirely outside the diagram, the point was discarded. About ten percent of the total available data points were regretably discarded for this

reason, including four events which were totally discarded.

Apparent values of wavefront autocorrelation in excess of unity sometimes occurred, due to ionospheric focusing. For the most part, the uncertainty bars derived from observation of slow variations in received flux accounted for these occurrences, and the points were retained. No serious problem of consistency with the assumed model arises in these instances.

The region beyond the bottom border of figure 36 is one of inconsistency with the assumption of a randomly phased angular spectrum. Negative coherence ratio has no physical meaning since zero coherence ratio corresponds to infinite optical depth. Five of the 58 visibility fades used in the analysis were found, on this basis, to be inconsistent with the model during a majority of their standard averaging periods. Among the remaining events, 12% of the standard averaging periods produced data points which, along with their uncertainty bars, fell beyond the bottom border of figure 36.

B3 Interpretation of Inconsistencies

There are two possible reasons for lack of random phasing in the angular spectrum. First, it is possible that the ionosphere is not acting as a random scatterer. Second, it is possible that the scattering structure is indeed random but that it is not sufficiently distant from the observer.

It will be recalled that the immediate effect of ionospheric irregularities on a passing wave (of sufficiently high frequency) is the imposition of spatial phase modulation, as discussed in section D1

of Chapter III. Even if the phase is a random function of position on the wavefront, the corresponding angular spectrum is not randomly phased. It was shown in section D1 of Chapter II that signals corresponding to randomly phased angular spectra also display amplitude variations.

In section A of Chapter III, the propagation of angular spectral components and their resultant waves was discussed. The manner in which spatial amplitude fluctuations develop along the wavefront during propagation was described. It was pointed out that the phase of the angular spectral components tend to become uniformly distributed as the composite wave propagates. A wave leaving a random scattering layer is made up of a large number of angular components, whose phases gradually tend toward "randomization" in subsequent propagation, amplitude variations simultaneously developing in the wavefront. If such a wave were observed before the phases in the angular spectrum had become fully random, a paucity of amplitude fluctuations would be observed.

Now the curves of constant Δ_A shown in figure 36 represent curves of constant amplitude fluctuation which are to be expected from interferometric observation of signals whose angular spectra are randomly phased. It will be noted that the value of Δ_A increases with decreasing coherence ratio. Thus the forbidden region of negative coherence ratio corresponds to excessive rather than insufficient signal amplitude fluctuation. The observed instances of apparently negative coherence ratio, therefore, cannot be explained on the basis of a random scatter-

ing layer whose distance from the ground is too small to allow randomization of the phases in the angular spectrum. They must have resulted, instead, from a scattering layer having nonrandom structure.

VC MEASURED IONOSPHERIC CHARACTERISTICS

C1 Structural Autocorrelation Functions and Scale Sizes

Of the 58 visibility fades retained after calculation of estimated uncertainties, nine were discarded - five because of inconsistency with the assumption of random phasing, as discussed in section B1. As pointed out in section B2, among the 49 remaining events, 12% of the total data were found also to be inconsistent with the assumption. The remaining 88% produced well over 200 ionospheric autocorrelation functions and measurements of 68 MHz optical depth. About 69% of the autocorrelation functions yielded measurements of structural scale size, the remainder yielding lower limits.

The observed autocorrelation functions took a variety of forms. They have been classified according to certain criteria of physical interest. It will be recalled that it has been common practice in the literature to assume either a gaussian or an exponential function to describe ionospheric autocorrelation. These two functions have two recognizable features in common. They are both inherently positive, and they both decrease monotonically. On the other hand, they differ in that the gaussian contains an inflection point and the exponential does not. These features of the gaussian and exponential functions have been incorporated into the classification scheme.

Two major classes of autocorrelation functions were established. The first of these, which we shall refer to as PM, requires that the function remain positive and be monotonically decreasing throughout the range of observation. The PM class was divided into four subclasses. The first, PM1, requires continual (absolute) increase in the (negative) slope. The second, PM2, requires continual (absolute) decrease in the (negative) slope. The third, PM3, allows an inflection point with the slope changing from (absolute) increase to (absolute) decrease. The fourth, PM4, allows an inflection point with the slope changing from (absolute) decrease to (absolute) increase. The exponential and gaussian functions fall in classes PM2 and PM3, respectively.

Figure 50 displays three examples of each of the various PM autocorrelation types. Curves have been drawn through the measured points, with only slight deviations within the confines of the uncertainty bars permitted in a few instances where they seemed called for. Subclassification was made on the basis of best fit to the measured points although many of the examples could have been placed in alternative subclasses by drawing curves which ignore the measured points while remaining within the confines of the uncertainty bars. Relatively clear examples of the subclasses are shown in the right-hand column, more typical examples in the center column, and marginal examples in the left-hand column.

On the basis of the best-fit curves, 76 of the 227 autocorrelation functions classified fulfilled the requirements for PM classification.

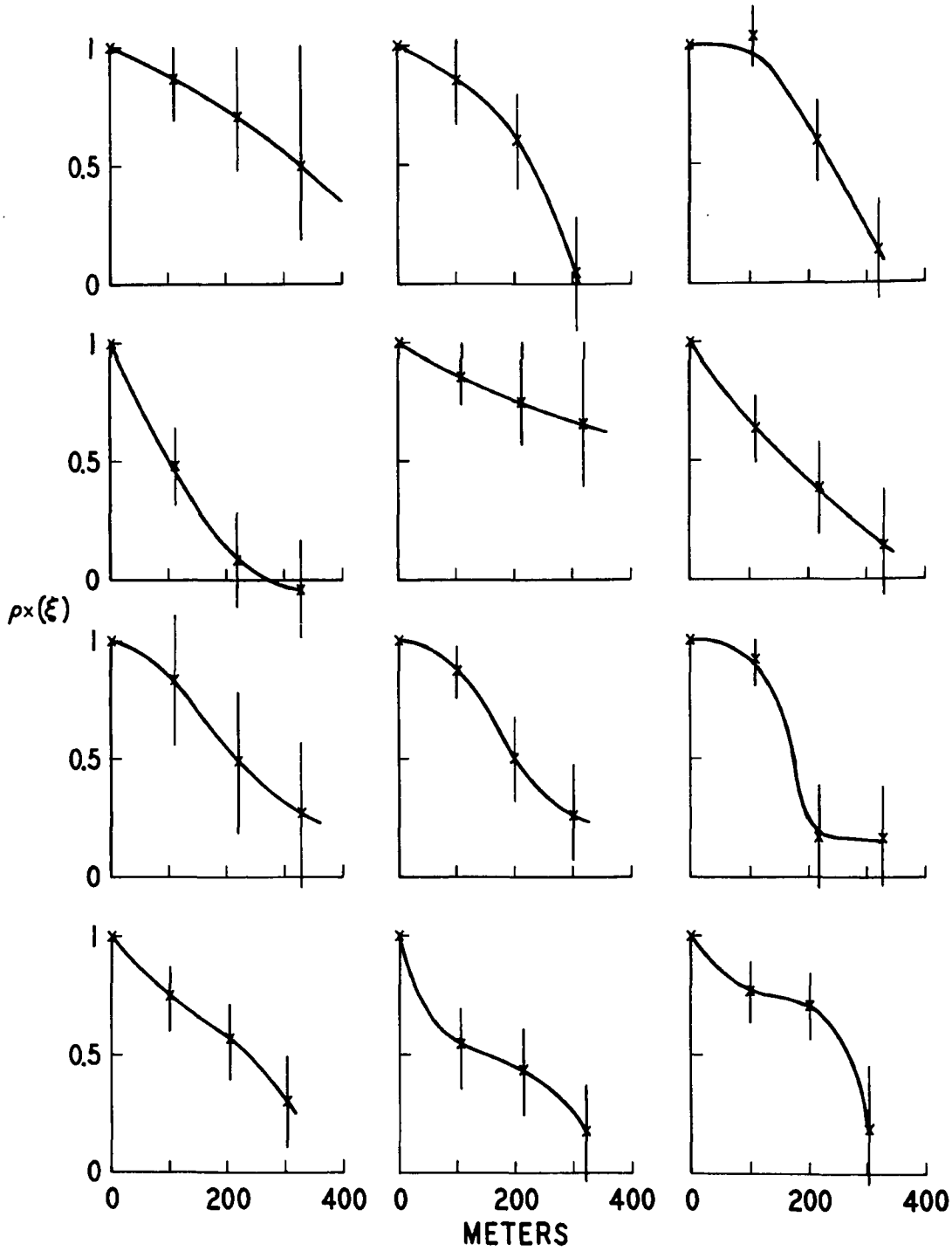

Fig. 50. Examples of positive, monotonic ionospheric autocorrelation functions. Top to bottom; types PM1, PM2, PM3, PM4.

Only six could be classified as PM2, while 29 fell in the PM3 group. The PM1 and PM4 classifications contained 20 and 21 examples, respectively. It will be noted that the PM2's are especially open to reclassification if the actual measured data points are ignored. For instance, the degree of confidence of the center (typical) example, as implied by the uncertainty bars, is about comparable to that of the left-hand (marginal) examples in the other subclasses. The left-hand (marginal) PM2 example could be classified as PM only by slightly relaxing the requirement of remaining positive.

The paucity of examples in the PM2 class represents an experimental argument against using the exponential function to represent structural autocorrelation in discussing the scattering of waves passing through the disturbed auroral ionosphere. (Note that any of our results may or may not relate to ionospheric structure responsible for backscatter. We have made no consideration of backscatter in the work.) The preponderance of classes PM1 and PM3 over classes PM2 and PM4 suggests that sharp-centered irregularities either are not common in the undisturbed auroral ionosphere or else do not contribute appreciably to scattering of waves propagating through it.

About 38% of the PM autocorrelation functions fell in the PM3 class, which is the class consistent with the gaussian function. Clearly the gaussian more often approximates the autocorrelation function of the disturbed auroral ionosphere than does the exponential. However, only about one-third of the 227 autocorrelation functions classified fulfilled the requirements for PM classification. The other two-thirds

failed either to remain positive or to be monotonically decreasing, or both. Since it is to be expected that all the functions approach zero at great distance, negative-going examples may be expected to become nonmonotonic even if they do not do so within the range of observation.

The second major class of autocorrelation functions, which we shall call NM, contains all those functions which failed to qualify as PM's. They were divided into two subclasses, NM1 and NM2. Both the NM1 and NM2 functions fulfill the requirements of NM classification when classified on the basis of the curve chosen as best fit to the measured data points. This procedure is the same as that used in the PM classification. The NM1 class fulfills the additional requirement that it would be impossible, within the confines of the uncertainty bars, to draw a curve which would fail the NM requirements.

Figure 51 displays some examples of NM autocorrelation functions. The top six functions are NM1's and the bottom six are NM2's. Of the 151 NM autocorrelation functions found, 68 qualified as NM1's. Thus 30% of all the observations classified could not be interpreted as representing positive and monotonically decreasing autocorrelation functions without exceeding the estimated experimental uncertainties. Another 36%,the NM2's, could be so interpreted within the limits of experimental uncertainty but not on the basis of best-fit curves. Thus, only 34% appear to be consistent with two necessary conditions for description by a gaussian (or exponential) function. Furthermore, there is no guarantee that the 34% would remain positive and monotonic if observed over a greater range of distances.

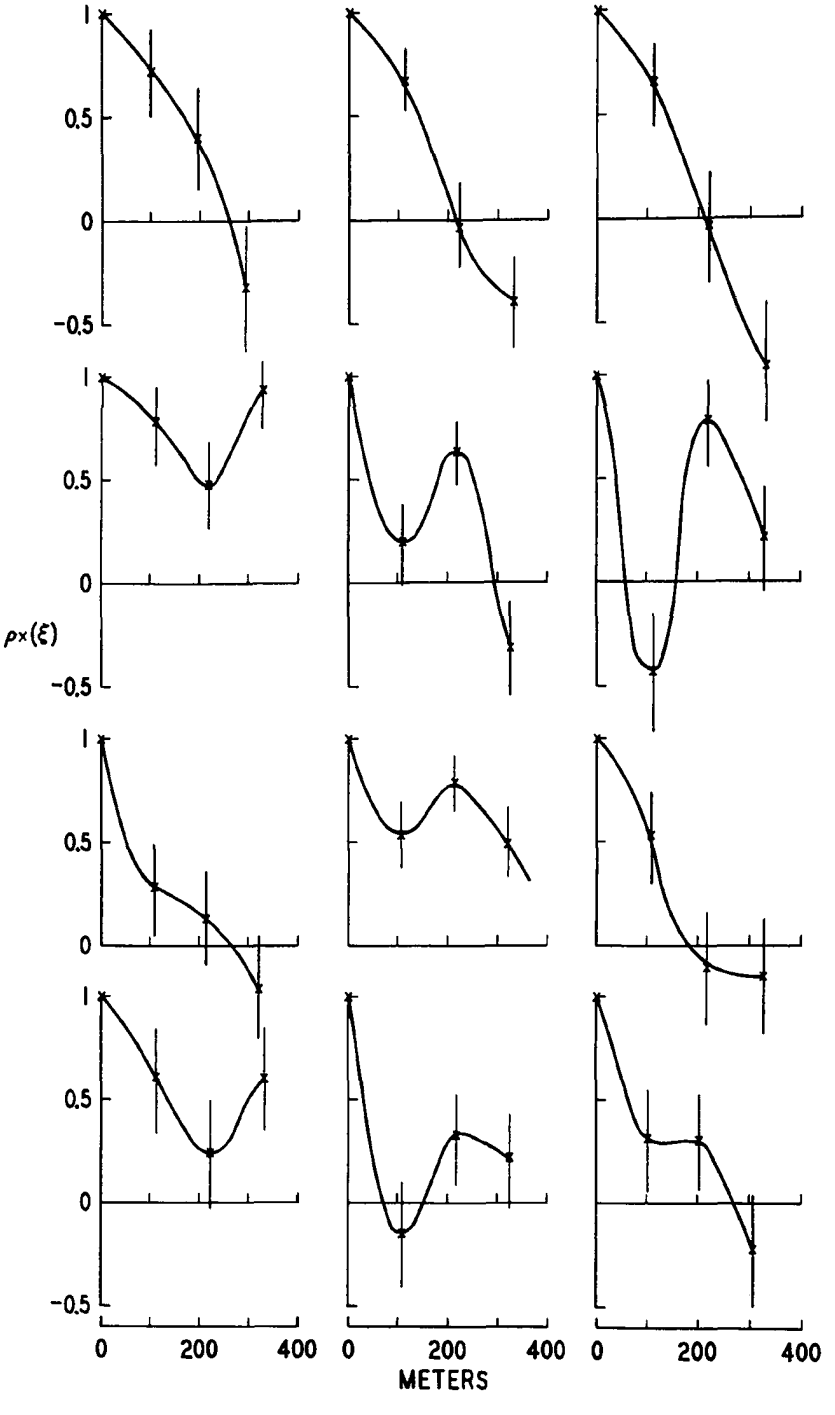

Fig. 51. Examples of ionospheric autocorrelation functions which are not positive and monotonic. Top six: type NM1. Bottom six: type NM2.

In view of the above results, it appears that the gaussian autocorrelation function does not often serve as an accurate description of the small-scale irregular structure of the disturbed auroral ionosphere. A more accurate description requires use of nonmonotonic, probably mildly oscillatory, functions. In other words, the disturbed auroral ionosphere displays quasi-periodicity in its hectometric-scale structure.

At times, the periodicity of the auroral ionosphere becomes so well developed that radio waves received after scattering in it cannot be assumed to have randomly phased angular spectra. We saw in section B that certain observations made in the present work were not consistent with the condition of random phasing because of overdevelopment of signal amplitude fluctuations. This was interpreted as the result of differential phase shifting by nonrandom structure, sufficiently distant from the observating interferometer that amplitude fluctuations became well developed in subsequent propagation. This condition would ensue, for instance, if there was a favored size in the scattering structure and the distance to the observer approximated the focal length of the favored-size irregularities, considered as lenses.

Now, as discussed in detail by Ratcliffe (1956) and described briefly in section A of our Chapter III, periodic structure produces alternate conditions of predominantly phase and predominantly amplitude fluctuation as a wave propagates after scattering. Thus, under conditions of well defined periodicity, we may expect sometimes to observe excessive phase scintillation just as we sometimes observe excessive amplitude scintillation. Such instances have indeed been noted in the present work. Thus, approximately 6% of the observations led to the

physically meaningless result that ionospheric autocorrelation dropped below minus one.

The observations of excessively negative autocorrelation invariably were accompanied by measurements of small optical depth. It will be recalled that small optical depth corresponds to large coherence ratio and that this condition results in virtual identity between ionospheric autocorrelation and wavefront autocorrelation. Thus the observations in question would result in data points in the upper half or so of figure 36 but far beyond its left border - in fact, to the left of R = -1. That is, they arose from observations of excessive visibility reduction (small r) in the presence of insufficient amplitude fluctuation (small Δ_A).

Now, in discussing the relationship between figures 34, 35, and 36, we pointed out that lines of constant visibility approximately represent curves of constant phase-difference variance $\overline{\eta^2}$. Comparing the three figures, it is easily seen that excessive visibility reduction results from excessive phase fluctuation (large $\overline{\eta^2}$). Thus the observation of physically meaningless values of ionospheric autocorrelation arose under conditions where the ratio of phase to amplitude fluctuation was too great to be consistent with the condition of random phasing in the angular spectrum.

Now, when excessive phase fluctuation is observed, one cannot say with certainty that the condition arose from non-random scattering rather than from insufficiently distant random scattering. However, when coupled with the complimentary observations of excessive amplitude fluctuation, the nonrandom interpretation seems to be the more likely.

Combining the two types of observations, it appears that at least about one-fifth of the total observations analysed in the present work can be explained on the basis of ionospheric structure having quasi-periodicity too well defined to produce randomly phased angular spectra. For the most part, this condition arose during isolated averaging periods in visibility fades which otherwise were consistent with the condition of random phasing. In these instances, the well defined quasi-periodicity appeared to be sustained for a few minutes at a time. In a few events, however, the nonrandom condition accounted for a majority of the fade duration.

In the 227 individual observations (standard averaging periods) which were consistent with the assumption of random phasing, the resulting autocorrelation functions were used to estimate the scale of the fade-producing irregularities. If the scale was greater than about 350 meters, no direct measurement was possible with the interferometer spacings employed. Fifty-nine of the 227 autocorrelation functions used in the analysis fell in this category. Figure 52 shows a histogram of the distribution of scales measured in the remaining 168 instances. There is a predominance of scales in the range from about 75 to about 225 meters, with 70% of the observations falling in this range. For quasi-periodic structure,this range of scales corresponds to spatial half-wavelengths between about 120 and 370 meters.

The measured scale sizes from which the distribution of figure 52 was constructed were obtained from smoothed autocorrelation functions such as those shown in figures 50 and 51. Since the smallest inter-

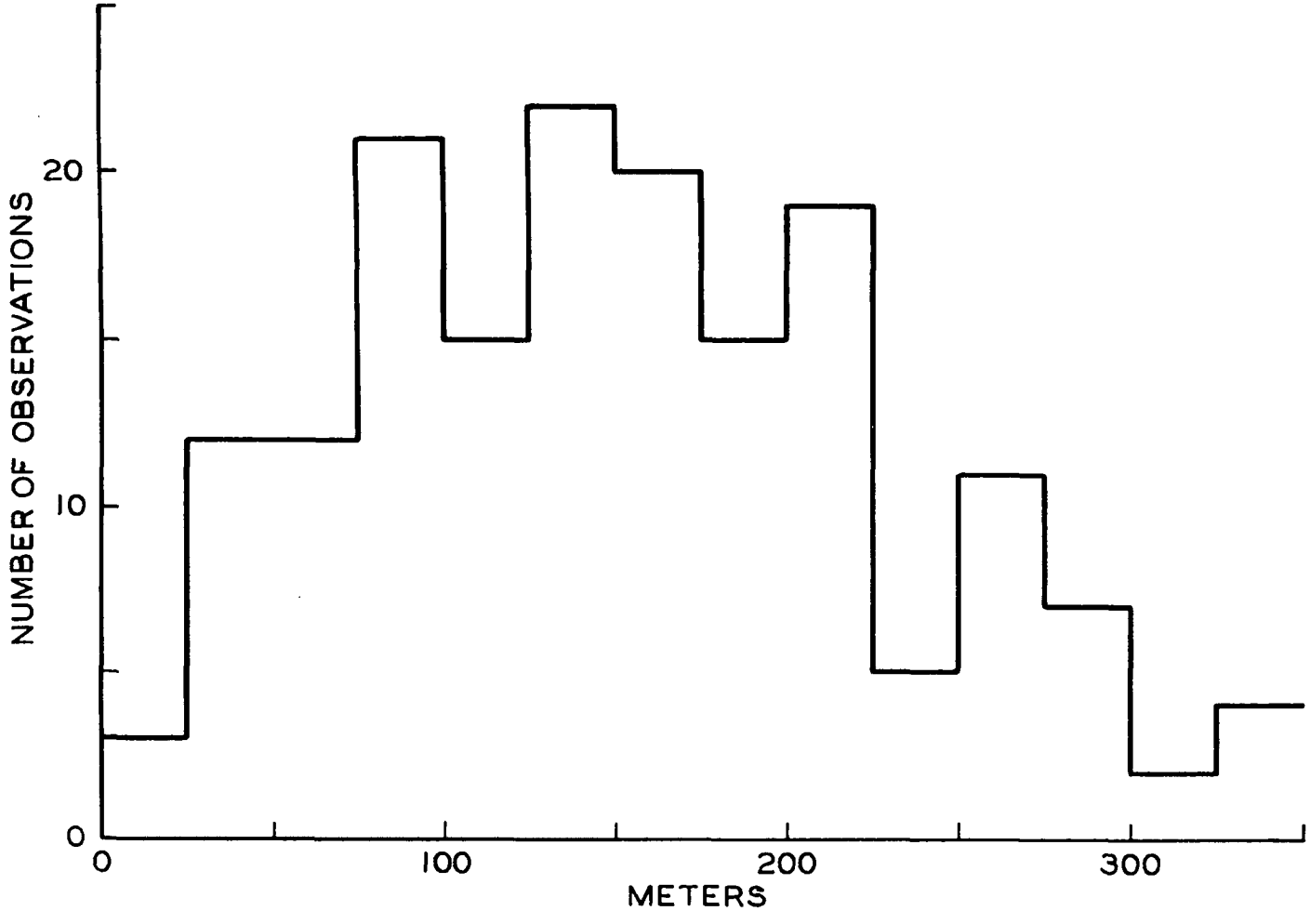

Fig. 52. Number distribution of 168 measured ionospheric scale sizes.

ferometer spacing used in the experiment was on the order of 100 meters, one cannot be certain that structure smaller than this did not occur. The distribution in figure 52 pertains only to the ionospheric structure which was responsible for the tri-spacing visibility observed. It does not preclude the occurrence - even the common occurrence - of smaller structure. If such structure occurred during the observed visibility fades, however, it either was extremely periodic or else it did not represent a major component in the ionospheric structural spectrum. In no case was the autocorrelation function observed to drop to zero within 100 meters and remain there.

C2 Optical Depth at 68 MHz

Corresponding to each autocorrelation function obtained, a single value of 68 MHz optical depth was measured. Figure 53 is a histogram showing the number distribution of values obtained. By far the majority of measurements produced values of optical depth less than unity. However, figure 53 includes the results of all measurements and not just those from well-developed portions of visibility fades. For instance, recall figures 37 and 48 in section IVE, relating to event number 42. A majority of the values of optical depth shown in figure 48 falls below the $\overline{\theta^2} = 1$ line. However, these same values correspond to portions of the record shown in figure 37 which do not readily show visibility fading. Reduction in visibility for these periods was detectable only from the smoothed interferometer records shown in figure 38. The period of obvious visibility fading in figure 37 corresponds to the period of

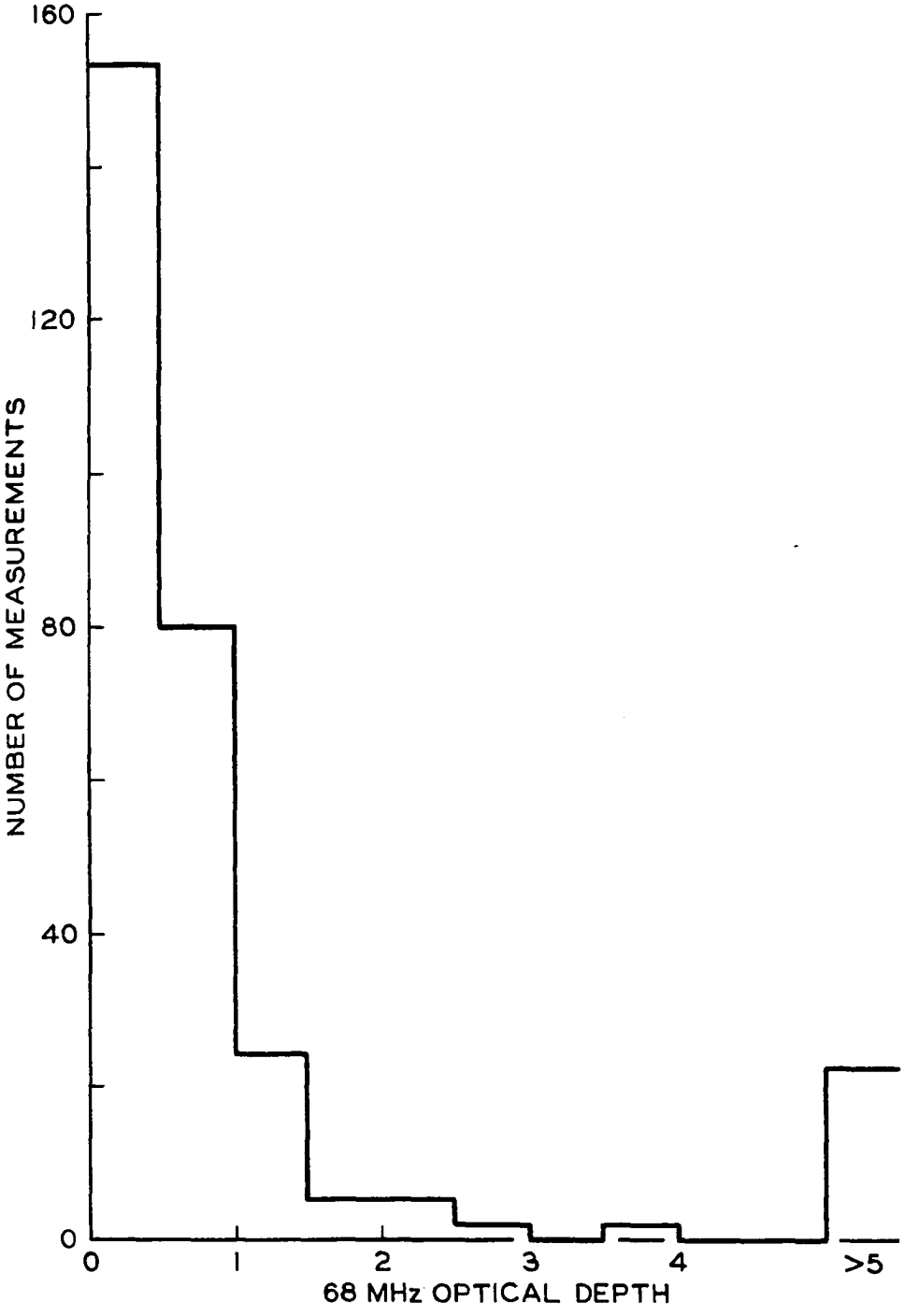

Fig. 53. Number distribution of 288 measured values of 68 MHz optical depth.

optical depth greater than unity in figure 48.

A better indicator of the values of optical depth to be associated with readily recognizable visibility fades is the maximum value measured in each of the 49 events used in the analysis. Thirty of the events, or about 60%, showed maximum values of optical depth in excess of unity. Fourteen, or 28%, showed maximum values greater than five. It is pointed out that, due to the relationship between optical depth and coherence ratio, the measured values of optical depth lie near the bottom end of the estimated uncertainty bars for large values of $\overline{\theta^2}$. When the measured value approaches about five, it becomes essentially an experimental lower limit on the actual optical depth.

Hence, one can conclude that a majority of well-developed visibility fades represents a condition of the ionosphere corresponding to a scattering optical depth in excess of unity, often considerably in excess of unity. It will be recalled that in event 42, a contributing factor to the increase in optical depth during the well-developed portion of the fade appeared to be an increase in scale of the scattering irregularities. This behavior was observed in about two-thirds of the visibility fades displaying a maximum optical depth greater than unity. Thus, obvious periods of visibility fading often - although not always - are brought on in part by short-term increases in the scale of decametric and hectometric ionospheric structure, rather than by decreases in the scale.

C3 Frequency Dependence of Optical Depth

As shown in section E4 of Chapter IV, the frequency dependence of

optical depth can be displayed as a plot of the logarithm of visibility versus frequency. In particular, if the ratio of ln r(f) to ln r(68 MHz) is plotted versus frequency on log-log paper, a power law frequency dependence for optical depth will result in a straight line whose slope is the spectral index. Figure 54 shows such a plot for 31 measurements of three-frequency visibility. Thirty-one visibility fades which showed a measurable decrease in visibility at all three observing frequencies, 68, 137, and 223 MHz, were chosen for the graph. The ratio of logarithms for the standard averaging period showing the greatest visibility reduction at 68 MHz was then chosen for each event.

Figure 54 shows considerable spread in the results. However, the spread arose mostly from experimental uncertainties stemming from the usually small decrease in visibility at the higher frequencies. The measurements do not allow a firm statement concerning the variability of spectral index from one instance to another. The circled points in figure 54 are the median measurements at each frequency. They fall on a common straight line passing through the necessary value of unity at 68 MHz, yielding a spectral index of -1.75. If the spectral indices implied by each of the data points shown are averaged, the same result is obtained. Furthermore, an essentially indentical result is obtained if the 137 and 223 MHz results are averaged independently. The dashed line in the figure, corresponding to a spectral index of -2.00, is shown for comparison.

The results of figure 54 imply that the frequency dependence of

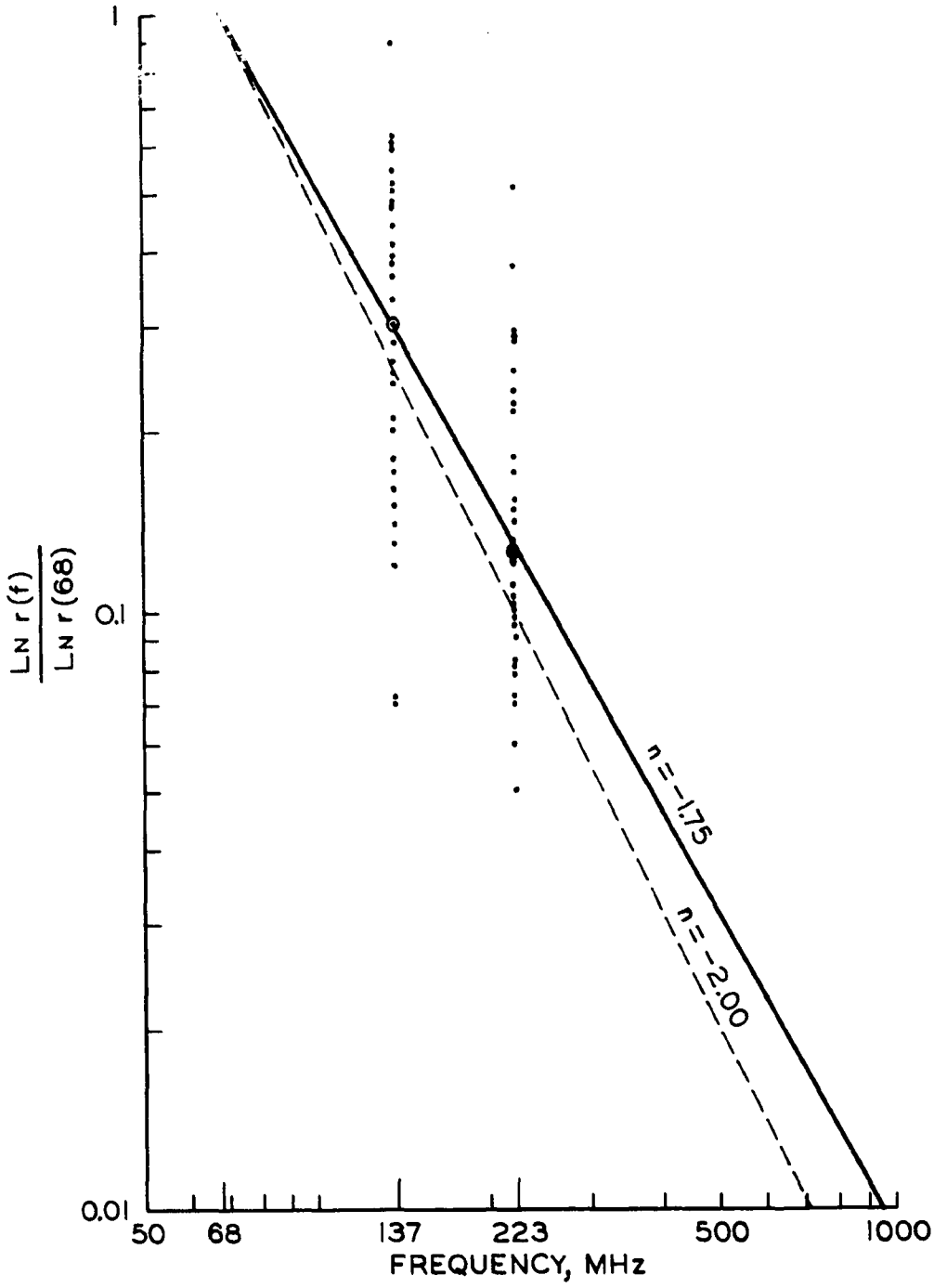

Fig. 54. Frequency dependence of the logarithm of equal-spacing visibility.

VHF visibility fades can be described by a negative power law for optical depth. The average spectral index may be slightly less negative than -2.00, but at least to the nearest integral value for spectral index, the optical depth may be said to obey an inverse frequency-squared law. A spectral index of -2.00 is to be expected for scattering in regions of the ionosphere where the collision frequency is completely negligible. The effect of collisions during the differential refraction process responsible for the scattering is to make the spectral index slightly less negative.

An attempt was made to extend the measurement of spectral index down into the HF band, using upper transit observations at 26 MHz. The experimental accuracy achieved, however, did not provide sufficient dynamic range in the measurement of visibility to make the attempt successful. The events picked for data reduction were chosen on the basis of 68 MHz visibility decrease, as described in section C of Chapter IV. Most of these events resulted in essentially complete loss of the source at 26 MHz, through the combined effects of visibility fading and absorption. Absorption usually could account for only about a quarter or less of the total decrease in 26 MHz record amplitude.

A number of instances of measurable fringe reduction at 26 MHz were noted at times when the higher frequency records did not satisfy the quantitative requirements established for event identification. These instances would allow extension of the spectral index to 26 MHz at the expense of simultaneous 223 and possibly 137 MHz observations, but such extension has not been carried out in the present work.

Suffice it to say here that the ionospheric optical depth for scattering continues to increase fairly steeply with decreasing frequency between 68 and 26 MHz, as is to be expected. Nonetheless, a number of extraterrestrial sources have been observed successfully from College at 26 MHz with an interferometer baseline of 215 meters. The observations nearly always display some scintillation, however.

VD THE RELATION OF VISIBILITY FADES TO THE AURORA

VHF radio-star visibility fades at high latitude are a direct manifestation of the overall auroral phenomenon.

During part of the 1964-65 northern auroral observing season and during most of the 1965-66 season, photometric observations were carried out as a part of the present work. Photometers were mounted on one of the antennas tracking the radio star. In February, March, and April of 1965, two photometers with one-degree circular fields of view were employed, using narrow-band filters centered at 5577 Angstroms and 4278 Angstroms. From October 1965 through April 1966, two photometers with three-by-ten-degree rectangular fields of view were employed, using narrow-band filters centered at 4278 Angstroms and 4858 Angstroms (hydrogen beta).

The narrow fields of view were used the first year in order to restrict reception of information as nearly as was feasible to the direction of the radio star under track. The wider fields were employed in the 1965-66 observations in order to achieve sufficient sensitivity for detection of the relatively weak hydrogen emission. In order to have consistent data on the two photometers, identical fields were

employed. In all instances, the fields of view were centered along the line of sight to the radio source.

When the photometer passbands were centered at 5577 and 4278 Angstroms, essentially identical traces were obtained. When 4278 and H_β were observed, considerable differences were noted, although the two emissions usually were detected together. The H_β records are being used to investigate the influence of ionospheric proton bombardment on the scintillation of radio stars. This work is only in a preliminary stage, and we shall not be concerned with it here. For the present discussion, we shall consider only the 5577 and 4278 Angstrom emissions, arising from the influx of auroral electrons.

Records from six and one-half months of line-of-sight photometric observations have been inspected. During this period, 52 visibility fades were observed while the photometers were in operation. The photometers detected auroral emission during 47 of these events. During the remaining five events, the sky was overcast. The College all-sky camera detected aurora through the clouds on two of these five occasions. Thus, during 90% of the visibility fades, auroral light was detected along the radio line of sight; during an additional 4%, there definitely was aurora in the sky, possibly in the line of sight; and on the remaining 6%, it was impossible to detect aurora because of cloud cover. It seems extremely likely that aurora was present along the line of sight to the radio star during 100% of the visibility fades observed.

The above results imply that formation of ionospheric irregularities small enough, strong enough, and numerous enough to produce visibility fades at 68 MHz with interferometer spacings of a few hundred meters

requires the influx of auroral-producing electrons.

The details of the relationship between the ion-density irregularities and the auroral luminosity are apt to be quite complicated. In the present work, we have concentrated on obtaining quantitative information about the ion-density structure from radio observations. Concerning the aurora, the prime objective has been to establish whether visibility fades constitute an aurorally produced or associated phenomenon, per se, or rather simply represent a general characteristic of the ionosphere in the auroral zones. We have found the first alternative to be the correct one.

Concurrently with the present experiment, observations have been carried out which, it is hoped, will lead to some insight concerning the detailed relation between the irregularities observed radio-interferometrically and the optical observed aurora. Thus, during the 1965-66 auroral season, a high sensitivity television camera, mounted alongside the photometer on one of the tracking antennas, has been for line-of-sight auroral observations. Many thousands of feet of movie film, exposed at ten frames per second, have been obtained. Preliminary inspection of the television films and all-sky-camera films suggests that visibility fades may be exclusively a feature of the active phases of auroral displays. Systematic analysis of the films has yet to be carried out, however.

In a number of instances, the simpler photometric observations have revealed a close relation between development of the irregularities and development of line-of-sight auroral luminosity. One of the clearest

of these instances occurred on the night of 17/18 April 1965. Figure 55 shows the photometer records for the period of interest along with records from several of the radio interferometers. The very top strip shows the pure amplitude record obtained from the 68 MHz phase-sweep interferometer, operating at a spacing of 220 meters. Next are shown the two photometer records. Three complex-information interferometer records appear below the photometer records. They are, from top to bottom, from the 223, 137, and 68 MHz interferometers having baselines of approximately 220 meters. Note that the time scale on the top three records is different from that on the bottom three. The chart speed for the radio amplitude and the photometer traces was about three times that for the complex-information interferometer traces. The records are aligned in time at the center of the strips.

The 68 MHz records display considerable scintillation activity throughout the period shown. Between about 2330 and 2400, the interference fringes are essentially lost, which constitutes the visibility fade in question. The time of commencement of the fade is most readily determined from the 223 MHz record, it being the least sensitive to prior scintillation activity. The 223 MHz interference fringe starting approximately at 2332 was the first one to be reduced in average amplitude. The time at which the fringe reduction began is marked by the left-most arrow on the photometer trace. This is seen to correspond closely to a brightening of the line-of-sight auroral intensity.[1]

---

[1]The photometer outputs are related approximately logarithmically to auroral intensity.

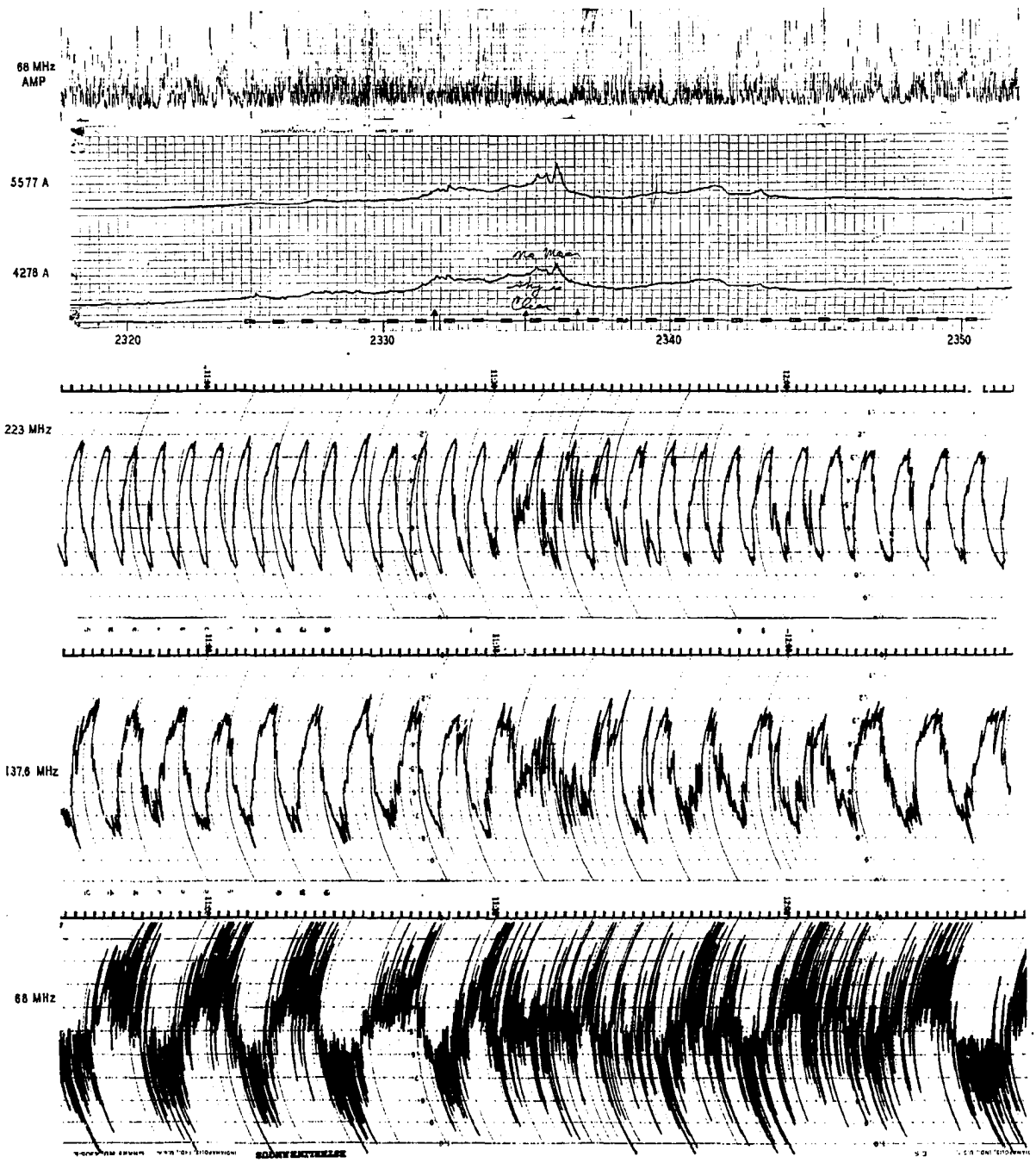

Fig. 55. Example of close association of visibility fading to line-of-sight auroral luminosity.

The next 223 MHz fringe recovered amplitude, but within a few seconds of 2335 the major fade effect commenced. The major effect lasted for one and three-quarters minutes, the period between the center and right-most arrows on the photometer trace. This period corresponded closely to the period of brightest line-of-sight aurora. Simultaneously, the 68 MHz pure-amplitude trace shows a very noticeable decrease in fluctuation. This represents a decrease in the parameter Δ_A and, when taken together with the decrease in fringe visibility, implies a loss of correlation between amplitude fluctuations at the two antennas of the 68 MHz, 220-meter interferometer. There is an attendent decrease in the average level of the pure-amplitude trace, in accord with a prediction of the amplitude distributions developed numerically in Chapter II under the assumption of a randomly phased angular spectrum.

Figure 56 shows the ionospheric structural autocorrelation functions and the optical depth development deduced from the 68 MHz observations. The structural scale varied from about 50 to about 290 meters during the time that it could be measured. Quasi-periodic structure clearly was present during at least a portion of the event. It would be impossible to draw monotonically decreasing autocorrelation functions through the data points of the third and fourth periods, without departing from the uncertainty bars. On the other hand, quasi-periodicity could have been considerably more well developed in periods two through four than that shown in the solid autocorrelation functions. Alternative functions, displaying greater periodicity, are indicated by the broken lines, for instance. The spatial wavelengths to be

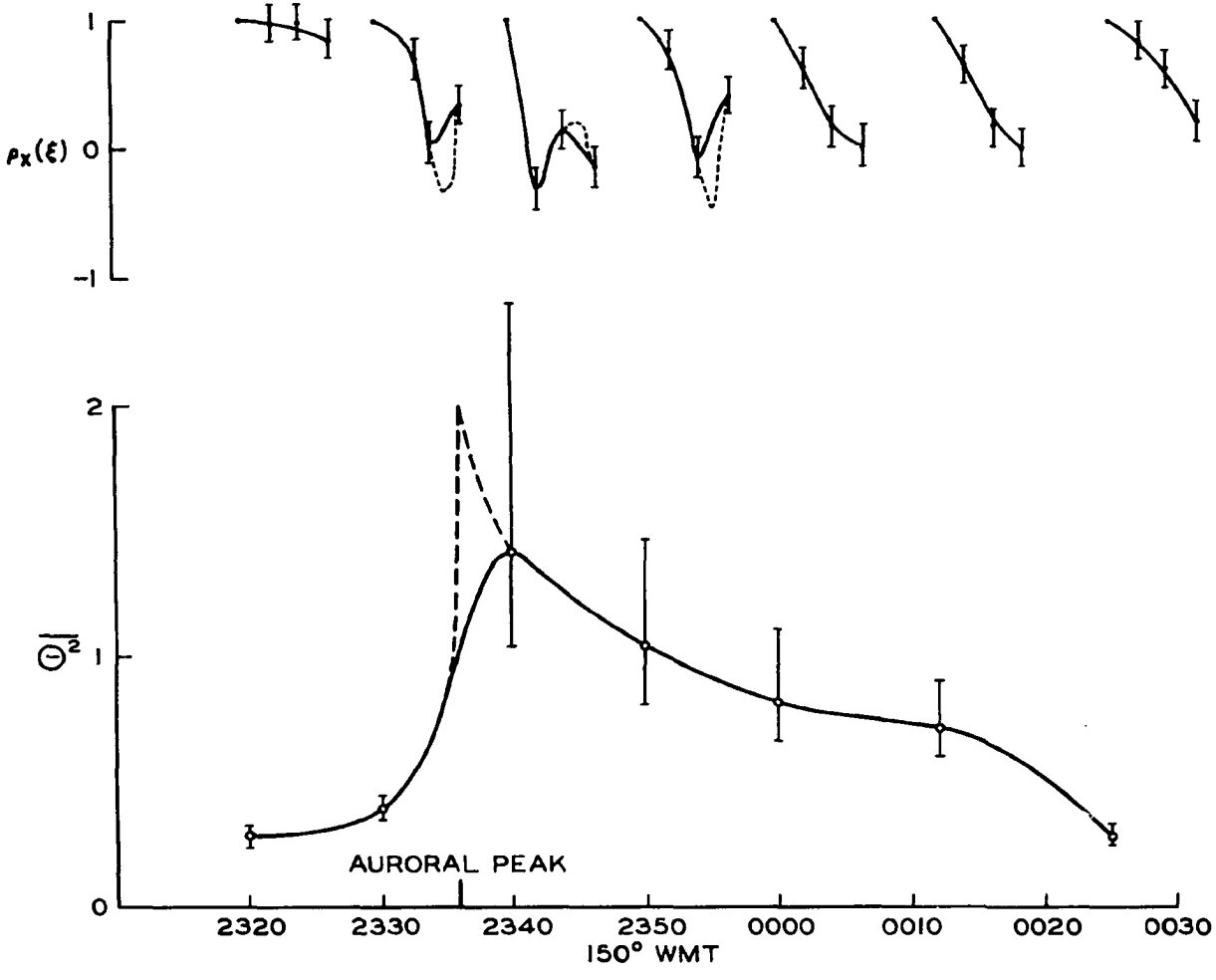

Fig. 56. Development of the ionospheric autocorrelation function and the 68 MHz optical for the event of figure 55.

associated with the suggested quasi-periodicity are on the order of 300 meters.

In contrast to many visibility fades, the present event showed no increase in scale size during the period of peak optical depth. Within the time resolution allowed by our data analysis technique, figure 56 shows that the peak in optical depth coincided with the peak in line-of-sight auroral intensity. The unreduced records of figure 55, of course, show that the time correspondence between auroral luminosity and the radio effects actually was much closer still. It appears that the optical depth increased essentially as an impulse upon arrival of a strong burst of auroral electrons in the line of sight. Since there is no evidence of increase in size of the scattering irregularities, the increase in optical depth must have been caused by an increase in the geometric thickness of the scattering layer, an increase in the strength of ion-density irregularities contained in the layer, or both.

The College all-sky camera film exposed on the night of 17/18 April 1965 shows considerable aurora through varying thin overcast during much of the night. Immediately prior to the visibility fade under discussion, the aurora was concentrated in a band near the zenith. The fade coincided with a northward sweep of the aurora, followed by a sudden brightening of a large part of the sky. The radio star under observation was located north of College in the suddenly luminous part of the sky.

While a large portion of the sky was involved in the auroral activity, the photometer records shown in figure 55 relate to a one-degree cone centered on the radio star. The effective radio resolving power is

determined by the apparent angular size of the source under track. Under undisturbed conditions, the apparent size of Cas A is a few minute of arc. During the visibility fade, ionospheric scattering increased the apparent size to a value comparable with the fringe width of the interferometers employed. This means that radio information was being received from a cone also on the order of a degree in diameter. Thus, the radio and optical information relate to the same small region of the ionosphere.

The scales measured in the present work are comparable with the size of auroral rays, and it seems likely that the fade-producing ionospheric structure is related to the visible structure of auroral forms. It is of some interest to ascertain whether the same ion-density structure is present in the absence of visible ray structure. This work is planned for the near future, using the television film now available. The radio technique developed for the present experiment could be extended to explore other parts of the ionospheric structural spectrum.

VE RESUMÉ OF RESULTS

Table 6 summarizes the quantitative results obtained from observation and analysis of 49 visibility fades. Start and end times are given for each event to the nearest tenth of an hour. The source in all cases was Cassiopeia A, so the hour angle completely fixes the angular position at which each fade occurred. The predominant type of autocorrelation function, listed in the final column, is that single type which occurred during the greatest number of fringe periods of the event. It did not necessarily occur in a majority of the event's periods.

TABLE 6

QUANTITATIVE RESULTS FROM 49 VISIBILITY FADES

Date	Start Time	End Time	Range of Hour Angle	Maximum 68 MHz Optical Depth	Range of Scale Size (Meters)	Predominant Type of Autocorrelation Function
7 Jan. 1965	0354	0430	11.9W-11.5E	1.5	70- 320	PM
7 Jan. 1964	2106	2330	5.1W- 7.5W	3.0	170->350	NM2
10 Jan. 1965	0318	0454	11.5W-10.9E	>5.0	80->350	NM2
12 Jan. 1965	0342	0354	12.0 -11.8E	0.5	200	PM3
16 Jan. 1965	0130	0254	10.1W-11.5W	0.7	190- 360	NM2
12 Mar. 1965	2318	2436	11.5W-11.2E	1.25	65->350	NM
14 Mar. 1965	2218	2306	11.6W-11.6E	0.6	90- 150	NM2
17 Apr. 1965	0418	0600	5.2E- 3.5E	2.2	215->350	PM
17 Apr. 1965	1718	1806	7.8W- 8.6W	0.3	240- 330	--
17 Apr. 1965	1954	2112	10.4W-11.7W	2.0	30->350	PM3
17 Apr. 1965	2124	2248	11.9W-10.7E	1.2	40->350	NM1
17 Apr. 1965	2312	2430	10.3E- 9.0E	1.1	50->350	NM
4 May 1965	1918	1954	10.9W-11.5W	1.0	80->350	NM2
4 May 1965	2142	2206	10.7E-10.3E	2.3	40- 255	NM2
4 June 1965	1454	1654	8.6W- 9.6W	3.9	210->350	NM2
4 June 1965	0406	0518	2.2E- 1.0E	0.8	240->350	NM2
19 July 1965	0200	0430	1.4E- 1.1W	>5.0	140->350	NM2
17 Aug. 1965	0024	0042	1.3E- 1.0E	0.4	200- 240	NM1
17 Aug. 1965	0100	0118	0.6E 0.3E	1.1	90- 175	NM
20 Aug. 1965	0148	0300	0.4W- 1.6W	>5.0	290->350	PM
24 Aug. 1965	2200	2224	3.1E- 2.7E	0.0	--	--
2 Sept.1965	0130	0200	1.0W- 1.5W	1.1	120- 190	NM2
4 Sept.1965	0106	0200	0.7W- 1.6W	>5.0	140->200	NM2
15 Sept.1965	0642	0730	5.0W- 5.9W	0.7	90- 210	--
15 Sept.1965	0730	0906	7.8W- 9.4W	>5.0	100->350	NM2
17 Sept.1965	0024	0112	0.8W- 1.6W	0.4	260- 270	--
26 Sept.1965	0042	0148	1.8W- 2.9W	>5.0	190->350	PM3
27 Sept.1965	0642	1024	7.9W-11.6W	0.9	55- 200	NM1
27 Sept.1965	2230	2330	0.3E	0.7	130- 160	NM
28 Sept.1965	0254	0312	4.1W- 4.4W	0.3	230	NM2
31 Oct. 1965	0548	1012	9.2W-10.4E	>5.0	10->300	NM1
2 Nov. 1965	0342	0424	7.2W- 7.9W	0.4	115	PM4
4 Nov. 1965	0412	0506	7.9W- 8.8W	>5.0	35->300	NM
5 Nov. 1965	2142	2500	1.4W- 4.7W	1.0	30->300	NM
6 Nov. 1965	2236	2300	2.4W- 2.8W	0.0	--	--
7 Nov. 1965	2336	2424	3.5W- 4.3W	1.0	115- 150	PM
13 Nov. 1965	1142	1242	8.0E- 7.0E	1.2	60->350	NM2
15 Nov. 1965	0824	1000	11.2E- 9.6E	1.1	40->350	NM2
16 Nov. 1965	2300	2412	10.6E- 9.4E	0.6	80->350	NM1

TABLE 6 (Cont'd)

Date	Start Time	End Time	Range of Hour Angle	Maximum 68 MHz Optical Depth	Range of Scale Size (Meters)	Predominant Type of Autocorrelation Function
19 Nov. 1965	1948	2006	4.0W- 4.3W	0.0	--	--
19 Nov. 1965	2248	2336	7.0W- 7.8W	0.4	190	NM1
25 Nov. 1965	0512	0536	10.2E- 9.7E	>5.0	310->350	NM2
30 Nov. 1965	0442	0512	10.4E- 9.9E	0.5	270->350	NM1
30 Nov. 1965	0912	1006	5.9E- 4.0E	1.3	60->350	NM1
1 Dec. 1965	0318	0518	11.7E- 9.7E	0.8	50- 260	NM1
4 Dec. 1965	0136	0306	10.8W-11.7E	1.1	40- 150	--
4 Dec. 1965	0642	0718	8.1E- 7.5E	>5.0	50->350	NM1
21 Dec. 1965	0554	0748	7.8E- 5.9E	>5.0	85->350	PM
24 Dec. 1965	0354	0542	9.6E- 7.7E	>5.0	90->350	PM

CHAPTER VI

SUMMARY AND CONCLUSIONS

VIA SUMMARY

In this work we have developed and applied a radio interferometric technique for quantitative description of small-scale structure in the disturbed auroral ionosphere. The technique is based on scattering of radio waves by the structure. In the present case, signals propagating through the ionosphere from the extraterrestrial radio source Cassiopeia A were monitored. The scattering mechanism may be termed differential refraction, and it results in spatial irregularities in the radio-frequency phase of the signal at a plane immediately beneath the scattering layer. Thus, the effect of the structured layer is to render the surfaces of constant phase nonplanar even though the source of the wavefield may be regarded as an infinitely distant point.

At any plane, the wavefield may be described in either of two ways. First, its complex amplitude may be given as a function of position on the plane. If such a description were given at a plane above the scattering layer, the complex amplitude would be found to be constant over the plane. Beneath the scattering layer, irregularities would be found. Second, the Fourier transform of the complex amplitude distribution may be given. The independent variable in the result is an angle measured from the original propagation direction of the wave. The result itself is called the angular spectrum of the wave. Above the scattering layer, the angular spectrum is a Dirac delta funtion at the direction of

propagation. Beneath the scattering layer, it is a measure of the angular breadth of scattering.

The components of the angular spectrum are plane waves, each propagating in its own direction. The angular distribution of power - the angular power spectrum - is the same at any plane beneath the scattering layer. Since the component plane waves are travelling in slightly different directions, however, the distribution of phase in the angular spectrum is different at different planes. That is, the phasors describing the complex amplitudes of the component waves rotate relative to one another as one examines the wavefield along a straight line from the ionosphere to the ground.

While only phase deviations are found across a plane immediately beneath the scattering layer, the relative rotation of component phasors in subsequent propagation causes amplitude deviations to develop at lower planes. That is, a diffraction pattern develops. The distribution of amplitude across any plane could be explored using a simple receiver, i.e., a radiometer. A complete description of the wavefield, however, must include measurement of phase. A radio interferometer is sensitive to both the amplitude and phase distributions of the wave on the plane containing the interferometer antennas.

A phase-switch interferometer measures the temporal covariance of the antenna output voltages. If the distribution of complex amplitude across the ground - i.e., the complex diffraction pattern or complex "shadow pattern" - changes with time, then the interferometer output also is a measure of the spatial autovariance of complex amplitude.

The result is the same whether the pattern drifts across the antenna positions, changes without drifting, or drifts and changes. In any of these cases, the equivalence requires only that the two antenna positions represent typical positions on the wavefront at the ground.

If the spatial autovariance of complex amplitude is measured using interferometers of various antenna spacings, then the spatial autocorrelation function of complex amplitude can be built up.[1] This fact is the foundation of our experimental technique. Using multiple interferometer spacings, several points on the spatial autocorrelation function (i.e., several values of source visibility)[1] at the ground can be established. Now, the spatial autocorrelation (or visibility) of a nonscattered plane wave is unity for any value of spacing. For a completely scattered wave, the autocorrelation drops from unity at zero spacing to zero at infinite spacing. For a partially scattered wave, the autocorrelation function drops from unity to some value between zero and unity.

The value of the autocorrelation of complex amplitude at infinite antenna spacing depends upon the fraction of flux scattered by the ionospheric irregularities. A quantitative measure of the degree of scattering is the ratio of nonscattered to scattered flux, which we defined in Chapter II as the coherence ratio, b. In the angular spectrum, b is the ratio of flux travelling in the direction of pre-scattering propagation to that contained in all other components of the spectrum.

---

[1]See section IIIB and the footnote in section IIID1 for definitions of these various quantities and relations between them.

The rate at which the complex-amplitude autocorrelation function drops from unity to its infinite-spacing value depends upon the width of the angular spectrum, wider-angle components producing smaller structure in the wavefront than narrower-angle components. We defined the wavefront autocorrelation function, $R(\xi)$, as the spatial autocorrelation function of the irregular part of the (complex) wavefront. For any finite value of coherence ratio, the wavefront autocorrelation drops from unity at zero spacing to zero at infinite spacing. The rate at which $R(\xi)$ drops to zero or to some other specified small value, then, is an inverse measure of the width of the angular spectrum, regardless of the degree of scattering.

According to the above, the ratio of flux in the nondeviated component of the angular spectrum to that in the scatter components is given by the coherence ratio b, and the angular width of the scatter spectrum is given by the wavefront autocorrelation function, $R(\xi)$. The angular power spectrum, then, could be specified quite completely if b could be determined by observation with a radio interferometer of infinite spacing and $R(\xi)$ determined for several spacings. Since the angular power spectrum is the same at any plane beneath the scattering layer, one then would have a statistical description of the wavefield immediately after scattering.

Since one cannot build an interferometer with infinite spacing, he must devise some other means for determining the coherence ratio. We showed in development of equation 2-100 how the parameters b and R are related to the (complex) output of a phase-switch interferometer. In

particular, a phase-switch instrument can yield the source visibility, r, which is given by

$$r = \frac{b + R}{b + 1}$$

A phase-sweep interferometer can yield independent (real) amplitude and phase information, which also are related to b and R.

In much of Chapter II, we reviewed and scrutinized the analytical work of Bramley (1951), who developed expressions relating various characteristics of the amplitude and phase to the parameters b and R for the two special cases of very large and very small coherence ratio. The major assumption underlying Bramley's work was that the component phases in the angular spectrum at the ground are independent and uniformly distributed between zero and 2π. This assumption allows application of the work of Rice (1944, 1945), on the statistics of random signals to be applied to the problem of ionospheric scattering.

In section D3 of Chapter II, we showed that Bramley's results could be extended, in principle, to the general case of arbitrary coherence ratio by application of the work of Middleton (1947). Middleton's analytical work on the statistics of random signals is much more general than that of Rice. Unfortunately, the statistical distributions for amplitude and phase which Middleton developed in the general case are extremely complicated. They are so complicated, in fact, as to preclude their usefulness for our problem. Accordingly, a numerical means for attacking the general case of arbitrary coherence ratio was devised. The results were given in section D3E of Chapter II. The

assumption underlying the results is the same as that made by Bramley (1951), namely that the scatter spectrum is randomly phased at the ground.

In section A of Chapter III, we explored the consequences of the assumption of random phasing. We found two requisites of the assumption: that the ionosphere act as a random scattering layer, and that the observing interferometer be sufficiently distant from the layer that amplitude deviations in the wavefront are fully developed. In sections B, C, and D of Chapter III, we related the visibility, $r(\xi)$, the coherence ratio, b, and the wavefront autocorrelation function, $R(\xi)$, to ionospheric parameters. We found that b depends upon the geometric thickness of the scattering layer and on its scattering coefficient. The coherence ratio is related to the optical depth, $\overline{\theta^2}$, of the ionosphere, considered as a purely scattering medium, by

$$\overline{\theta^2} = \ln\left(1 + \frac{1}{b}\right)$$

The parameter $\sqrt{\overline{\theta^2}}$ is the rms phase deviation, in radians, across a plane at the base of the scattering layer.

Section IIID is based on further work of Bramley (1955), in which he attacked the special case of scattering by a random layer in which the structural autocorrelation function of electron density is of the form $\exp(-\xi^2/\xi_o^2)$, the so-called gaussian autocorrelation function. We have generalized his work to include other autocorrelation functions, including those which represent quasi-periodic rather than purely random scattering layers. The assumption of a randomly phased angular

spectrum does not preclude quasi-periodicity in the sense of band-limited noise theory.

While b depends solely on the scattering optical depth of the ionosphere, $R(\xi)$ depends jointly on the optical depth and the size of the scattering structure. Thus, small-scale structure produces more widely scattered components of the angular spectrum than does larger-scale structure. Consequently, small-scale ionospheric structure produces small-scale wavefront structure, and similarly for large-scale components, as one would expect. However, the structure in the wavefront is not a simple reproduction of the ionospheric structure, even in a statistical sense, because of the dependence of $R(\xi)$ on the optical depth of the scattering layer. Thus, the autocorrelation function describing the scattering structure[1] is obtained from $R(\xi)$ and b as follows:

$$\rho_x(\xi) = \frac{\ln\left(1 + \frac{R}{b}\right)}{\ln\left(1 + \frac{1}{b}\right)}$$

In Chapter IV, the radio interferometric experiment which leads to determination of the scattering optical depth and the structural autocorrelation function of the ionosphere was described. From observations of (complex) visibility and (real) amplitude fluctuation, the coherence ratio and single-spacing wavefront autocorrelation were determined for a single observing frequency. From observations of visibility for two other spacings at the same frequency, three points on the wavefront autocorrelation function were determined. From the experimental results, the optical depth and three points on the ionospheric structural

---

[1] For mathematical definition, see page 132.

autocorrelation function were calculated. From the values of structural autocorrelation obtained, it was possible to estimate the size and idealized statistical shape of the scattering ionospheric irregularities.

From the relationship of visibility to optical depth, it was possible to use multi-frequency observations of visibility to measure the frequency dependence of optical depth. Three frequencies were used, and only an average spectral index could be obtained because of experimental uncertainties.

The measured values of 68 MHz optical depth, the average spectral index of optical depth, and the observed structural autocorrelation functions reported in Chapter V relate to the disturbed auroral ionosphere. The measurements were taken at times of radio-star visibility fades, which correspond to times of enhanced small-scale structure. Visibility fades are highly dynamic events. They represent an extreme case of source scintillation, and the parameters measured are averages over many scintillations. The parameters themselves change over periods of minutes, and the technique developed in this work allows tracing the development of the fade-producing structure.

VIB CONCLUSIONS

The conclusions to be drawn from this work fall into two general categories. The first has to do with the propagation and interferometric observation of scattered waves. The second concerns the physical characteristics of small-scale structure in the disturbed auroral ionosphere and the nature of radio-star visibility fades.

Concerning the propagation of scattered waves, there are two main conclusions. First, the work of Bramley (1955), with which most workers in the field of radio-star and satellite scintillations are familiar, has been found to be open to generalization. In particular, many of his results hold without the assumption of a gaussian autocorrelation function to describe the scattering medium. Second, the conclusion that strong - or multiple - scatter produces structure in the wavefront which is smaller than the structure in the scattering medium is only a special-case statement of a more general conclusion.

For general autocorrelation functions, what happens is that a given value of structural autocorrelation produces a value of wavefront autocorrelation which is closer to zero, the stronger the scattering. Thus, for autocorrelation functions which remain positive, such as the gaussian and the exponential, the stronger scatter results in faster drop-off of the wavefront autocorrelation function. In other words, smaller-scale structure is observed.

For oscillatory autocorrelation functions, such as those describing quasi-periodic structure, the wavefront autocorrelation falls off more rapidly for positive values of the function when the scatter is strong but also takes on (absolutely) smaller negative values. In this case, the wavefront scale size is smaller only if scale is defined as that distance over which the autocorrelation function first drops to some small non-zero value, such as e^{-1}. If the scale is defined in terms of spatial wavelength, the wavefront scale is the same as the structural scale.

A major effect of strengthened scatter is that quasi-periodicity in the wavefront is less pronounced than in the ionospheric structure. In addition, the wavefront autocorrelation function becomes sharper, so its Fourier transform would show higher-frequency components. In this sense, the statement that stronger scatter produces smaller structure is still ture. Just as important, however, is the fact that quasi-periodic structure in the ionosphere tends to be de-emphasized in the wavefront for strong scatter.

Concerning interferometric observation of scattered waves, it is difficult to state specific conclusions in words. A numerical technique was used and graphical results obtained. Suffice it to say that the results were based on the assumption of a randomly phased angular spectrum and again represent a generalization of the work of Bramley (1951). The graphical results reduce to Bramley's analytical application of the work of Rice (1944, 1945) in special cases. In the general case of arbitrary degree of scatter, the graphical results represent a numerical approach to problems analagous to those attacked by Middleton (1947), who obtained analytical results too complicated to be applied to our specific problem.

The analytical results which we have obtained concerning scattered-wave propagation and the graphical ones concerning interferometric observation of such waves need not be limited, in their application, to problems of ionospheric scatter. They may find application to scattering of radio waves in the solar corona and in the interplanetary medium. In particular, the techniques developed herein could possibly be applied

to ascertain the optical thickness of the interplanetary scattering regions which have been reported by Douglas (1965). If it could be shown observationally that the regions satisfy the assumptions underlying development of the technique, then both the optical depth and the structural autocorrelation function of the regions might be obtained with a judicious choice of observing frequency and interferometer baselines. Since the baselines probably would turn out to be quite long, it might be necessary to adapt the technique to observations involving post-detection correlation. On the other hand, the observations might be easier and more directly interpretable than those carried out in the present work because temporal changes in the structural characteristics of the interplanetary scattering regions may not take place so rapidly as those in the disturbed auroral ionosphere.

Concerning the disturbed auroral ionosphere and VHF visibility fades observed in the auroral zone, we have reached six specific conclusions.

1. VHF visibility fades in the auroral zone are produced by ion-density irregularities which are directly associated with auroral luminosity in the radio line of sight.

2. The ionospheric structure responsible for the fades falls in the decametric and hectometric scale range and is comparable to the scale of auroral rays.

3. The structure usually displays evidence of quasi-periodicity and seldom is consistent with a positive, monotonic autocorrelation function, such as the gaussian.

4. Most visibility fades are caused by scattering regions which attain an optical depth in excess of unity at 68 MHz.

5. On an average basis, the optical depth of the fade-producing scattering region displays a power-law wavelength dependence with a spectral index of two or slightly less than two at VHF. No statement can be made about the variability of the spectral index.

6. The most highly developed portion of a visibility fade often is brought on by an increase rather than a decrease in the size of the scattering structure. This result can be explained on the basis of two-dimensional isotropy in the growth of the structural scale size. Isotropy of the irregularities is not required - only isotropy in the growth.

With the present tri-spacing interferometric arrangement, the scale of ionospheric structure which could be measured was severely restricted. There is evidence of a statistical preference for scales between about 75 and about 225 meters during visibility fades. Especially at the small-scale end of this range, the dropoff most likely received a contribution from the experimental circumstances. The large-scale dropoff is probably mostly a true representation of ionospheric conditions. There is no reason that the technique developed and employed in the present work ought not to be extended to explore other regions of the ionospheric scale-size spectrum, by employing additional interferometer spacings. The consequences of backscatter, expecially by very small-scale structure, should be investigated as a generalization of the present work. The technique developed herein could be employed to describe ionospheric structure under less disturbed conditions by extension to lower frequencies, keeping in mind that absorption would have to be accounted for.

The work herein reported has uncovered a need for theoretical work on the scattering properties of quasi-periodic media. About one-fifth of the observations performed produced results which were

inconsistent with the assumption that the ionosphere acts as a random scattering medium, even in the presence of active auroral displays. A majority of the observations which were consistent with such an assumption displayed quasi-periodicities in the ionospheric structure. It is important to develop a theory of scattered-wave propagation which will allow transition from a quasi-periodic medium in the sense of band-limited noise theory to a medium containing highly developed quasi-periodicity.

It would be of interest to employ the technique developed herein to observations of the equatorial ionosphere. Visibility fades have been reported there by Koster (1958). In particular, it would be interesting to establish whether quasi-periodicities exist in the equatorial ionosphere with scales comparable to those reported herein for the disturbed auroral ionosphere, and if so, under what conditions of magnetic activity.

APPENDICES

APPENDIX 1

SOME CALCULATIONS PERTAINING TO SIGNAL STATISTICS

1a Statistical Independence of Real and Imaginary Components of the Complex Amplitude of Antenna Voltage

Let v_1 represent the varying antenna voltage arising from observation of a randomly phased angular spectrum, and let V_1 represent its complex amplitude. Then the real and imaginary components of V_1, A_{1c} and A_{1s} respectively, are given by

$$v_1 = \mathrm{Re}\left\{ V_1 e^{i\omega t} \right\} = A_{1c} \cos \omega t - A_{1s} \sin \omega t \qquad (1)$$

Now let v_1 be Fourier analyzed. Thus

$$v_1 = \sum_{n=1}^{N} c_n \cos (\omega t + \gamma_{1n}) = \cos \omega t \sum_{n=1}^{N} (c_n \cos \gamma_{1n}) - \sin \omega t \sum_{n=1}^{N} (c_n \sin \gamma_{1n}) \qquad (2)$$

For equations (1) and (2) to hold simultaneously for all t, we must have

$$A_{1c} = \sum_{n=1}^{N} c_n \cos \gamma_{1n} \quad \text{and} \quad A_{1s} = \sum_{n=1}^{N} c_n \sin \gamma_{1n} \qquad (3)$$

Since, in any observational situation, N is restricted to finite values, we are free to multiply the sums in equations (3) term by term. Thus

$$A_{1c} A_{1s} = \sum_{n=1}^{N} c_m c_n \cos \gamma_{1m} \sin \gamma_{1n} \qquad (4)$$

Since the average of any sum of stochastic variables is equal to the

sum of the averages (cf, Munroe, 1951, p. 104-5), we can write the following, where the bars denote averages[1]

$$\overline{A_{1c}A_{1s}} = \sum_{\substack{m=1 \\ n=1}}^{N} c_m c_n \overline{\cos \gamma_{1m} \sin \gamma_{1n}} \tag{5}$$

For a randomly phased angular spectrum, γ_{1m} and γ_{1n} are independent and uniformly distributed between zero and 2π. Under these conditions the average on the right of equation (5) is zero. Thus we have

$$\overline{A_{1c}A_{1s}} = 0 \tag{6}$$

For the same reason, A_{1c} and A_{1s} each have zero mean. Therefore equation (6) is the condition of zero covariance for the A's. For gaussian random variables, zero covariance is a necessary and sufficient condition for statistical independence. Hence, A_{1c} and A_{1s} are statistically independent.

1b Covariance of Antenna Voltages

Now let v_2 represent the varying output voltage of a neighboring atenna. Then, from equation (2) above, we obtain

$$\overline{v_1 v_2} = \sum_{\substack{m=1 \\ n=1}}^{N} c_m c_n \overline{\cos (\omega t + \gamma_{1m}) \cos (\omega t + \gamma_{2n})} \tag{7}$$

[1] We make no distinction between ensemble and time averages. This is justified if we are dealing with ergodic processes. For the gaussian random process with which we are concerned, ergodicity is insured by stationarity under very general conditions. Our identification of time averages with ensemble averages here implies only that we are assuming stationary conditions.

which expands into

$$\overline{v_1 v_2} = \sum_{\substack{m=1 \\ n=1}}^{N} c_m c_n \overline{[\cos \gamma_{1m} \cos \gamma_{2n} \cos^2 \omega t + \sin \gamma_{1m} \sin \gamma_{2n} \sin^2 \omega t - (\cos \gamma_{1m} \sin \gamma_{2n} + \sin \gamma_{1m} \cos \gamma_{2n}) \sin \omega t \cos \omega t]} \tag{8}$$

which reduces to

$$\overline{v_1 v_2} = \tfrac{1}{2} \sum_{\substack{m=1 \\ n=1}}^{N} c_m c_n \overline{(\cos \gamma_{1m} \cos \gamma_{2n} + \sin \gamma_{1m} \sin \gamma_{2n})} \tag{9}$$

Under the assumption of random phasing, equation (9) yields the following simple expression for the covariance of voltages:

$$\overline{v_1 v_2} = \tfrac{1}{2} \sum_{n=1}^{N} c_n^2 \cos (\gamma_{1n} - \gamma_{2n}) = \tfrac{1}{2} \sum_{n=1}^{N} c_n^2 \cos 2\chi_n \tag{10}$$

where $\chi_n = \tfrac{1}{2} (\gamma_{1n} - \gamma_{2n})$.

1c The Elements of the Moment Matrix

Let M denote the moment matrix for the four gaussian random variables A_{1c}, A_{1s}, A_{2c}, and A_{2s}. The diagonal elements μ_{ii} of M are the variances, equal for the four variables and denoted by σ^2. The off-diagonal elements μ_{ij} are the covariances.

Equation (6) above shows that $\mu_{12} = 0$. Similarly, $\mu_{34} = 0$. Further, the same result would arise upon commutation of the factors on the left of equation (6). Under the condition of random phasing, we have, further that

$$\mu_{13} = \overline{A_{1c} A_{2c}} = \sum_{n=1}^{N} c_n^2 \overline{\cos \gamma_{1n} \cos \gamma_{2n}} = \sum_{n=1}^{N} c_n^2 \overline{\cos \gamma_{1n} \cos (\gamma_{1n} - 2\chi_n)} \tag{11}$$

$$\text{or} \qquad \mu_{13} = \sum_{n=1}^{N} c_n^2 [\overline{\cos^2 \gamma_{1n} \cos 2\gamma_n} + \overline{\cos \gamma_{1n} \sin \gamma_{1n} \sin 2\chi_n}] \tag{12}$$

$$\text{so} \qquad \mu_{13} = \tfrac{1}{2} \sum_{n=1}^{N} c_n^2 \cos 2\chi_n \tag{13}$$

In similar fashion, it can be shown that

$$\mu_{31} = \mu_{24} = \mu_{42} = \tfrac{1}{2} \sum_{n=1}^{N} c_n^2 \cos 2\chi_n \tag{14}$$

and

$$-\mu_{14} = -\mu_{41} = \mu_{23} = \mu_{32} = \tfrac{1}{2} \sum_{n=1}^{N} c_n^2 \sin 2\chi_n \tag{15}$$

The above can be summarized by writing the moment matrix as follows:

$$M = \begin{pmatrix} \sigma^2 & 0 & \mu_c & -\mu_s \\ 0 & \sigma^2 & \mu_s & \mu_c \\ \mu_c & \mu_s & \sigma^2 & 0 \\ -\mu_s & \mu_c & 0 & \sigma^2 \end{pmatrix} \tag{16}$$

$$\text{where} \qquad \sigma^2 = \tfrac{1}{2} \sum_{n=1}^{N} c_n^2 \tag{17}$$

$$\mu_c = \tfrac{1}{2} \sum_{n=1}^{N} c_n^2 \cos 2\chi_n \tag{17}$$

$$\mu_s = \tfrac{1}{2} \sum_{n=1}^{N} c_n^2 \sin 2\chi_n \tag{19}$$

1d The Matrix Elements and the Wavefront Correlation for a Narrow, Symmetrical Angular Spectrum

Let the elements of the moment matrix be given by their integral definitions. Thus,

$$\sigma^2 = \int_{-\infty}^{\infty} p(\alpha)d\alpha \tag{20}$$

$$\mu_c = \int_{-\infty}^{\infty} p(\alpha) \cos 2\chi \, d\alpha \tag{21}$$

$$\mu_s = \int_{-\infty}^{\infty} p(\alpha) \sin 2\chi \, d\chi \tag{22}$$

where $\chi = (2\pi d/\lambda) \sin \alpha$. Now make the following change of variables:

$$\alpha = \alpha_o + \delta \tag{23}$$

$$p(\alpha) = F(\delta) = F(-\delta) \tag{24}$$

Then equation (20) can be replaced by

$$\sigma^2 = \int_{-\infty}^{\infty} F(\delta) \, d\delta \tag{25}$$

By direct substitution, we have also that

$$\mu_c = \int_{-\infty}^{\infty} F(\delta) \cos [(2\pi d/\lambda) \sin (\delta + \alpha_o)] \, d\delta \tag{26}$$

and

$$\mu_s = \int_{-\infty}^{\infty} F(\delta) \sin [2\pi d/\lambda) \sin (\delta + \alpha_o)] \, d\delta \tag{27}$$

Under the condition that F is appreciable only for values of δ

which are sufficiently small that cos δ may be approximated by unity and sin δ by δ, we may make the following substitutions:

$$\cos [2\pi d/\lambda) \cos (\delta + \alpha_o)] = \cos [(2\pi d/\lambda) (\delta \cos \alpha_o + \sin \alpha_o)] \quad (28)$$

$$\sin [2\pi d/\lambda) \cos (\delta + \alpha_o)] = \sin [(2\pi d/\lambda) (\delta \cos \alpha_o + \sin \alpha_o)] \quad (29)$$

which yield the following:

$$\mu_c = \int_{-\infty}^{\infty} F(\delta) \left[\cos\left(\frac{2\pi d}{\lambda} \delta \cos\alpha_o\right)\cos\left(\frac{2\pi d}{\lambda} \sin\alpha_o\right)\right.$$

$$\left. - \sin\left(\frac{2\pi d}{\lambda} \delta \cos\alpha_o\right)\sin\left(\frac{2\pi d}{\lambda}\sin\alpha_o\right)\right] d\delta \quad (30)$$

$$\mu_s = \int_{-\infty}^{\infty} F(\delta) \left[\sin\left(\frac{2\pi d}{\lambda} \delta \cos\alpha_o\right)\cos\left(\frac{2\pi d}{\lambda}\sin\alpha_o\right)\right.$$

$$\left. + \cos\left(\frac{2\pi d}{\lambda} \delta \cos\alpha_o\right)\sin\left(\frac{2\pi d}{\lambda}\sin\alpha_o\right)\right] d\delta \quad (31)$$

If F (δ) is assumed to be an even function, the terms within the brackets above which are odd functions of δ vanish in the integration. Recalling that $\chi = (2\pi d/\lambda) \sin \alpha$, we are left with

$$\sigma^2 = \int_{-\infty}^{\infty} F(\delta)\, d\delta \quad (32)$$

$$\mu_c = \cos 2\chi_o \int_{-\infty}^{\infty} F(\delta) \cos [(2\pi d/\lambda)\, \delta \cos \alpha_o]\, d\delta \quad (33)$$

$$\mu_s = \sin 2\chi_o \int_{-\infty}^{\infty} F(\delta) \cos [(2\pi d/\lambda)\, \delta \cos \alpha_o]\, d\delta \quad (34)$$

Now the wavefront correlation R is defined as

$$R = \frac{(\mu_c^2 + \mu_s^2)^{\frac{1}{2}}}{\sigma^2} \tag{35}$$

Substitution of equations (32), (33), and (34) into equation (35) yields

$$R = \frac{\int_{-\infty}^{\infty} F(\delta) \cos [(2\pi d/\lambda)\, \delta \cos\alpha_o]\, d\delta}{\int_{-\infty}^{\infty} F(\delta)\, d\delta} \tag{36}$$

le Covariance of Antenna Voltages in the Presence of a Nondeviated Component in the Angular Spectrum

If a nondeviated component of amplitude S is added to a randomly phased angular scatter spectrum of variance $\sigma^2 = \overline{B_{1c}^2} = \overline{B_{1s}^2}$, then the antenna voltages, v_1 and v_2, become

$$v_1 = S \cos(\omega t + \chi_o) + B_{1c} \cos \omega t - B_{1s} \sin \omega t \tag{37}$$

$$v_2 = S \cos(\omega t - \chi_o) + B_{2c} \cos \omega t - B_{2s} \sin \omega t \tag{38}$$

The covariance of voltages then is given by

$$\begin{aligned}\overline{V_1 V_2} = {} & S^2 \overline{\cos(\omega t+\chi_o)\cos(\omega t-\chi_o)} + \overline{B_{1c}B_{2c}}\ \overline{\cos^2\omega t} + \overline{B_{1s}B_{2s}}\ \overline{\sin^2\omega t} \\ & + S\, \overline{B_{2c}}^{\,0}\ \overline{\cos(\omega t+\chi_o)\cos\omega t} - S\, \overline{B_{2s}}^{\,0}\ \overline{\cos(\omega t+\chi_o)\sin\omega t} \\ & + S\, \overline{B_{1c}}^{\,0}\ \overline{\cos(\omega t-\chi_o)\cos\omega t} - S\, \overline{B_{1s}}^{\,0}\ \overline{\cos(\omega t-\chi_o)\sin\omega t} \\ & + \overline{B_{1c}B_{2s}}\ \overline{\cos\omega t \sin\omega t}^{\,0} + \overline{B_{1s}B_{2c}}\ \overline{\cos\omega t \sin\omega t}^{\,0}\end{aligned} \tag{39}$$

so

$$\overline{V_1 V_2} = \tfrac{1}{2} S^2 [\cos 2\chi_o + \overline{\cos 2\omega t}] + \tfrac{1}{2} \mu_{13} + \tfrac{1}{2} \mu_{24} \tag{40}$$

or

$$\overline{V_1 V_2} = \tfrac{1}{2} S^2 \cos 2\chi_o + \mu_c \tag{41}$$

1f The mean Amplitude and Power Products in the Case of Dominance by the Nondeviated Component

Now designate the amplitudes and phases of the two atenna voltages by A_1, θ_1, A_2, and θ_2, so that

$$v_1 = A_1 \cos(\omega t + \theta_1) \quad \text{and} \quad v_2 = A_2 \cos(\omega t + \theta_2) \tag{42}$$

Comparison of equations (42) with equations (37) and (38) yields, for $\frac{S}{\sqrt{2}\sigma} \gg$ unity[1],

$$\begin{aligned}\overline{A_1 A_2} = {} & S^2 + S(\overline{B_{1c}}^{\,o} \cos\chi_o - \overline{B_{2s}}^{\,o} \sin\chi_o + \overline{B_{1c}}^{\,o} \cos\chi_o + \overline{B_{1s}}^{\,o} \sin\chi_o) \\ & + \tfrac{1}{2}(\overline{B_{2c}^2}^{\,\sigma^2} \sin^2\chi_o + \overline{B_{2s}^2}^{\,\sigma^2} \cos^2\chi_o \\ & + 2\overline{B_{2c}B_{2s}}^{\,o} \cos\chi_o \sin\chi_o + \overline{B_{1c}^2}^{\,\sigma^2} \sin^2\chi_o + \overline{B_{1s}^2}^{\,\sigma^2} \cos^2\chi_o - 2\overline{B_{1c}B_{1s}}^{\,o} \cos\chi_o \sin\chi_o) \\ & + \overline{B_{1c}B_{2c}}^{\,\mu_{13}} \cos^2\chi_o - \overline{B_{1c}B_{2s}}^{\,\mu_{14}} \cos\chi_o \sin\chi_o + \overline{B_{2c}B_{1s}}^{\,\mu_{32}} \cos\chi_o \sin\chi_o \\ & - \overline{B_{1s}B_{2s}}^{\,\mu_{24}} \sin^2\chi_o \end{aligned} \tag{43}$$

$$\overline{A_1 A_2} = S^2 + \sigma^2 + \mu_c(\cos^2\chi_o - \sin^2\chi_o) + 2\mu_s \cos\chi_o \sin\chi_o \tag{44}$$

---

[1] See also equations 2-68 and 2-69 in Chapter II.

so

$$\overline{A_1 A_2} = S^2 + \sigma^2 + \mu_c \cos 2\chi_o + \mu_s \sin 2\chi_o \tag{45}$$

We have also[2]

$$\overline{A_1^2 A_2^2} = S^4 + 2S^3 [(\overset{o}{B}_{1c} + \overset{o}{B}_{2c}) \cos \chi_o + (\overset{o}{B}_{1s} - \overset{o}{B}_{2s}) \sin \chi_o]$$

$$+ S^2 (\overset{\sigma^2}{B^2_{1c}} + \overset{\sigma^2}{B^2_{1s}} + \overset{\sigma^2}{B^2_{2c}} + \overset{\sigma^2}{B^2_{2s}}) + 4S^2(\overset{\mu_{13}}{B_{1c}B_{2c}} \cos^2 \chi_o - \overset{\mu_{24}}{B_{1s}B_{2s}} \sin^2 \chi_o$$

$$+ \overset{\mu_{23}}{B_{1s}B_{2c}} \sin \chi_o \cos \chi_o - \overset{\mu_{14}}{B_{1c}B_{2s}} \sin \chi_o \cos \chi_o) \tag{46}$$

$$\overline{A_1^2 A_2^2} = S^4 + 4\sigma^2 S^2 + 4S^2 [\mu_c(\cos^2 \chi_o - \sin^2 \chi_o) + 2\mu_s \sin \chi_o \cos \chi_o] \tag{47}$$

$$\overline{A_1^2 A_2^2} = S^4 + 4\sigma^2 S^2 + 4S^2 (\mu_c \cos 2\chi_o + \mu_s \sin 2\chi_o) \tag{48}$$

---

[2] See equations 2-61 and 2-62 in Chapter II.

APPENDIX 2

SCHEMATIC DIAGRAMS

FOR

NEW PHASE-SWITCH INTERFEROMETERS

This appendix contains circuit diagrams for one of the two new phase-switch interferometers built for the present work. The instrument shown was operated at 68 MHz. The second instrument was operated at 137 MHz and is identical following frequency conversion to the intermediate frequency of 30 MHz.

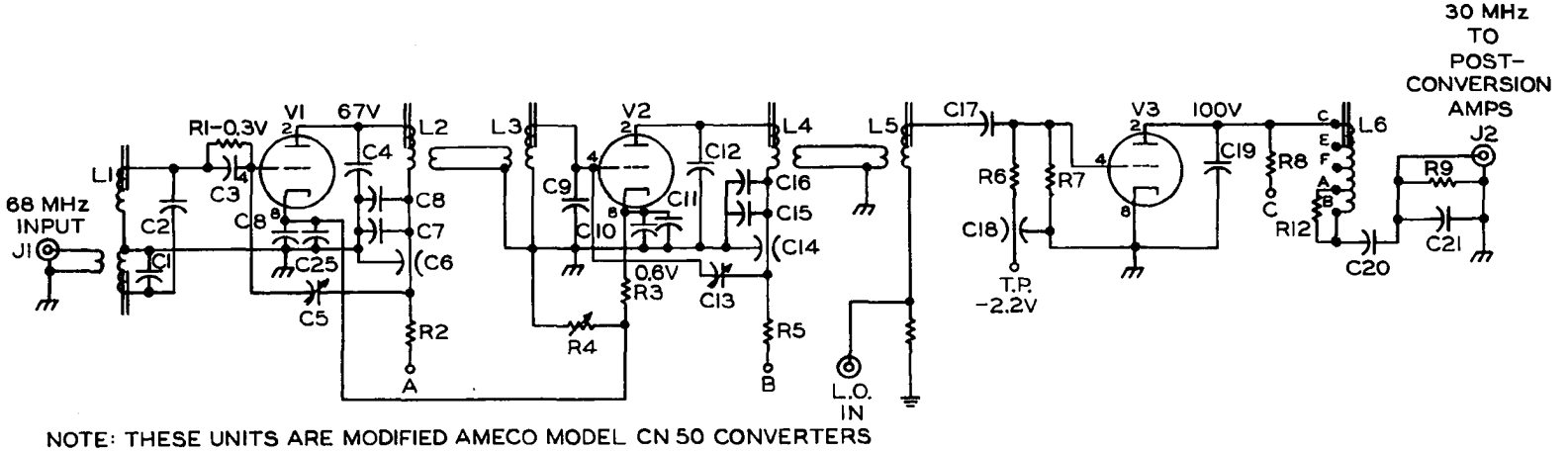

NOTE: THESE UNITS ARE MODIFIED AMECO MODEL CN 50 CONVERTERS

R-F PREAMPLIFIERS AND MIXERS (68 MHz)

Fig. A1

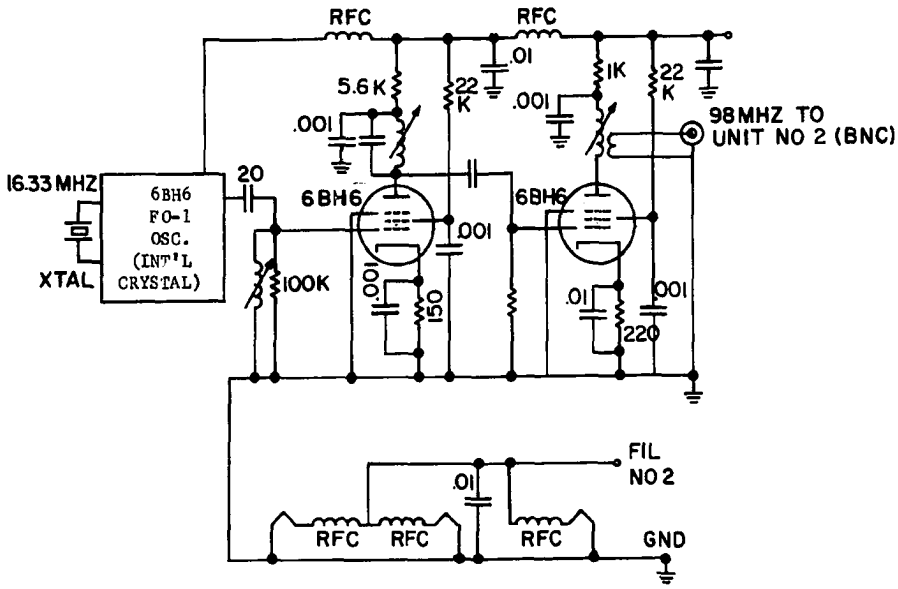

LOCAL OSC UNIT NO 1

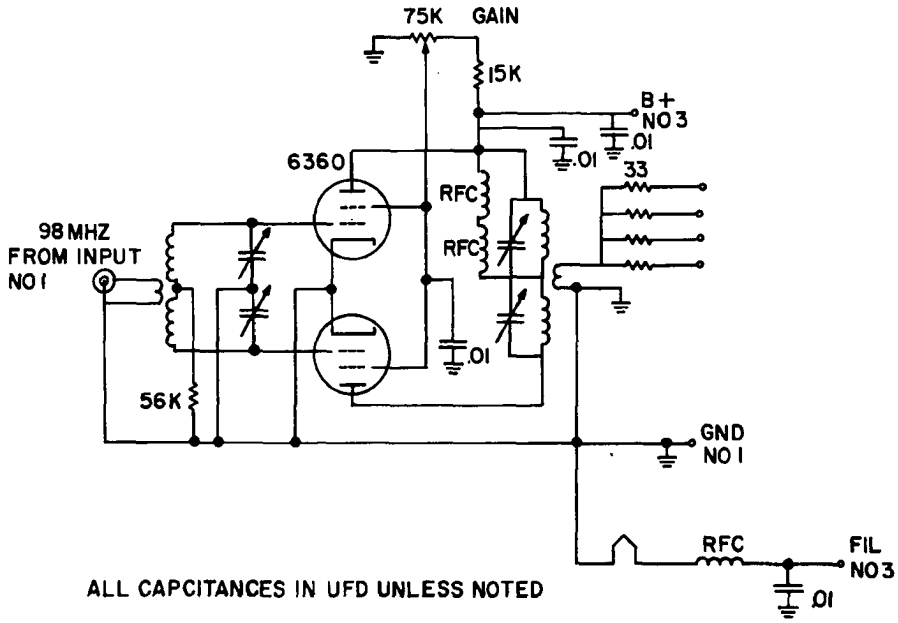

LOCAL OSC UNIT NO 2

Fig. A2

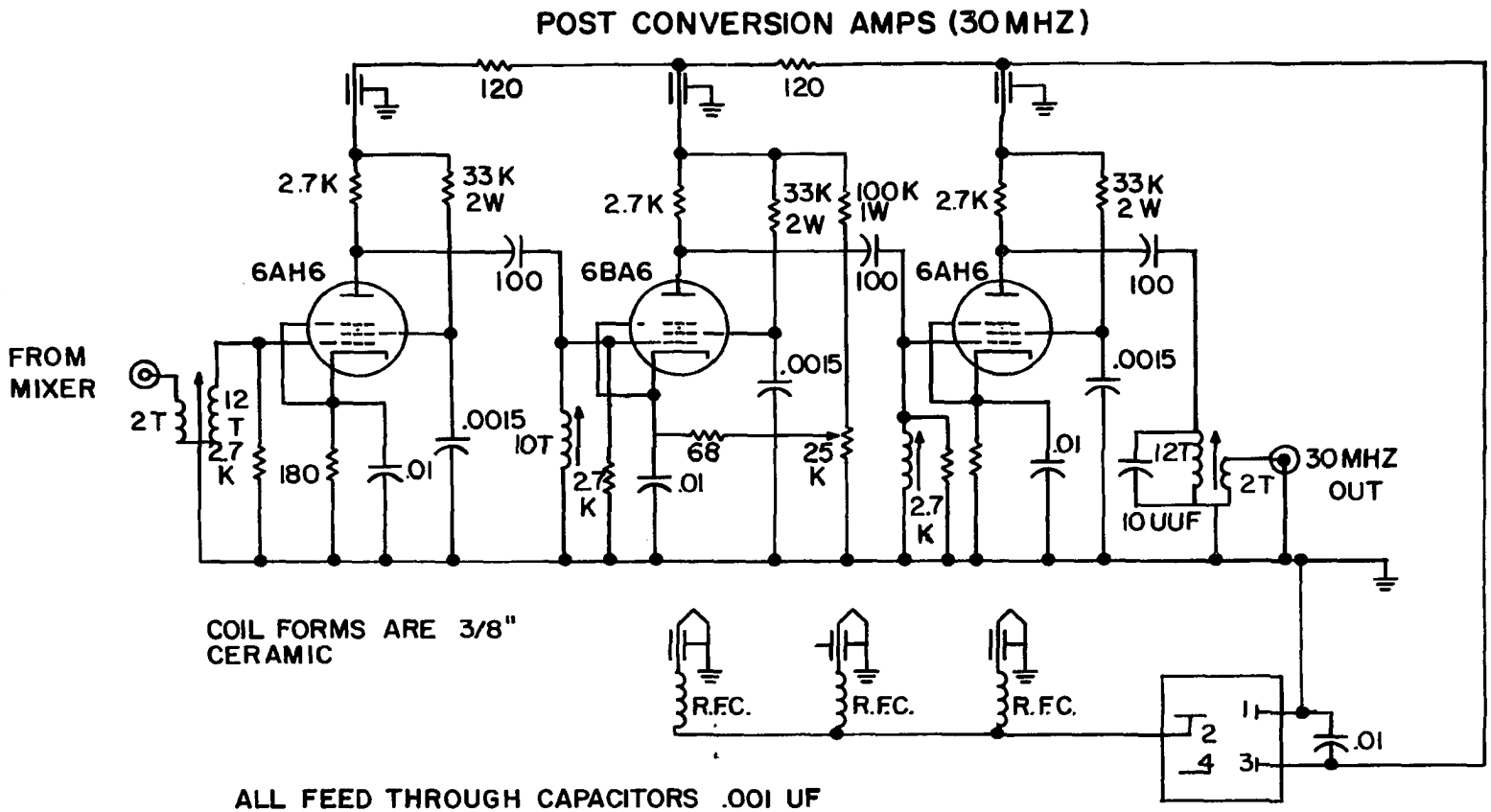

Fig. A3

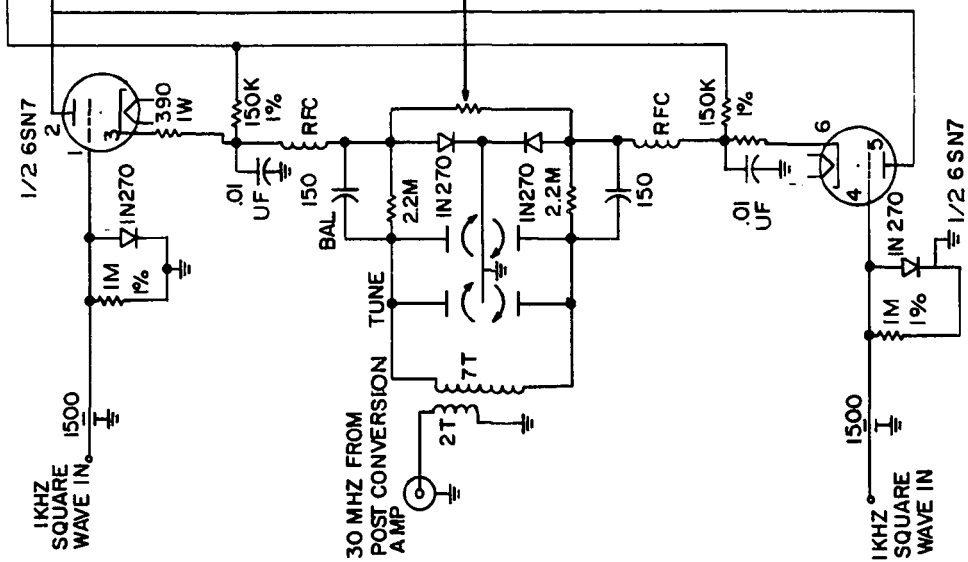

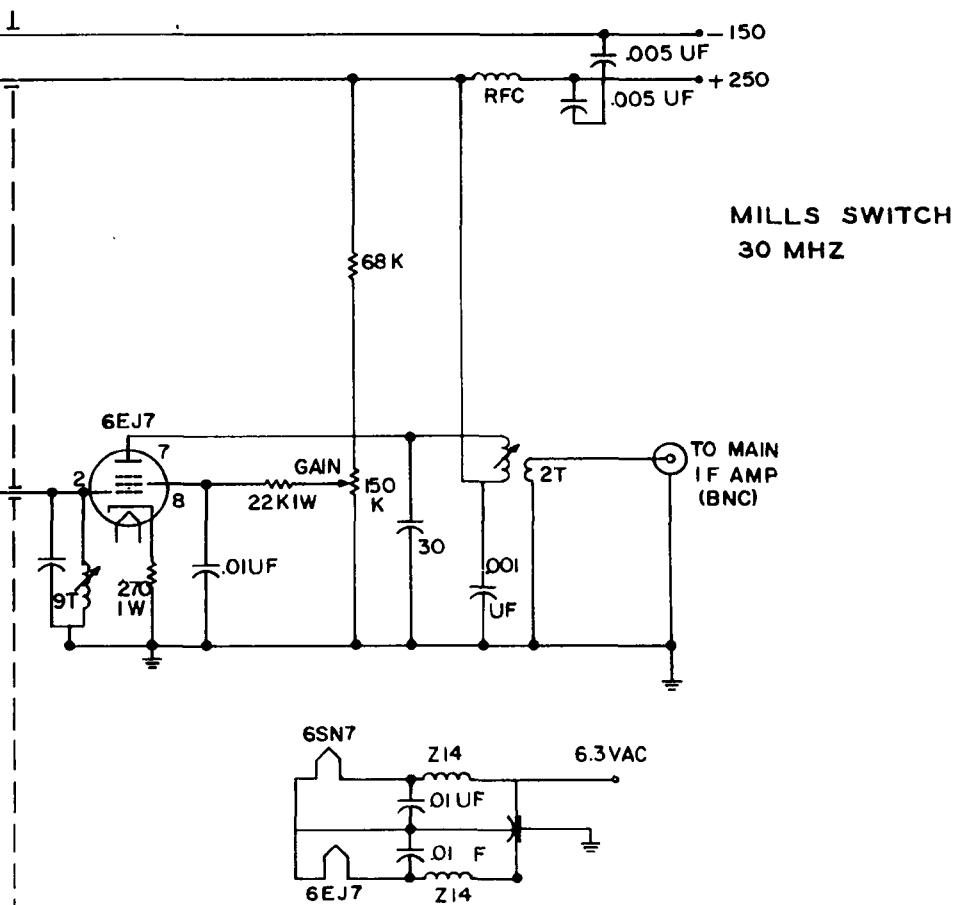

ALL CAPACITANCES IN UUF UNLESS NOTED
ALL RESISTORS 1/2W UNLESS NOTED

Fig. A4

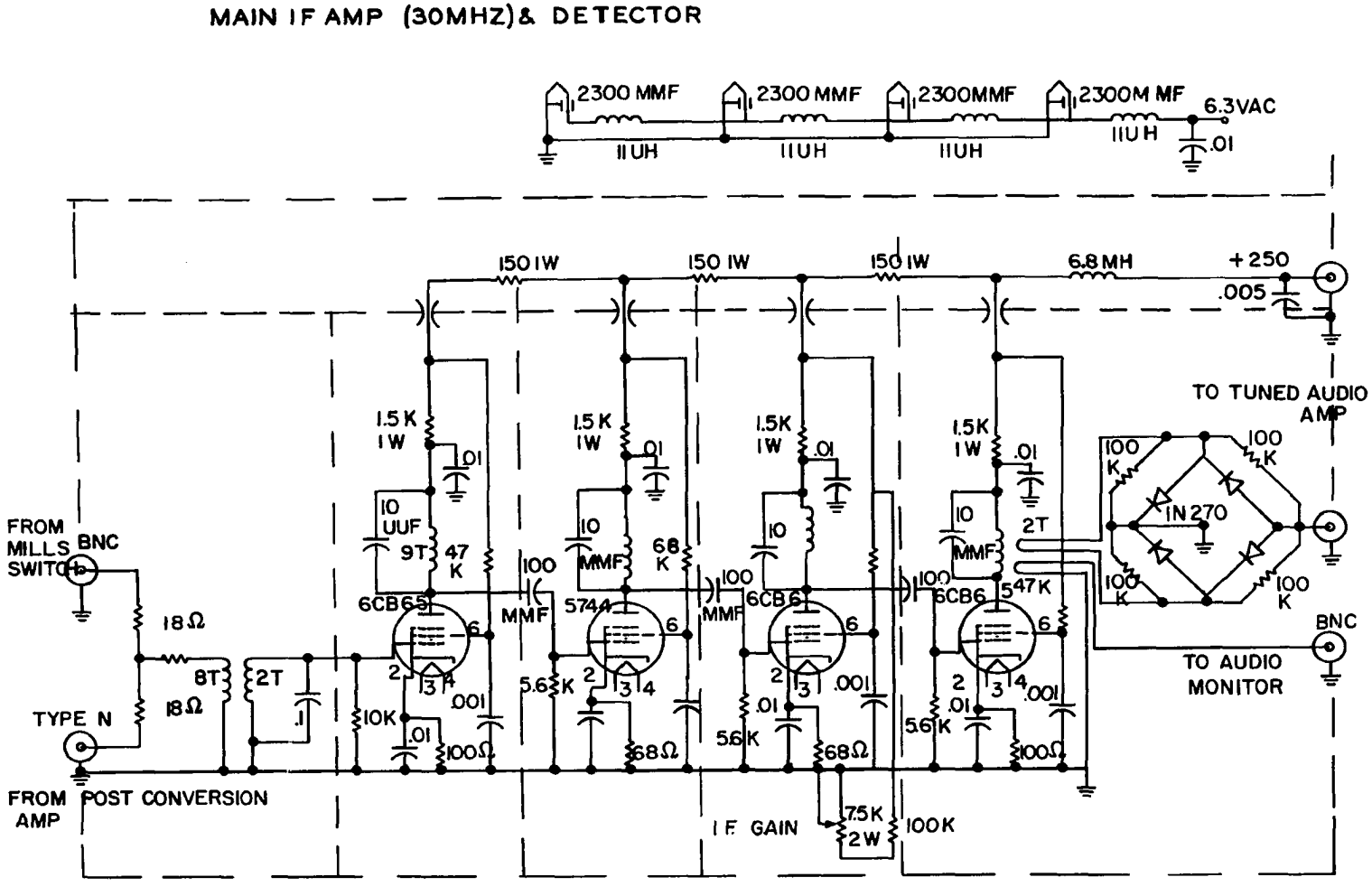

Fig. A5

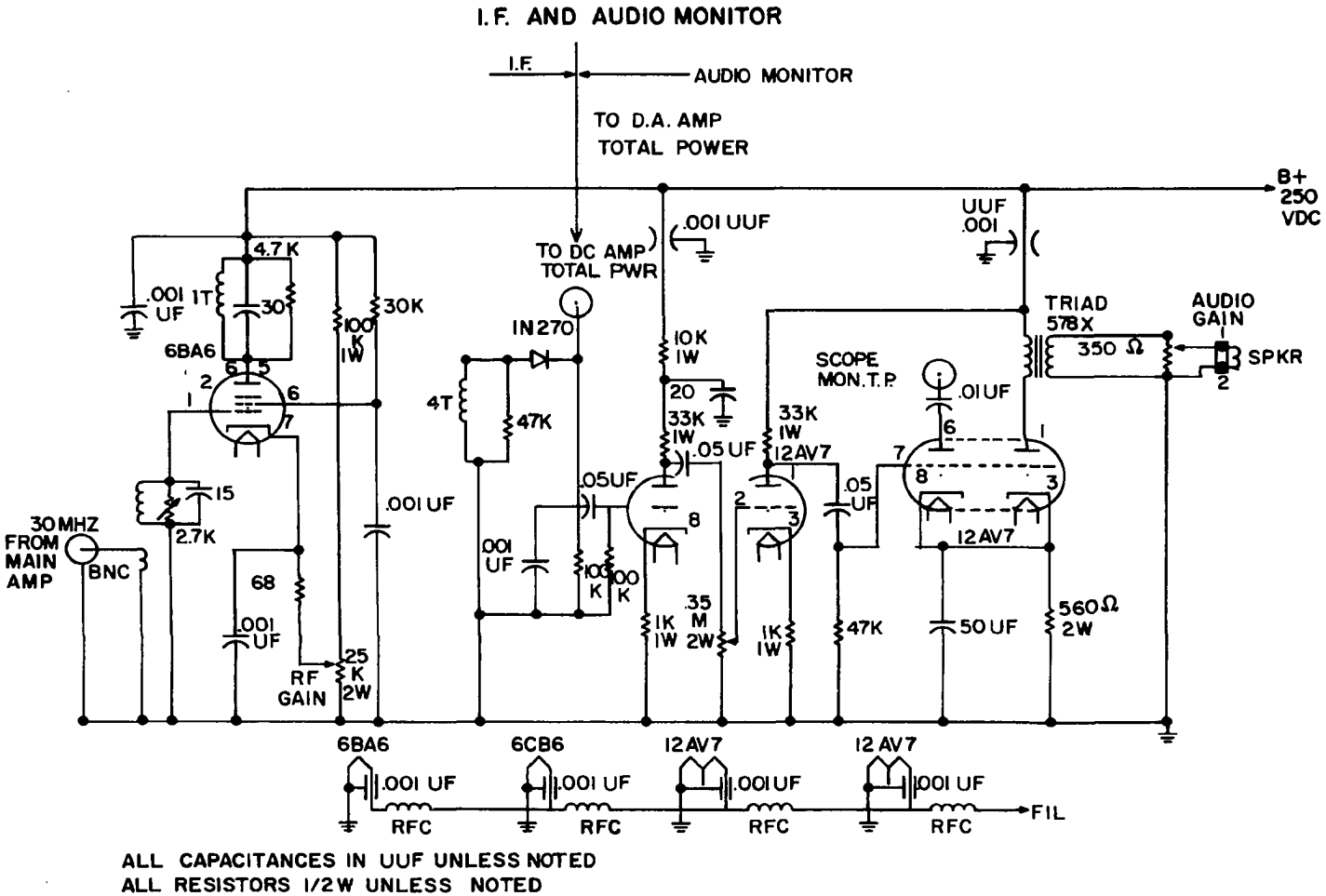

Fig. A6

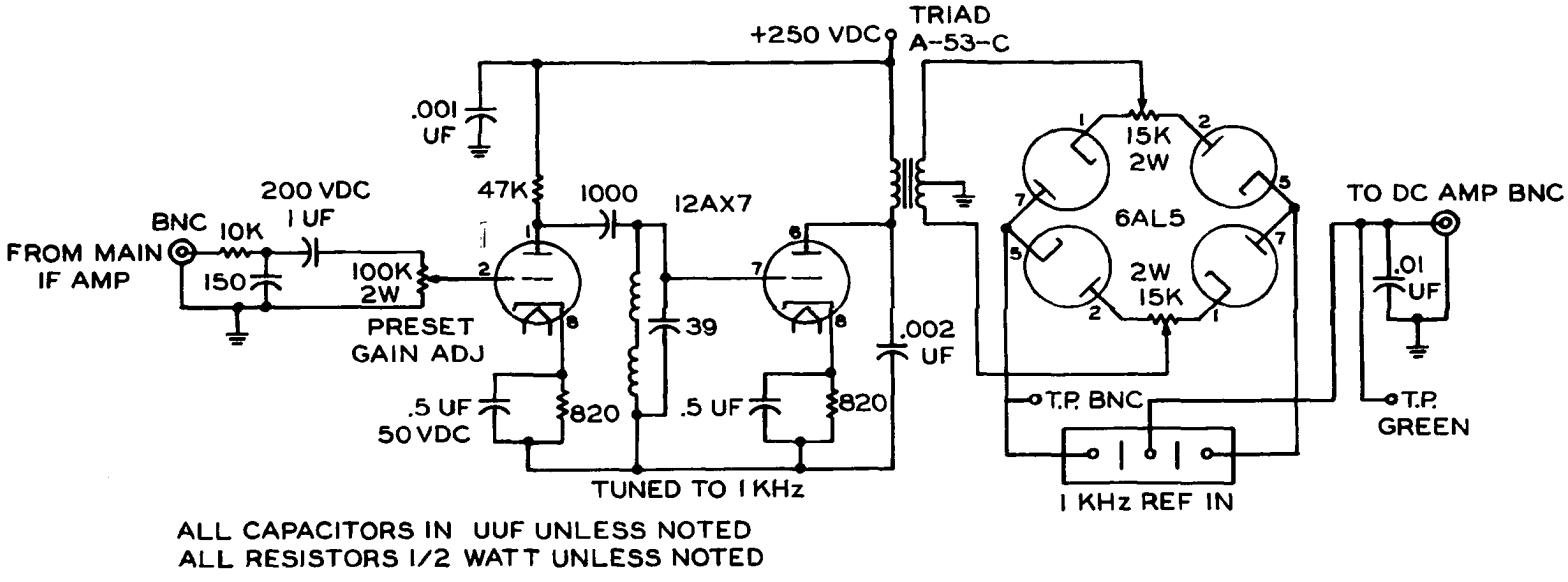

TUNED AUDIO AMPLIFIER, 1 KHz, AND SYNCHRONOUS DETECTOR

Fig. A7

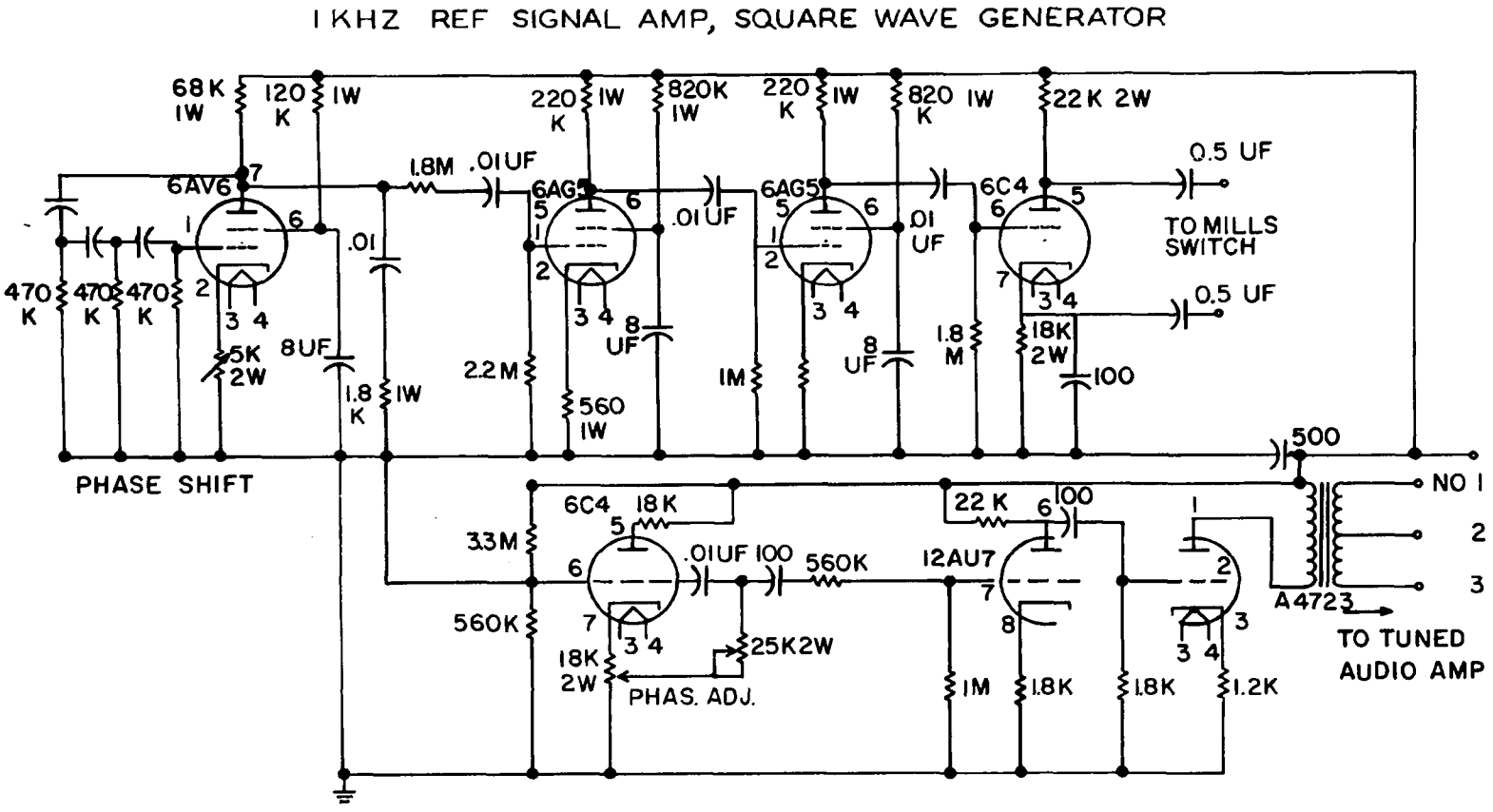

ALL CAPACITANCES IN UUF UNLESS NOTED
ALL RESISTORS 1/2 WATT UNLESS NOTED

Fig. A8

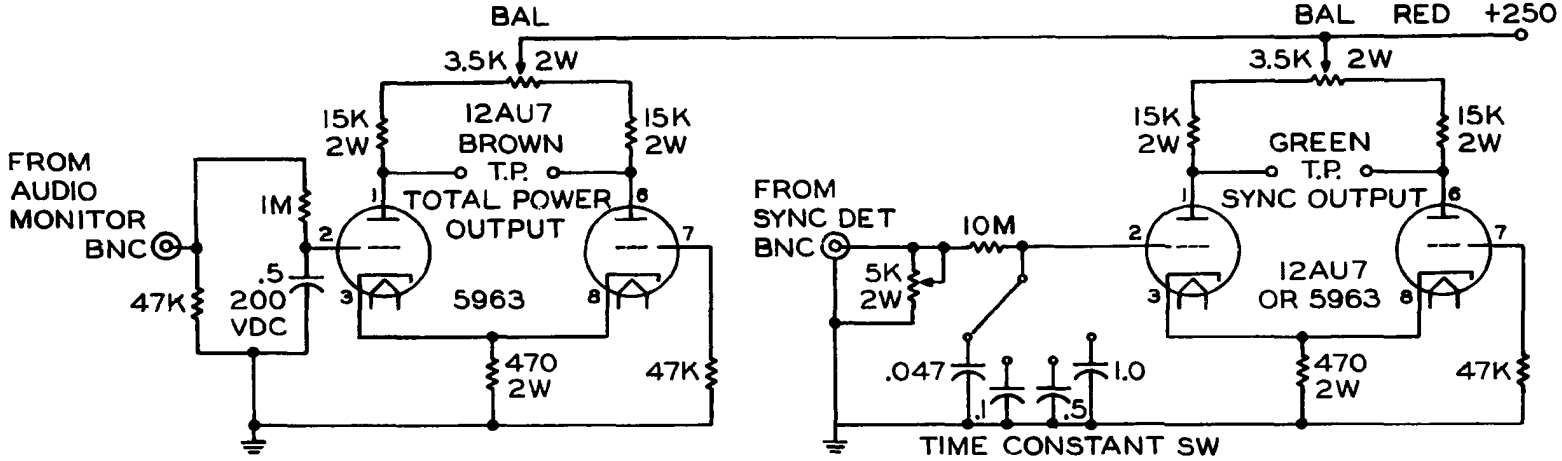

Fig. A9

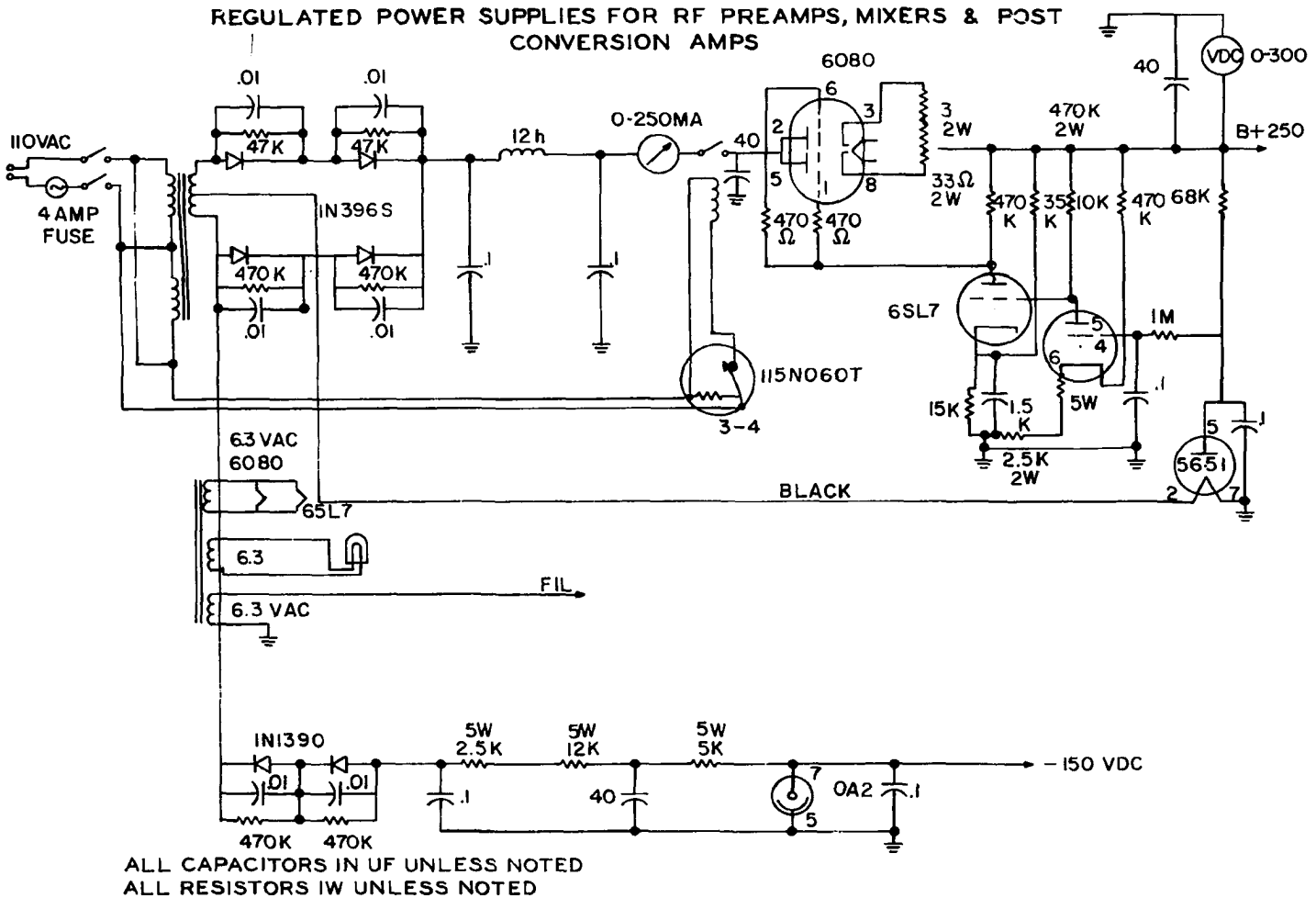

Fig. A10

ANTENNA CONTROL PANEL

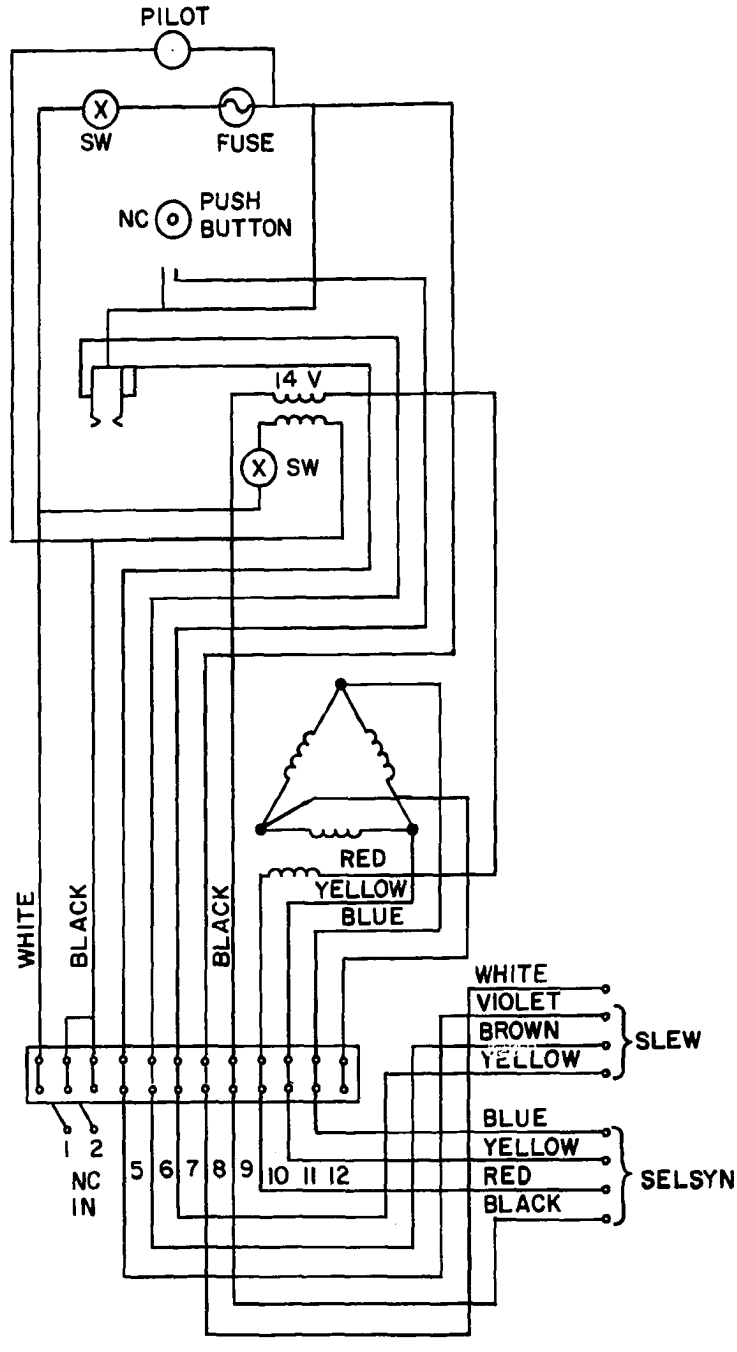

Fig. A11

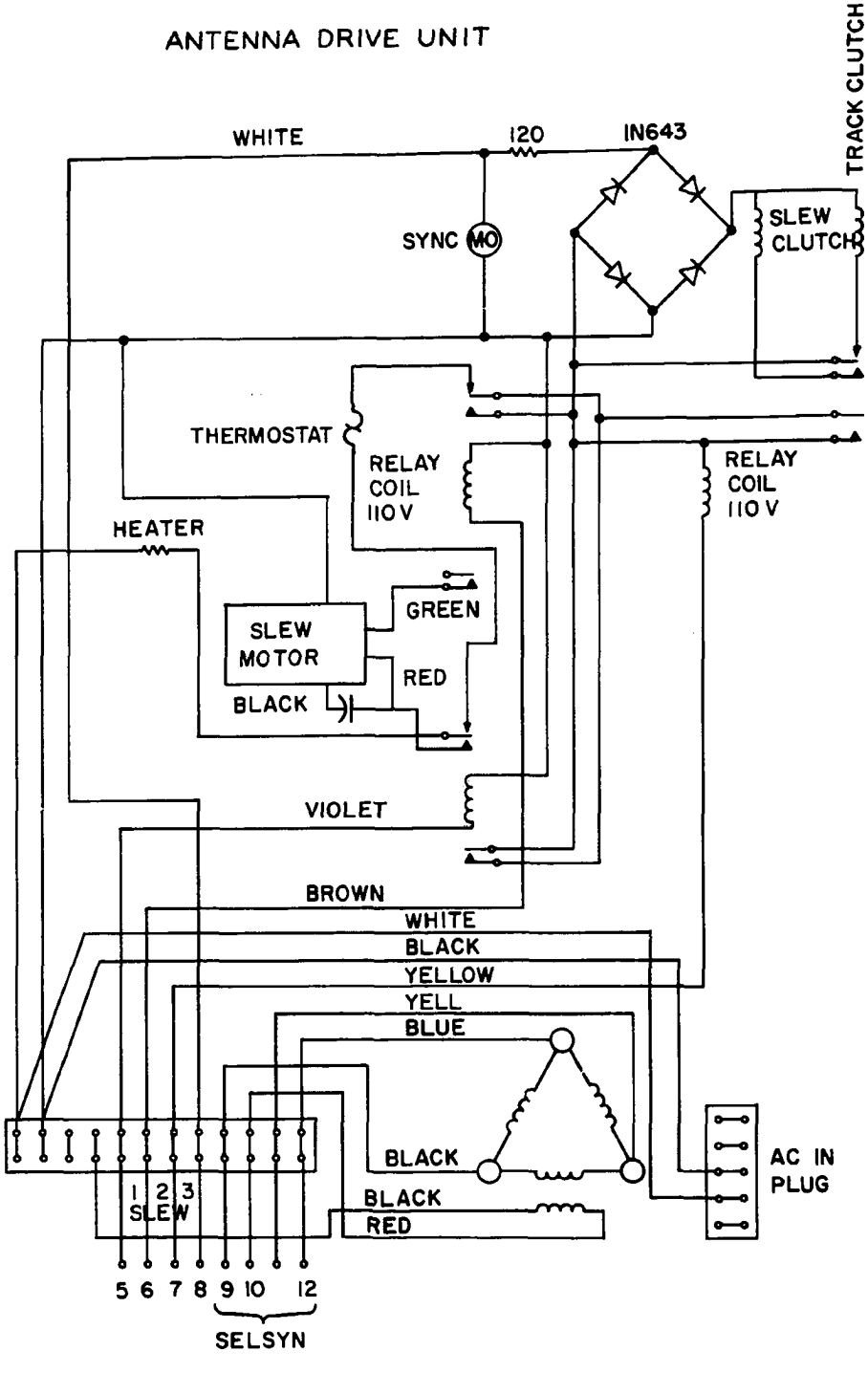

Fig. A12

ANTENNA SYSTEM DRIVE 400 Hz FREQUENCY GENERATOR

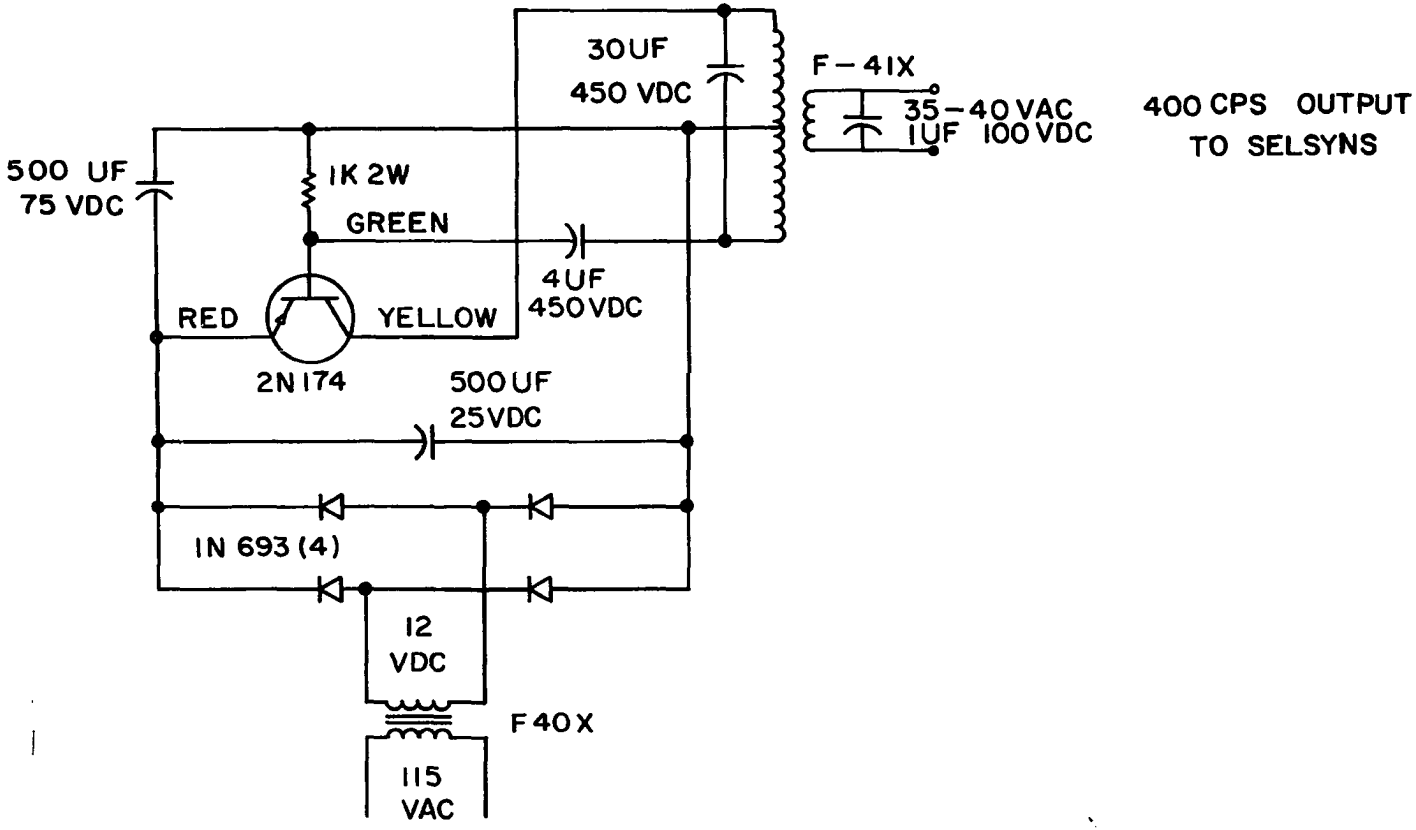

Fig. A13

APPENDIX 3

COMPUTER PROGRAMS

3a Computation of Radio-star Visibility and Reduction to Standard Averaging Period

```
0809
C     AIM 5 PASS 1  MAY 4,65 R. PORTER
      DIMENSION  K(20)
    1 ICC=0
      ICG=0
    2 READ 100,ICH,ICODE,(K(N),N=1,15),ICN,IDATE,ISOUR
      IF(IDATE)200,3,9
    3 READ 101,IHOUR,IMIN,IXR,IYR,IEVEN,IDATE,ISOUR
      IF(IDATE)200,4,5
    4 PRINT 102
      GO TO 1
    5 ICG=ICG+1
      L=IHOUR*60
      L2=(L+IMIN)*10
      IXC=L2-IXR
      IF(IEVEN)200,7,6
    6 IENR=IEVEN
    7 READ 103,ICK1,ICK2
      ICK3=ICK1+ICK2
      IF(ICK3)8,2,8
    8 PRINT 104
      PAUSE
      GO TO 2
    9 ICC=ICC+1
      IT1=IXC+K(1)
      IT2=IXC+K(14)
      IS=0
      DO 10 N=3,12
      IS=IS+K(N)
   10 CONTINUE
      IA=IS-(K(13)*10)
      IF(ICODE-8)11,12,12
   11 IB=IA*1570
      GO TO 13
   12 IB=IA*1000
   13 IC1= K(2)+K(15)
      IC2=IC1/2
      IC3=IC2-K(13)
      IC=IC3*10
      IR=ABSF(IB/IC)
      ITH1=(IT1*10)/6
      ITH2=(IT2*10)/6
      IF(ICODE-9)14,15,14
   14 PUNCH106,ICH,IDATE,ISOUR,IENR,ICC,ICN,ICG,IT1,IT2,IR,ITH1,ITH2
      GO TO 2
   15 PUNCH107,ICH,IDATE,ISOUR,IENR,ICC,ICN,ICG,IT1,IT2,IR,ITH1,ITH2
      GO TO 2
```

```
  100 FORMAT(2I1,15I4,I5,I6,I1)
  101 FORMAT(2I2,2I4,I5,I6,I1)
  102 FORMAT(15HTWO BLANK CARDS)
  103 FORMAT(18X,I6,44X,I6)
  104 FORMAT(28HNO BLANK FOLLOWING TIME CARD)
  105 FORMAT(30HERROR CORRECT DATA PRESS START)
  106 FORMAT(I2,I6,I2,3I5,I3,1X,5I6)
  107 FORMAT(I2,I6,I2,3I5,I3,1X,5I6,17X,4HLL 9)
  200 PRINT 105
      PAUSE
      GO TO 2
      END



*0810
C       AIM 5  PASS 2  JUNE 4, 1965  R PORTER
        DIMENSION M(50),MM(50),I(200),II(200),ICH31(50),ICH32(50),
       1ICHX1(200),ICHX2(200)
    1   READ100,ICH,IDATE,ISOUR,IENR,ICC,ICN,ICG,IT1,IT2,IR
        IF(ICH-8)7,8,9
    9   K=0
        L=0
        DO 50 N=1,50
        M(N)=0
        MM(N)=0
        ICH31(N)=0
        ICH32(N)=0
   50   CONTINUE
        DO 51 N=1,20
        I(N)=0
        II(N)=0
        ICHX1(N)=0
        ICHX2(N)=0
   51   CONTINUE
        GO TO 1
    7   IF(ICH-7)10,77,601
   10   IF(ICH-3)60,3,60
    3   K=K+1
        ICH31(K)=IT1
        ICH32(K)=IT2
        ICH31(K+1)=IT2
        MM(K)=IR
        IENRL=IENR
        GO TO 1
    8   M(1)=ICH31(1)
        DO 200 N=1,K
```

```
      IK=ABSF(ICH31(N+1)-ICH32(N))
      IF(IK-10)199,602,602
  602 PRINT 104,IENRL,ICH31(N+1),ICH32(N)
  199 M(N+1)=(ICH31(N+1)+ICH32(N))/2
  200 CONTINUE
      K=K+1
      GO TO 1
   60 ICHL=ICH
      IDATL=IDATE
      ISOUL=ISOUR
      IENRL=IENR
      L=L+1
      ICHX1(L)=IT1
      ICHX2(L)=IT2
      ICHX1(L+1)=IT2
      II(L)=IR
      GO TO 1
   77 I(1)=ICHX1(1)
      DO 300 N=1,L
      IJ=ABSF(ICHX1(N+1)-ICHX2(N))
      IF(IJ-10)299,603,603
  603 PRINT 105,IENRL,ICHL,ICHX1(N+1),ICHX2(N)
  299 I(N+1)=(ICHX1(N+1)+ICHX2(N))/2
  300 CONTINUE
      L=L+1
  400 KK=1
      LL=1
      IA=0
      IB=0
  401 IF(K-KK)604,1,402
  402 IF(M(KK+1)-I(LL+1))501,501,503
  503 IA=IA+(I(LL+1)-I(LL))
      IB=IB+((I(LL+1)-I(LL))*II(LL))
      LL=LL+1
      GO TO 402
  501 IA=IA+(M(KK+1)-I(LL))
      IB=IB+((M(KK+1)-I(LL))*II(LL))
      ICA=IB/IA
      ITH1=(M(KK)*10)/6
      ITH2=(M(KK+1)*10)/6
      PUNCH101,ICHL,IDATL,ISOUL,IENRL,KK,M(KK),M(KK+1),M(KK),ICA,
     1ITH1,ITH2
      IA=0
      IB=0
      L=0
      I(LL)=M(KK+1)
```

```
      KK=KK+1
      GO TO 401
  100 FORMAT(I2,I6,I2,3I5,I3,1X,3I6)
  101 FORMAT(I2,I6,2I2,I3,6I6)
  102 FORMAT(15HPROGRAM ERROR 1)
  103 FORMAT(15HPROGRAM ERROR 4)
  104 FORMAT(23HTIMES MISMATCHED--EVENT,I4,5X,12HCHAN 3     T1,I6,5X,
     12HT2,I6/)
  105 FORMAT(23HTIMES MISMATCHED--EVENT,I4,4HCHAN,I2,4X,2HT1,I6,5X,
     12HT2,I6/)
  601 PRINT 102
      PAUSE
      GO TO 1
  604 PRINT 103
      PAUSE
      GO TO 1
      END
```

```
*0810
C  CONVERT BOEING KEYPUNCH DATA TO INPUT TO PASS 2   R. HUNTER  1-20-66
      DIMENSION I(15)
    1 READ 100,IEV,IDATE,IST,(I(N),N=1,12)
  100 FORMAT(I3,I5,I5,12I4)
      DO 2 N=1,12
      K=N-1
      K1=K*50
      K2=K*8333
      K3=K2/100
      K4=K1+50
      K5=K3+83
      K6=(IST*6) +5
      K7=K6/10
      ITM1=K7+K1
      ITM2=K7+K4
      ITH1=IST+K3
      ITH2=IST+K5
      IF(I(N))3,1,3
    3 PUNCH 101,IDATE,IEV,N,ITM1,ITM2,I(N),ITH1,ITH2
  101 FORMAT(2H06,I6,2H 3,2I5,9X,5I6)
    2 CONTINUE
      GO TO 1
      END
```

```
C      AIM 5 PLOT PROGRAM  JULY 7,65  R. PORTER
C      CONTROL CARDS COL. 2 (CHAN. NUMBER)
C      9=BEGIN EVENT    8=AT END OF EACH CHAN.   7=END OF EACH CHAN. FOR
C      PASS 1 PLOTS    0=BEGINING OF DECK FOR PASS 1 PLOTS
       DIMENSIONR3(200),RX(200),T1(200),T2(200)
       ISYM0=0
       ICON2=0
     2 IF(ICON2)4,3,4
     4 READ 110,ICH,T1M,T2M,RXC
       IF(ICH-8)5,7,9
     5 IF(ICH-7)6,43,70
     6 IF(ICH)200,7,200
   200 T1H=T1M/60.0
       T2H=T2M/60.0
       ICHL=ICH
       K=K+1
       RX(K)=RXC
       T1(K)=T1H
       T2(K)=T2H
       GO TO 4
    70 PRINT 112
   112 FORMAT(16HERROR IN PROGRAM)
       GO TO 6
     3 READ 100,ICH,IDATE,ISOUR,IEV,ICN,R3C,RXC,T1C,T2C
       IF(ICH-9)13,9,13
    13 IF(ICH-8)14,8,14
    14 IF(ICH-7)15,7,15
    15 IF(ICH)26,10,26
     9 ICON1=0
       ICON2=0
       K=0
       GO TO 2
    26 IDATL=IDATE
       ISOUL=ISOUR
       ICHL=ICH
       IEVL=IEV
       K=K+1
       R3(K)=R3C
       RX(K)=RXC
       T1(K)=T1C
       T2(K)=T2C
       GO TO 2
     8 IF(ICON1) 43,30,43
    30 T1A=T1(1)*10.0
       IT1A=T1A
       IT1B=IT1A-3
```

```
      T1C=IT1B
      T1S=T1C/10.0
      T2A=T2(K)*10.0
      IT2A=T2A
      IT2B=IT2A+5
      T2C=IT2B
      T2E=T2C/10.0
      PRINT 101
      PRINT 102,IEVL,ISOUL,IDATL,T1S,T2E
      PRINT 103
      PRINT 104
      GO TO 31
  101 FORMAT(80H=.=.=.
```

```
 53 IF(ICHL-4)54,55,56
 54 S=4.000
    GO TO 60
 55 S=2.000
    GO TO 60
 56 IF(ICHL-6)57,66,71
 57 S=0.000
    GO TO 60
 66 S=0.000
    PRINT 105
    GO TO 60
 71 PRINT 106
    GO TO 60
 60 RX(1)=RX(1)+S
    CALL PLOTU(T1(1),RX(1),ISYMC)
    KK=1
 61 CALL PLOTD(T2(KK),RX(KK))
    KK=KK+1
    IF(K-KK)63,62,62
 62 RX(KK)=RX(KK)+S
    CALL PLOTD(T1(KK),RX(KK))
    GO TO 61
 63 ICON1=1
    K=0
    GO TO 2
 10 ICON2=1
    PRINT 107
    PAUSE
    GO TO 2
  7 PRINT 111,IEVL
111 FORMAT(32HERROR IN CARD ARRANGEMENT EVENT ,I3,2X,20H(OR FOLLOWING
   1EVENT))
    GO TO 2
    END
```

3b Computation of Wavefront and Ionospheric Parameters

```
*0605
C       PLOT FOR E. FREMOUW BY B. MORTON.  22 FE. 66.
C       ARRAYS FOR INPUT AND RESULTS FOR 1 EVENT.
        DIMENSION B(11,3),R(11,9),C(11,3),T(11,3),A(11,3),P(11,9),CN(3),RN
       1(3),MA(3),MP(9)
C       SET EVENT TO 0 TO SHOW NO OLD EVENT IN MEMORY.
      1 LEVN=0
C       READ A CARD AS A PASS II OUTPUT CARD.
      2 READ 3,MDAY,MEVN,MFRN,TIM1,TIM2,NO
      3 FORMAT(2X,I6,2X,I2,I3,24X,2F6.3,28X,I1)
C       TEST TYPE OF CARD.
        IF(NO)6,6,4
C       ERROR FOR NEW CARD W/OUT OLD CARD.
      4 PRINT 5,MDAY,MEVN,MFRN
      5 FORMAT(14HCARD ERR, DAY ,I5,5HEVNT ,I3,5HFRNG ,I3)
        GO TO 2
C       READ A NEW INPUT CARD.
     60READ 7,NDAY,NEN,NEVN,NFRN,CN(1),CN(2),CN(3),BN,BE,RN(1),RN(2),
       1RN(3),RE,NO
      7 FORMAT(2X,I6,1X,I1,I2,I3,3F6.0,6F6.2,10X,I1)
C       TEST FOR NEW CARD.
        IF(NO)8,8,10
C       OLD CARD. SWITCH DATA FIELDS. GO READ A NEW CARD.
      8 MDAY=NDAY
        MEVN=NEVN
        MFRN=NFRN
        TIM1=BE*.1
        TIM2=RN(1)*.1
        GO TO 6
C       TEST ID FOR SAME EVENT AND FRINGE NO.
     10 IF(NEVN-MEVN)12,11,12
     11 IF(NFRN-MFRN)12,15,12
C       TYPE ERROR MESSAGE.
     12 PRINT 5,NDAY,NEVN,NFRN
        GO TO 2
C       IS THIS A NEW EVENT. GO PLOT LAST EVENT IF IT IS.
     15 IF(LEVN-MEVN)16,20,16
C       ANY OLD EVENT TO PLOT. LEVN = 0 IF NOT.
     16 IF(LEVN)17,17,50
C       INITIALIZE NEW EVENT.
     17 I=0
        LEVN=MEVN
        LKVN=NEN*100+NEVN
        LDAY=MDAY
C       STORE DATA FOR THIS FRINGE
     20 I=I+1
        T(I,1)=TIM1
        T(I,2)=.5*(TIM1+TIM2)
```

```
      T(I,3)=TIM2
      KEVN= NEN*100+NEVN
      C(I,1)=CN(1)
      C(I,2)=CN(2)
      C(I,3)=CN(3)
      B(I,1)=BN+BE
      B(I,2)=BN
      B(I,3)=BN-BE
C     TEST SIZE OF B. SPECIAL CASE WHEN B GR OR EQ 5.
      IF(BN-5.)25,21,21
   21 A(I,1)=.18
      A(I,2)=0.
      A(I,3)=0.
      DO 22 J=1,9
      R(I,J)= -9.99
   22 P(I,J)= -9.99
      GO TO 40
C     NORMAL CASE. B LESS THAN 5. TEST FOR B=0.
   25 A(I,1)=99.99
      A(I,2)=99.99
      IF(B(I,3))27,27,26
   26 A(I,1)=LOG(1./B(I,3)+1.)
   27 IF(BN)29,29,28
   28 A(I,2)=LOG(1./BN+1.)
   29 A(I,3)=LOG(1./B(I,1)+1.)
C     COMPUTE R S AND RHO S.
      R(I,1)=RN(1)+RE
      R(I,2)=RN(1)
      R(I,3)=RN(1)-RE
      R(I,4)=RN(2)+RE
      R(I,5)=RN(2)
      R(I,6)=RN(2)-RE
      R(I,7)=RN(3)+RE
      R(I,8)=RN(3)
      R(I,9)=RN(3)-RE
C     SET RHO=1. WHEN B IS LESS OR EQ ZERO.
      DO 31 J=1,8
   31 P(I,J)=1.
      IF(B(I,3))33,33,32
   32 X=A(I,1)
      Y1=B(I,3)
      P(I,1)=LOG(R(I,1)/Y1+1.)/X
      P(I,4)=LOG(R(I,4)/Y1+1.)/X
      P(I,7)=LOG(R(I,7)/Y1+1.)/X
   33 IF(BN)36,36,35
   35 X=A(I,2)
      P(I,2)=LOG(RN(1)/BN+1.)/X
```

```
      P(I,5)=LOG(RN(2)/BN+1.)/X
      P(I,8)=LOG(RN(3)/BN+1.)/X
   36 X=A(I,3)
      Y1=B(I,1)
      P(I,3)=LOG(R(I,3)/Y1+1.)/X
      P(I,6)=LOG(R(I,6)/Y1+1.)/X
      P(I,9)=LOG(R(I,9)/Y1+1.)/X
C     PUNCH 1 CARD OF RESULTS.
   40 MTIM=T(I,2)*1000.+.5
      DO 41 J=1,3
      MA(J)=A(I,J)*1000.+.5
      IF(MA(J))44,41,41
   44 MA(J)=MA(J)-1
   41 CONTINUE
      DO 42 J=1,9
      MP(J)=P(I,J)*1000.+.5
      IF(MP(J))45,42,42
   45 MP(J)=MP(J)-1
   42 CONTINUE
      PUNCH 43,MDAY,KEVN,MFRN,MTIM,(MA(J),J=1,3),(MP(J),J=1,9)
   43 FORMAT(I6,I4,I3,I6,3I5,9I4)
C     GO READ ANOTHER PAIR OF INPUT CARDS.
      GO TO 2
C     PLOT RESULTS FOR LAST EVENT. COMPUTE LENGTH OF PLOT.
C     INITIALIZE INPUT PLOT AND TYPE LABEL.
   50 PRINT 51,LKVN,LDAY,T(1,1),T(I,3)
   51 FORMAT(1X/1X/15HINPUT    EVENT ,I3,21H    DATE(DAY MON YR) ,I5/
     19X,16HSTART TIME (HRS),F7.3,12H    END TIME,F7.3/1X/1X)
C    COMPUTE SIZE PARAMETERS FOR PLOT.
      NX=10.*T(1,1)
      XL=NX
      XL=XL*.1
      NX=10.*(T(I,3)-XL+.2)
      XSIZE=NX+NX
      CALL INIT(0.,0.,1.,.996,XSIZE,10.)
C     DRAW SEPARATION LINE AND AXIS FOR UPPER PLOT.
      Y1=.5
   57 Y2=Y1+.5
      CALL PLOTU(Y1,5.,0)
      CALL PLOTD(Y2,5.)
      Y1=Y1+1.
      IF(Y1-XSIZE)57,58,58
   58 CALL PLOTU(XSIZE,7.,0)
      CALL PLOTD(0.,7.)
C     PLOT B VS T AND R VS C FOR ALL FRINGES.
      DO 60 J=1,I
      Y1=AMIN1(B(J,1),5.)
```

```
      IF(B(J,3))52,52,53
   52 Y3=B(J,2)
      GO TO 54
   53 Y3=B(J,3)
   54 Y2=B(J,2)
      X=20.*(T(J,2)-XL)
      CALL PLOTU(X,Y3,.)
      CALL PLOTD(X,Y1)
      CALL PLOTU(X,Y2,1)
C     PLOT R VS C. OMIT PLOT IF B GR OR EQ 5.
      IF(B(J,2)-5.)55,60,60
C     LOCATE C=0, R=1 POINT.
   55 NX=200.*(T(J,1)-XL)
      CZ=NX
      CZ=CZ*.1
      CALL PLOTU(CZ,9.,1)
      N=1
      DO 56 K=1,9,3
      Y1=7.+2.*R(J,K)
      Y2=7.+2.*R(J,K+1)
      Y3=7.+2.*R(J,K+2)
      Y1=AMAX1(AMIN1(Y1,10.),5.)
      Y2=AMAX1(AMIN1(Y2,10.),5.)
      Y3=AMAX1(AMIN1(Y3,10.),5.)
      X=CZ+.005*C(J,N)
      CALL PLOTU(X,Y3,0)
      CALL PLOTD(X,Y1)
      CALL PLOTU(X,Y2,1)
   56 N=N+1
   60 CONTINUE
      CALL PLOTU(XSIZE,0.,0)
C     PLOT OUTPUT IN SAME FORM AS INPUT. INITIALIZE AND TYPE LABEL.
      PRINT 61,LKVN,LDAY,T(1,1),T(I,3)
   61 FORMAT(1X/1X/15HOUTPUT   EVENT ,I3,21H    DATE(DAY MON YR) ,I5/
     1 19X,16HSTART TIME (HRS),F7.3,12H    END TIME,F7.3/1X/1X)
      CALL INIT(0.,0.,1.,.996,XSIZE,10.)
C     DRAW SEPARATION LINE AND AXIS FOR UPPER PLOT.
      Y1=.5
   64 Y2=Y1+.5
      CALL PLOTU(Y1,5.,0)
      CALL PLOTD(Y2,5.)
      Y1=Y1+1.
      IF(Y1-XSIZE)64,67,67
   67 CALL PLOTU(XSIZE,7.,0)
      CALL PLOTD(0.,7.)
C     PLOT THETA VS T AND RHO VS C FOR ALL FRINGES.
      DO 70 J=1,I
```

```
      X= 20.* (T(J,2)-XL)
      Y1=AMAX1(AMIN1(A(J,1),5.),0.)
      Y3=AMAX1(AMIN1(A(J,3),5.),0.)
      CALL PLOTU(X,Y3,0)
      CALL PLOTD(X,Y1)
C     MARK CENTER VALUE IF POSSIBLE.
      Y2=A(J,2)
      IF(Y2-5.)62,63,65
   62 IF(Y2)65,63,63
   63 CALL PLOTU(X,Y2,1)
C     OMIT RHO PLOT IF B IS EQ OR GR THAN 5.
   65 IF(B(J,2)-5.)66,70,70
   66 NX=200.*(T(J,1)-XL)
      CZ=NX
      CZ=CZ*.1
      CALL PLOTU(CZ,9.,1)
      N=1
      DO 68 K=1,9,3
      Y1=7.+2.*P(J,K)
      Y2=7.+2.*P(J,K+1)
      Y3=7.+2.*P(J,K+2)
      Y1=AMAX1(AMIN1(Y1,10.),5.)
      Y2=AMAX1(AMIN1(Y2,10.),5.)
      Y3=AMAX1(AMIN1(Y3,10.),5.)
      X=CZ+.005*C(J,N)
      CALL PLOTU(X,Y3,0)
      CALL PLOTD(X,Y1)
      CALL PLOTU(X,Y2,1)
   68 N=N+1
   70 CONTINUE
C     POSITION PEN FOR NEXT PLOT.
      CALL PLOTU(XSIZE,0.,0)
C     SET ID AND INDEX. GO HANDLE NEW SET OF DATA.
      GO TO 17
      END
```

BIBLIOGRAPHY

Aarons, J. (ed.) (1963), Radio Astronomical and Satellite Studies of the Atmosphere, North-Holland, Amsterdam.

---------, (1964), Geophysical Aspects of Radio Star and Satellite Scintillation Observations, paper presented at Ninth AGARD/IRC meeting "Spread F and its Effects upon Radiowave Propagation and Communication," Copenhagen.

Akasofu, S.-I. (1964), The Latitudinal Shift of the Auroral Belt, J.A.T.P., 26, 1167.

Ansari, Z. A. (1964), The Aurorally Associated Absorption of Cosmic Noise at College, Alaska, J. Geophys. Res., 69, 4493.

Appleton, E. V., R. Naismith and L. J. Ingram (1937), British Radio Observations during the Second International Polar Year, 1932-33, Phil. Trans. Roy. Soc. A, 236, 191.

Axford, W. I. and C. O. Hines (1961), A Unifying Theory of High-latitude Geophysical Phenomena and Geomagnetic Storms, Can. J. Phys., 39, 1433.

Basler, R. P. and R. N. DeWitt (1962), The Height of Ionospheric Irregularities in the Auroral Zone, J. Geophys. Res., 67, 587.

Bates, H. F. (1959), The Height of F-layer Irregularities in the Arctic Ionosphere, J. Geophys. Res., 64, 1257.

----------, (1960a), Correction to the paper "The Height of F-layer Irregularities in the Arctic Ionosphere," J. Geophys. Res., 65, 1304.

----------, (1960b), Direct HF Backscatter from the F Region, J. Geophys. Res., 65, 1993.

----------, (1961), The Slant E_s Echo - A High-frequency Auroral Echo, J. Geophys. Res., 66, 447.

Bendat, J. S. (1958), Principles and Applications of Random Noise Theory, Wiley, New York.

Bolton, J. G. and G. J. Stanley (1948), Variable Source of Radio Frequency Radiation in the Constellation of Cygnus, Nature, 161, 312.

Booker, H. G. and P. C. Clemmow, (1950), The Concept of an Angular Spectrum of Plane Waves and its Relation to that of a Polar Diagram and an Aperture Distribution, Proc. I.E.E., 97, Pt. 3, 11.

Booker, H. G. and W. E. Gordon (1950), The Theory of Radio Scattering in the Troposphere, Proc. I.R.E., 38, 401.

Booker, H. G. and H. W. Wells (1938), Scattering of Radio Waves by the F Region of the Ionosphere, Ter. Mag. and Atm. Elec., 43, 249.

Booker, H. G., J. A. Ratcliffe and D. H. Shinn (1950), Diffraction from an Irregular Screen with Applications to Ionospheric Problems, Phil. Trans. Roy. Soc. A, 242, 579.

Born, M. and E. Wolf (1959), Principles of Optics, Pergamon, New York.

Bowles, K. L. (1954), Doppler Shifted Radio Echoes from the Aurora, J. Geophys. Res., 59, 553.

Bowles, K. L. and R. Cohen (1962), Studies of Scattering Phenomena in the Equatorial Ionosphere Based upon VHF Transmissions across the Magnetic Equator, Some Ionospheric Results Obtained during the International Geophysical Year, edited by Beynon, Elsevier, Amsterdam, 192.

Bracewell, R. N. (1958), Radio Interferometry of Discrete Sources, Proc. I.R.E., 46, 97.

Bramley, E. N. (1951), Diversity Effects in Spaced-Aerial Reception of Ionospheric Waves, Proc. I.E.E., 98, Pt. 3 and 4, 19.

----------, (1953), Direction-finding Studies of Large-scale Ionospheric Irregularities, Proc. Roy. Soc. A, 220, 39.

----------, (1954), The Diffraction of Waves by an Irregular Refracting Medium, Proc. Roy. Soc. A, 225, 515.

----------, (1955), Some Aspects of the Rapid Directional Fluctuations of Short Radio Waves Reflected at the Ionosphere, Proc. I.E.E., 102, Pt. B, 533.

Briggs, B. H. (1958), A Study of the Ionospheric Irregularities which cause Spread-F Echoes and Scintillations of Radio Stars, J.A.T.P., 12, 34.

Briggs, B. H., G. J. Phillips and D. H. Shinn (1950), The Analysis of Observations on Spaced Receivers of the Fading of Radio Signals, Proc. Phys. Soc. B, 63, 106.

Briggs, B. H. and M. Spencer (1954), Horizontal Movements in the Ionosphere, Rep. Progr. Phys., 17, 245.

Calvert, W., R. W. Knecht and T. E. VanZandt (1964), Ionospheric Explorer I Satellite, First Observations from the Fixed-frequency Topside Sounder, Science, 146, 391.

Calvert, W. and C. W. Schmid (1964), Spread-F Observations by the Alouette Topside Sounder Satellite, J. Geophys. Res., 69, 1839.

Chandrasekhar, S. (1960), Radiative Transfer, Dover, New York.

Davenport, W. B. and W. L. Root (1958), Random Signals and Noise, McGraw-Hill, New York.

Dexter, D. L. and W. W. Beeman (1949), Multiple Diffuse Small Angle Scattering of X-rays, Phys. Rev., 76, 1782.

Douglas, J. N. (1965), 22.2 Mc/s Observations of Interplanetary Electron Inhomogeneities Using Jupiter as a Probe, paper presented at Second Symposium on Radio Astronomical and Satellite Studies of the Atmosphere, Boston.

du Castel, F. and P. Vila, (1964), Topside Spread-F and Field-aligned Structure, paper presented at the Ninth AGARD/IRC meeting "Spread F and its Effects upon Radiowave Propagation and Communications," Copenhagen.

Eckersley, T. L. (1937), Irregular Ionic Clouds in the E Layer of the Ionosphere, Nature, 140, 846.

----------, (1939), Scattering of Wireless Waves in the Ionosphere, Nature, 143, 33.

Eckersley, T. L., G. Millington and J. W. Cox, (1944), Ground and Cloud Scatter of Electromagnetic Radiation, Nature, 153, 341.

Ellison, T. H. (1952), The Propagation of Sound Waves through a Medium with Very Small Random Variations in Refractive Index, J.A.T.P., 2, 14.

Farley, D. T. (1963), A Plasma Instability Resulting in Field-Alinged Irregularities in the Ionosphere, J. Geophys. Res., 68, 6083.

Fejer, J. A. (1953), The Diffraction of Waves in Passing through an Irregular Refracting Medium, Proc. Roy. Soc. A, 220, 455.

Flood, W. A. (1963), A Study of Radio Star Fadeouts and their Application to Radar Resolution, J. Geophys. Res., 68, 4129.

Forsyth, P. A. and K. V. Paulson (1961), Radio-star Scintillations and the Auroral Zone, Can. J. Phys., 39, 502.

Fremouw, E. J. (1963), Radio-star Visibility Fades Observed in the Auroral Zone, (M.S. Thesis), Report UAG-R134, Geophysical Institute of the University of Alaska, College.

Furth, R. and D. K. C. MacDonald (1947), Statistical Analysis of Spontaneous Electrical Fluctuations, Proc. Phys. Soc., 59, 388.

Gotwols, B. L., W. C. Erickson, E. J. Fremouw and L. Owren (1966), Two Lunar Occultations of the Crab Nebula, submitted for publication in Pub. A.S.P.

Gröbner, W. and N. Hofreiter (1961), Integraltafel, Erster Teil, Springer-Verlag, Wien.

Hanbury Brown, R., H. P. Palmer and A. R. Thompson (1955), A Rotating-lobe Interferometer and its Application to Radio Astronomy, Phil. Mag., 46, 857.

Harang, L. and B. Landmark (1954), Radio Echoes Observed during Aurorae and Geomagnetic Storms using 35 and 75 Mc/s Waves Simultaneously, J.A.T.P., 4, 322.

Herman, J. (1964), Charged Particle Production Mechanism for Spread-F Irregularities, paper presented at Ninth AGARD/IRC meeting "Spread F and its Effects upon Radiowave Propagation and Communication," Copenhagen.

Hewish, A. (1951), The Diffraction of Radio Waves in Passing through a Phase-changing Ionosphere, Proc. Roy. Soc. A., 209, 81.

---------, (1952), The Diffraction of Galactic Radio Waves as a Method of Investigating the Irregular Structure of the Ionosphere, Proc. Roy. Soc. A, 214, 494.

Hey, J. S., S. J. Parsons, and J. W. Phillips (1946), Fluctuations in Cosmic Radiation at Radio-Frequencies, Nature, 158, 234.

Hines, C. O. (1964), Ionospheric Movements and Irregularities, Chapter 12 in Research In Geophysics, Vol. 1, edited by Odishaw, MIT Press, Cambridge.

Hodgman, C. D. (ed.) (1955), C.R.C. Standard Mathematical Tables, 10th ed., Chemical Rubber, Cleveland.

Hook, J. L. and L. Owren (1962), The Vertical Distribution of E-Region Irregularities Deduced from Scintillations of Satellite Radio Signals, J. Geophys. Res., 67, 5353.

Hunsucker, R. D. and L. Owren (1962), Auroral Sporadic-E Ionization, J. of Res. of the Nat. Bur. of Stds., 66D, 581.

Kelly, P. E. (1965), The Association between Radio and Visual Aurora, Can. J. of Phys., 43, 1167.

Kelso, John M. (1964), Radio Ray Propagation in the Ionosphere, McGraw-Hill, New York.

Knecht, R. W. (1956), Relationships between Aurora and Sporadic-E Echoes at Barrow, Alaska, J. Geophys. Res., 61, 59.

Koster, J. R. (1958), Radio Star Scintillations at an Equatorial Station, J.A.T.P., 12, 100.

Lansinger, J. and R. Gagnon (1961), Boeing Lobe-Sweep Interferometer System, Report D1-82-0122, Boeing Scientific Research Laboratories, Seattle.

Lawrence, R. S., J. L. Jespersen and R. C. Lamb (1960), Amplitude and Angular Scintillations of the Radio Source Cygnus A Observed at Boulder, Colorado, J. of Res. of the Nat. Bur. of Stds., 65D, 333.

Little, C. G. and A. C. B. Lovell (1950), Origin of the Fluctuations in the Intensity of Radio Waves from Galactic Sources, Jodrell Bank Observations, Nature, 165, 423.

Little, C. G. and A. Maxwell (1951), Fluctuations in the Intensity of Radio Waves from Galactic Sources, Phil. Mag., 42, 267.

Little, C. G., G. C. Reid, E. Stiltner and R. P. Merritt (1962), An Experimental Investigation of the Scintillation of Radio Stars Observed at Frequencies of 223 and 456 Megacycles per Second from a Location Close to the Auroral Zone, J. Geophys. Res., 67, 1763.

Lyon, A. J., N. J. Skinner and R. W. Wright (1962), The Geomorphology of Equatorial Spread-F, Some Ionospheric Results Obtained during the International Geophysical Year, edited by Beynon, Elsevier, Amsterdam, 153.

MacDonald, D. K. C. (1949), Some Statistical Properties of Random Noise, Proc. Cam. Phil. Soc., 45, 368.

McNicol, R. W. E. (1949), The Fading of Radio Waves of Medium and High Frequencies, Proc. I.E.E., 96, Pt. 3, 517.

Middleton, D. (1947), Some General Results in the Theory of Noise through Non-Linear Devices, Quart. of App. Math., V, 445.

----------, (1960), Introduction to Statistical Communication Theory, McGraw-Hill, New York.

Moorcroft, D. R. (1963), Radio Star Fadeouts on Phase-switching Interferometer Records, J. Geophys. Res., 68, 111.

Moorcroft, D. R. and P. A. Forsyth (1963), On the Relation between Radio Star Scintillations and Auroral and Magnetic Activity, J. Geophys. Res., 68, 117.

Muldrew, D. B. (1963), Radio Propagation along Magnetic Field-Aligned Sheets of Ionization Observed by the Alouette Topside Sounder, J. Geophys. Res., 68, 5355.

Munro, G. H. (1950), Travelling Disturbance in the Ionosphere, Proc. Roy. Soc. A, 202, 208.

Munroe, M. E. (1951), Theory of Probability, McGraw-Hill, New York.

Newman, P. and R. Penndorf (ed.) (1966), Spread F and its Effects upon Radiowave Propagation and Communication, proceedings of Ninth AGARD/IRC meeting held in Copenhagen in August of 1964, to be published by Gordon and Breach, New York.

Nichols, B. (1957), Drift Motions of Auroral Ionization, J.A.T.P., 11, 292.

Nichols, B. (1960), private communication to L. Owren.

Owren, L. (1960), High-latitude Radio Aurora, Ionospheric Radio, edited by Beynon, Elsevier, Amsterdam, 160.

Owren, L. (1963), Multiple Scattering in the Auroral Ionosphere, Proceedings of the International Conference on the Ionosphere, (held in London in July of 1962), edited by Stickland, Institute of Physics and Physical Society, London, 277.

Owren, L., E. J. Fremouw and R. D. Hunsucker (1964), Radio-star Scintillations and Spread F in the Auroral Zone, paper presented at the Ninth AGARD/IRC meeting "Spread F and its Effects upon Radiowave Propagation and Communication," Copenhagen.

Penfield, H. (1958), A Phase-tracking Interferometer, Proc. I.R.E., 46, 321.

Penndorf, R. (1962), Geographic Distribution of Spread-F in the Arctic, J. Geophys. Res., 67, 2279.

----------, (1964), Frequency of Spread-F Occurrence over Antarctica, paper presented at Ninth AGARD/IRC meeting "Spread F and its Effects upon Radiowave Propagation and Communication," Copenhagen.

Ratcliffe, J. A. (1948), Diffraction from the Ionosphere and the Fading of Radiowaves, Nature, 162, 9.

----------, (1956), Some Aspects of Diffraction Theory and their Application to the Ionosphere, Rpts. Prog. Phys., XIX, 188.

----------, (1959), The Magnetoionic Theory and its Application to the Ionosphere, Cambridge Univeristy Press, Cambridge.

Ratcliffe, J. A. and J. L. Pawsey (1933), A Study of the Intensity Variations of Downcoming Wireless Waves, Proc. Cambridge Phil. Soc., 29, 301.

Rice, S. O. (1944, 1945), Mathematical Analysis of Random Noise, Bell Syst. Tech. J., 23, 282 and 24, 46.

Ryle, M. (1950), Radio Astronomy, Rpts. Prog. Phys., 13, 184.

-------, (1952), A New Radio Interferometer and its Application to the Observation of Weak Radio Stars, Proc. Roy. Soc. A., 211, 351.

Ryle, M. and A. Hewish (1950), The Effects of the Terrestrial Ionosphere on the Radio Waves from Discrete Sources in the Galaxy, Mon. Not. R. Astr. Soc., 110, 381.

Ryle, M. and F. G. Smith (1948), A New Intense Source of Radio-Frequency Radiation in the Constellation of Cassiopeia, Nature, 161, 462.

Shimazaki, T. (1962), A Statistical Study of Occurrence Probability of Spread-F at High Latitudes, J. Geophys. Res., 67, 4617.

Smith, E. K. and S. Matsushita (ed.) (1962), Ionospheric Sporadic E, Macmillan, New York.

Smith, F. G. (1950), Origin of the Fluctuations in the Intensity of Radio Waves from Galactic Sources, Cambridge Observations, Nature, 165, 422.

Sokolnikoff, I. S. and R. M. Redheffer (1958), Mathematics of Physics and Modern Engineering, McGraw-Hill, New York.

Starr, A. T. (1953), Radio and Radar Technique, Pitman, London.

Thomas, J. A. (1962), Report on Recent E_S Work in Brisbane, Ionospheric Sporadic-E, edited by Smith and Matsushita, Macmillan, New York, 123.

Thomas, J. A. and E. K. Smith (1959), A Survey of the Present Knowledge of Sporadic-E Ionization, J.A.T.P., 13, 295.

Watson, G. N. (1948), A Treatice on the Theory of Bessel Functions, Macmillan, New York.

Wells, H. W., J. M. Watts and D. R. George (1946), Detection of Rapidly Moving Ionospheric Clouds, Phys. Rev., 69, 540.

Yeh, K. C. and G. W. Swenson (1964), F-region Irregularities Studied by Scintillation of Signals from Satellites, paper presented at Ninth AGARD/IRC meeting "Spread F and its Effects upon Radiowave Propagation and Communication," Copenhagen.